JYU DISSERTATIONS 569

Samu Forsblom

Design and Construction of Metal-Organic Polyhedra

UNIVERSITY OF JYVÄSKYLÄ
FACULTY OF MATHEMATICS
AND SCIENCE

JYU DISSERTATIONS 569

Samu Forsblom

Design and Construction of Metal-Organic Polyhedra

Esitetään Jyväskylän yliopiston matemaattis-luonnontieteellisen tiedekunnan suostumuksella
julkisesti tarkastettavaksi yliopiston Ylistönrinteen salissa Kem1
marraskuun 11. päivänä 2022 kello 12.

Academic dissertation to be publicly discussed, by permission of
the Faculty of Mathematics and Science of the University of Jyväskylä,
in Ylistönrinne, auditorium Kem1, on November 11, 2022 at 12 o'clock noon.

JYVÄSKYLÄN YLIOPISTO
UNIVERSITY OF JYVÄSKYLÄ

JYVÄSKYLÄ 2022

Editors
Manu Lahtinen
Department of Chemistry, University of Jyväskylä
Ville Korkiakangas
Open Science Centre, University of Jyväskylä

ISBN 978-951-39-9216-3 (PDF)
URN:ISBN:978-951-39-9216-3
ISSN 2489-9003

Permanent link to this publication: http://urn.fi/URN:ISBN:978-951-39-9216-3

ABSTRACT

Forsblom, Samu
Design and Construction of Metal-Organic Polyhedra
Jyväskylä: University of Jyväskylä, 2022, 212 p.
(JYU Dissertations
ISSN 2489-9003; 569)
ISBN 978-951-39-9216-3 (PDF)

This thesis describes the design, synthesis, and characterization of metallosupramolecular capsules and cages from cationic multivalent ligands. In the first half of the thesis, an overview of supramolecular and metallosupramolecular chemistry is provided with short introduction to different families of polyhedra as a basis for metal-organic polyhedra (MOPs). The thesis additionally presents a general design methodologies for the ligands and metal nodes suitable for obtaining supramolecular coordination complexes. This section also presents a brief review of metallosupramolecular cages and capsules obtained using O-donor based anionic ligands.

This is followed by a section outlining different strategies used for constructing discrete metallosupramolecular assemblies using N-donor based ligands. Strategies discussed involve two-component systems, utilizing edge-directed and face-directed approaches, together with multicomponent systems and subcomponent systems, with several examples shown. Various applications for supramolecular assemblies, such as storage containers and catalysis or reaction vessels are also demonstrated.

The second half of the thesis describes the methods used to synthesize and characterize supramolecular coordination structures obtained in the experimental part of the thesis using cationic multivalent N-donor ligands based on bipyridinium moiety. The assemblies include large supercationic $[M_6L_8]^{36+}$ cage-like assemblies containing Cu^{II} and Ni^{II} metal nodes, while encapsulating and coordinating various anions. Additionally, herein this work is reported for the first-time new type of dimeric capsules containing two different types of Zn^{II} metal nodes.

Keywords: metallosupramolecular chemistry, coordination chemistry, structural chemistry, self-assembly, crystallization, X-ray crystallography, N-donor ligands, quaternized ligands

TIIVISTELMÄ (ABSTRACT IN FINNISH)

Forsblom, Samu
Metalli-orgaanisten monitahokkaiden suunnittelu ja synteesi
Jyväskylä: University of Jyväskylä, 2022, 212 p.
(JYU Dissertations
ISSN 2489-9003; 569)
ISBN 978-951-39-9216-3 (PDF)

Tämä väitöskirja tarkastelee kationisiin monivarauksellisiin ligandeihin perustuvien metallisupramolekulaaristen kapselien ja häkkirakenteiden suunnittelua, synteesiä sekä karakterisointia. Väitöskirjan ensimmäisessä puolikkaassa annetaan yleiskuvaus supramolekyyli- ja metallisupramolekyylikemiasta, sekä esitellään lyhyt johdanto erilaisiin monitahokkaisiin kappaleisiin, joita voidaan käytetään metalli-orgaanisten monitahokkaiden suunnittelun pohjana. Väitöskirja käy läpi lisäksi yleisiä ligandien ja metallikeskusten suunnitteluperiaatteita, joiden avulla supramolekulaarisia koordinaatio-yhdisteitä voidaan syntetisoida. Tämä osio esittelee myös katselmuksen O-donoriligandeihin pohjautuvia metalli-orgaanisia häkkirakenteita sekä kapseleita.

Seuraava osio hahmottelee erilaisia strategioita, joita voidaan käyttää metallisupramolekulaaristen häkkirakenteiden valmistuksessa hyödyntäen N-donori pohjaisia ligandeja. Esiteltäviä strategioita ovat mm. kaksikomponentti sekä monikomponentti ja alakomponentti rakennejärjestelmistä, jotka hyödyntävät esimerkiksi särmä- ja tahko-ohjaavia ligandeja. Kirjallisen osuuden lopuksi käydään läpi muutamia metallisupramolekulaarisille kapseli- ja häkkirakenteille tyypillisiä sovelluskohteita, joista voidaan mainita mm. erilaiset vierasmolekyylien varastointiprosessit, nano- ja katalyysireaktorit sekä selektiivinen ionien talteenotto.

Väitöskirjan kokeellisessa osassa käydään läpi väitöskirjatyössä kehitettyjä polykationisten N-donori ligandeihin pohjautuvia supramolekulaaristen häkkirakenteiden rakennekemiallisia ominaisuuksia, syntetiikkaa sekä yhdisteiden termisiä ominaisuuksia. Työssä syntetisoidut ja karakterisoidut yhdisteet ovat superkationisia $[M_6L_8]^{36+}$ häkkimäisiä rakennelmia, jotka koostuvat joko Cu^{II} tai Ni^{II} metallikeskuksista sekä bipyridyyli-johdannaisesta ligandista. Väitöskirjassa raportoidaan myös ensimmäistä kertaa uudentyyppisiä dimeerisiä kapseleita, jotka pitävät sisällään sekä tetraedrisesti, että oktaedrisesti koordinoituneita Zn^{II} metallikeskuksia.

Avainsanat: metallisupramolekyylikemia, koordinaatiokemia, rakennekemia, itsejärjestäytyminen, kiteytyminen, röntgenkristallografia, N-donoriligandit, kvaternisoidut ligandit

Author's address

Samu Forsblom
Department of Chemistry
P.O. Box 35
FI-40014 University of Jyväskylä
Jyväskylä, Finland
samu.h.forsblom@jyu.fi

Supervisors

Adjucant Professor Manu Lahtinen
Department of Chemistry
University of Jyväskylä
Finland

Reviewers

Professor Risto Laitinen
Department of Chemistry
University of Oulu
Finland

Associate Professor Ivica Đilović
Faculty of Science
Department of Chemistry
University of Zagreb
Croatia

Opponent

Professor Guido Clever
Department of Chemistry and Chemical Biology
TU Dortmund University
Germany

PREFACE

"But, it was so artistically done"
-Mitth'raw'nuruodo

The work presented in this doctoral thesis was conducted at the Department of Chemistry at the University of Jyväskylä between 2015–2021. Financial support from the Academy of Finland, Magnus Ehrnrooth Foundation and the Department of Chemistry, University of Jyväskylä is gratefully acknowledged.

First and foremost, I want to express my deepest gratitude to my supervisor, Adjunct Professor Manu Lahtinen, for introducing me to the fascinating world of crystallography and for the opportunity to work in his group throughout these years, starting from my master's thesis.

Second, my reviewers, Professor Risto Laitinen and Associate Professor Ivica Đilović, are greatly acknowledged for the detailed pre-examination of my dissertation thesis and valued comments.

I also would like to thank all members of Lahtinen research group, past and present, as well as other co-workers in the Department of Chemistry for inspiring conversations and memories accumulated over the years.

Finally, I would like to thank my family and friends for all the timely and not-so-timely distractions during this hectic time. My sisters, thank you for occasional distractions and stupid questions. My parents, thank you for your continuous support, patience, love and for believing in me. I would never have made it here without you, and for that I'm eternally grateful.

Jyväskylä, July 2022
Samu Forsblom

CONTENTS

ABBREVIATIONS, ACRONYMS AND DEFINITIONS

[9]aneS_3	1,4,7-Trithiacyclononane
A	Anion
a^3s	anion-anion-anion sandwich
Ac	Acetyl
acac	Acetylacetone
A_x	Atom or molecule in the axial-position of a metal node
bdc	Benzenedicarboxylic acid
bpy	Bipyridine
btc	Benzenetricarboxylic acid
Bu	Butyl
cdc	Carbazoledicarboxylic acid
cod	1,5-Cyclooctadiene
Cp	Cyclopentadiene
DCM	Dichloromethane
DMA	Dimethylacetamide
dmesp	2,9-Dimesityl-1,10-phenathroline
DMF	Dimethylformamide
DMSO	Dimethyl sulfoxide
dppf	1,1'-Bis(diphenylphosphino)ferrocene
en	1,2-ethylenediamine
Et	Ethyl
Et_2O	Diethyl ether
Et_3N	Triethylamine
EtOAc	Ethyl acetate
EtOH	Ethanol
HB	Hydrogen bond
hmtp	2,3,6,7,10,11-Hexamethoxytriphenylene
HOAc	Acetic acid
^{i}Pr	iso-Propyl
IUPAC	International Union of Pure and Applied Chemistry
L	Ligand
M	Metal
Me	Methyl
MeCN	Acetonitrile
MeOH	Methanol
MOF	Metal-organic framework
MOP	Metal-organic polyhedra
MS	Mass Spectrometry
^{n}Bu	"normal" (linear chain) Butyl
NMP	*N*-Methyl-2-pyrrolidone
NMR	Nuclear Magnetic Resonance
NTf_2	Bis(trifluoromethane)sulfonylimide (Bistriflimide)
OAc	Acetate

octapy	Octapyridine (tetrakis(bipyridine))
OTf	Trifluoromethanesulfonate (Triflate)
PEt_3	Triethylphosphine
Ph	Phenyl
phen	1,10-Phenanthroline
PMe_3	Trimethylphosphine
PPh_3	Triphenylphosphine
$PPhMe_2$	Dimethylphenylphosphine
Pr	Propyl
R	Organic group / ligand
RCSB PDB	Research Collaboratory for Structural Bioinformatics Protein Data Bank
SBU	Secondary building unit
SCC	Supramolecular Coordination Complex
SCXRD	Single-crystal X-ray diffraction
SM	Solvent mask
S-nicI	(–)-*N*'-Methylnicotinium iodide
spy	Sexipyridine (trisbipyridine)
tapp	Tetrakis(4-aminophenyl)porphyrin
^{t}Bu	*tert*-Butyl
TEG	Triethylene glycol
THF	Tetrahydrofuran
X	Halogen / Halide
XB	Halogen bond

1 INTRODUCTION

1.1 Supramolecular and metallosupramolecular chemistry

One of the main contributors to the field of supramolecular chemistry, Jean-Marie Lehn defined supramolecular chemistry as "…*chemistry of the intermolecular bond, covering the structures and functions of the entities formed by association of two or more chemical species.*"[1] in his Nobel lecture after winning the Nobel Prize in Chemistry 1987 together with Donald Cram and Charles Peterson for "development and use of molecules with structure-specific interactions of high selectivity". Cram and co-workers[2,3] described the same area as *host-guest chemistry*, and yet another way to express supramolecular chemistry is to say that it is *chemistry beyond the molecule*, a way to develop highly complex systems from components held together *via* noncovalent intermolecular bonds.[4] The roots of supramolecular chemistry date back to 1894 when Emil Fischer introduced a lock and key-principle which describes the basic concepts of what later was dubbed host-guest chemistry, where a molecule ('host') binds to another molecule ('guest'), forming a 'host-guest' complex.[5,6]

The construction of supramolecular entities and the nature of supramolecular chemistry rests on the making and breaking of noncovalent intermolecular bonds. These bonds typically have lower energies than covalent bonds, but more importantly, they are reversible which provides the supramolecular complex an ability to break and reform again. This is the reason why noncovalent intermolecular bonds are also referred as *weak interactions*. This term encompasses a large array of different interactions such as Coulombic ion-ion, ion-dipole, dipole-dipole, and van der Waals interactions, together with π-interactions (cation-π, anion-π and π-π), the closed shell or metallophilic interactions and the hydro- or solvophobic interactions.[7] Along these there is the all-famous hydrogen and halogen bonding that are also classified under non-covalent interactions. Out of these interactions the ion-based Coulombic interactions are comparable in strength to covalent bonding and hydrogen bonding is also shown to occasionally rival that of weak covalent bonding.[8,9]

Though sometimes classified as an ion-dipole interaction, the coordinative or *dative* bond between metal ion and ligand(s) are closer to features of covalent bonds as they also involve a shared electron pair. Unlike a covalent bond, where two molecular entities both donate a single electron each, the coordinative bond is formed when only one of the molecular entities donate both electrons essentially forming a Lewis acid-base pair.[10] These coordination compounds are often formed via irreversible reactions, whereas classically formed supramolecular assemblies are typically constructed by reversible reactions. Due to resulting assemblies obtained via coordinative bonds resembling to that of classically formed supramolecular assemblies, this has led to the formation of the growing field of *metallosupramolecular chemistry*.[11] Research in this field is mainly focused on either infinite one-, two-, or three-dimensional networks known as *metal-organic frameworks* (*MOF*s) or finite assemblies such as cages, capsules, cylinders or macrocycles known as *supramolecular coordination complexes* (*SCC*s) that usually have polygonal or polyhedral geometries. It is noteworthy that it is possible to create analogous supramolecular assemblies using different interactions; for example, a tetrahedron can be obtained either via hydrogen bonding (*HB*)[12] (1) or metal coordination[13] (2). In addition, Turunen *et al*. have recently shown that halogen bonding (*XB*)[14] (3) is also applicable interaction (Figure 1) for making cage-like structures. As noted above, there is a wide range of different assemblies classified under SCCs, of which this dissertation will mostly focus on a subsection of SCCs: a cage-like *metal-organic polyhedra* (*MOP*s).

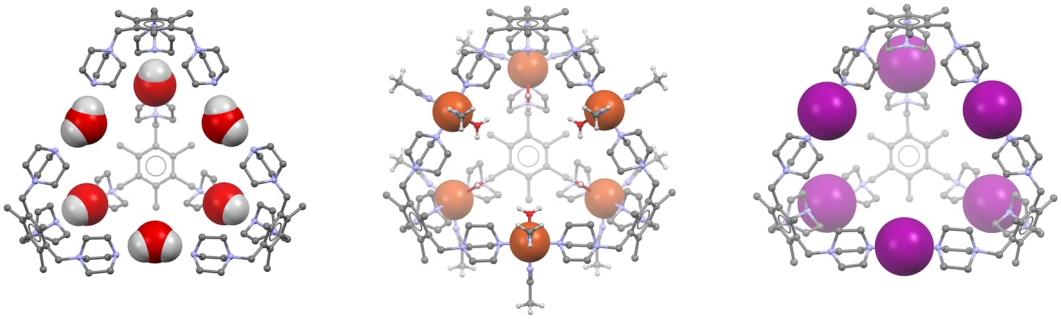

1 2 3

FIGURE 1 Crystal structures of analogous supramolecular tetrahedrons obtained using different interactions; 1) HBs *via* water molecule nodes,[12] 2) dative bonds *via* Cu^{II} nodes[13] and 3) XBs *via* iodonium (I^+) nodes.[14] Anions, free solvent molecules and ligand hydrogen atoms are omitted for clarity.

1.2 Polyhedra

The natural world contains a large number of polyhedral cage-like structures, such as C_{60}-fullerene (truncated icosahedron)[15], icosahedral capsid of human adeno-virus[16] and dodecahedral procapsid of cystovirus ϕ6[17] (Figure 2) to name a few. In order to design metallo-organic polyhedra, it is important to first define what a polyhedron is. In geometrical terms, a polyhedron is a three-dimensional (3D) solid with flat polygonal faces, straight edges and sharp vertices (*i.e.* corners). These solids thus represent a concave, finite 3D object with a clearly defined border between interior and exterior space, and so are excellent models for designing chemical cages. As there are essentially infinite ways to organize polygons into different kinds of polyhedra (or polyhedrons), these solids are classified under unique families, with each family having a different set of rules that need to be fulfilled to be qualified as a member of that particular family of polyhedra. To fully utilize these geometrical solids as a starting point for cage design, it is important to understand how these three-dimensional objects are constructed from simple straight lines. And so, the simplest solids, the classical Platonic and Archimedean solids will be described below among other noteworthy solids.

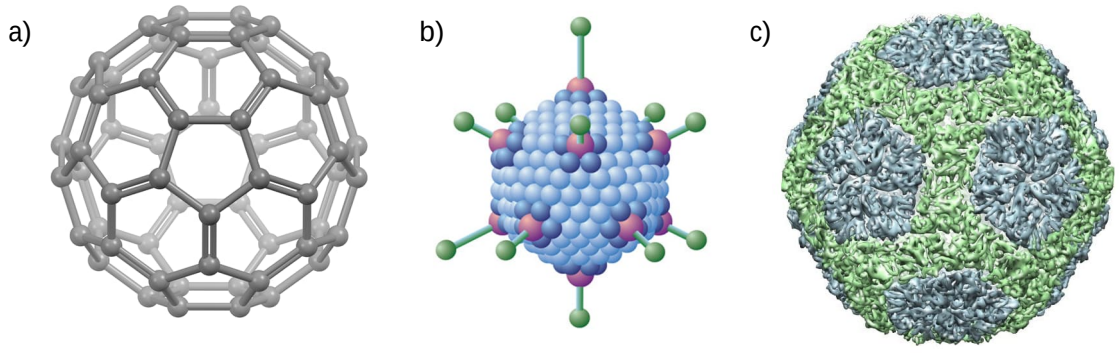

FIGURE 2 a) Buckminsterfullerene (C_{60}), b) schematic representation of the icosahedral viral capsid (adapted from ref.[16] Copyright © 2021 The Authors), and c) procapsid of a cystovirus ϕ6 (Image from the RCSB PDB (rcsb.org) of PDB ID 4BTQ), original publication ref.[17]

1.2.1 Platonic solids

A Platonic solid is a regular, three-dimensional convex polyhedron that is made by arranging polygonal faces in a manner that all edges and vertices are equivalent.[18,19] These polygonal faces are required to be regular *i.e.* they must be equiangular (all angles are identical) and equilateral (all sides have the same length). Additionally, polygonal faces must be congruent (identical shape and size) and the same number of faces need to be adjoined in each vertex. To achieve a convex corner required, the sum of the angles around each vertex must be less than 360°. To achieve this, equilateral triangles can be adjoined in three different ways, with each vertex containing either three, four, or five polygons. While equilateral squares and pentagons can be adjoined only in a single manner, with each vertex containing three polygons, any polygon with six or more sides will always have a sum angle greater or equal to 360° around each vertex and thus is unable to form a convex corner alone. The number of Platonic solids is thereby limited to five possible solids (Figure 3, Table 1): tetrahedron, octahedron and icosahedron constructed *via* equilateral triangles, cube *via* equilateral squares and dodecahedron *via* equilateral pentagons.

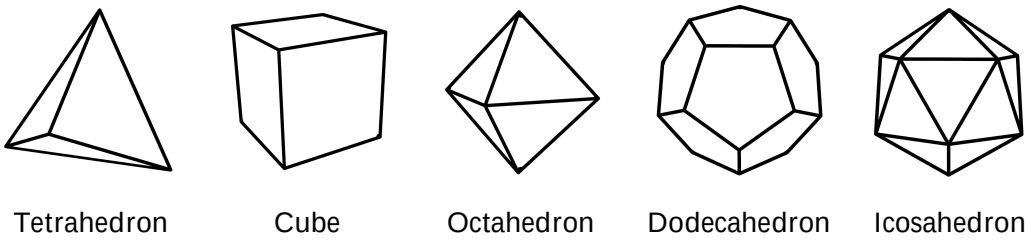

FIGURE 3 The five Platonic solids.

TABLE 1 Platonic solids.

Solid	Vertices	Edges	Faces	Face polygon
Tetrahedron	4	6	4	Triangle
Cube	8	12	6	Square
Octahedron	6	12	8	Triangle
Dodecahedron	20	30	12	Pentagon
Icosahedron	12	30	20	Triangle

1.2.2 Archimedean solids

An Archimedean solid is a semiregular, convex polyhedron made by arranging regular polygon faces in a manner that all edges and vertices are equivalent.[18,19] Unlike Platonic solids, the Archimedean solids are constructed using two or more different regular polygons and this will increase the number of possible combinations to 13 (Figure 4, Table 2) which all can be derived from at least one Platonic solid either by twisting the faces or by truncation of the solid. This also results in two chiral members, the snub cube and the snub dodecahedron.

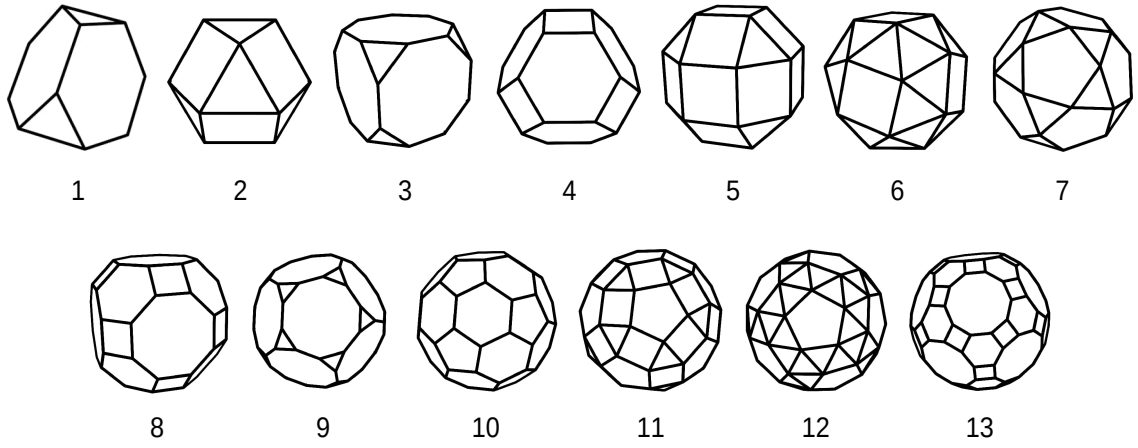

FIGURE 4 The 13 Archimedean solids: truncated tetrahedron (1), cuboctahedron (2), truncated cube (3), truncated octahedron (4), rhombicuboctahedron (5), snub cube (6), icosidodecahedron (7), rhombitruncated cuboctahedron (8), truncated dodecahedron (9), truncated icosahedron (10), rhombicosidodecahedron (11), snub dodecahedron (12), rhombitruncated icosidodecahedron (13).

TABLE 2 Archimedean solids.

Solid	V	E	f_3	f_4	f_5	f_6	f_8	f_{10}
(1) Truncated tetrahedron	12	18	4	–	–	4	–	–
(2) Cuboctahedron	12	24	8	6	–	–	–	–
(3) Truncated cube	24	36	8	–	–	–	6	–
(4) Truncated octahedron	24	36	–	6	–	8	–	–
(5) Rhombicuboctahedron	24	48	8	18	–	–	–	–
(6) Snub cube	24	60	32	6	–	–	–	–
(7) Icosidodecahedron	30	60	20	–	12	–	–	–
(8) Rhombitruncated cuboctahedron	48	72	–	18	–	8	6	–
(9) Truncated dodecahedron	60	90	20	–	–	–	–	12
(10) Truncated icosahedron	60	90	–	–	12	20	–	–
(11) Rhombicosidodecahedron	60	120	20	30	12	–	–	–
(12) Snub dodecahedron	60	150	80	–	12	–	–	–
(13)Rhombitruncated icosidodecahedron	120	180	–	30	–	20	–	12

The number of: vertices (V), edges (E) and faces (f_n), where n defines the number of sides of the face (f_3: triangle, f_4: square, f_5: pentagon, f_6: hexagon, f_8: octagon, f_{10}: decagon)

1.2.3 Prisms and antiprisms

The two infinite families of convex polyhedra made from regular polygons are known as prisms and antiprisms.[18] In prisms the bases are congruently joined by *n* squares joined in corresponding sides of the two *n*-gon bases and in antiprisms the bases are related by a twist and connected by an alternating band of *2n* triangles. Unlike in Platonic or Archimedean solids the faces do not have to be equilateral (Figure 5, Table 3).

TABLE 3 Prisms and antiprisms.

Solid	Vertices	Edges	Base	Faces
Prism	2*n*	3*n*	2 *n*-gons	*n* squares (or rectangles)
Antiprism	2*n*	6*n*	2 *n*-gons	2*n* triangles

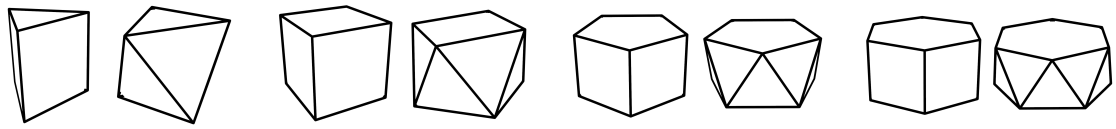

Triangular prism + antiprism | Square prism + antiprism | Pentagonal prism + antiprism | Hexagonal prism + antiprism

FIGURE 5 Prisms and antiprisms.

1.2.4 Pyramids and bipyramids

The other polyhedra worth mentioning are pyramids and bipyramids (Figure 6), both of which belong to a family of Johnson solids[20] containing a total of 92 solids. Pyramids are formed by connecting the faces of an *n*-gon base to a single point, the apex, while bipyramids have the second apex mirrored on the other side of the base. Thus each face is a triangle and the number of sides is dependent on the base of a pyramid or bipyramid.

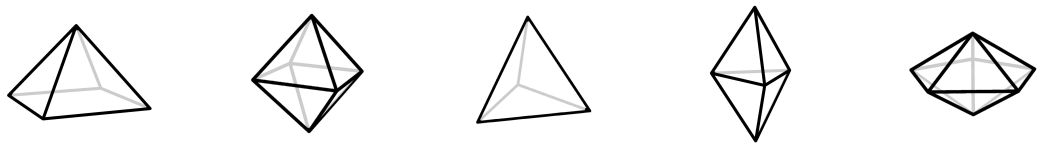

Square pyramid | Square bipyramid | Triangular pyramid | Trigonal bipyramid | Pentagonal bipyramid

FIGURE 6 Pyramids and bipyramids.

1.2.5 Goldberg polyhedra

A relatively new family of solids is the Goldberg polyhedra, first described in 1937, a group of solids consisting of hexagons and pentagons.[21,22] Each Goldberg polyhedra will always contain 12 pentagons whereas the number of hexagons can be anything as long as each of the vertices are trivalent and the polyhedron has rotational symmetry of the icosahedron. This in turn makes Goldberg polyhedra into a family containing infinite number of solids. The Goldberg polyhedra is described as GP(*a*,*b*), where *a* and *b* indicate a '60-degree knights move' required to 'travel' between two pentagons. The simplest one of these is GP(1,0) where all pentagons are connected with no hexagons present, a solid better known as a dodecahedron. Similarly, the truncated icosahedron can be described as GP(1,1). An easy way to visualize these polyhedra is to lay them out in a 2D-plane as a schematic representation, as shown in Figure 7. GP(7,0) (Figure 7a) requires to move only one direction, whereas GP(2,4) (Figure 7b) requires the 60-degree turn. The Goldberg polyhedra have also been expanded to tri- and tetravalent systems consisting of squares and triangles.[23] As an example schematic representations mirror symmetrical tetravalent Goldberg polyhedra tet-G(2,4) and tet-G(4,2) are shown in Figures 7c and 7d respectively.

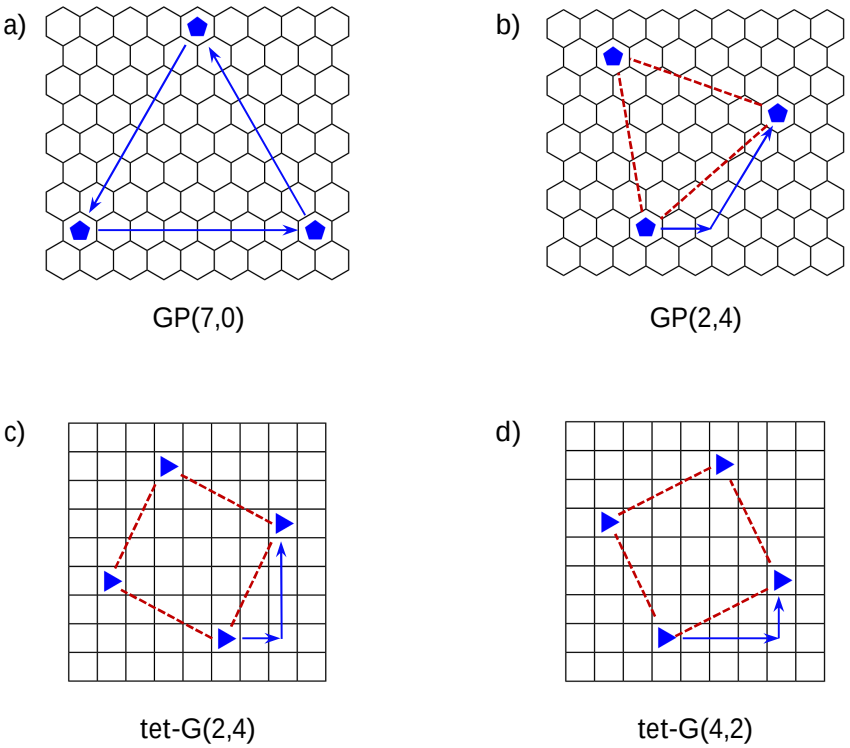

FIGURE 7 a) and b) Schematic representation of classical Goldberg polyhedra, c) and d) schematic representation of tetravalent Goldberg polyhedra.

2 DESIGN METHODOLOGIES

2.1 Metal nodes

Metals are an integral part of metallosupramolecular chemistry and the metals used in the synthesis of MOPs are typically transition metals, which according to the Gold Book of IUPAC (International Union of Pure and Applied Chemistry)[10] are elements whose atom has an incomplete *d* sub-shell, or which can give rise to cations with an incomplete *d* sub-shell. This encompasses groups 3-12 with platinum and palladium being the most prevalently used metals. Also, a few examples of post-transition metal (*e.g.* Al, Ga, Sn) and silicon (Si) based structures exist. Transition metals are preferred due to their known coordination geometry, usually binding preferences of either 4 or 6 ligands, and thus forming predictable structures with various ligands. Key features of metal nodes will be discussed below.

2.1.1 Electronic configuration of metal node

Electronic configuration depicts the number and distribution of electrons residing on an atom taking the oxidation state into account. When it comes to the transition metals, the outermost electron shell and *d*-electrons from previous electron shell are taken into account in chemical bonding. The remaining electrons are considered to act as core electrons not participating in bonding and can be described with an electronic configuration of preceding noble gas,[24] for example Cu: $1s^2 2s^2 2p^6 3s^2 3p^6 3d^{10} 4s^1$ or $[Ar]3d^{10}4s^1$. Since the metals used in MOP synthesis are essentially always positively charged, *i.e.* cations, the electron configuration is further reduced to include only the electrons from the outermost *d*-orbital, for example electron configuration for Cu^{2+} cation is $[Ar]3d^9$. The transition metals can thus be described as d^n (n = 1–10) metals depending on their electronic configuration.

2.1.2 Coordination geometry

In a vacuum the five *d*-orbitals of a free atom, shown in Figure 8a, are degenerated in energy but when a coordination complex is formed the atom is surrounded by ligands, which leads to a collapse of orbital degeneration as the *d*-orbitals interact with the ligands. Crystal field theory[25] describes the collapse of degeneration by treating the ligand lone pairs as negative point charges located around positively charged metal atom repelling the metal ions *d*-electrons; on an assumption of purely ionic metal-ligand interactions. The orbitals are then filled with electrons, the number of which is dependent on metal in question, starting from the lowest in energy.

The three most relevant geometries for the perspective of this thesis are octahedral, square-planar and tetrahedral, of which the first two are the most conventional motif found in MOPs. The approximations of *d*-orbital diagrams are depicted in Figure 8b. For the boundary surfaces, it is assumed that all ligands are identical and all M-L -distances are identical, which in reality is not often true. The diagrams also do not take the repulsion of *d*-electrons into account.[26]

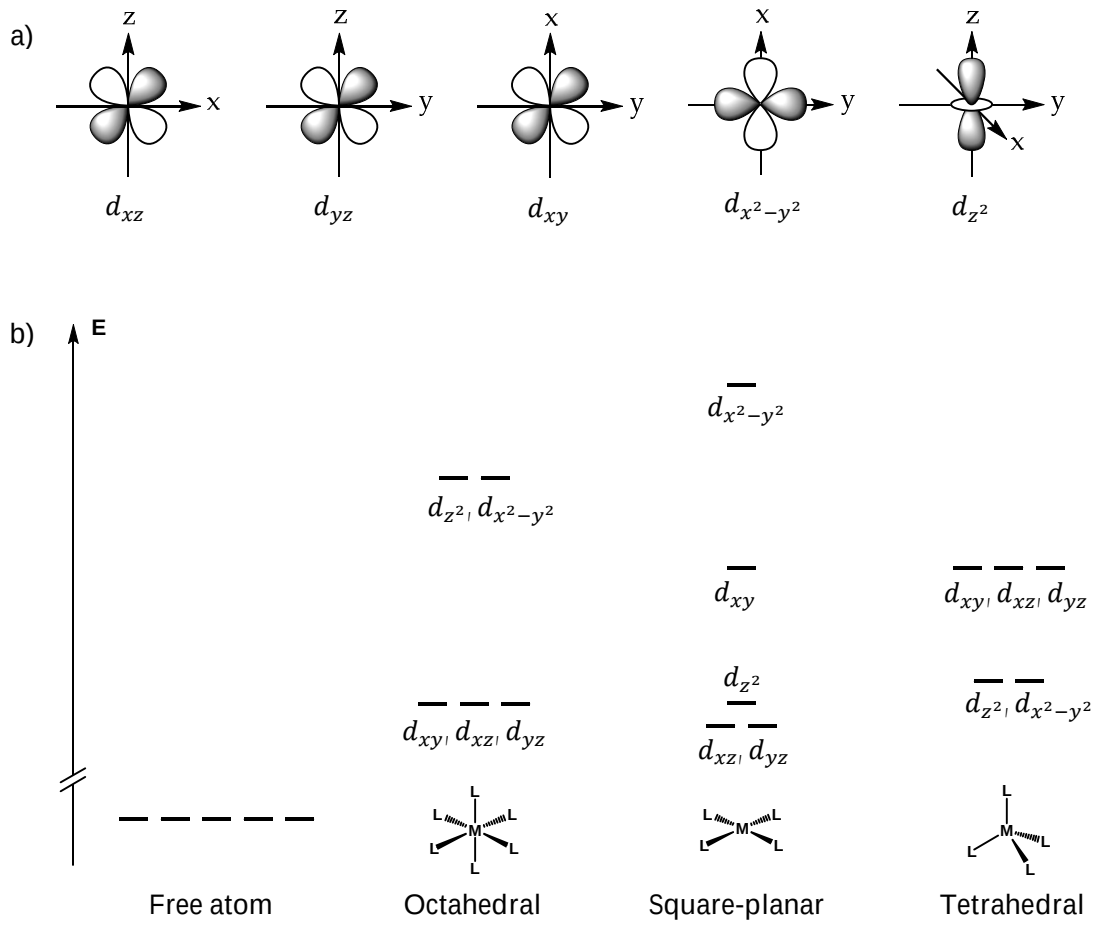

FIGURE 8 a) The five *d*-orbital diagrams, b) splitting of *d*-orbitals in energy in case of octahedral, square planar and tetrahedral complexes according to crystal field theory.

The characteristic features of splitting of a particular *d*-orbital are affected by the specific properties of the ligands, nature of metal ion and its oxidation state. For a more detailed description of the bonding occurring between ligands and the metal center, ligand field theory[27] can be used as it combines both crystal field and molecular orbital theories. However, the somewhat rudimentary models of the crystal field orbital splitting theory are sufficiently representative for the dissertation. It is noteworthy to mention that the reason why Pd^{II} and Pt^{II} complexes are square-planar is due to that a d^8 configuration, coupled with a strong crystal field, favors the formation of square-planar complexes. The tendency of this is enhanced with the 4*d* and 5*d* transition metal ions because of their larger ion size and thus greater ease of electron pairing.

2.1.3 Unprotected vs. protected metal nodes

Unprotected or 'naked' metal nodes are metal ions obtained from metal salts such as $FeCl_3$, $Cu(OTf)_2$ or $Pd(BF_4)_2(MeCN)_4$, *i.e.* metal compounds containing only poorly coordinating counter anions and possible complexed solvent molecules. These metal nodes have all their coordination sites available for complexation with only restricting factors being the steric hindrance of a targeted ligand or potential interactions with solvent molecules instead of the targeted ligands, as well as overly coordinating anions not releasing the metal center for complexation. In order to obtain finite and concave three-dimensional assemblies sometimes it is necessary to restrict the coordination geometry of a metal node, as using unprotected metal ions is not always favorable. The metal coordination restriction technique is particularly necessary when attempting to create MOPs using ligands that would otherwise lead to the formation of infinite networks when unprotected metal nodes are used in complexation. Commonly this is done by capping two of the coordination sites of a square-planar geometry-favoring metal ion with a chelating secondary ligand, such as 2,2'-bipyridine (2,2'-bpy), 1,2-ethylenediamine (en) or its derivatives (Figure 9). Bulky groups such as triethylphosphine (PEt_3) can also be used to obtain *cis*-protected metal nodes that will act as a 90° corner piece in the complexation of cage-like structures. It should also be noted that with secondary ligands the binding to the metal center needs to be stronger than that of the primary ligands. Otherwise, primary ligands may replace protecting groups during complexation, thereby negating their capping function.

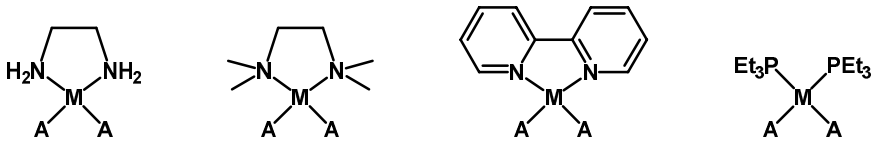

FIGURE 9 Examples of *cis*-protected metal nodes, where M is either Pt^{II} or Pd^{II} and A represents anion such as nitrate (NO_3^-), triflate (OTf^-) or halide (usually Cl^-).

An example of MOP utilizing capped octahedral metal node is Ru^{II}-based cube (4) reported by Roche *et al*.[28] This cube is formed when [([9]aneS_3)Ru(DMSO)Cl_2] is reacted with excess 4,4'-bipyridine (4,4'-bpy, N1) in solution for a few weeks as the exchange rates of DMSO and chlorides are slow. As the ([9]aneS_3) acts a *fac*-capping secondary ligand, thereby occupying three of the Ru^{II} octahedral coordination sites, the remaining three coordination sites of the cube are occupied by three 4,4'-bipyridines all at about 90° angle with the respect to each other (Scheme 1). Albeit Roche *et al*. were unable to crystallize the cube itself, they manage to obtain crystal structure of a corner, namely, [([9]aneS_3)Ru(4,4'-bpy)$_3$]$(PF_6)_2$, showing that the 4,4'-bipyridines are indeed ≈ 90° angle with the respect to each other.

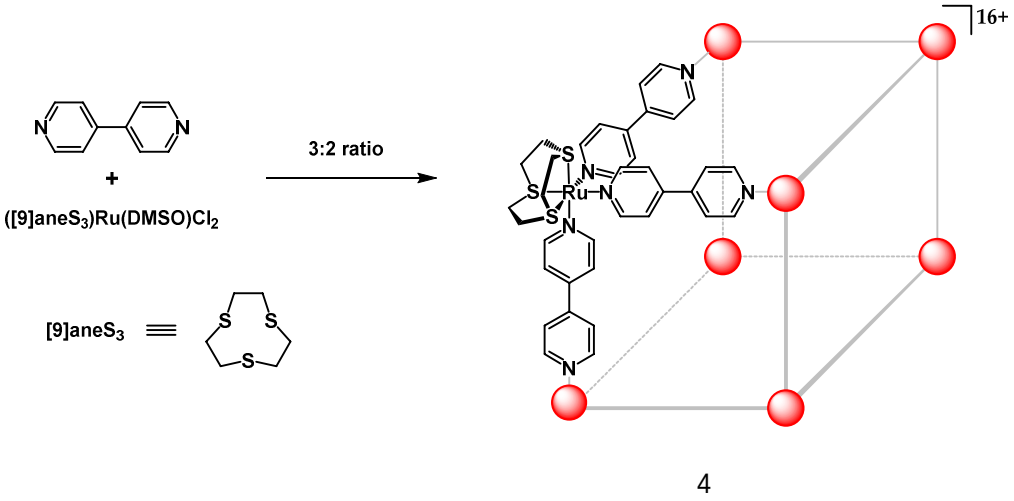

4

SCHEME 1 Formation of metallosupramolecular M_8L_{12} positively charged (16+) cube.

Stang's group has utilized a series of organoplatinum compounds as metal nodes for various caged (Figure 10). Examined compounds are something of a hybrid between a ligand and a protected metal node, where the platinum is directly bonded to an organic linker and its coordination geometry is further restricted using either PEt_3 or triphenylphosphine (PPh_3) groups. Depending on the organic linker, the binding angle of metal is 0°, 60°, 120°, or 180° and the nodes are either bi- or tridentate. These 'nodes' have been employed for the creation of truncated tetrahedral,[29] cuboctahedron,[30] dodecahedron[31] and trigonal prisms.[32]

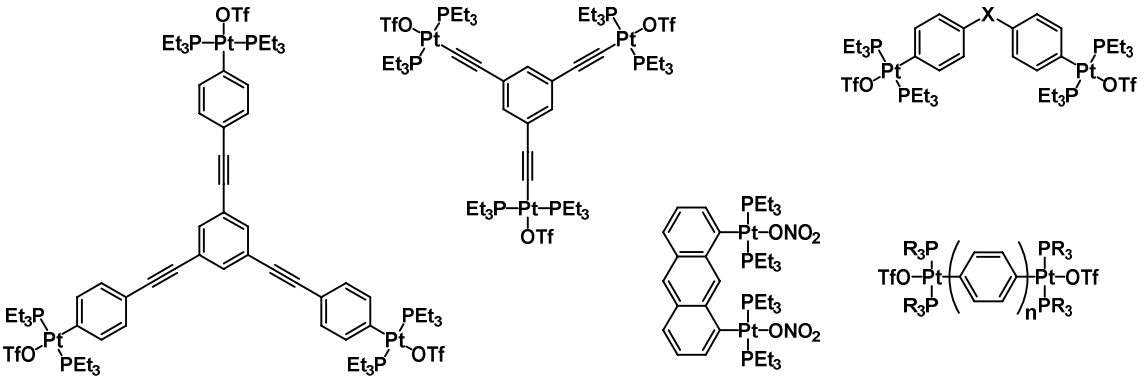

FIGURE 10 Examples of organoplatinum metal nodes.

2.2 General design principles of ligands

In principle, there are essentially limitless number of different ligands that can potentially be used for obtaining MOPs by reacting the targeted ligands with metal nodes. Thus, some general requirements for ligands need to be accomplished to successfully obtain MOPs more systematically.

Firstly, the ligand must act as a Lewis base. As the coordinative bond is based on Lewis acid-base theory, and the metal node is acting as a Lewis acid this naturally means that ligand must then acts as Lewis base; *i.e.* ligand must contain a free electron pair that acts as a metal binding site. This means that even though pure hydrocarbon ligand can form complexes with metals, for example Pt^{II} complex with 1,5-cyclooctadiene[33], they are generally not suitable for creating MOPs. Instead, the ligand needs to contain heteroatoms that act as a binding site, and essentially all ligands used in the construction of MOPs contain either nitrogen or oxygen atoms. When nitrogen acts as a binding site, the ligand is an N-donor, and O-donor when oxygen acts as a binding site. Alternatively, ligand can also contain both, for example in case of isonicotinic acid. In the MOP synthesis, the N-donor-based ligands are more prevalent than O-donor-based ligands.

Secondly, the ligand must be at least ditopic *i.e.* contain at least two binding sites, as ligand with a single site would act as a termination point instead of providing a continuous structure, and so ligands, such as phenylpyridine are thus excluded from suitable ligand candidates (Figure 11). Depending on the type of structure sought (see Section 3), the ligands in MOP synthesis typically contain 2, 3, 4 or 6 binding sites in a single ligand. To achieve continuous extended network of M–L -interactions the ligands must be overall nonchelating, which is the last requirement for suitable ligands.

According to the definition by IUPAC[10], *chelation* occurs when two or more separate binding sites within the same ligand form bonds to a single central atom. Meaning that the binding sites are converging to a single node instead of diverging into separate ones.[34] In a similar fashion to the previous requirement, if all binding sites coordinate to a single metal node this will again act as a termination point. For example, even though ligands such as terpyridine and 2,2'-bipyridine fulfill the previous two requirements, the binding sites in these molecules are typically converging to a single point as shown in Figure 11. The ligand can contain chelating sites as long as there are at least two separate diverging sites binding to different metal nodes. Although fully chelating ligands are excluded from being suitable ligand candidates for MOP synthesis it does not mean that these ligands are unusable; as mentioned previously, bi- and tridentate converging ligands can be used as secondary ligands to partially restrict the coordination geometry of a metal node.

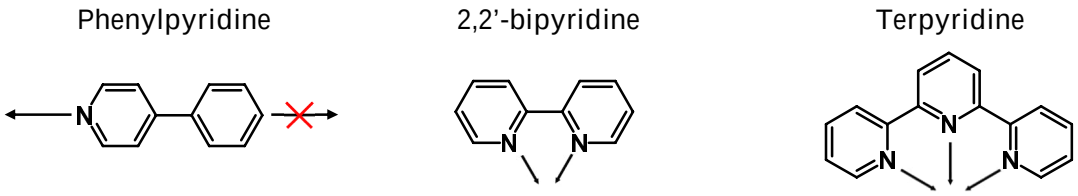

FIGURE 11 Different binding orientations of terminating N-donor ligands.

One occasionally overlooked aspect of ligands is their charge. Majority of the ligands used to form MOPs, and SCCs in general, are charge-neutral, minority are anionic, and the fraction of the ligands are cationic by the nature. The net charge of a complex is the combination of the individual charges of the ligands and the metal nodes; using neutral or cationic ligands yield cationic or super-cationic complexes whereas using anionic ligands usually yields either neutral or anionic complexes. Examples of these kinds of ligands and structures are shown in Chapter 5.

2.2.1 O-donor-based ligands

O-donor-based ligands are commonly based on either carboxylate or hydroxyl groups and contain two electron pairs per O-atom to form the metal coordination. The anionic nature of O-donor-based ligands acts as a counterbalance to cationic metal nodes used, so it is possible to obtain assemblies with no counterions. Carboxylates typically come in three different binding modes: monodentate, bidentate (chelate) and bridge, represented in Figure 12. These alternative modes of binding make carboxylate ligands somewhat more unpredictable in their use than the N-donor-based ligands. Carboxylates can occasionally form a $M_2(O_2CR)_4(A_x)_2$ paddlewheel unit with unprotected metal ions as shown in Figure 12. The axial positions (A_x) of metal ions can either be empty, occupied by coordinated solvents, the very same ligand in monodentate binding mode, or bonded to a secondary ligand depending on the system. This paddlewheel unit, classified as a secondary building unit (SBU), can be utilized as a rigid planar four-connected node for building SCCs. Another attractive property of the paddlewheel is that the node unit itself is always of charge neutral when paired with M^{II} metal salts. As O-donor ligands are rarer than N-donor-ligands when it comes to creating MOPs, some examples of O-donor-based ligands and MOPs will be now examined below.

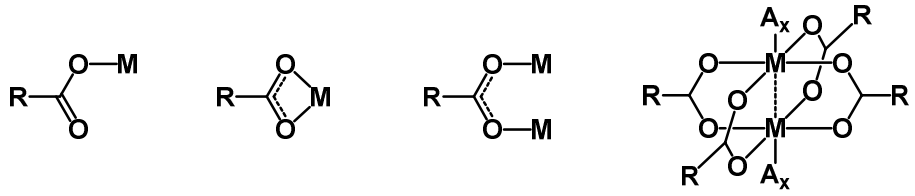

FIGURE 12 Carboxylate group binding modes and paddlewheel unit. R = organic group, M = metal; A_x = any secondary binding unit (O- or N-donor, solvent).

Obtaining the paddlewheel unit by using linear bidentate or planar tridentate ligand will ultimately result infinite structures (MOFs). For example, 1,4-benzenedicarboxylic acid [H_2(1,4-bdc)] O1 paired with Zn^{II} forms a two-dimensional MOF $[Zn(bdc)(H_2O)]_n$ and 1,3,5-benzenetricarboxylic acid (H_3btc) O2 paired with Cu^{II} forms a three-dimensional MOF $[Cu_3(btc)_2(H_2O)_3]_n$, structures more commonly termed as MOF-2[35] and HKUST-1[36] respectively (Scheme 2). Therefore, a bend ligand is preferred to promote the formation of finite assemblies when utilizing the paddlewheel binding motif.

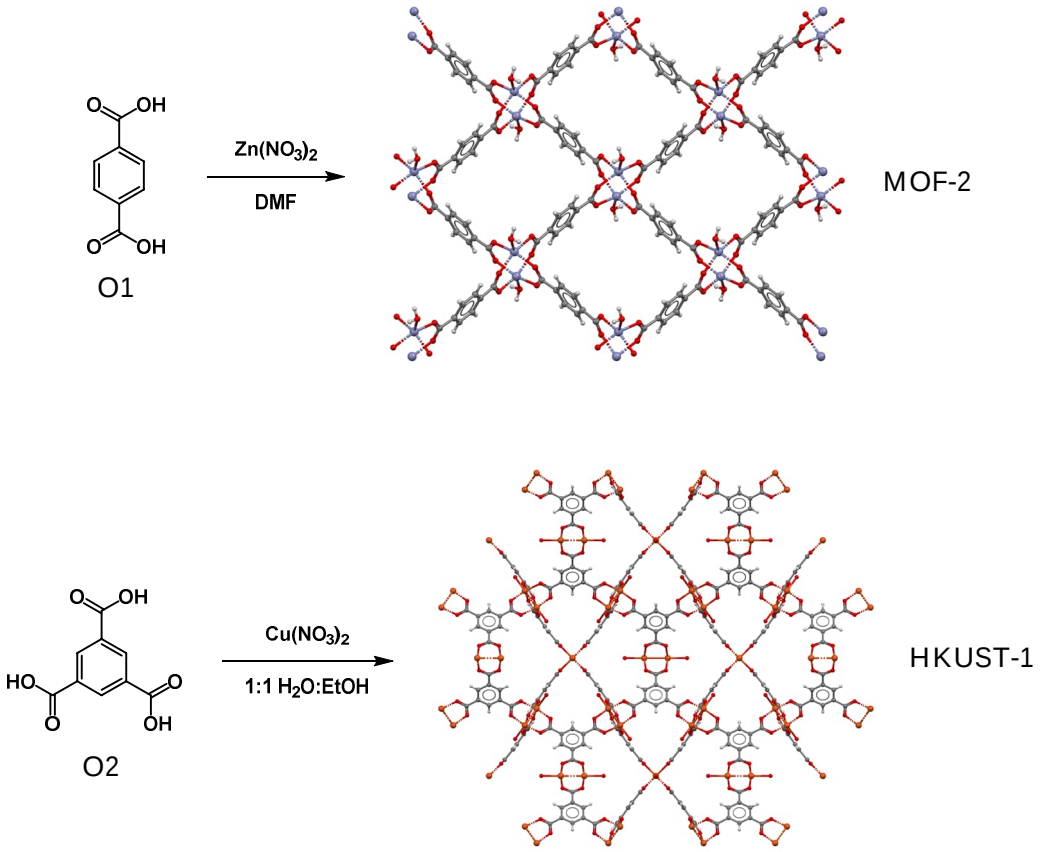

SCHEME 2 General formation of MOF-2 and HKUST-1. Free solvent molecules are omitted for clarity.

This has been achieved by groups such as Yaghi[37], Zaworotko[38], Bloch[39,40] and Zhou[41–45] by reacting various Cu^{II}, Ni^{II}, Mo^{II}, Cr^{II} and Ru^{II} salts in either solvothermal or ambient conditions with O-donors based on 1,3-benzene-dicarboxylate acid [H_2(1,3-bdc)] O3a and 9*H*-3,6-carbazoledicarboxylic acid [H_2(9*H*-3,6-cdc)] O4a with the respectively 5- and 9- positions functionalized derivatives of these acids. The MOPs obtained by the aforesaid ligands were $[M_2(cdc)_2]_6$ cube 5 and $[M_2(bdc)_2]_{12}$ cuboctahedron 6 (Scheme 3). Also $[M_2L_2]_2$ type of micro cage 7 and $[M_2L_2]_3$ prism 8 were prepared by them using different carboxylate ligands O5 and O6 with 0° and 60° bend angles (Scheme 3)[44]. Li *et al.* were also able to obtain two hendecahedra, an solid with 11 faces and 9 vertices, using a mixture of 120° and 90° bend angle O-donor ligands.[45] It is also possible to convert a finite MOP structure into an infinite MOF structure by replacing the solvents on axial positions with linear linker such as 4,4'-bpy.[43] Using bend ligands does not, however, guarantee that the forming assembly is a MOP, as noted by Bloch.[39] Reacting Ni^{II} and Co^{II} salts with H-bdc (O3a), ^{t}Bu-bdc (O3c), Me-bdc (O3e), OEt-bdc (O3f) as well as O4a in solvothermal conditions yielded 2- and 3-dimensional MOFs whereas reacting the same salts with OH-bdc (O3b) and ^{i}Pr-cdc (O4b) produced cages analogous of 5 and 6. This shows that the R-groups, at least partly, guide the formation to either MOF or MOP.

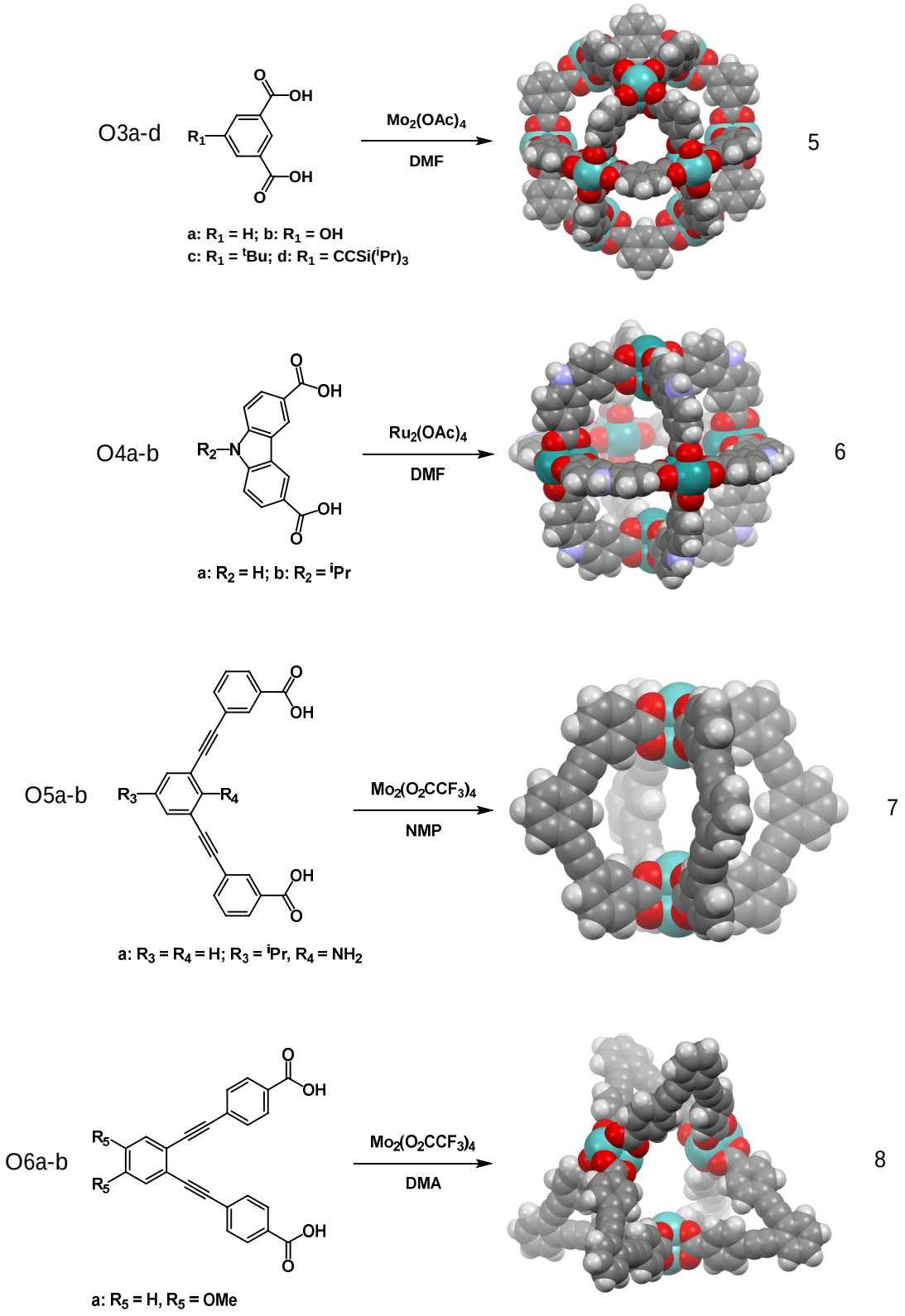

SCHEME 3 Preparation schemes for carboxylate-based MOPs. Only R = H is shown on each structure. NMP: *N*-methyl-2-pyrrolidone, DMA: dimethylacetamide. All solvent molecules, including those coordinated on paddlewheel units are omitted for clarity.

A small number of anionic MOPs have been created by Raymond's group utilizing O-donor ligands with catechol (1,2-hydroxybenzene) functionality.[46–50] In alkaline conditions the hydroxyl groups of the neutral catechol group undergo deprotonation to form an anionic catecholate (charge of 2–), and this in turn gives ditopic ligands O7-8 negative charges of 4–, and 6– for tritopic ligand O9. Reacting these ligands with transition metals (Fe, Ti), post-transition metals (Ga, Sn) and even with silicon (Si) will give rise to M_4L_6 like tetrahedrons 9 and 10 for O7 and O8, and M_4L_4 like tetrahedron 11 for O9, respectively (Scheme 4). As the ligand possesses a negative charge, the overall net charge for the cage is dependent on the charge of the metal node. Thus, in the case of Ga^{III} or Fe^{III} the net charge for the formed cage is 12–, and with Ti^{IV}, Sn^{IV} or Si^{IV} the net charge for the formed cage is 8–. The negative charge is then balanced solely by or a mixture of endo- and exohedral Na^+, K^+ and / or R_4N^+ cations.

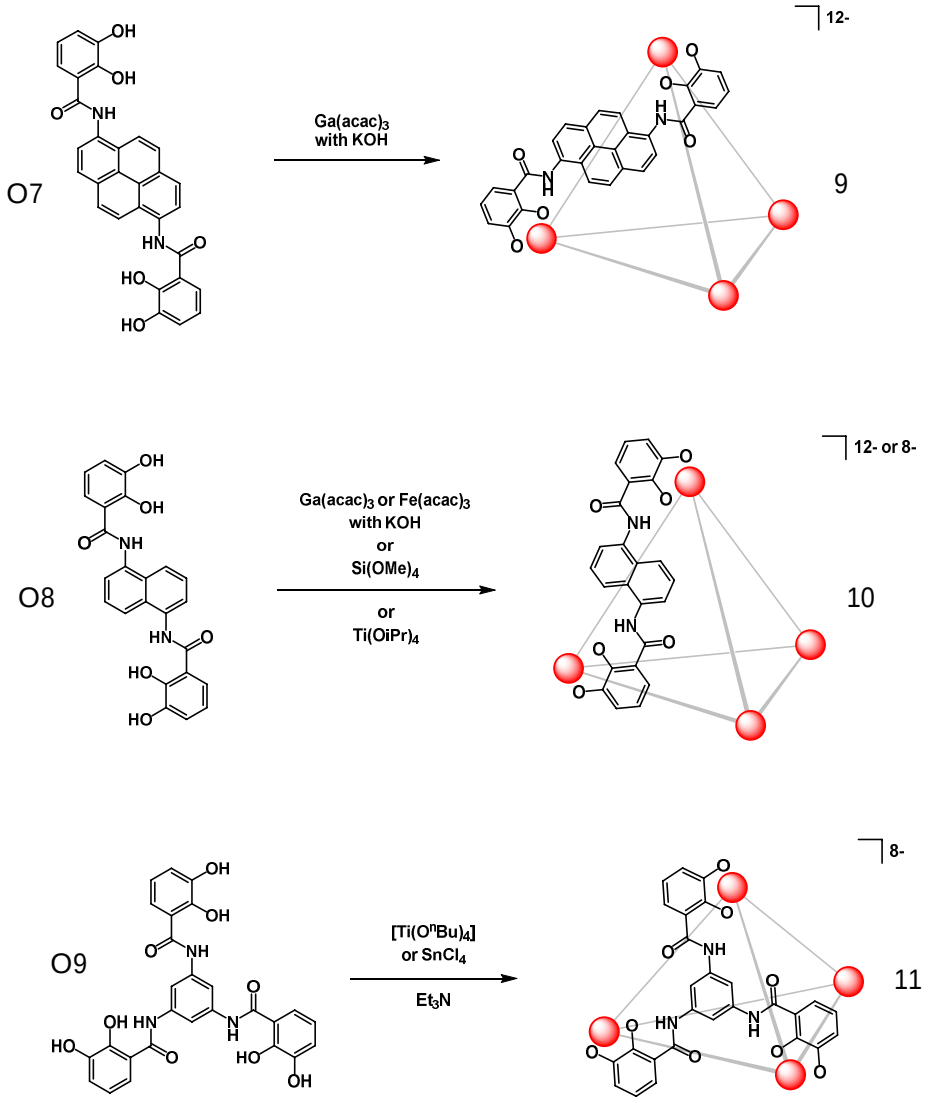

SCHEME 4 Preparation of anionic MOPs that are based on catechol subgroup.

Clegg *et al*.[51,52] have created neutral M_4L_6 tetrahedrons using ligands based on bis-β-diketones together with $FeCl_3$ or $GaCl_3$ in THF solution (Scheme 5). Ligands have two aryl-linked 1,3-diketone groups that act similarly to acetylacetone (acacH) and the doubly deprotonated ligands bind to metal nodes so that some of the ligands have their bis-β-diketonato groups in approximate *trans*-arrangements and some in *cis*-arrangements in order to obtain octahedral geometry. Using phenylene-linked ligand O10 paired with either Ga^{III} or Fe^{III} under alkaline conditions yielded cage 12 which was shown to encapsulate one tetrahydrofuran (THF) molecule. Increasing the length of the ligand by using biphenylene-linked ligand O11, paired with Fe^{III} under alkaline conditions, yielded cage 13 which encapsulated four THF molecules. Essentially by switching the linker from phenylene to diphenylene the interior volume of the cage has increased almost fivefold.

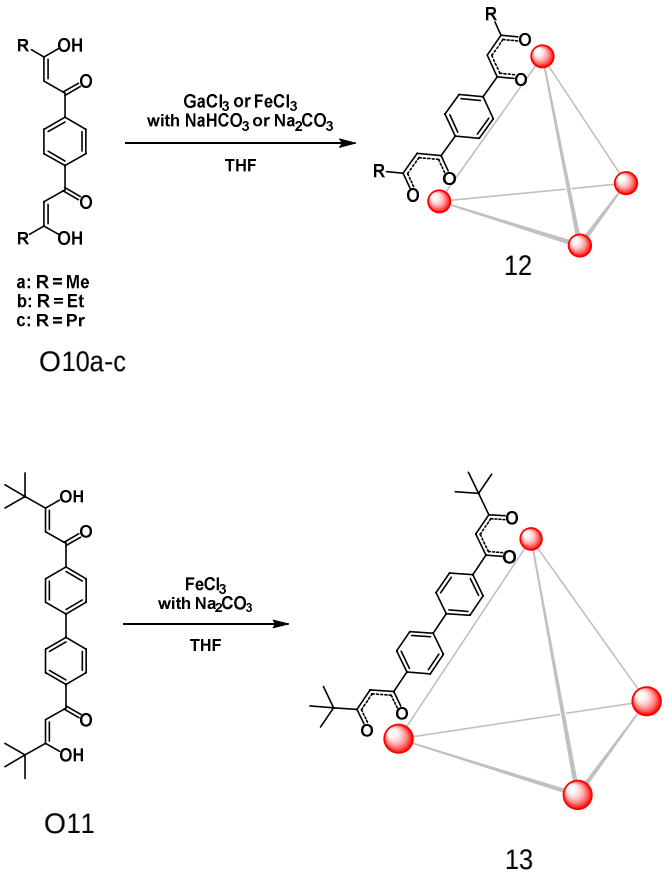

SCHEME 5 Preparation of neutral tetrahedrons, based on bis-β-diketones.

2.2.2 N-donor-based ligands

N-donor-based ligands are typically based on heterocyclic compounds or mixed imine-heterocyclic compounds, of which the most widely used N-containing ligands are based on pyridine or imidazole derivatives. Both moieties offer a single electron pair for coordination which is parallel with planar molecular fragment. With a single pyridyl group in an organic ligand R, three different coordination bond orientations (ortho, meta or para) with bend angles of 60°, 120° and 180° respectively can be afforded depending on the location of the nitrogen atom in ring with respect to the organic group as shown in figure 13a. Expanding this to bipyridine, six isomers can be achieved with bend angles ranging from 0–180° and the distance between N-atoms varying from ≈2.7 to ≈7.1 Å with the only chelating ligand being 2,2'-bipyridine (Figure 13b).[53] Adding an organic linkers such as benzene, furan, thiophene or something chemically more complex between the two pyridyl groups will further increase variation in the bend angle and N···N distance. In that sense simply using two pyridyl-groups linked with an organic intermediate unit already yields an enormous number of potentially viable ligands to be used in MOP synthesis. Furthermore, if the N-donor -group is bound to an organic linker via CH_2-bridge, even wider range of conformational freedom of the ligand can be achieved depending on the number of methylene joints in the bridging unit. Since N-donor-based ligands are the most widely used ligands in the synthesis of MOPs, the ligands discussed in more detail in Chapter 3.

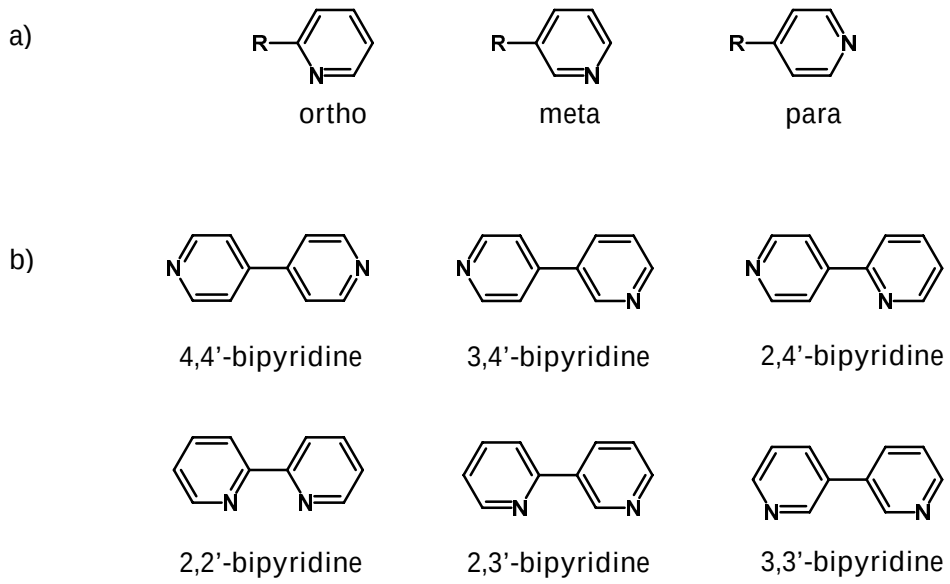

FIGURE 13 a) Single R-substituted pyridine isomers, b) six bipyridine isomers.

3 SELF-ASSEMBLY OF COORDINATION CAGES

Self-assembly, is a process where in favorable conditions molecules or ions spontaneously arrange to form larger assemblies, can occur naturally among compounds or it can be induced by the design of targeted compounds.[54] As the number of interacting components increases, the number of possible products also increases. To increase the chance of affording the desired result, the number of possible alternative outcomes can be limited for instance by controlling the reaction parameters (*e.g.* pH-value, temperature, or solvent environment) or pre-designing starting materials to be more appropriate for desired outcome *e.g.* by adding bulky protecting groups to narrow possible angles. As has already been pointed out, SCCs show concave finite structures, thus ruling out infinite MOFs, are discrete, closed and either 2D (polygonal) or 3D (polyhedral) assemblies usually resembling well-known geometric shapes.[55] As such they can be formed by mimicking the characteristics of their geometrical counterparts. With proper design or selection of metal ions and ligand precursors and mixing them in suitable solvent and favorable reaction conditions, they will spontaneously form metal-ligand bonds and eventually self-assemble to a single product. There are a few different approaches to make SCCs resembling polyhedra but, in the scope of this dissertation the plausible pathways to acquire MOPs are considered as follows:

1. Two-component systems, involving a single type of ligand and a single type of a metal node self-assembling into a MOP.
2. Multicomponent systems, involving two or more different ligands interacting with a single type of metal node.
3. Subcomponent systems, which involve the simultaneous formation of the ligand and the complex (one pot system).

The two-component systems can be further separated into two sub-techniques; *edge-directed* or *face-directed* approaches. The edge-directed approach typically utilizes convergent ligands jointly with divergent metal nodes, so that the ligands typically take the role of a polyhedral shaping, thus connecting the metal nodes located at the vertices. Whereas the face-directed approach usually utilizes divergent ligands in conjunction with protected convergent metal nodes, so that the ligands act as face units for the polyhedral shape. The latter approach is also referred as *molecular paneling*, a term coined by prof. Makoto Fujita[56,57] whose group has done tremendous work in the field of SCCs for the last couple of decades. Of the assemblies shown previously, structures 1–3 (p.12) and 11 (p.27) represent face-directed approach whereas structures 4–10 (pp.21, 26-27) with 12–13 (p.28) exemplify edge-directed approach. In the following sections, further examples involving different approaches will be discussed.

In classical supramolecular assemblies involving multiple noncovalent interactions (representing the second pathway), the kinetic factors start to play a key role in determining the outcome of the self-assembling processes.[58] In these systems due to competing interactions the self-assembled structure can be lead to be kinetically trapped in a local minimum rather than achieving thermodynamic equilibrium state. The two states are separated by an energy barrier and so it is possible to switch between two energy states with external stimuli, for example by heat (Figure 14). Kinetic traps are more commonly found in biochemistry regarding the folding of proteins.[59] Usually long reaction time, high temperature and low concentration favors the thermodynamic state whereas short reaction time, low temperature and high concentration favor the kinetically trapped states.

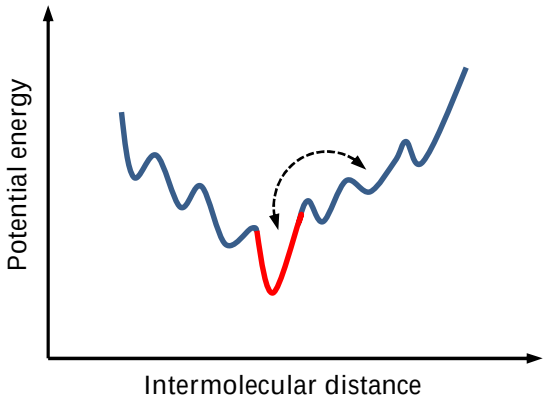

FIGURE 14 General depiction of the energy landscape of kinetic traps (blue) vs. thermodynamic equilibrium state (red). The dotted arrow represents an external stimulus that cause the transition between the two states.

Though kinetic trapping is more common in classical supramolecular assemblies, Fujita *et al*. were able to show that kinetic trapping can also play a part in metallosupramolecular assemblies.[60] By reacting ligand N2 with $Pd(BF_4)_2$ to form $M_{12}L_{24}$ cuboctahedron 14 (Scheme 6) and tracing the self-assembly by time-dependent NMR spectroscopy and mass spectroscopy they were able to identify two metastable intermediates: the short-lived M_8L_{16} and the relatively long-lived M_9L_{18}. Heating a mixture containing both intermediates for 1 h at 60 °C caused the NMR-peaks of M_8L_{16} to disappear and additional heating for 6 h at 80 °C caused the NMR signals of M_9L_{18} to disappear as well as verifying that these compounds are indeed kinetically trapped intermediates and are not side products. Using a ligand N3, similar to N2 but with a smaller bend angle, they were able to crystallize the M_9L_{18} intermediate 15 (Scheme 6).

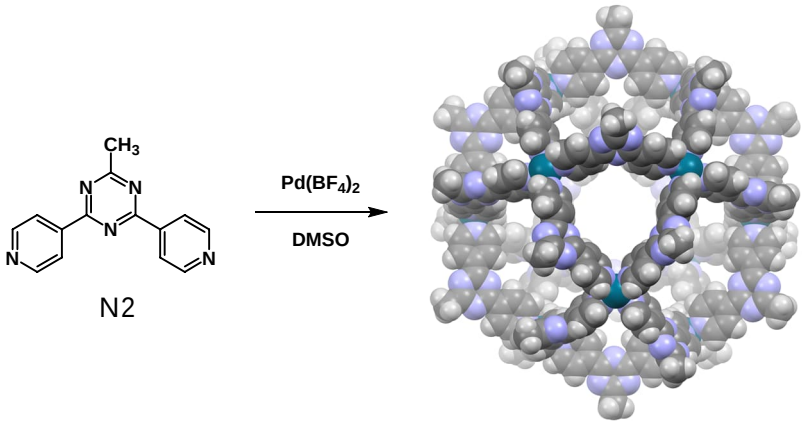

N2

14

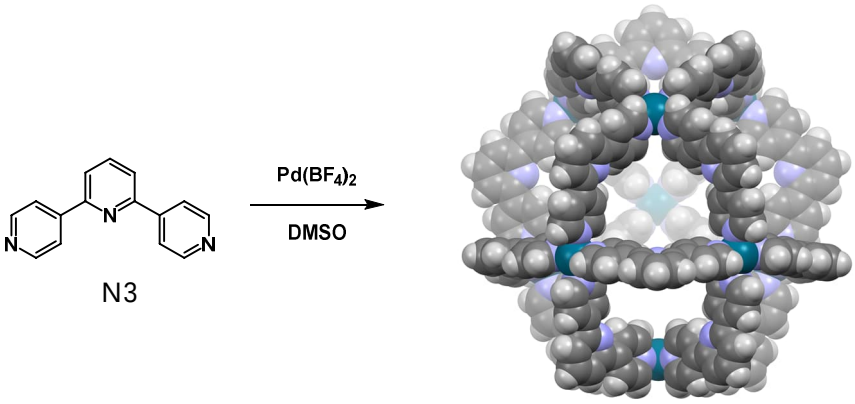

N3

15

SCHEME 6 Preparation of $M_{12}L_{24}$ cuboctahedron 14 and M_9L_{18} intermediate 15. Anions and solvent molecules were omitted for clarity.

3.1 Two-component systems

3.1.1 Cavitand-based systems

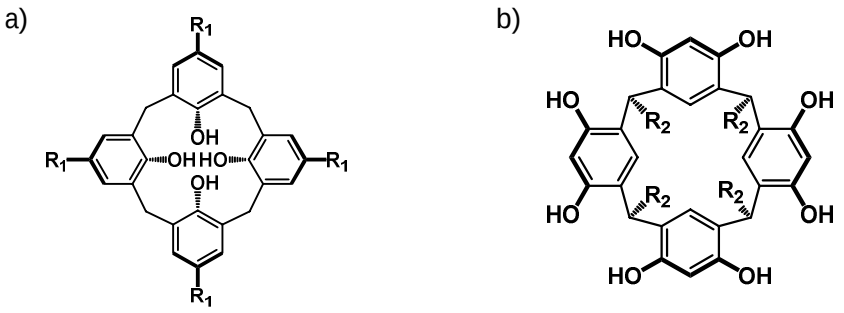

FIGURE 15 Structures of a) calix[4]arene and b) [4]resorcinarene molecules.

Cavitands, such as calix[4]arenes and [4]resorcinarenes (Figure 15), are rigid concave organic molecules with the permanent and intrinsic cavities usable for molecular recognition, and are widely used in classical supramolecular chemistry to from host-guest complexes and hydrogen bonded cages. The first metal-induced cavitand-based cages were reported in 1997 by Jacopozzi *et al*.[61] and those structures were obtained by using methylene-bridged tetracyano-cavitands N4a and N4c paired with *cis*-protected Pd^{II} or Pt^{II} salts (Scheme 7). The reported assemblies were $[M_4L_2]^{8+}$ type structures in which one of the eight counter anions were encapsulated inside the structural cavity, and it was later shown that this cavity has an affinity to bind different anions with a selectivity trend of $BF_4^- > OTf^- \gg PF_6^-$.[62] The size of the internal cavity can be increased by changing the cyano groups to a pyridine-based groups or by adding an organic linker between the cyano group and the calixarene ring as was done by Kobayashi *et al*.[63] or by switching the group to a bipyridine-based group as reported by Haino *et al*.[64] Mainly these structures have been characterized by NMR and mass spectrometry (MS) but the structure 16 obtained using ligand N4c has been characterized by single crystal X-ray diffraction. Similar assemblies can be obtained by functionalizing the bridge between the hydroxyl-groups instead of the resorcinarene itself, as shown by Dalcanale's group.[65,66] Using pyridine as the N-donor, the obtained structure had an internal cavity size of 840 $Å^3$ whereas using a longer N-donor 4-tolylpyridine, the cavity had an internal size of 1800 $Å^3$. Both of these structures have been characterized using X-ray diffraction and cage 17 obtained using N9c is shown in Scheme 7.

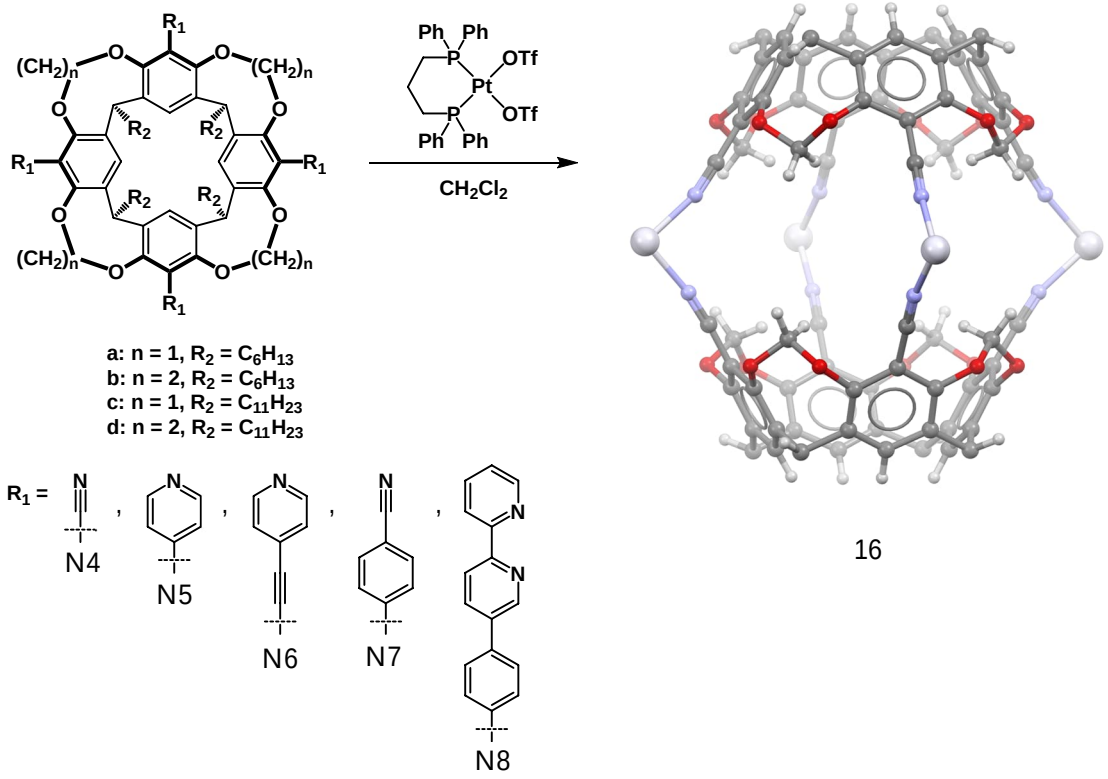

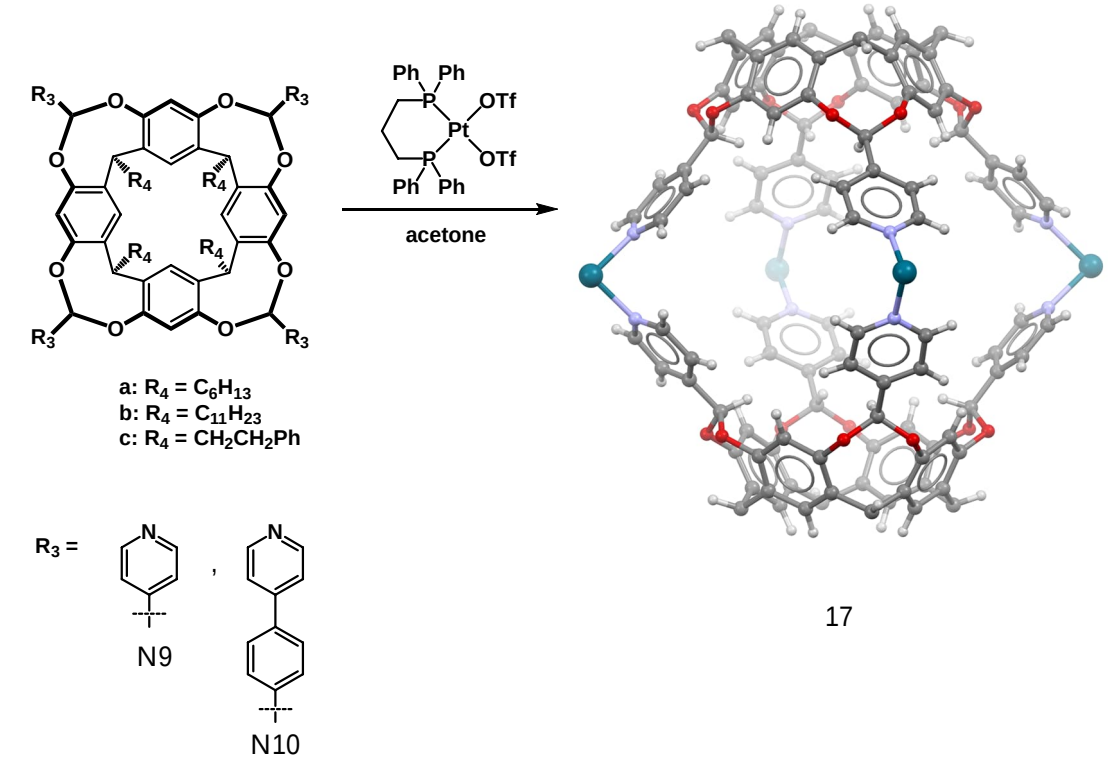

SCHEME 7 Preparation of M_4L_2 cavitand-based assemblies 16 and 17. For 16 ligand N4c and for 17 ligand N9c are shown. R_2 and R_4-groups, anions, solvent molecules and protecting groups of metal nodes have been omitted for clarity.

3.1.2 Edge-directed approach: directional bonding

Ward's group has utilized ligands containing chelating pyrazolyl-pyridine binding sites connected by an organic linker.[67–69] These ligands have CH_2-bridge connecting the two pyrazolyl-pyridine arms to the organic linker adding further flexibility to the ligand. Reacting ligand N11 with cobalt(II) acetate, followed by addition of $NaBF_4$ led to the formation of $[Co_4(N11)_6](BF_4)_8$ tetrahedron 18 (Scheme 8). In this structure the ligands 'twirl' around the edges of the tetrahedron and individual ligands are interacting *via* π–π stacking occurring between the aromatic rings. Analogous structure was also obtained by changing the organic linker from 1,2-phenyl to 2,3-naphthyl and reacting that ligand (N12) with cobalt(II) acetate, followed by the addition of sodium tetrafluoroborate or perchlorate leading to the formation of $[Co_4(N12)_6](BF_4)_8$ 19 and $[Co_4(N12)_6](ClO_4)_8$ 19' respectively. Switching the organic linker to pyridyl and reacting this ligand (N13) with zinc(II) acetate in 3:2 ratio followed by addition of sodium perchlorate lead to the formation of $[Zn_8(N13)_{12}](ClO_4)_{16}$ cube 20 (Scheme 9). Similarly to tetrahedrons, the ligands twirl around the edges of the cube, which is slightly skewed. In all these structures one of the anions is encapsulated inside the structure and it is presumed that the formation of the structures themselves are formed by the anion-directed template effect.

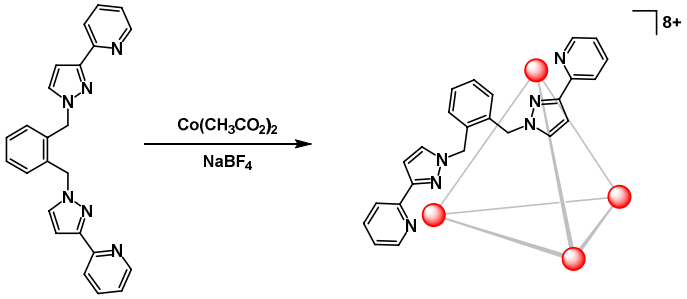

N11 14

SCHEME 8 Formation of $[Co_4(N4)_6](BF_4)_8$ tetrahedron.

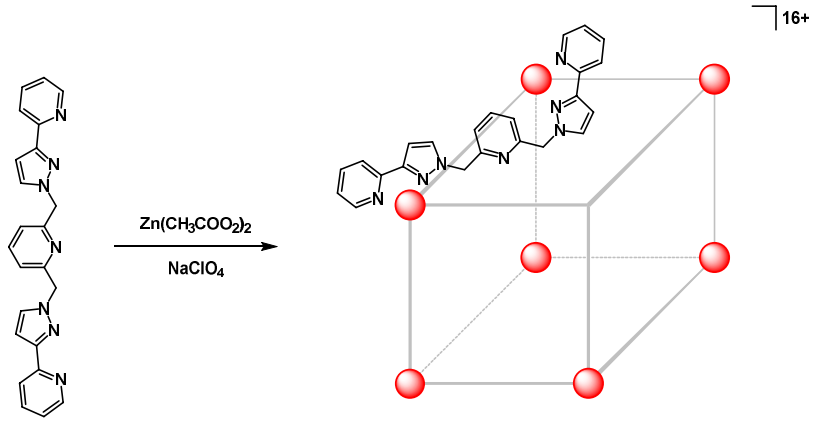

N13 20

SCHEME 9 Preparation of $[Zn_8(N20)_{12}](ClO_4)_{16}$ cube-like assembly.

Fundamental and thorough research has been done by Fujita and co-workers utilizing bent bidentate bis(pyridine) ligands and unprotected metal ions in order to create Platonic and Archimedean M_nL_{2n} assemblies. So far they have managed to create several M_6L_{12}[70], $M_{12}L_{24}$[71] and $M_{24}L_{48}$[72–74] assemblies along with the currently largest of M_nL_{2n} assemblies $M_{30}L_{60}$[75] and $M_{48}L_{96}$.[76] It was found that the bend angle (θ) of the ligand is the key factor determining what sort of assembly is produced. Using a ligand such as N14 ($\theta = 90°$) with unprotected Pd^{II} ions, a M_6L_{12} cube 21 can be obtained in which the metal node resides in the middle of each face and ligands acts as a corner as shown in Scheme 10.[70]

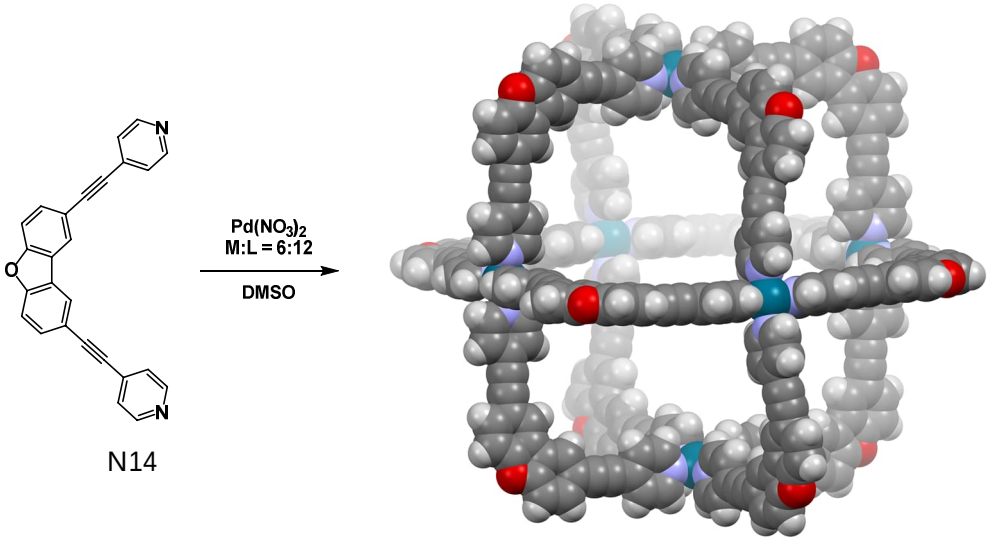

N14 21

SCHEME 10 Preparation $Pd_8(N14)_{12}$ cube. Anions and solvent molecules are omitted for clarity.

A more elegant example of how the bend angle affects the formation of the polyhedra is the work done by Tominaga *et al.*, where they showed how a change in bend angle can drastically change the composition of the formed polyhedra. For M_nL_{2n} types of Archimedean solids, the ideal edge angles (θ) are 120° for cuboctahedron ($M_{12}L_{24}$) and 135° for rhombicuboctahedron ($M_{24}L_{48}$). The first $M_{12}L_{24}$ structures obtained were made using ligands N15 (θ = 127°), N16 and N17 (θ = 120°), and it was shown that extending the ligand length did not affect the polyhedron formation as long as the correct bend angle remained intact.[71] Later this was further shown to be true by creating a sphere-within-sphere 22 using dual ligand N18 with θ = 120° connected via triethylene glycol (TEG) chain (Scheme 11).[77] To further investigate the principle, an $M_{24}L_{48}$ structure was obtained using substituted thiophene-based ligands N19a-c (θ = 149°) followed by a series of experiments where ligands N15 and N19c were mixed sequentially from 1:9 to 9:1 ratio, in order to vary the average bend angle.[72] Interestingly $M_{24}L_{48}$ formed exclusively until the ratio of N19c:N15 was 1:4 and afterward only $M_{12}L_{24}$ formed. This switch threshold corresponded to an average bend angle between 131° and 134°, which in turn suggested that a ligand with a bend angle higher than this threshold should form $M_{24}L_{48}$ complex and a ligand with a bend angle lower than the threshold would form $M_{12}L_{24}$ complex. To confirm this, a series of ligands with varying bend angles were prepared and complexed with Pd^{II} metal nodes, and it was shown that ligands N20–N22 (θ = 135°, 143° and 147° respectively) all formed purely $M_{24}L_{48}$ assembly exclusively, proofing that the threshold lies between 131-134°.[73] This was further shown to be true using ligands N23 (θ = 130°) and N24 (θ = 134°) that still formed exclusively $M_{12}L_{24}$ and $M_{24}L_{48}$ assemblies respectively.[74] Preparation of cuboctahedra $M_{12}L_{24}$ and rhombicuboctahedra $M_{24}L_{48}$ are presented in Scheme 12.

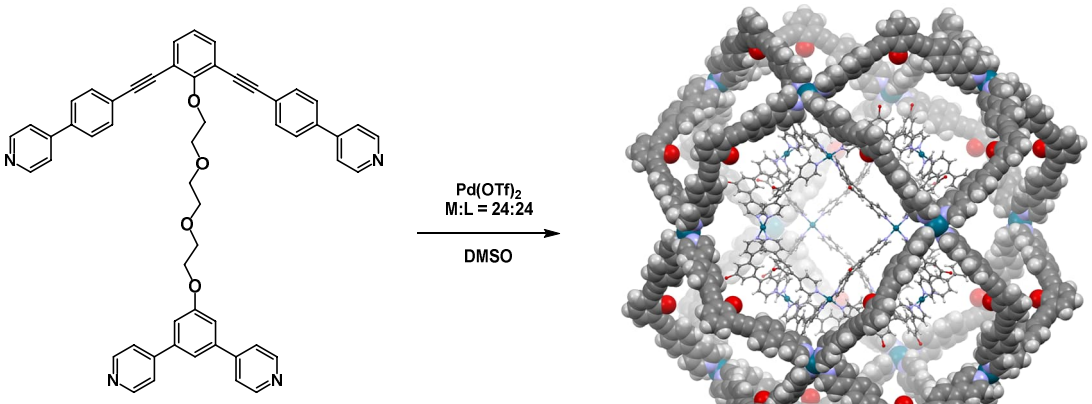

N18 22

SCHEME 11 Preparation of sphere-within-sphere 22. Anions and solvent molecules are omitted for clarity. TEG chains were not modelled due to high degree of disorder.

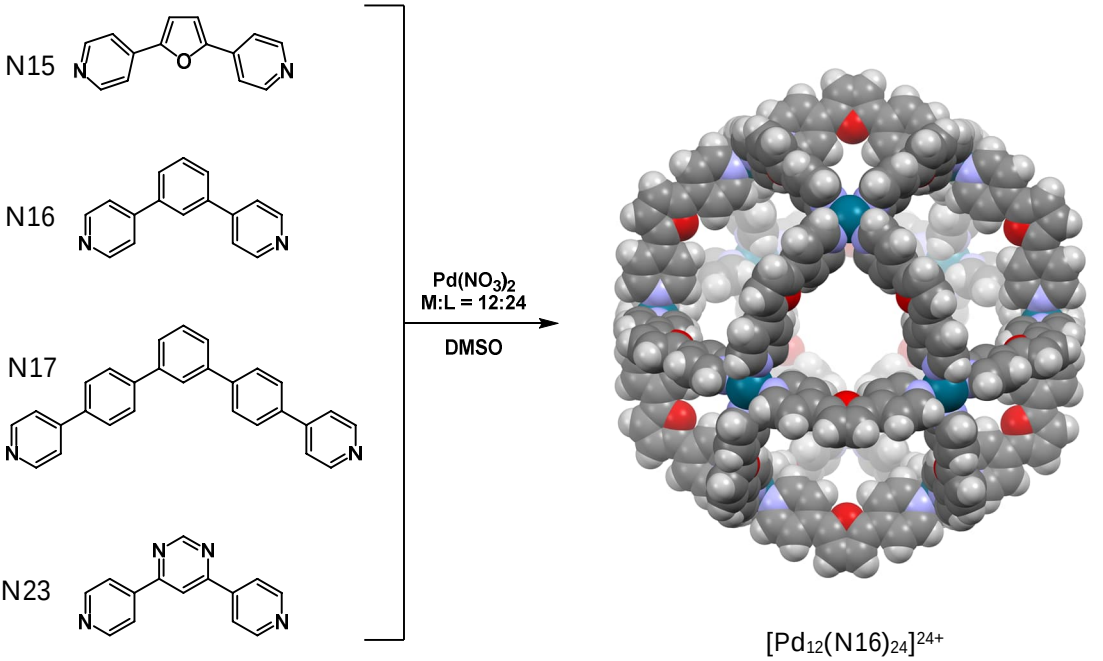

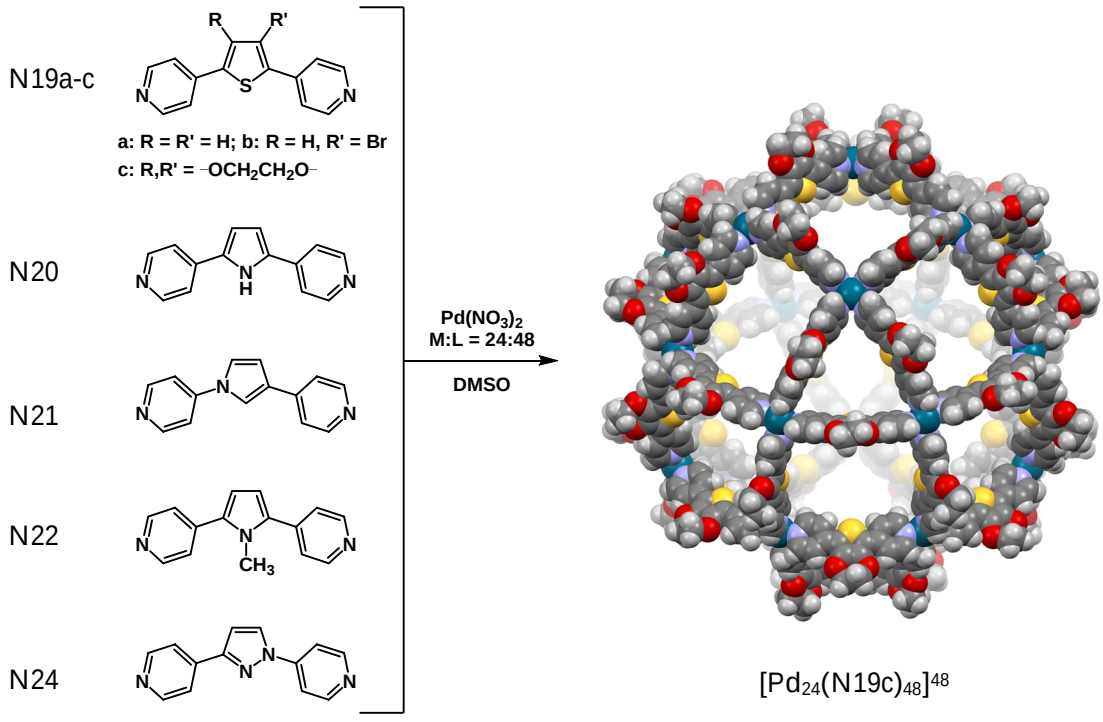

SCHEME 12 Preparations of analogous $M_{12}L_{24}$ and $M_{24}L_{48}$ assemblies, only structures obtained using ligands N16 and N19c are shown. Anions and solvent molecules are omitted for clarity.

The next logical step for Fujita's group was to design $M_{30}L_{60}$ complex but as was previously discovered, thiophene-based ligands N19 still formed $M_{24}L_{48}$ assemblies despite the bend angle (θ = 149°) being close to the ideal angle of 150° for icosidodecahedron ($M_{30}L_{60}$). This is suggested that when n > 24 the effect of kinetic trapping becomes dominant. So to bring the trapped structure out from the local minimum, the solution of N19a and $Pd(NO_3)_2$ was heated at 70°C for 12 hours in order to turn the kinetic product $M_{24}L_{48}$ into a thermodynamic product $M_{30}L_{60}$. However, prolonged heating led to a mixture of both $M_{24}L_{48}$ and $M_{30}L_{60}$, thus not further affecting the initial ratio of the products. Therefore a new more flexible ligand with longer spacers N25 was synthesized and reacted with $[Pd(MeCN)_4](BF_4)_2$ to obtain $M_{30}L_{60}$ icosidodecahedron 23 as shown in Scheme 13. The cage has an impressive interior volume of 157 000 Å^3 and an exterior diameter of 8.2 nm.[75]

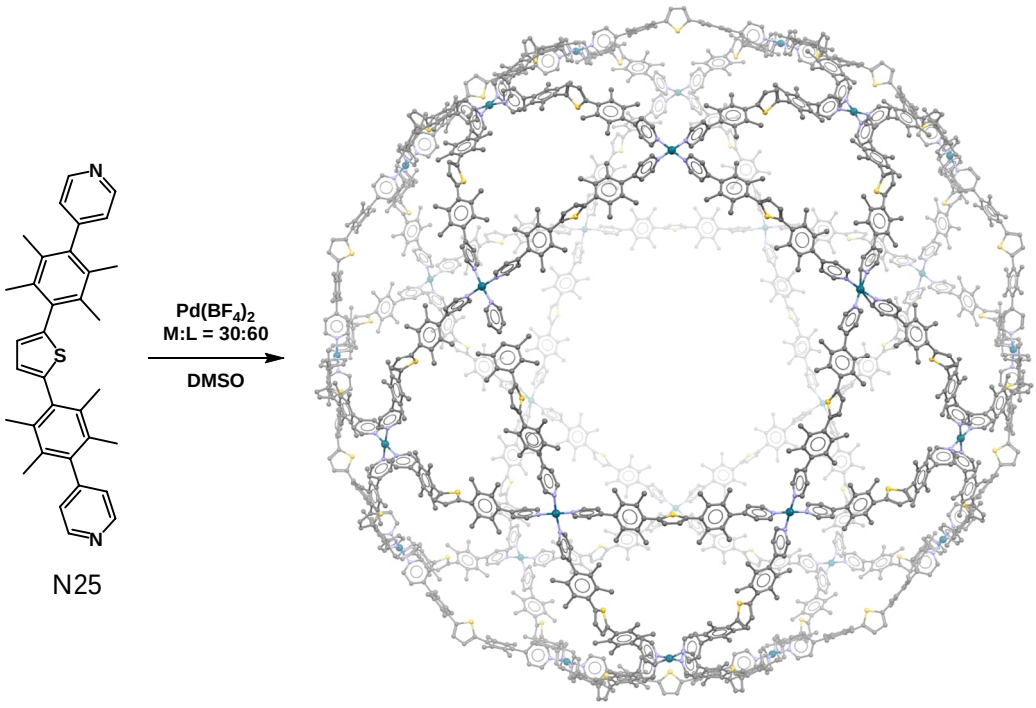

N25

23

SCHEME 13 The formation of $M_{30}L_{60}$ icosidodecahedron. Anions and solvent molecules are omitted for clarity whereas hydrogen atoms were not included in the model.

On their ongoing quest to design and create larger and larger M_nL_{2n} assemblies Fujita *et al*. managed to create two assemblies of previously unreported convex polyhedra, namely $M_{30}L_{60}$ tet-G(2,1) (24) and $M_{48}L_{96}$ tet-G(2,2) (25) tetravalent Goldberg polyhedrons (Scheme 14).[76] Utilizing a selenophene-based bidentate ligand N26 with a bend angle of 152° together with naked Pd^{II} metal node, the two polyhedrons were obtained as an undetermined ratio when the reaction mixture was heated for 48 hours at 70 °C. As complex 24 is also obtained at room temperature, it is presumed that 24 is a kinetically trapped product, which upon heating is partly turned into thermodynamic product 25 (minor product). This was also the first time that tetravalent Goldberg polyhedra had been reported on a molecular level, opening the way to obtain more such assemblies in the future.

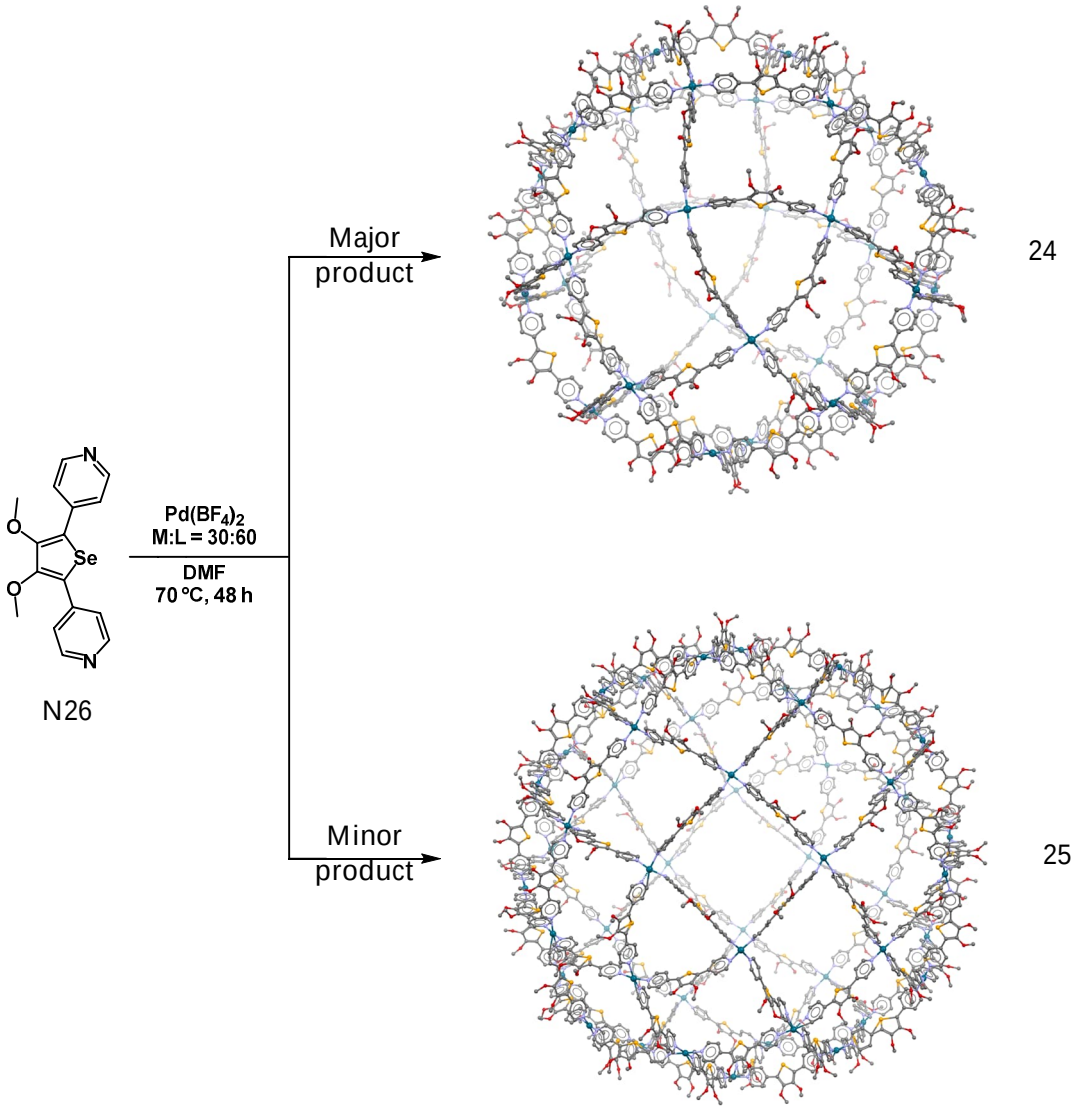

SCHEME 14 The formation of $M_{30}L_{60}$ (24) and $M_{48}L_{96}$ (25) Goldberg polyhedra. Anions are omitted for clarity whereas hydrogen atoms and solvent molecules were not included in the model.

3.1.3 Face-directed approach: molecular paneling

In 1995 Fujita *et al*. treated tridentate ligand N27 with *cis*-protected corner $[Pd(en)](NO_3)_2$ in 2:3 ratio to obtain a M_6L_4 open octahedron 26.[78] In this assembly protected Pd^{II} nodes act as vertices of the octahedron and tridentate ligands act as triangular panels covering half of the eight faces of the octahedron in such a manner that every alternating face of the octahedron either has a molecular panel or vacancy (Scheme 15). the analogous structure has also been obtained using $[Pt(en)](NO_3)_2$ instead of $[Pd(en)](NO_3)_2$.[79] Similarly, extended cages were obtained by adding phenylene (N28) or bisphenylene (N29) spacers between triazine core and pyridine arms, although their crystal structures could not be verified, as X-ray diffraction suitable crystals were not obtained.[78] With both Pd and Pt cages, the formation and stability of the cage was enhanced when a hydrophobic anion, 1-adamantanecarboxylate, was introduced to the system and in fact crystals of 26 suitable for X-ray diffraction were not obtained without the anionic guest. Analogous structures have since been obtained utilizing 2,2'-bpy 27, 1,10-phenanthroline (phen) 28 and even bulkier 2,9-dimesityl-1,10-phenanthroline (dmesp) 29 protected Pd^{II} corners (Scheme 16). These systems were able to encapsulate neutral guests, such as diphenyl-methane, *o*-carborane, 1-adamantanol and tetraphenylsilane.[80,81] It has also been possible to obtain an adamantanoid $(H_2O)_{10}$ cluster within the hydrophobic cavity[82]. Recently Cai *et al*. linked two N27 ligands together with a *p*-xylene linker (N30) and paired it with 2,2'-bpy protected Pd^{II} corner, yielding M_4L_2 structure 30 which resembles structure 22 but has an 82% larger interior capable of encapsulating large polyoxometallates (Scheme 17).[83]

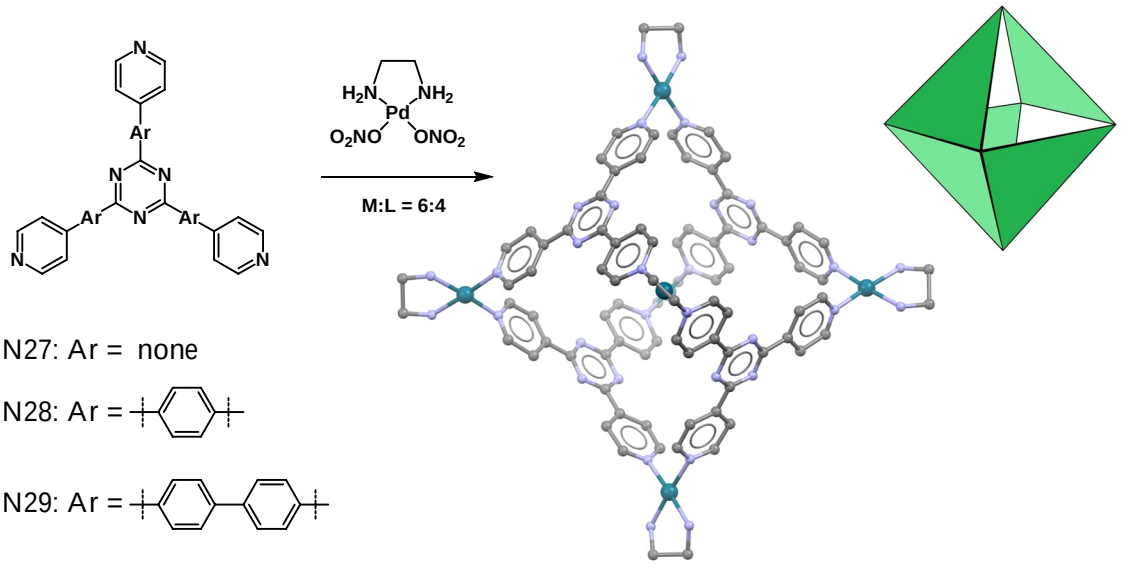

26

SCHEME 15 Assembly of M_6L_4 open octahedron from triangular panels, only $[Pd_6(N27)_4]$ 26 is shown. Hydrogen atoms and solvent molecules were not included in the model while anions are omitted for clarity.

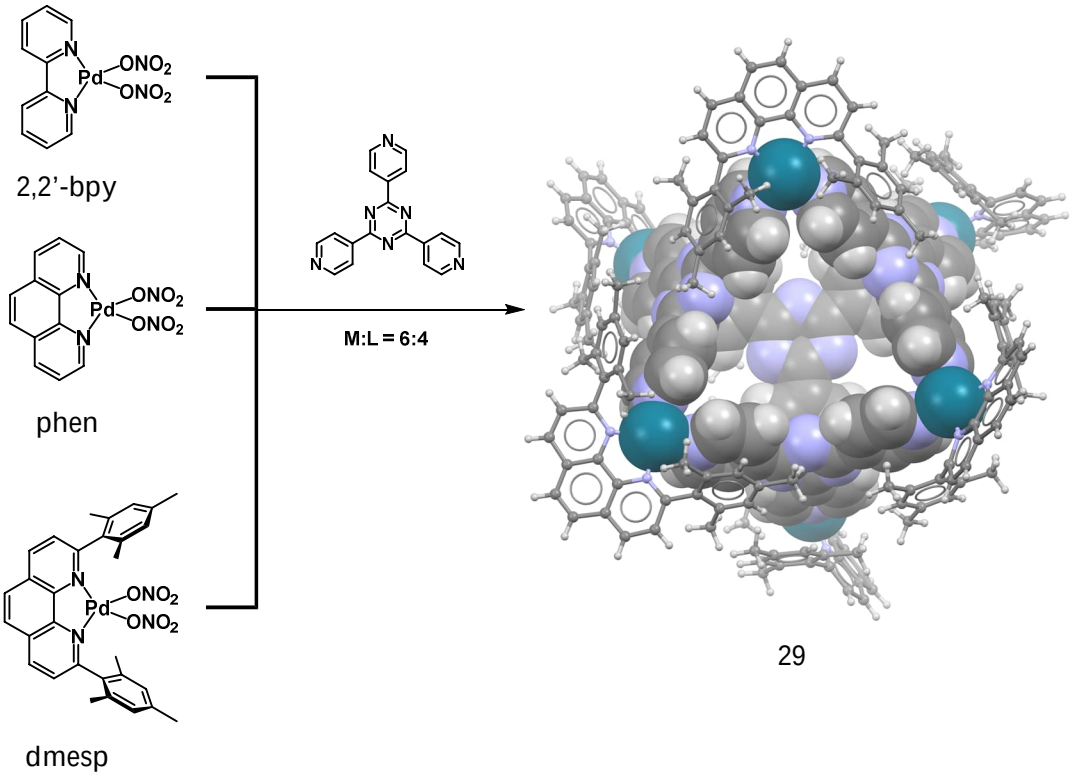

SCHEME 16 Assembly of $M_6(N27)_4$ open octahedron using bulky *cis*-protecting groups, only dmesp structure is shown with $Pd_6(N27)_4$ presented in spacefill and dmesp in ball and stick. Anions are omitted for clarity.

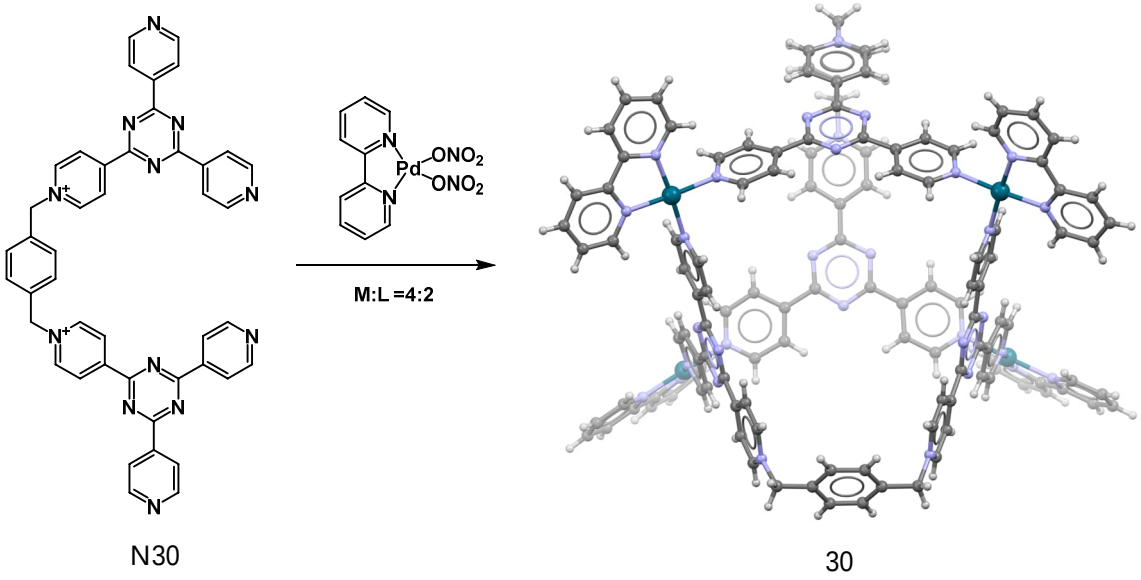

SCHEME 17 Assembly of M_4L_2 open octahedron 30. Anions are omitted for clarity.

Slightly modifying the ligand N27 by switching the orientation of pyridyl groups from *para*- to *meta*-substitution, and pairing this new ligand N31 with $[Pd(en)]^{2+}$ corner, yielded an M_6L_4 square pyramid 31 with an open apex, as shown in scheme 18.[84] In this structure, one of the pyridyl arms rotates in the way that instead of binding on all sides of the triangle, the binding only occurs on two sides. Later it was shown that this assembly could encapsulate terphenyl quests in aqueous solution by forming a dimeric capsule, and thus creating a hydrophobic cavity for the neutral hydrocarbon guests to reside in.[85] Hexadentate ligand N32, utilizing benzene core and 3,5-pyrimidal arms paired with $[Pd(en)]^{2+}$ corner provided a $M_{18}L_6$ trigonal bipyramidal structure of 32 as shown in Scheme 18.[86] Similar structure $M_{15}L_6$ 33 was also obtained by using a ligand containing two pyramidal arms and one pyridine arm in a benzene core (Scheme 19).[87] This change essentially created three openings to the structure, allowing thus encapsulation of small guest, such as CBr_4 and $CHCl_3$.

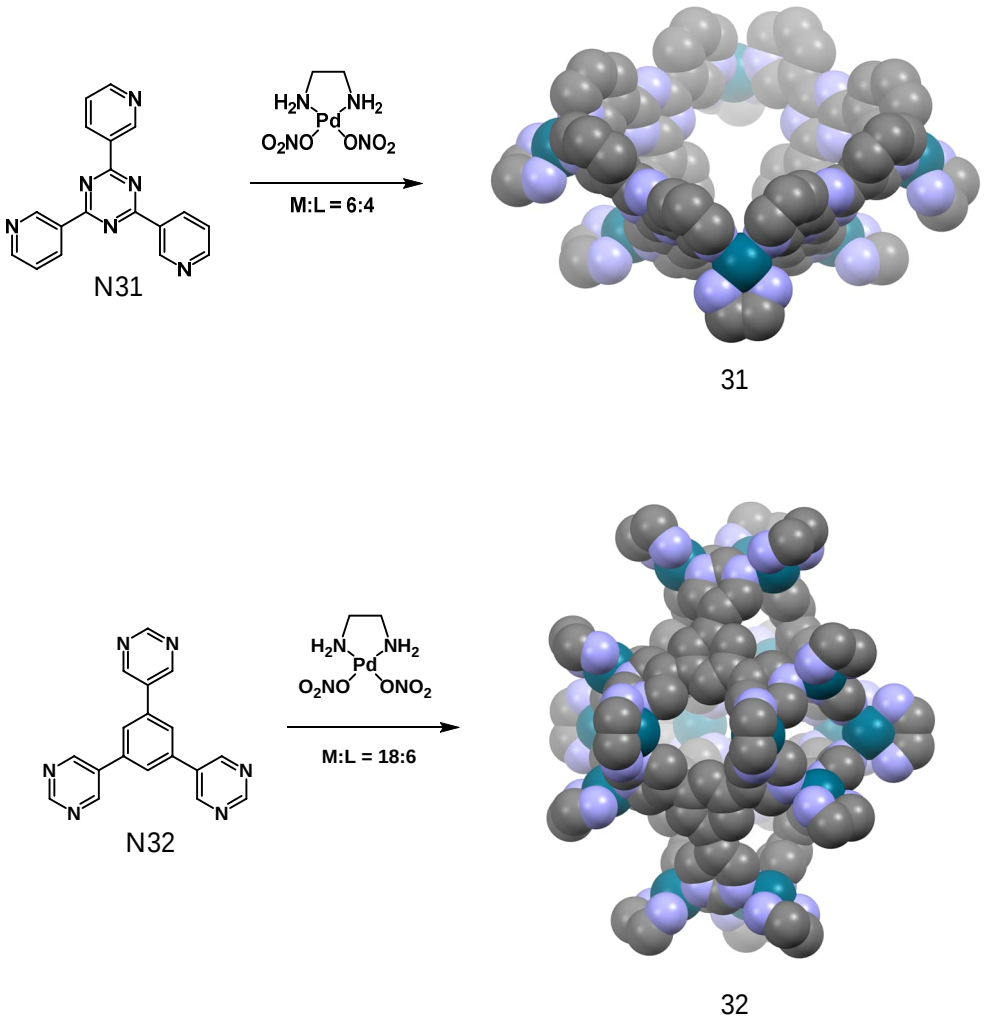

SCHEME 18 Assembly of M_6L_4 square pyramid 31 and $M_{18}L_6$ trigonal bipyramid 32. Anions and solvent molecules were omitted for clarity while hydrogen atoms were not included in the models.

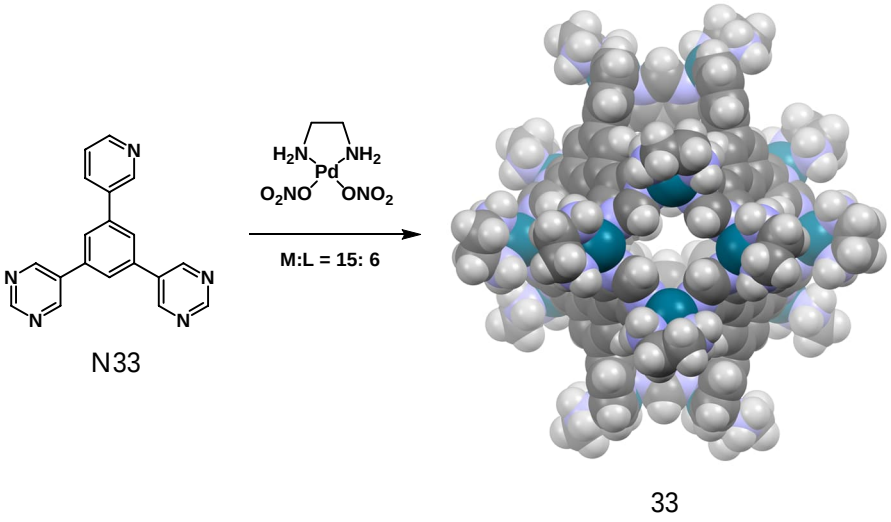

SCHEME 19 Assembly of $M_{15}L_6$ trigonal bipyramid 33. Anions and solvent molecules are omitted for clarity.

Switching from triangular panels to rectangular panels by using a tetradentate ligand N34 with $[Pd(en)]^{2+}$ corners, Yamanoi *et al*. obtained a dynamic library of different box structures according to both NMR and MS studies.[88] From this mixture a triangular box 34 was isolated using a biphenyl (Ph_2) template, as 34 would form around two biphenyl molecules resulting in a clathrated 34·2(Ph_2) structure. Crystallization by slow vapor diffusion instead yielded rectangular box 35, shown in Scheme 20. Dissolving extracted clathrate of 34, would liberate biphenyl molecules and the structure would reorganize to 35 through pentameric intermediate according to NMR studies.

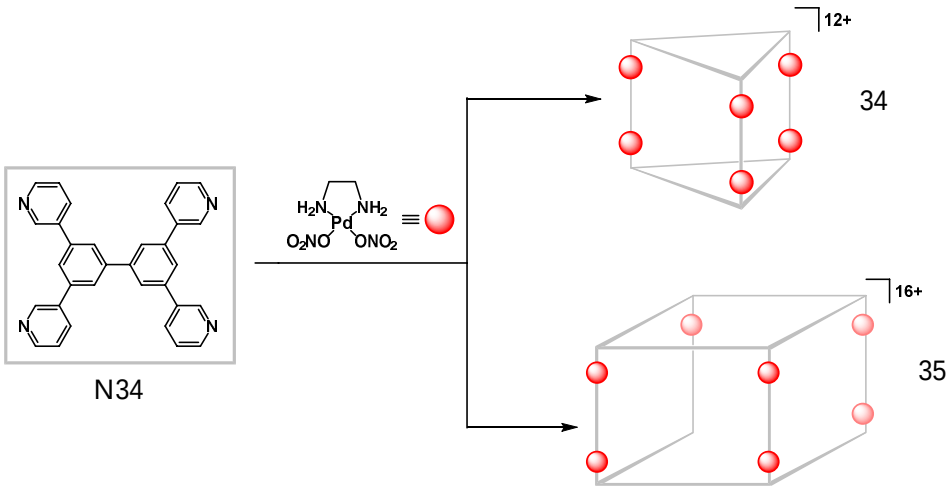

SCHEME 20 Formation of M_6L_3 triangular box 34 and M_8L_4 rectangle box 35.

With different tetradentate ligands, a series of M_6L_3 trigonal prisms has been obtained by Fujita *et al*.[89] by treating zinc(II) tetrakis(3-pyridyl)porphyrin N35 with $[Pd(en)]^{2+}$ corners (36). Similarly, Caskey *et al*.[90] used various extended ligands N36–N38 paired with trimethylphosphine protected $[Pt(PMe_3)_2]^{2+}$ corners (37–39), as presented in Scheme 21. Unlike in the case of the ligand N34 these structures were not part of dynamic equilibrium and were formed without template assistance. Bar *et al*.[91] on the other hand have obtained an $M_{12}L_6$ open hexagonal prism 40, shown in Figure 16, by treating tetrakis(4-pyridyl)porphyrin (N39) with 1,1'-bis(diphenylphosphino)ferrocene (dppf) protected *cis*-$[Pt(dppf)]^{2+}$ corner.

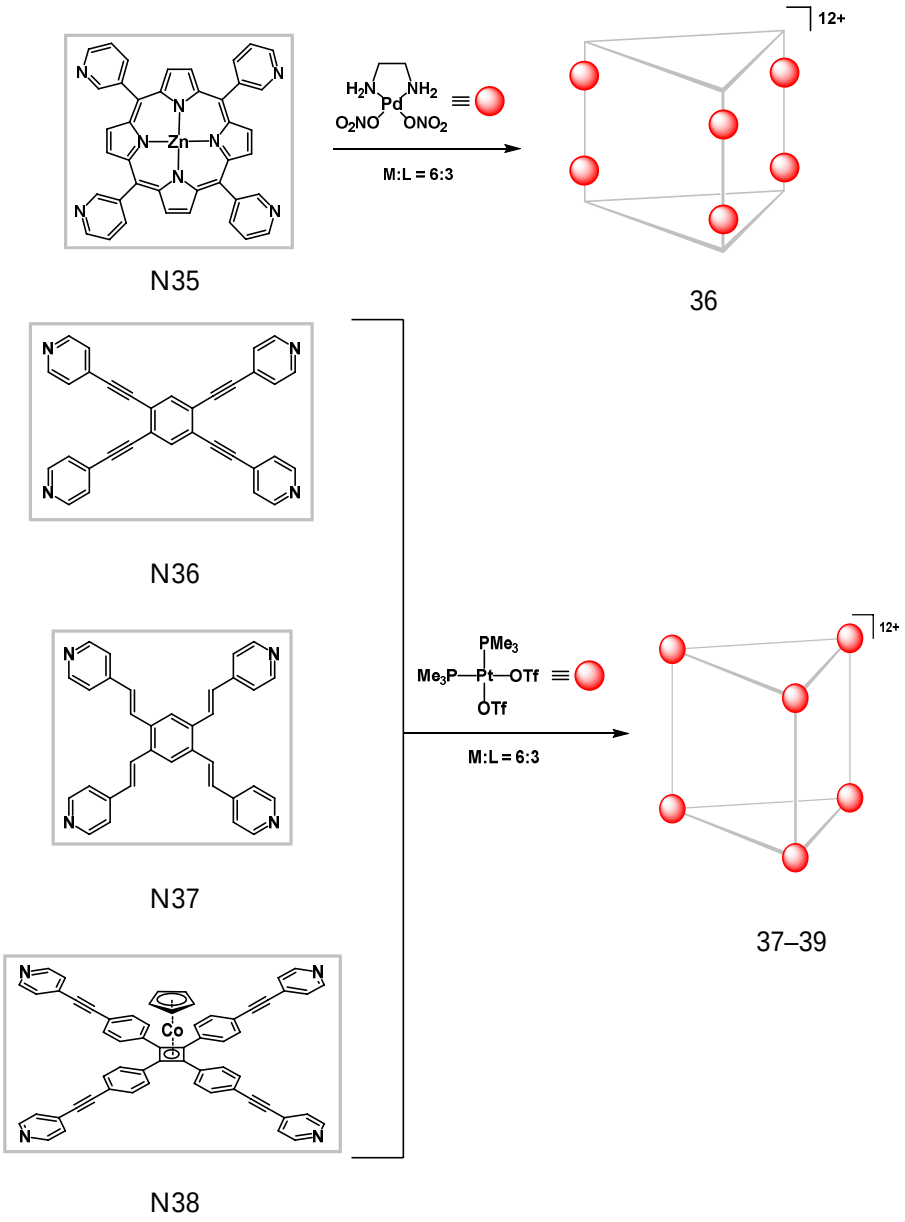

SCHEME 21 Formation of M_6L_4 trigonal prisms with various tetradentate ligands.

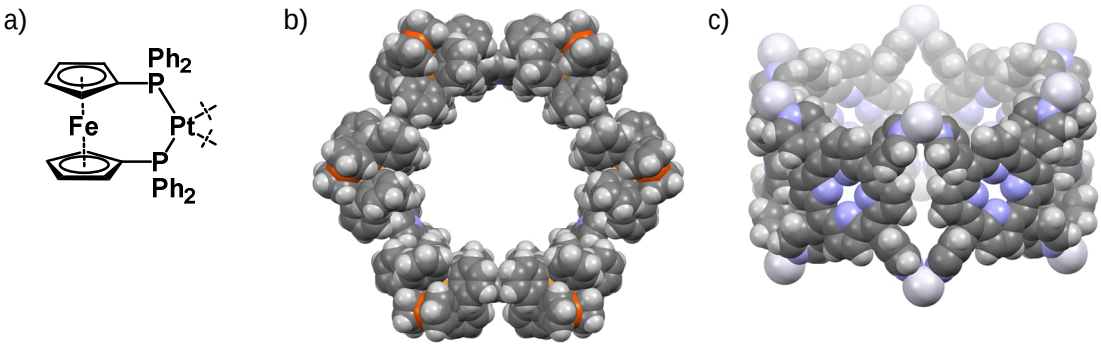

FIGURE 16 a) *cis*-[Pt(dppf)]$^{2+}$; b) top view of 40; c) side view 40. Anions are omitted for clarity, and in c) dppf-groups are also omitted.

Hiraoka *et al*. obtained 10 isostuctural octahedral M_6L_8 assemblies by reacting disk-shaped tritopic ligand N40 with various M^{II} transition-metal ions (Hg, Mn, Fe, Co, Ni, Pd, Pt, Cu, Zn and Cd).[92] Out of these they obtained a crystal structure by pairing the ligand with $Hg(OTf)_2$. The octahedral M_6L_8 cage structure 41 (Scheme 22) shows densely arranged ligands through π-π stacking and the interior of the assembly is thus almost completely isolated from the outside. The ligands lay on the equatorial positions of the metal ion, whereas anions are occupying the axial positions, which in turn corresponds to a charge neutral complex.

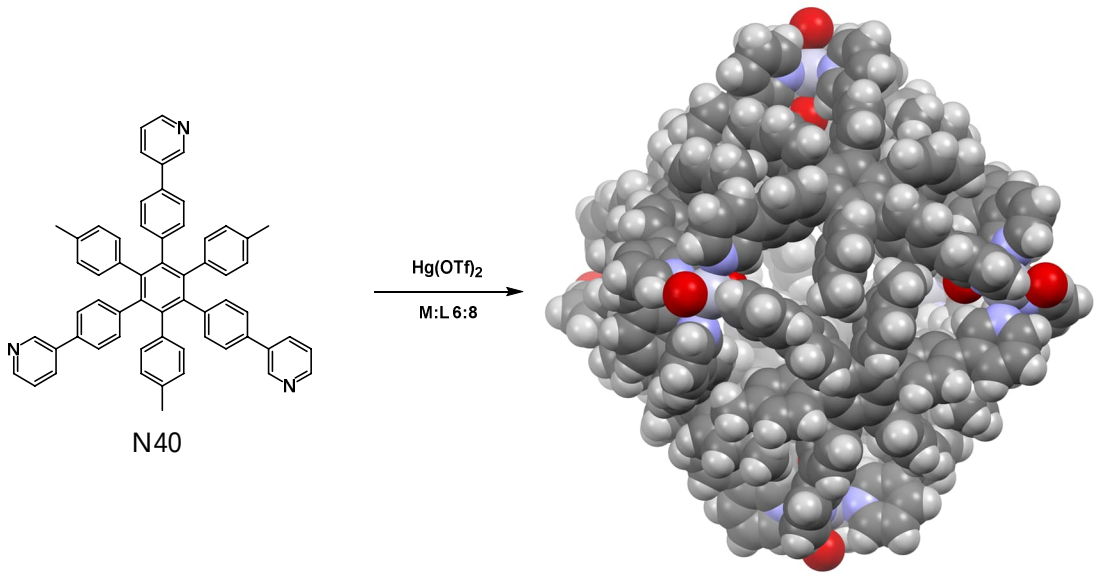

N40

41

SCHEME 22 Assembly of M_6L_8 octahedron 41. Anions and free solvent molecules are omitted for clarity.

Fujita *et al*. reacted flexible tridentate ligand 1,3,5-tris(4-pyridylmethyl)-benzene N41 with $[Pd(en)]^{2+}$ corner in water that gave rise to a mixture of oligomers. However if an organic anionic guest such as 4-methoxyphenylacetate was introduced to the reaction, M_3L_2 micro cage 42 was formed (Scheme 23). Other organic anions containing a hydrophobic moiety as well as neutral molecules like *p*-xylene were also found to template the assembly with varying yields, depending on the type of encapsulated guest.[93] Reacting this ligand in DMSO with a square-planar metal $Pd(NO_3)_2$ node yielded M_6L_8 sphere 43 (Scheme 23), without the need for an anionic template.[94]

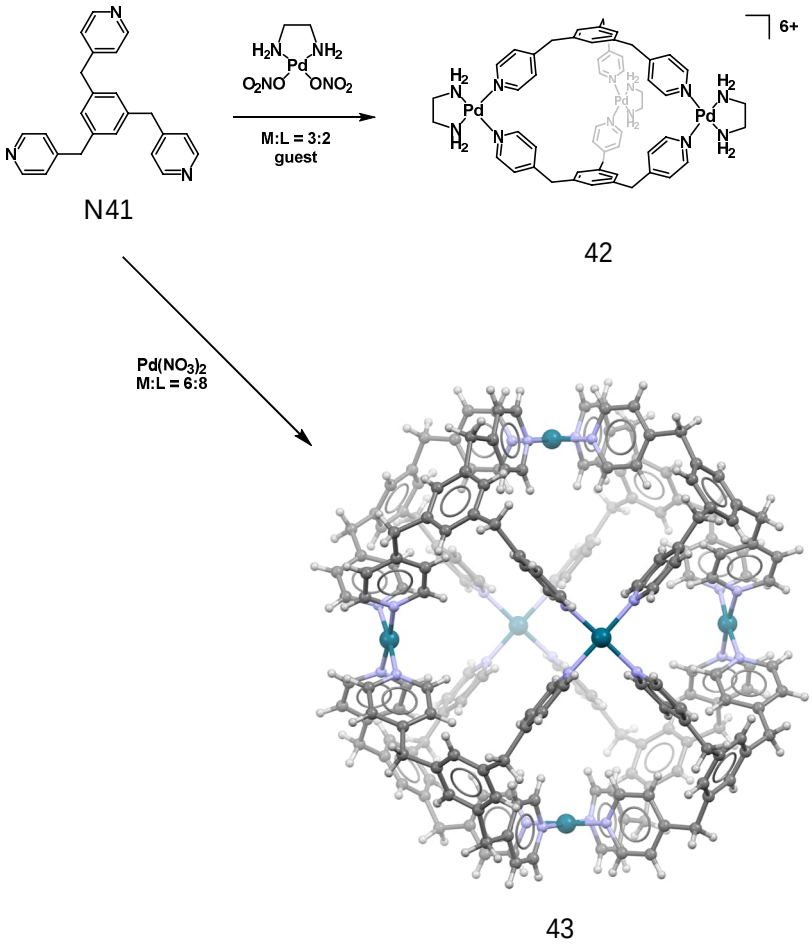

SCHEME 23 Formation of M_3L_2 micro cage (42), M_6L_8 sphere (43), encapsulated guest, anions and solvent molecules are omitted for clarity.

Switching the pyridine arms to imidazole arms yields another flexible ligand 1,3,5-tris(imidazol-1-ylmethyl)benzene N42. Reacting this ligand with zinc(II) acetate provides a charge-neutral M_3L_2 complex 44 wherein the imidazole arms form a helical assembly with $Zn(OAc)_2$ nodes due to the tetrahedral nature of the Zn^{II} metal (Figure 17). Similar ligand with a trimethylbenzene core, 1,3,5-tris(imidazol-1-ylmethyl)-2,4,6-trimethylbenzene N43, also forms M_3L_2 structures when reacted with two-coordinate silver perchlorate 45[95] or copper(I) sulphate 46[96] but with less helical assemblies than in 44, as shown in Figure 17. This opens up the micro cage and allows the exchange of the encapsulated anion.[97] With $Pd(MeCN)_2Cl_2$, an M_6L_8 assembly 47 is formed, which is similar to cage 43, but is squashed from one side due to orientational differences of pyridine *cf*. imidazole.[98]

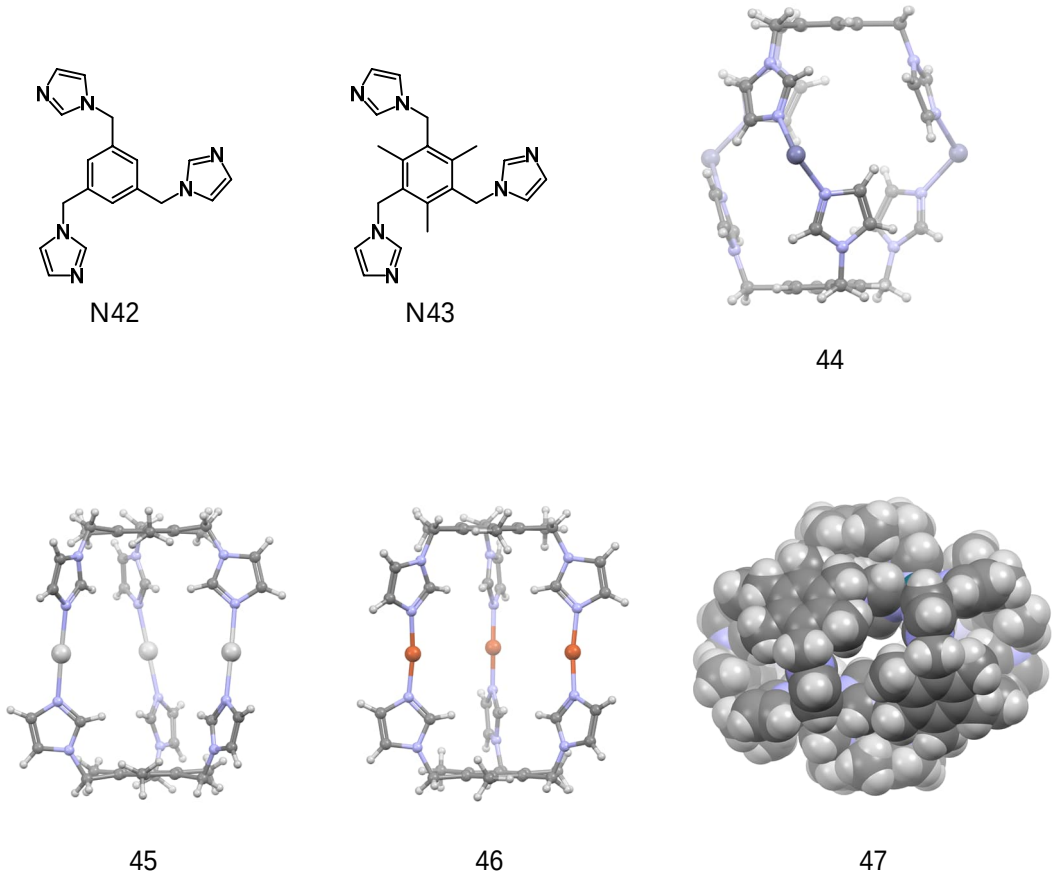

FIGURE 17 Assemblies obtained by flexible tridentate ligands. Anions are omitted from all structures, and solvent molecules are omitted from 45 and 47 for clarity. Solvent molecules in 44 were not included in the model.

Hong *et al*. used a flexible tridentate ligand N44 in conjunction with $NiCl_2$ to obtain a charge-neutral M_6L_8 assembly of $[Ni_6(N44)_8Cl_{12}]$ 48 (Scheme 24).[99] The near spherical assembly resembles that of a truncated cube, in which the $NiCl_2$ nodes are in the center of the octagonal face and the C_3N_3 rings are the triangular faces (corners of the cube).

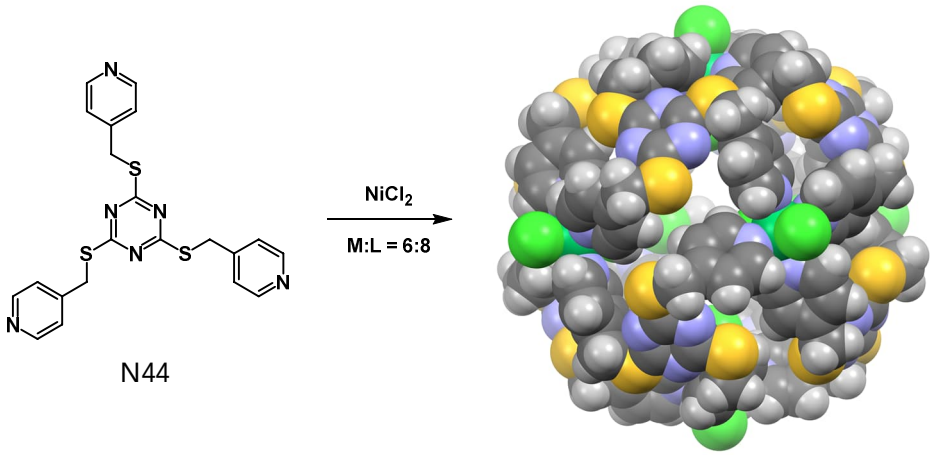

N44 48

SCHEME 24 Formation of M_6L_8 truncated cube 48, solvent molecules are omitted for clarity.

3.2 Multicomponent systems

One of the early examples of multicomponent triangular prisms is reported by Baxter *et al*. They used ligand with three individual binding sites, hexaphenyl-hexaazatriphenylene N45 as triangular bases and quaterpyridine ligand N46 as pillars in conjunction with copper(I) tetrafluoroborate to obtain $[(N45)_2(N46)_3Cu_6]^{6+}$ assembly 49.[100] Crystal structure of 49 showed a triple helical cylindrical complex that was further enhanced when using longer pillar ligands trisbipyridine (or sexipyridine, spy) N47 or tetrakis(bipyridine) (or octapyridine, octapy) N48 to yield multicompartmental structures $[(N45)_3(N47)_3Cu_9]^{9+}$ 50 and $[(N45)_4(N48)_3Cu_{12}]^{12+}$ 51, respectively presented in Scheme 25.[101] In the compartmental structures 50 and 51 each cage 'floor' is occupied by two encapsulated anions and one solvent molecule, whereas in 47 the cavity is occupied only by solvent molecules. Reacting N45 and N46 with silver triflate it is possible to obtain structure 49' which is no longer helical but is shaped into an almost perfect trigonal prism, and where the cavity is occupied by two encapsulated anions and one solvent molecule. It is also shown that larger noncompartmental structures can be made using ligands with two bipyridine subunits separated by an organic linker.[102]

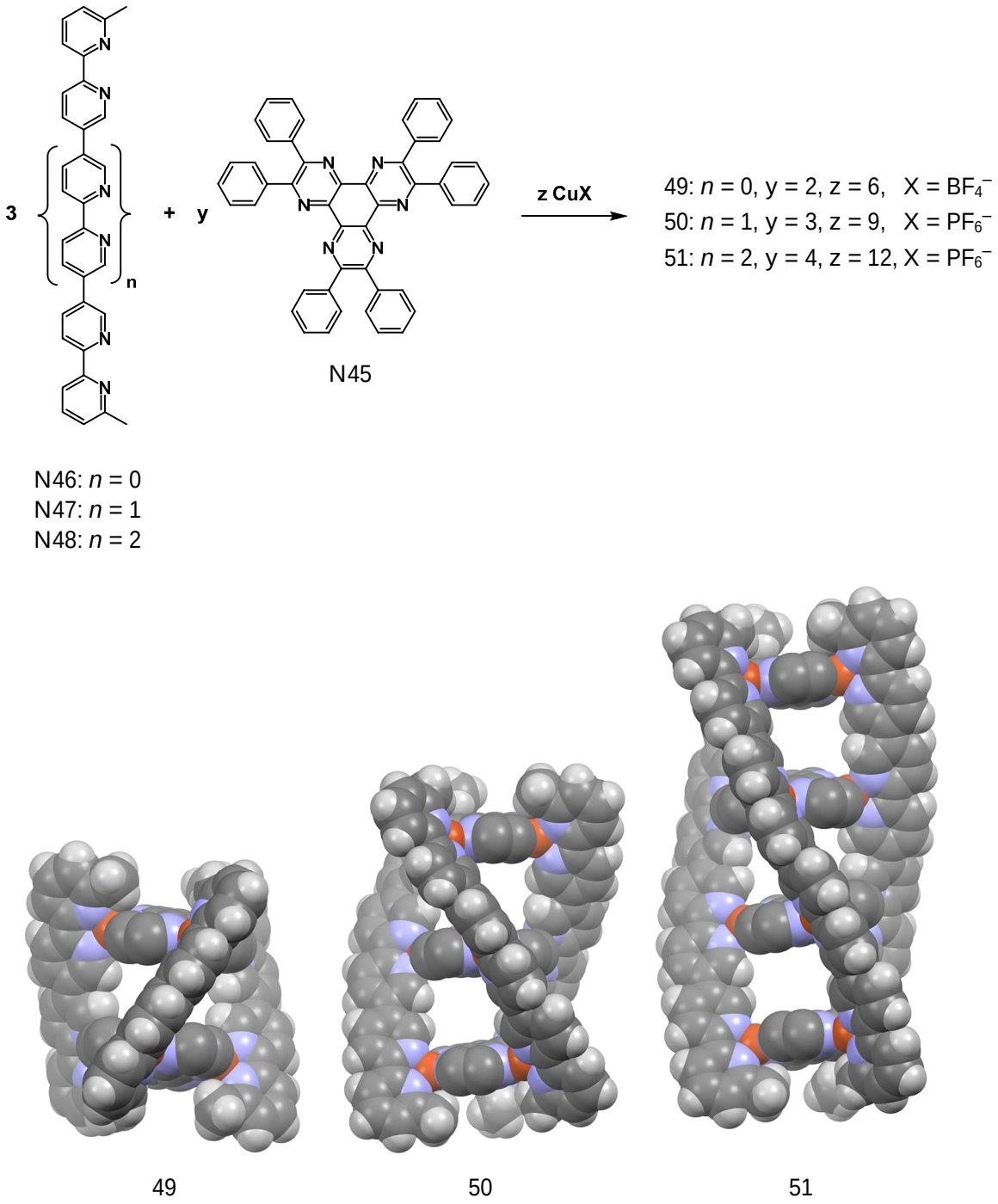

SCHEME 25 Formation of triple helical triangular prisms. Anions, solvent molecules and phenyl groups from the N45 ligand are omitted for clarity.

Combining trigonal tridentate ligand N27 with short linear bidentate ligand N49 (pyrazine) with $[Pt(en)]^{2+}$ corner should, in theory, produce $(N27)_2(N49)_3Pt_6$ trigonal prism. Unfortunately, due to parallel competing reactions, so far only homotopic assemblies have been obtained, namely cage 26 and square $(N49)_4Pt_4$. After introducing 2,3,6,7,10,11-hexamethoxytriphenylene (hmtp) as a template, the reaction between N49 and $[Pt(en)]^{2+}$ would produce a triangular prism 52 as shown in Scheme 26.[103] Once formed, 52 proved to be stable even after the template is removed, and the empty cage has a high affinity to encapsulate other large aromatic molecules. Taller prisms have been obtained with $[Pd(en)]^{2+}$ corner by extending the linear bidentate pillars, as shown in Figure 18. Due to longer linear ligands, the obtained assemblies were able to encapsulate several large aromatic guests such as pyrene, triphenylene, coronene, prophyrins and prophyrazines by stacking.[104–107] A nice example of quest stacking is demonstrated by Yamauchi *et al*.[107] as they were able to obtain stacks of pyrene-4,5-dione ranging from two to five simply by varying the length of the linear pillar. Stack of two was obtained with N50, and stacks of three to five were obtained with ligands N51, N54 and N55b, respectively. With ligands N51, N53 and N55a paired with either pyrene or triphenylene guests they obtained interpenetrated assemblies, wherein two triangular prisms were intertwined while stacking three to five guest molecules.[105]

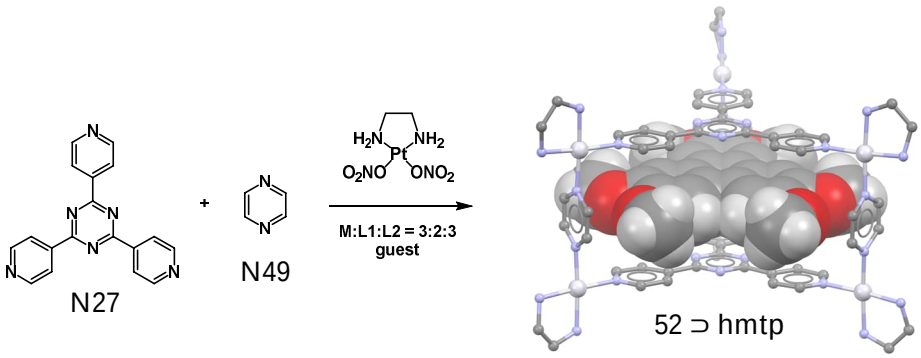

SCHEME 26 Formation of multicomponent triangular prism. Hydrogen atoms of 52, anions and solvent molecules are omitted for clarity.

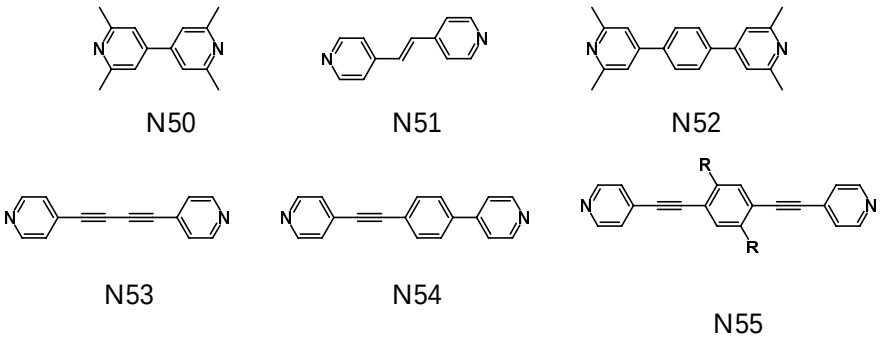

FIGURE 18 Examples of extended bidentate ligands.

Stang's group has created a series of template-free tetragonal[108–110] prisms utilizing tetradentate ligand N56 and hexagonal[111,112] prisms with hexadentate ligand N57 together with *cis*-protected $[Pt(PEt_3)_2]^{2+}$ corner, and either N-donor or O-donor -based ligands as pillars (Figure 19). Tetragonal prisms were obtained using ligands N1, N51, N58, O12 and O13a-c whereas hexagonal prisms were resulted from ligands O12, O13a, O14 and O15. Multinuclear ^{31}P and ^{1}H NMR analyses clearly indicated the formation of single discrete product, and mass spectrometry further verified the existence of these products. While some of these cages could be obtained as a solid, no single crystal could be analyzed.

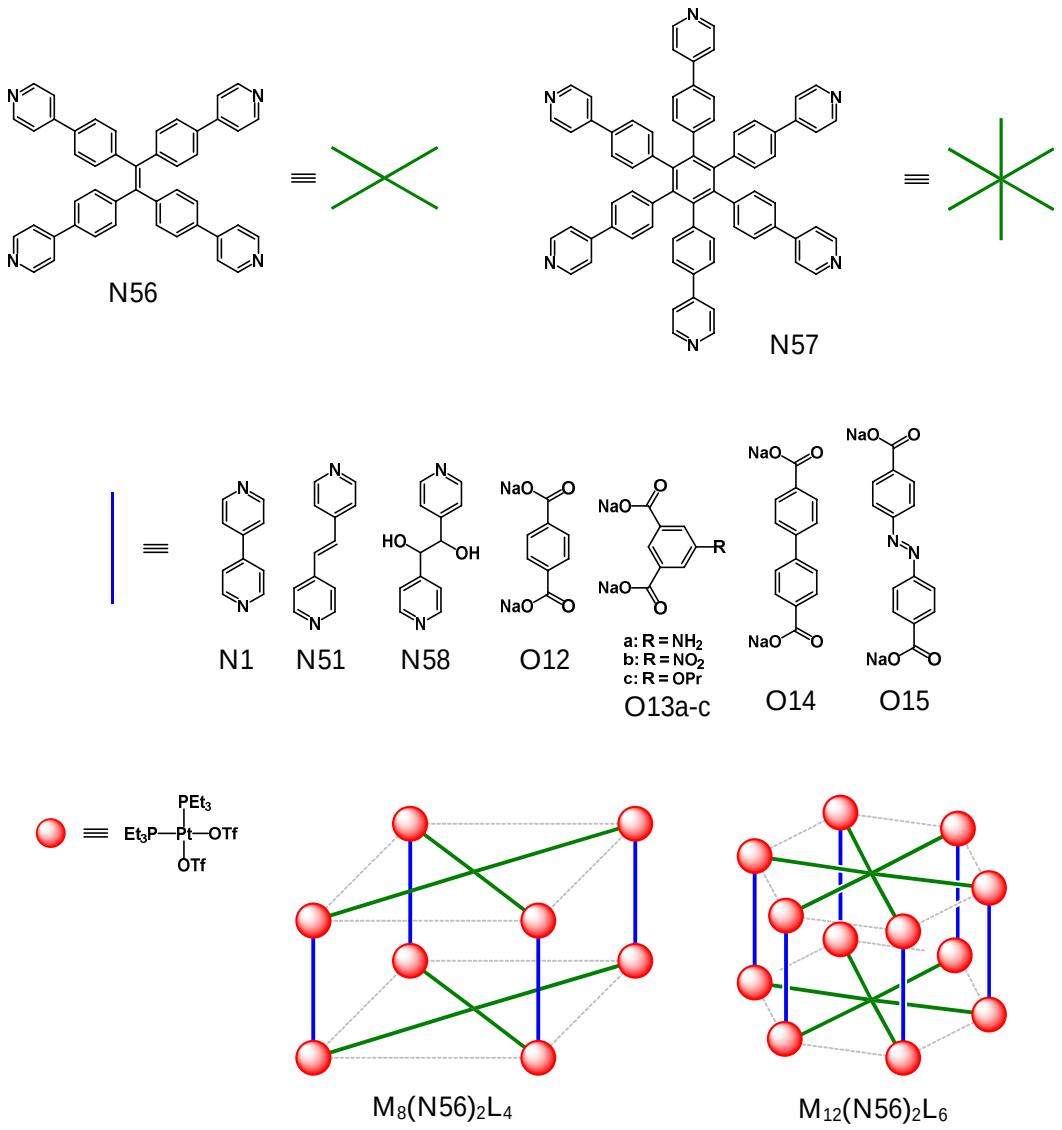

FIGURE 19 Schematic depiction of tetragonal and hexagonal prisms. Two tetradentate (N56) or hexadentate (N57) ligands (green) form the top and bottom faces of the prism, while four or six linear ligands (blue) form the vertical pillars joined together with 90° *cis*-protected Pt^{II} corners (red).

3.3 Subcomponent systems

A relatively recent method for synthesizing SCCs is the subcomponent self-assembly where the ligand and complex simultaneously self-assemble via formation of carbon-heteroatom (covalent) and metal-heteroatom (coordination) bonds, the two parallel synergic processes driving toward thermodynamic minimum. Though not the first example of subcomponent self-assembly, Nitschke *et al*. reacted taurine and 2-formylpyridine in water to obtain a mixture of compounds in a dynamic combinatorial library. This library of compounds then collapses upon addition of Cu_2O to the mixture, yielding a single stable product 53 (Scheme 27a).[113–115]

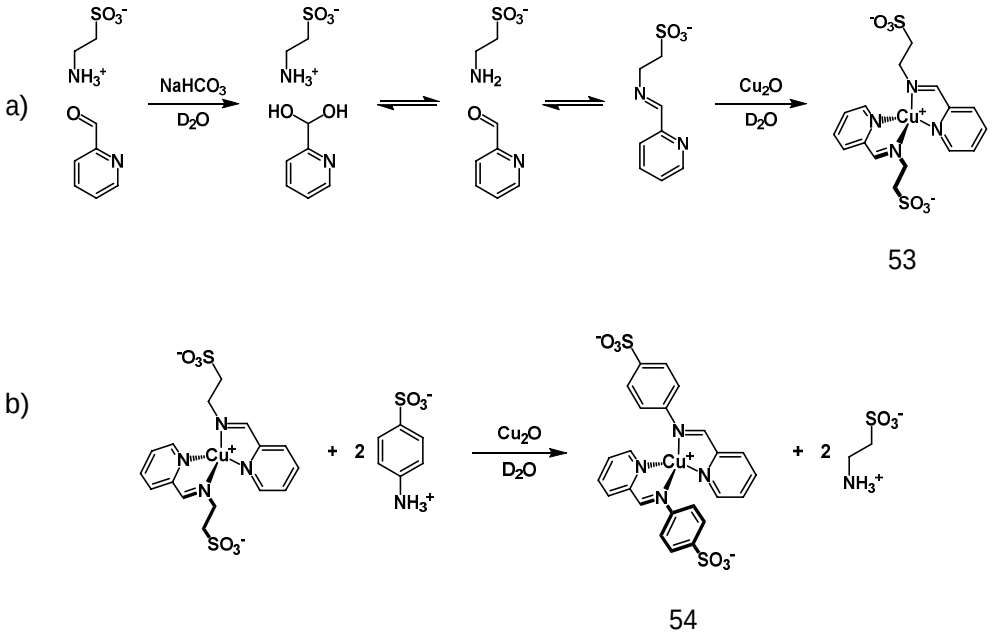

SCHEME 27 a) Subcomponent assembly of 53, b) subcomponent exchange.

Individually both imines and Cu^{I} ions are ordinarily unstable in water, meaning that in 53 the imines and Cu^{I} ions are mutually stabilized. Furthermore, it was shown that it's possible to exchange the subcomponent of 53; adding sulfanilic acid to an aqueous solution of 53, compound 54 is formed by liberating taurine *via* transamination (Scheme 27b). Furthermore, from a mixture containing 2- ,3- and 4-formylpyridine isomers only compound 53 was formed. Similarly from a mixture containing 2-formylpyridine, 3,4-dihydroxybenzaldehyde and sodium 2-formylbenzenesulfonate, only compound 53 was formed. It was also shown that transmetallation is also possible in a similar system by switching Cu^{I} to Fe^{II}, with ligand remaining unchanged despite of system changing from Cu_2L_2 to Fe_2L_3, *i.e.* from tetrahedrally coordinated to octahedrally coordinated metal.[116]

To further broaden this principle, Mal *et al*. synthesized a water-soluble M_4L_6 tetrahedron 54[117] using 2-formylpyridine, 4,4'-diaminobiphenyl-2,2-disulfonic acid and iron(II) sulfate with tetramethylammonium hydroxide as base (Scheme 28). It was also possible to encapsulate cyclopentane and -hexane into the cage, and the guest molecules could be released by reversible unlocking of the cage using acid, and again relock the cage *i.e.* reassembling the cage using a base. Guest could also be released irreversibly *via* subcomponent exchange by adding tris(2-ethylamino)amine.

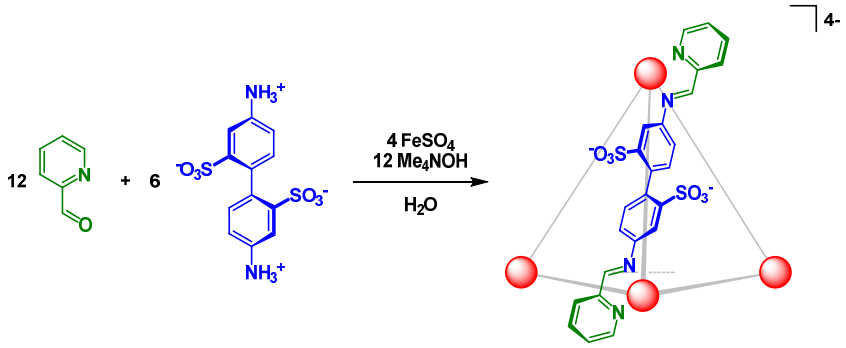

54

SCHEME 28 Subcomponent assembly of 54.

Following the same principle, Meng *et al*. used 2-formylpyridine jointly with tetrakis(4-aminophenyl)porphyrin (H_2-tapp) and $Fe(OTf)_2$ in DMF to produce an hollow M_8L_6 cube 55 (Scheme 29).[118] Similar cages were also obtained by using Ni^{II} and Zn^{II} substituted tetrakis(4-aminophenyl)porphyrins (Ni-tapp and Zn-tapp respectively), suggesting that the formation of structures like 55 is a general feature of tetrakis(4-aminophenyl)porphyrins. Obtained cubes had an interior volume of >1300 $Å^3$ and the cavity that was surrounded by π-electron rich porphyrins making them suitable for encapsulating large aromatic guests. Both H_2-tapp and Ni-tapp based cages (H_2-55 and Ni-55) were able to encapsulate three coronene molecules whereas Ni-tapp based cage captured either one fullerene C_{60} or C_{70} molecule. Interestingly it was possible to exchange [C_{60} ⊂ Ni-55] to either [C_{70} ⊂ Ni-55] or [(coronene)$_3$ ⊂ Ni-55] by adding an excess of C_{70} or coronene to solution of [C_{60}⊂Ni-55]. However, it was not possible to turn [C_{70} ⊂ Ni-55] to [(coronene)$_3$ ⊂ Ni-55] by adding excess coronene to the solution or *vice versa*.

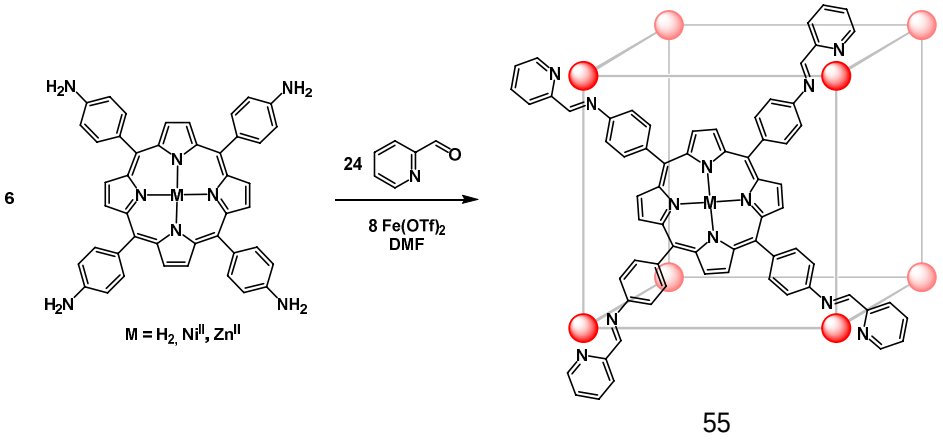

SCHEME 29 Subcomponent assembly of 55.

Series of face-capped M_4L_4 tetrahedra were obtained when using tritopic precursors as starting materials.[119] The four trianilines from A to D, as shown in Scheme 30, were reacted in acetonitrile with 2-formylpyridine and iron(II) triflate, to yield four assemblies 56–59 with increasing interior void cavity volumes of 31, 45, 229 and 823 Å^3, respectively. The structural similarities of trianilines A and B and thus assemblies 56 and 57, allowed the former to be incorporated into a mixed-ligand assemblies, whereas mixing any other trianiline ligands yielded only homoleptic assemblies. When mixed, the two ligands (A and B) formed assemblies of A_4, A_3B, A_2B_2, A_1B_3 and B_4 in a 1:4:6:4:1 ratio, making the ligands practically interchangeable.

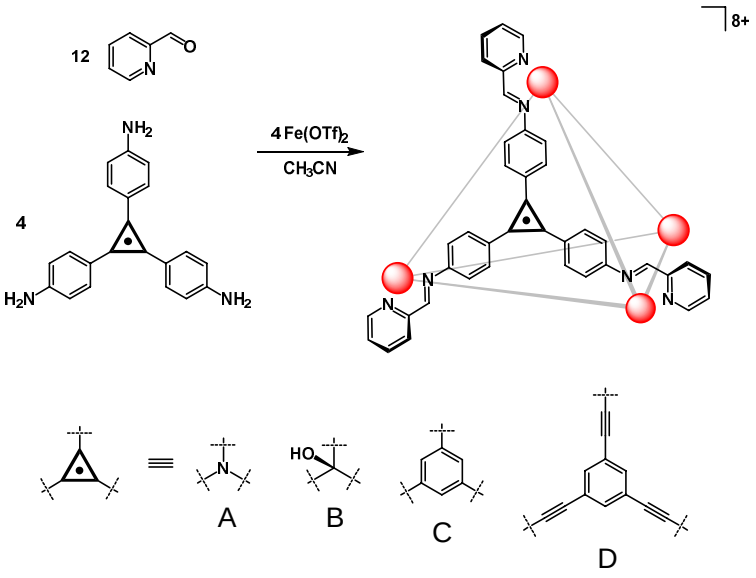

SCHEME 30 General procedure for subcomponent assembly of M_4L_4 tetrahedra.

Starting with 4-(pyridine-4-yl)aniline, a square-planar tetrakis(pyridine)-platinum(II) tetrafluoroborate precursor can be obtained and isolated, and then reacting this precursor with 2-formylpyridine and iron(II) triflate (6:24:8 ratio) in acetonitrile yield a heterometallic cube $Fe_8Pt_6L_{24}$ 60.[120] According to ^1H and ^{13}C NMR as well as mass spectrometry, compound 60 is a discrete assembly. This compound can also be obtained in a one-pot synthesis; reacting 4-(pyridine-4-yl)aniline (24 equiv.), $Pt(PhCN)_2Cl_2$ (6 equiv.), $AgBF_4$ (12 equiv.), $Fe(OTf)_2$ and 2-formylpyridine (24 equiv.) in acetonitrile at 65 °C yielding compound 52 as a major product. This route involves self-assembly of 62 building blocks forming total of 96 new bonds to yield a singular compound. Scheme 31 illustrates the two different routes through which the assembly 60 can be prepared.

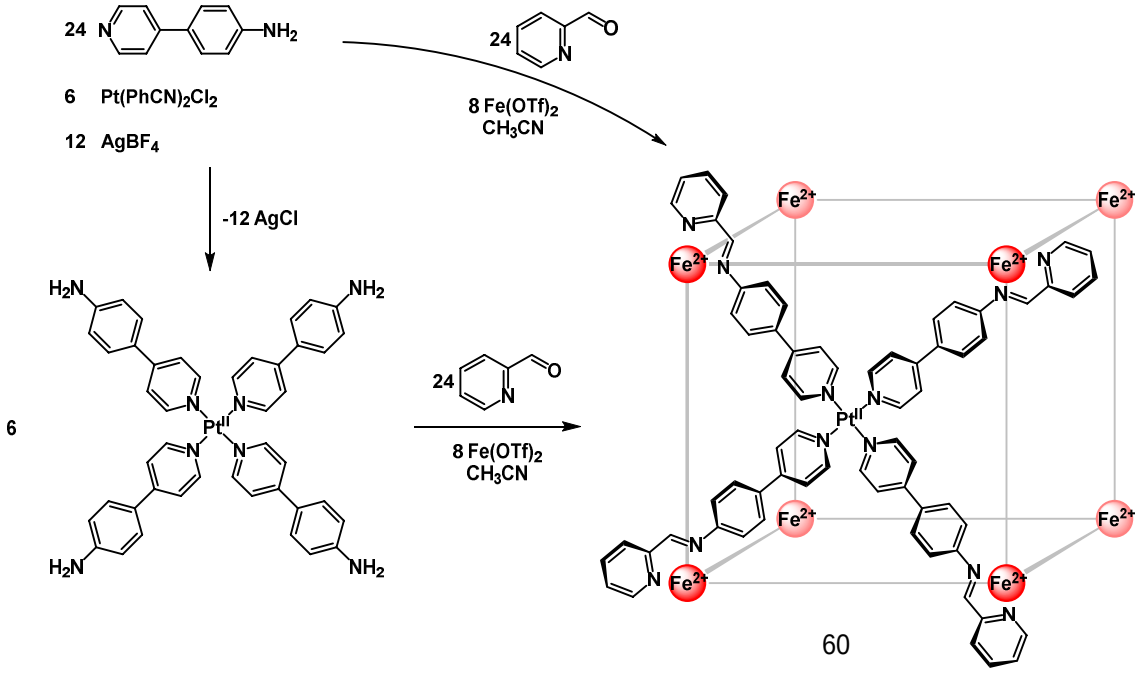

SCHEME 31 Preparation of heterometallic $Fe_8Pt_6L_{24}$ cube *via* two-step and one-pot routes.

4 APPLICATIONS FOR MOP

As shown above, a wide range of different assemblies can be obtained by pairing metal nodes with organic ligands in suitable conditions. Some of these assemblies have a well-defined interior cavity, which creates an environment that differs from the surrounding solution. This in turn creates a possibility to encapsulate guest molecules within the assembly, though the level of how effortlessly guest (or solvent) molecules can be encapsulated within the cavity is dependent on several factors. The openings of the cage determine the size of the molecule that can freely travel to the cavity, while the properties of the assembly determine which kind of molecules can be encapsulated. These properties include Coulombic, van der Waals, hydrogen and halogen bonding, π–π and CH$\cdots\pi$ interactions, hydrophilic/-phobic properties among others. Generally speaking, these factors can be fine-tuned by modifying the ligands and/or metal nodes to further improve desired encapsulation. Because the size of the cavity is relatively small, usually few ångströms wide, these assemblies can be described as nanovessels; tiny containers that can encapsulate as few as one single molecule. Furthermore this creates a unique opportunity to utilize these assemblies as nanoreactors; a reaction vessel, where the reaction occurs sometimes to only a single molecule at a time. The following section offers a series of examples of how MOPs have been utilized in different applications.

4.1 Storage

4.1.1 Stabilization of reactive molecules and intermediates

Raymond's group has shown that $[Ga_4(O8)_6]^{12-}$ cage (10) can be used to stabilize a series of phosphonium,[121,122] diazonium,[123] tropylium[123] and iminium ions,[124] as well as reactive organometallic intermediates[125] in an aqueous medium (Figure 20). The reactive phosphonium species tend to decompose in aqueous medium but once encapsulated inside the hydrophobic interior of 10, the molecules were stable for several days to even for weeks. Decreasing pH value of the solution also increases the stability of the guest. Moreover, the size of the encapsulated quest also significantly contributes to the stability of the host-guest complex; *e.g.* $[Me_2C(OH)PMe_3]^+$ is the least stable, next the $[MeEtC(OH)PMe_3]^+$ then followed by $[MeEtC(OH)PPhMe_2]^+$ whereas the $[MeEtC(OH)PMe_3]^+$ is the most stable of the cations. Contrary, the presence of fluorine atoms decreases the stability of the guest; *e.g.* $[Me(CFH_2)C(OH)PMe_3]^+$ is table up to one week, but $[Me(CF_3)C(OH)PMe_3]^+$ is only stable for a few days inside the 10.[122] In similar fashion it was shown that cage 10 can also encapsulate diazonium and tropylium cations and thereby slowing down the decomposition of these compounds.[123]

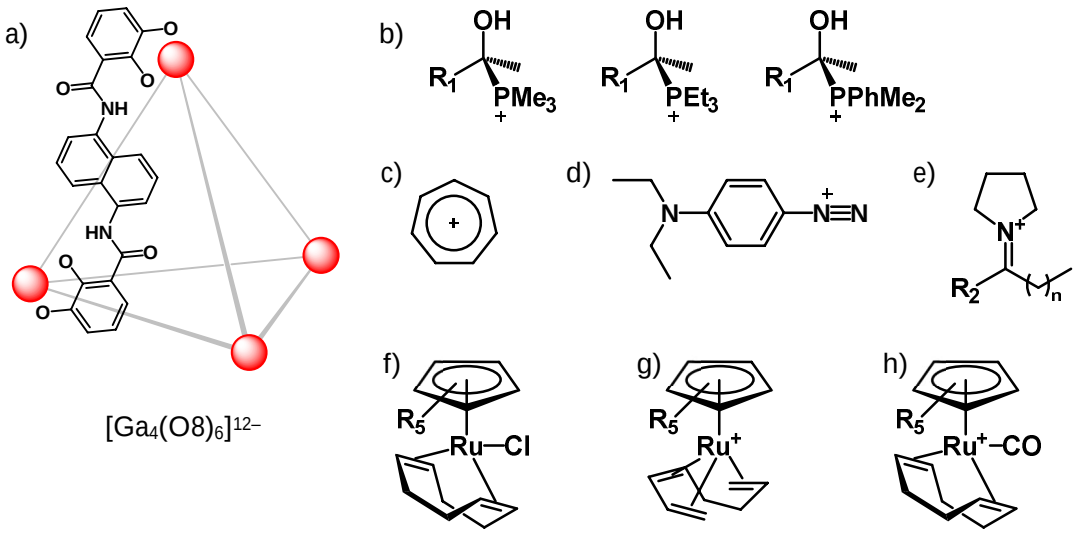

FIGURE 20 a) Anionic cage 10, b) different phosphonium cations, c) tropylium cation, d) diazonium cation, e) iminium cations and f-h) organometallic intermediates. R_1 = Me, Et, CFH_2 or CF_3; R_2 = Me (*n* = 0–6) or Et (*n* = 2–5); R_5 = H or Me.

Iminium ions generated *in situ* from amines and ketones possess a negligible concentration in an aqueous solution at neutral or alkaline pH value. However, in the presence of 10 it was found that a series of pyrrolidine-based iminium ions were detected in an aqueous solution using ^{1}H NMR.[124] In the absence of 10, no iminium ions were observed, indicating that the iminium ion is encapsulated inside the hydrophobic interior. Based on binding efficiencies, the optimal size for iminium ions derived from 2-ketones was found to be n = 3 and n = 4, with both shorter and longer 2-ketones have lower efficiencies. Once the alkyl chain was too long to fit inside the host cavity, no iminium ions could be detected. A similar trend was also observed with iminium ions derived from 3-ketones. Once encapsulated inside the host, the iminium ions were stable for months at room temperature.

Similarly, the host 10 has also been shown to encapsulate ruthenium half-sandwich complexes $[CpRu(cod)]^{+}$ (Cp = cyclopentadiene, cod =1,5-cyclo-octadiene, Figure 20f-h), compounds used as a catalyst for C-C bond formations, in aqueous solution.[125] [CpRuCl(cod)] (Figure 20f) encapsulates as a highly unstable ruthenium complex $[CpRu(1,3,5\text{-octatriene})]^{+}$ (Figure 20g) within the cavity of the host 10. Free $[CpRu(1,3,5\text{-octatriene})]^{+}$ decomposes in aqueous solution within minutes but once encapsulated is stable for weeks, and still able to react with carbon monoxide, CO, to form $[CpRu(cod)(CO)]^{+}$ (Figure 20h) inside the host 10. Similarly, once formed separately, $[CpRu(cod)(CO)]^{+}$ can also be encapsulated. Also, similar encapsulation results were observed using pentamethylcyclopentadiene analogies of the guest molecules.

Mal *et al*. showed that host 54 can encapsulate highly reactive and hydrophobic white phosphorus (P_4) and stabilize it to a point where it is both air-stable and water soluble (Scheme 32).[126] Despite enough room in the cavity for oxygen molecule, P_4 won't react with O_2, as it would lead to the formation of oxidized intermediates that are too large for the cavity. Encapsulated P_4 can be stored for months in room temperature and can easily be released from the cavity with benzene, after which it'll regain its air-sensitivity. The encapsulation was also observed by X-ray diffraction (Figure 21a).

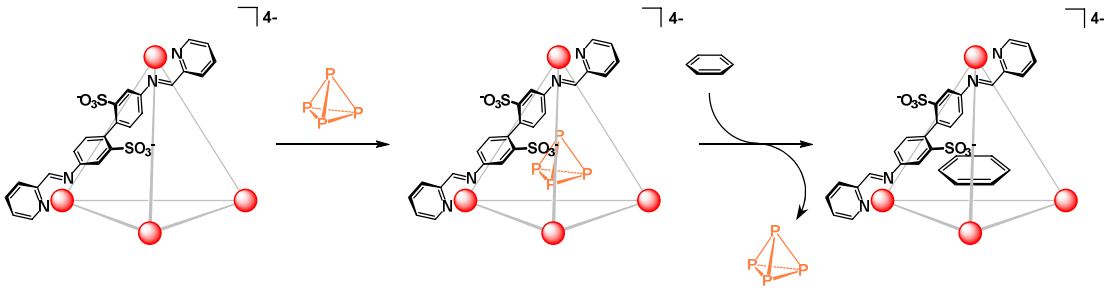

SCHEME 32 Schematic representation of encapsulation and release of P_4 inside host 54.

4.1.2 Molecular encapsulation and recognition

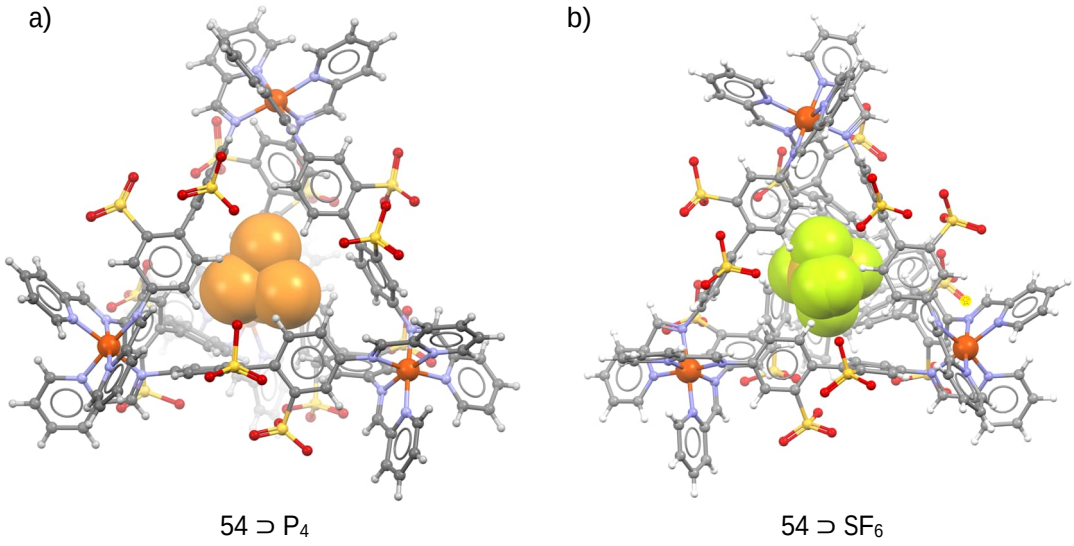

FIGURE 21 Encapsulated P_4 (a) and SF_6 (b) inside host 54. Solvent molecules and counter cations are removed for clarity.

Riddell *et al*. also showed that host 54 can encapsulate sulfur hexafluoride (SF_6) both in solution and solid state.[127] Solution of [54 ⊃ SF_6] left open to the atmosphere for one week showed negligible loss of gas, and preliminary experiments indicated that the host 54 has no affinity toward Xe, Ar, N_2, O_2, C_2H_4, CO_2 or N_2O gases, so it could be used to separate SF_6 from other gases. SF_6 can be easily released from the host by either increasing the temperature or chemically opening the host cage. In the solid state, the encapsulation of SF_6 was observed by X-ray diffraction (Figure 21b).

Preston *et al*. used ligand N59 with $Pd(BF_4)_2$ to obtain a multi-cavity $[Pd_4L_4]^{8+}$ cage 60 capable of selectively binding different guests (Scheme 33).[128] According to ^1H NMR studies, the host selectively binds four cisplatin ($Pd(NH_3)_2Cl_2$) entities in peripheral cavities and one triflate (OTf, $CF_3SO_3^-$) anion in the central cavity and two triflate anions in exohedral faces. When both guests are present, all binding sites are occupied forming a host-guest complex $[61 \supset (\text{cisplatin})_4(OTf)_3]^{5+}$.

Glasson *et al*. have reported the selective encapsulation of $[Fe^{III}Cl_4]^-$ anion over $[Fe^{II}Cl_4]^{2-}$ anion inside tetrahedral cage 62.[129] Treating ligand N60 with $FeCl_2 \cdot 5\ H_2O$ in acetonitrile under refluxing conditions, led to the formation of $[62 \supset Fe^{III}Cl_4]^{7+}$ (Scheme 34). Due to the mix of Fe^{II} and/or Fe^{III} chloro species undoubtedly present in the solution during the formation of the $[62 \supset Fe^{III}Cl_4]^{7+}$, it is clear that 62 selectively encapsulates $[Fe^{III}Cl_4]^-$ anion rather than $[Fe^{II}Cl_4]^{2-}$ anion.

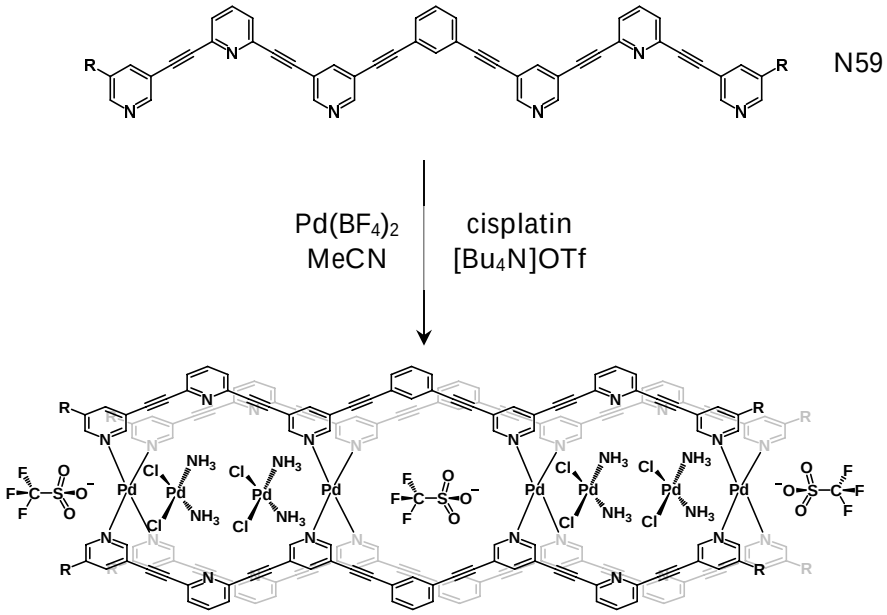

SCHEME 33 Formation of multicavity complex with selective binding sites. R = $O(CH_2)_2O(CH_2)_2OCH_3$

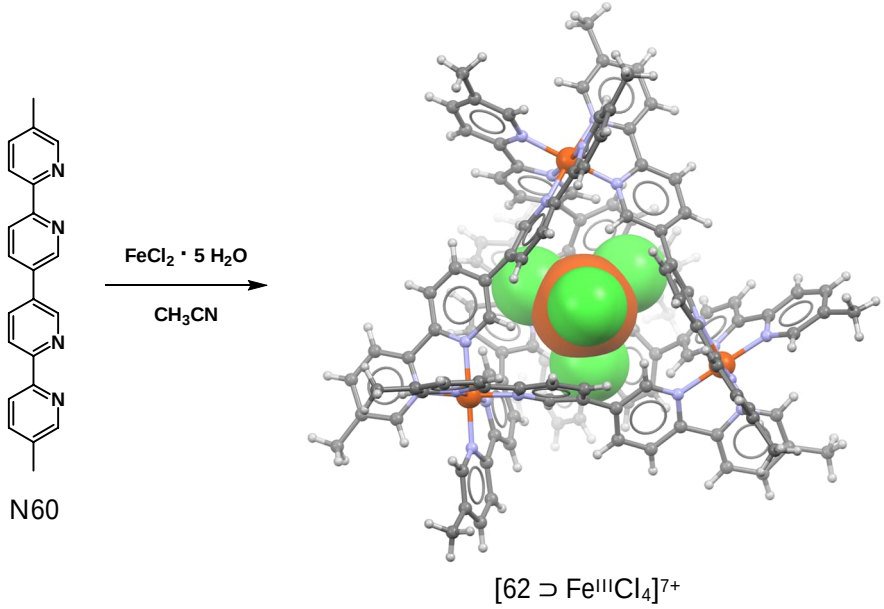

SCHEME 34 Assembly of tetrahedral host 62 incorporating anionic guest $[Fe^{III}Cl_4]^-$. Nonencapsulated anions, solvent molecules and hydrogen atoms are omitted for clarity.

Yamashina *et al*. showed that M_2L_4 host 63a, obtained from ligand N61a with $Pd(NO_3)_2$ (Scheme 35), can encapsulate a wide range of neutral planar and spherical guests shown in Figure 22.[130] Planar guests such as pyrenes, triphenylene, phenanthrene and corannulene formed host-guest complexes in 1:2 ratio, while spherical guests like paracyclophanes, adamantanes and fullerene C_{60} formed complexes in 1:1 ratio. Similar M_2L_4 host 63b, obtained from ligand N61b with $PtCl_2$, was shown to selectively encapsulate d-sucrose in water from the mixture of other natural disaccharides.[131] The strict selectivity of d-sucrose for host 63b stems from the effective steric match and multiple CH···π -interactions between the sucrose and polyaromatic cage interior. Artificial sugars such as sucralose and aspartame were shown to have an even higher affinity towards host 63b. The same host was also shown to encapsulate benzene and xanthine derivatives with three methyl groups (mesitylene and caffeine) over those with two methyl groups (*m*-xylene, theobromine and theophylline) or one methyl group (toluene and 3-methylxanthine) in water.[132]

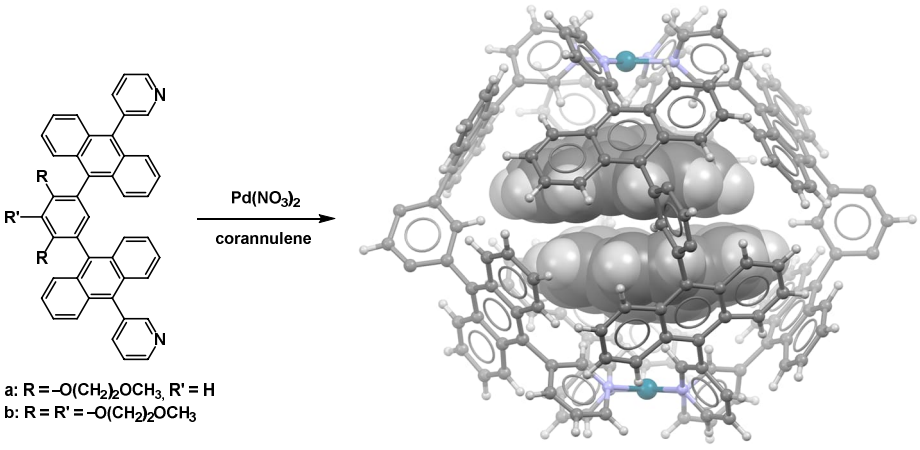

SCHEME 35 Assembly of host 63a encapsulating two corannulene molecules. Anions, solvent molecules and R-groups other than hydrogen atoms are omitted for clarity.

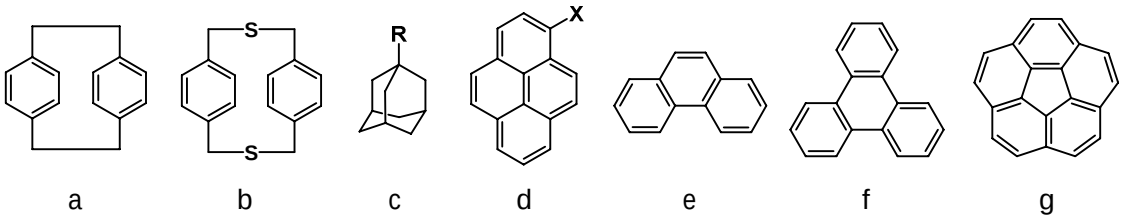

FIGURE 22 Guest molecules encapsulated by host 63a. a) [2.2]-paracyclophane, b) dithia-[3.3]paracyclophane, c) adamantanes (R = Ac, Et or H), d) pyrenes (X = Me, H, Br or NH_2), e) phenanthrene, f) triphenylene and g) corannulene.

Freye *et al*. demonstrated the formation of a interpenetrated dimeric cage [Pd_4L_8] 64 using ligand N62 and $Pd(BF_4)_2$.[133] One BF_4^- anion serves as a template for dimerization of Pd_2L_4 cage to form [$Pd_4L_8{\cdot}BF_4$] double-cage (Scheme 36a). Addition of halide (F^-, Cl^- or Br^-) anions to the system will remove BF_4^- anions that are loosely situated in the outer cavities, which in turn will make otherwise locked-in center BF_4^- anion able to be removed. The outer cavities have such a high affinity towards chloride anions that those, unlike fluoride or bromide anions, cannot be removed by introducing Ag salts to the system.[133] Adding bulky aryl groups to from ligand N63, forms only monomeric Pd_2L_4 cage 65 when mixed with $Pd(BF_4)_2$, by preventing the BF_4^- anion to act as a template.[134] Addition of chloride anion will in turn induce dimerization to form [$Pd_4L_8{\cdot}Cl$] double-cage 65'. The outer cavities are then enlarged enough to encapsulate large anions, such as ReO_4^- (Scheme 36b).

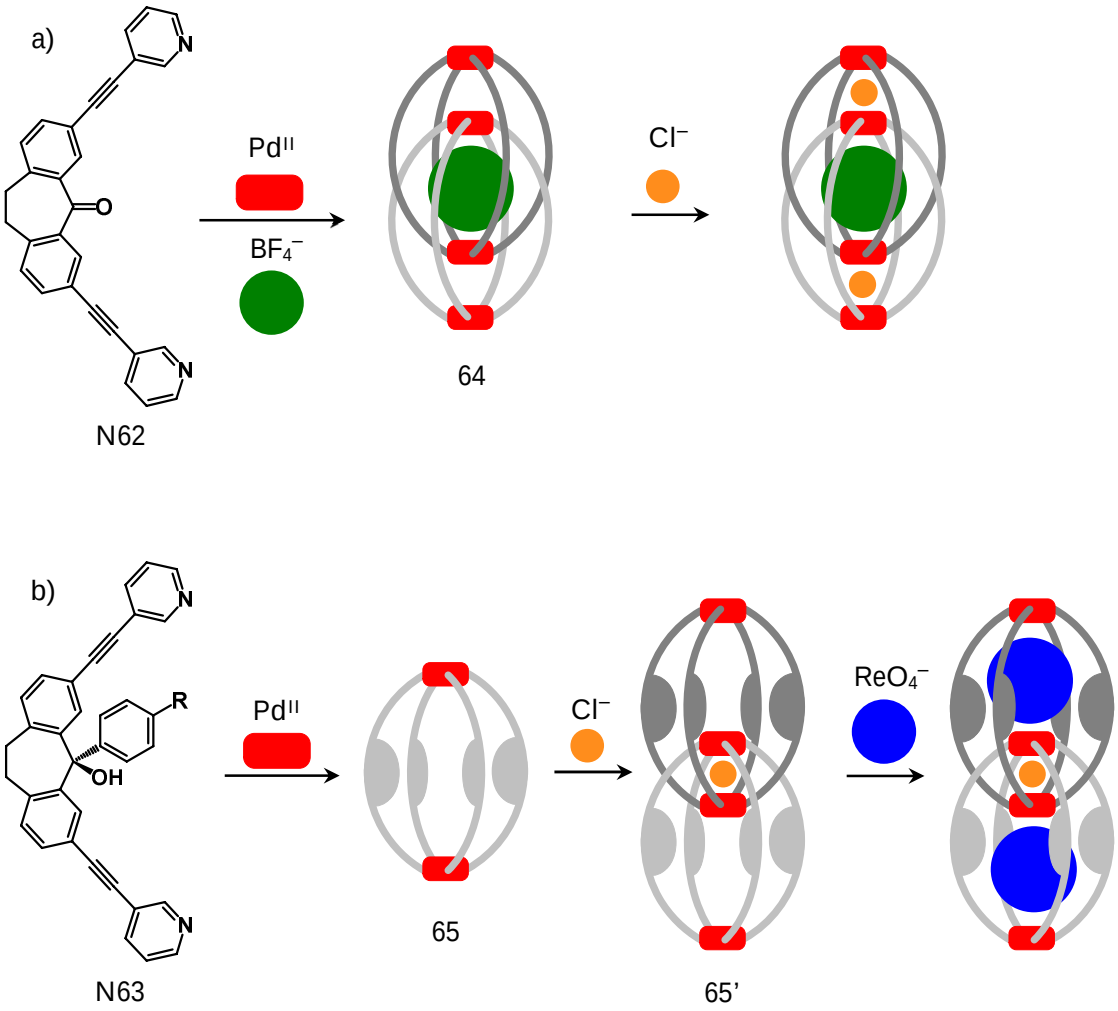

SCHEME 36 a) Formation of double-cage [$Pd_4(N62)_8{\cdot}BF_4^-$] 64 *via* BF_4^- anion template and chloride encapsulation, and b) formation of monomeric cage [$Pd_2(N62)_4$] 65, its dimerization to [$Pd_4(N63)_8{\cdot}Cl^-$] 65' *via* Cl^- template and encapsulation of ReO_4^- anions. R = CF_3, OMe or Me.

4.2 Catalysis inside the cage

Cullen *et al*. showed that water-soluble cubic M_8L_{12} cage $[Co_8(N64)_{12}](BF_4)_{16}$ 66 is capable to catalyze the Kemp elimination reaction of benzisoxazole with hydroxide to produce 2-cyanophenolate (Scheme 37).[135] The guest (benzisoxazole) molecule is encapsulated into the hydrophobic cavity of the 66, and in an alkaline solution is surrounded by partially desolvated hydroxide ions due to ion pairing between cationic cage and hydroxide anions. The Kemp elimination will then take place inside the cavity and the hydrophilic product (2-cyanophenolate) is ejected from the cavity, thus enabling catalytic turnover. Introduction of cyclodecanone, which has a higher affinity towards 66 than benzisoxazole, rendered the reaction rate to that of the uncatalyzed reaction. The same was observed without the cage when only Co^{II} ions were present.

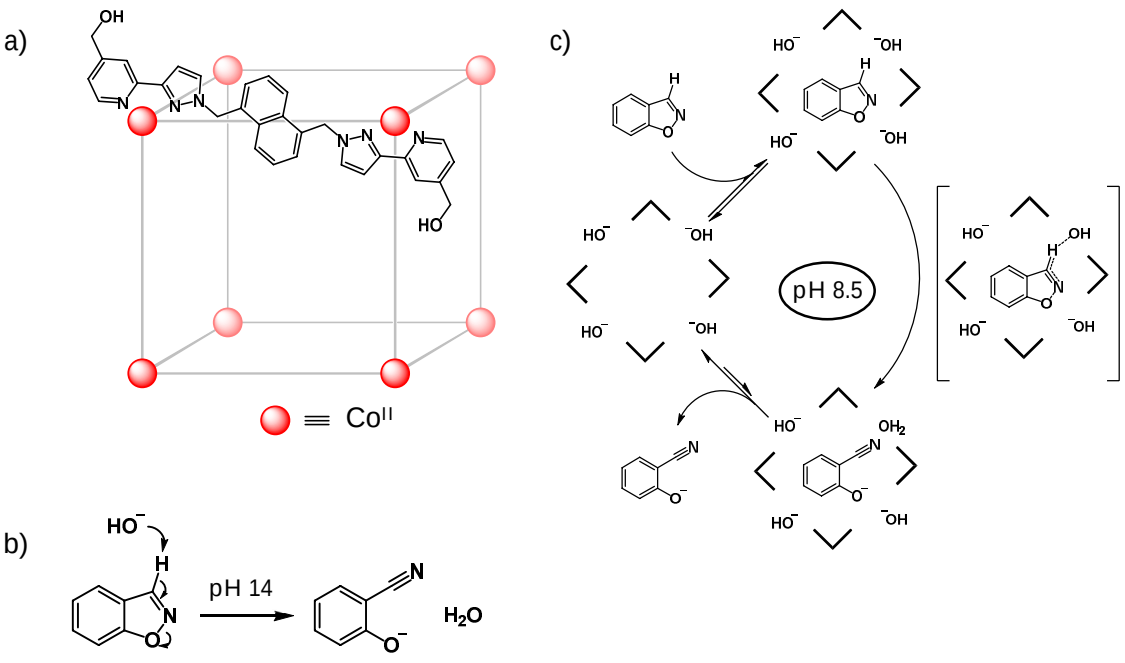

SCHEME 37 a) Cage $[Co_8(N64)_{12}]^{16+}$ (66), b) The Kemp elimination reaction, and c) schematic representation of catalytic reaction cycle inside the 66, adapted from ref.[135]

Hastings *et al*. reported in a detailed study an impressive 2.1 million-fold rate enhancement for Nazarov cyclization of pentamethylcyclopentadiol inside tetrahedral host 10 (Figure 23).[136] The enhancement was ascribed to the stabilization of transient protonated species inside the cage. Though there are no functional groups inside the cavity, the protonation of the guest and the subsequent reaction products are favorable due to the negative charge of the host and cation–π interactions with the naphthalene rings of the ligands. The proposed mechanism is presented in Scheme 38.

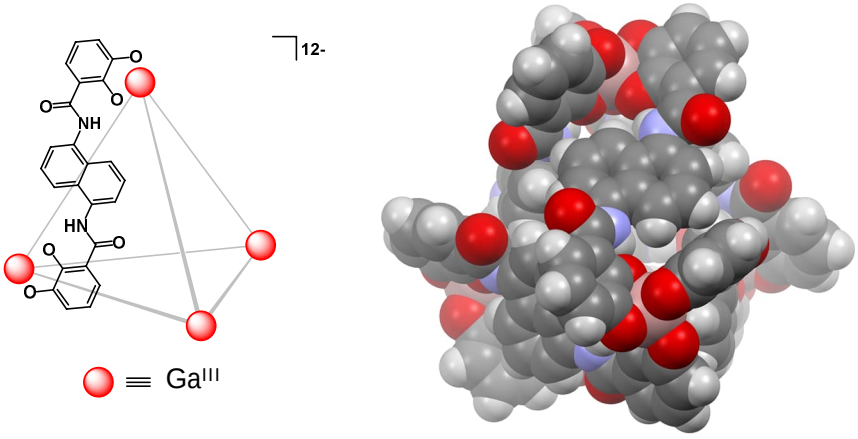

FIGURE 23 Anionic $[Ga_4(O8)_6]^{12-}$ host 10. Cations and free solvent molecules omitted for clarity.

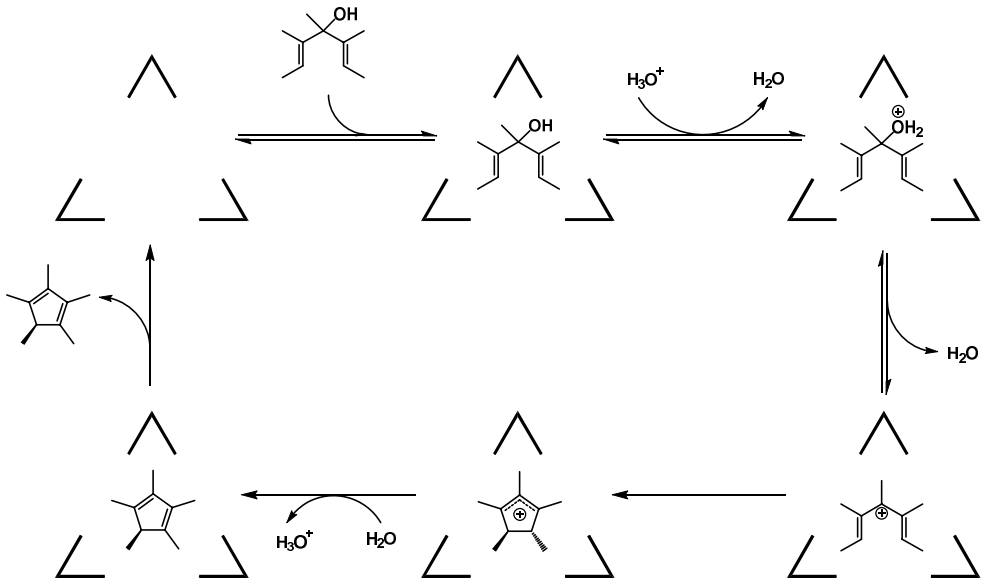

SCHEME 38 Proposed mechanism for Nazarov cyclization of 1,4-pentadien-3-ol catalyzed by tetrahedral host 10, adapted from ref.[136]

Hart-Cooper *et al*. showed that host 10 is capable of chemoselective carbonyl-ene cyclization of 3,3,7-trimethyl-oct-6-enal (3-methylcitronellal) 67 to form alkenes 68a and 68b (Scheme 39) with *trans*-alkene (68a) being the major product (83 % *trans* / *cis*).[137] Without the catalytic amount of cage 10 being present, diols 68c and 68d (75 % *trans* / *cis*), meaning that encapsulation in 10 afforded conformational control during cyclization. The main downside of cage 10 was its stability towards air oxidation in elevated temperatures or low pH value. Cage 10 also forms a racemate, which needs to be treated with (−)-*N'*-methylnicotinium iodide (*S*-nicI) to obtain enantiopure samples of ΔΔΔΔ-(S-nic) ⊂ 10 or ΛΛΛΛ-(S-nic) ⊂ 10. For these reasons Zhao *et al*. prepared a chiral ligand O16, that produced either enantiopure ΔΔΔΔ -69 or ΛΛΛΛ -69 (Figure 24).[138] With the catalytic amount of this cage, the previous cyclization reaction produced selectively compounds 68a and 68b with a higher yield (92 % *trans* / *cis*) and a sevenfold faster rate than with cage 10. This cage also exhibited the desired stability towards air oxidation.

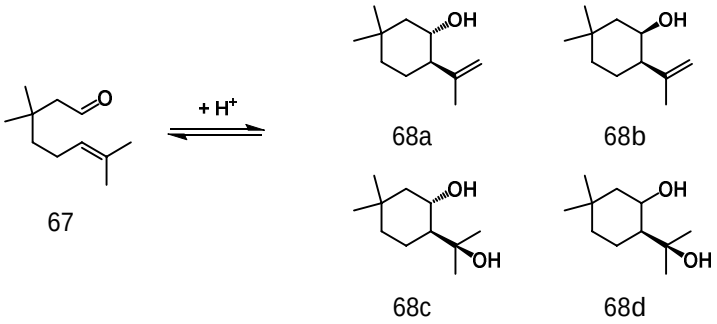

SCHEME 39 Proton mediated carbonyl-ene cyclization of 67.

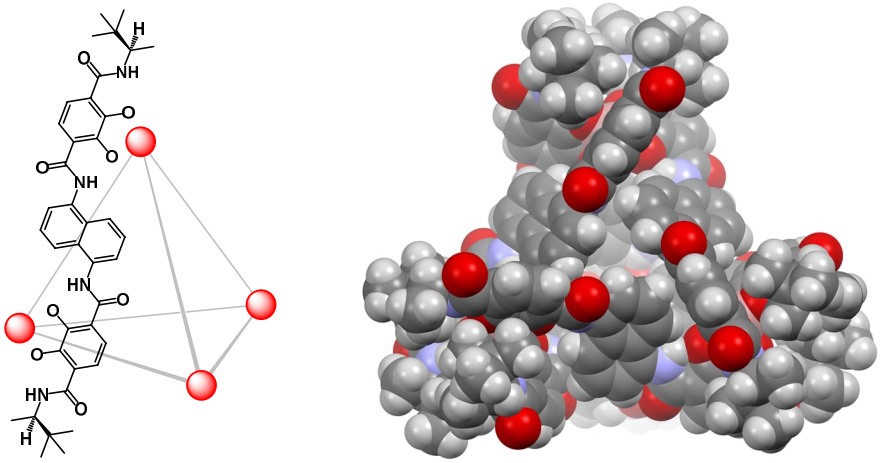

FIGURE 24 Cage ΔΔΔΔ-$[Ga_4(O16)_6]^{12-}$ (ΔΔΔΔ-69). Anions and solvent molecules were not included in the model.

Jiao *et al*. prepared a flexible cubic host $[Zn_8L_6]^{16+}$ 70, shown in Scheme 40, using subcomponent assembly and showed that the host is capable of catalyzing cascade reactions.[139] In solution this host encapsulates anthranilamides (71) and aromatic aldehydes (72), which will undergo sequential condensation and cyclization to yield 2,3-dihydroquinazolinines (73) which have useful pharmacological applications. The proposed catalytic reaction mechanism is presented in Scheme 40. With 0.1 mol % of the host 70 present, the product is isolated with high yields (87–99 %, depending on R-groups) and the reaction itself is highly efficient with 38 000-fold improvement *cf*. uncatalyzed reaction. Without the host only imine intermediate was produced and similarly in the presence of inhibitor no product was obtained. The substrates have a high binding affinity towards the host, whereas the product has a far lower affinity towards the host. This with the unfavorable conformations of the products promoted dissociation of the product and thus allowing the host to undergo multiple catalytic turnovers.

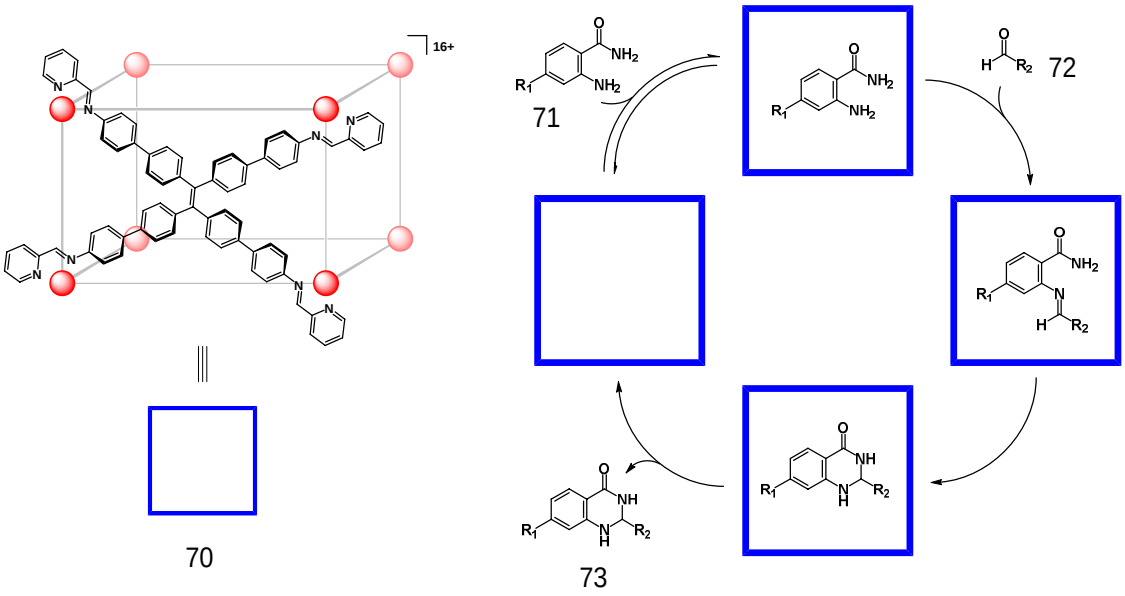

SCHEME 40 Cage $[Zn_8(N65)_6]^{16+}$ (70) and proposed catalytic reaction mechanism inside the host, adapted from ref.[139] R_1 = H, Me or Cl; R_2 = Ph, 4-FPh, 4-MeOPh or 1-naphthyl.

4.3 Cavity Controlled Reactions

Yoshizawa *et al*. have shown that unusual regio- and stereoselective Diels-Alder reactions between anthracenes and maleimides can occur inside M_6L_4 open octahedron 74 (Scheme 41a, R = Me).[140] When 9-hydroxymethylanthracene 75a and *N*-cyclohexylmaleimide 76 were suspended in an aqueous solution of cage 74 at room temperature, resulted a host-quest complex of 74 ⊃ (75a · 76) within minutes. Upon heating the solution to 80 °C, 1,4-Diels-Alder adduct 77a is formed with above 98% yield (Scheme 41b) and 74 ⊃ 77a has been verified with NMR and single crystal X-ray diffraction. This is unusual as the conventional product is the 9,10-Diels-Alder adduct, which was obtained in the absence of 74 at a 44 % yield. The limited space inside the cage restricts the orientation of the two starting compounds in a way that the expected 9,10-position is sterically restricted, thus preventing the reaction from occurring. Similarly, carboxyl-, cyano- and vinyl substituted anthracenes produced the corresponding 1,4-adduct with 92, 88 and 80 % yields respectively, while unsubstituted anthracene afforded 1,4-adduct with 55 % yield. The lower yield is due to a poor inclusion of the substrate before reaction instead of reduced regio- or stereoselectivity.

Similarly, Yoshizawa *et al*. showed that host 26 (Scheme 41a, R = H) can be used to selectively photodimerize [2+2] olefins.[141] Suspension of acenaphthylene 78a to an aqueous solution of 26 at 80 °C, followed by filtration of excess 78a, leads to the formation of host-guest complex 26 ⊃ $(78a)_2$. Irradiation of the solution at room temperature for 30 minutes causes 78a to undergo [2+2] photodimerization and *syn*-dimer 79a was extracted with >98 % yield (Scheme 41c). No *anti*-dimer was formed and without the host, only at high concentrations (150 mM vs. 2 mM), were adducts formed with poor stereoselectivity (*syn*: 19 %, *anti*: 17 % yield). 1-methylacenaohthylene 78b also produced *syn*-dimer 79b with a similar yield, and no other region- or stereoisomers were observed, and no adducts formed even at higher concentrations.

It was also shown to be possible to perform cross-photodimerization inside the host 26 for different olefins, namely between acenaphthylene and naphtoquinones.[142] Introduction of 78a and 5-ethoxynaphtoquinone 80a to a solution containing host 26 forms ternary hetero complex 26 ⊃ (78a · 80a). Upon irradiation substrates undergo [2+2] cross-photodimerization to produce hetero *syn*-dimer 81a with 92 % yield (Scheme 41d). No homo *syn*-dimers were detected, and neither were any *anti*-dimers. Switching to 5-methoxynaphtoquinone 80b and unsubstituted naphtoquinone 80c leads to the formation of homo *syn*-dimers 82 and 79 respectively, together with hetero *syn*-dimer 81a. This contributed to the steric effect of 5-ethoxy substituent as no homo complex 26 ⊃ $(80a)_2$ were observed, whereas in the case of 80b and 80c homo complexes did exist to some extent.

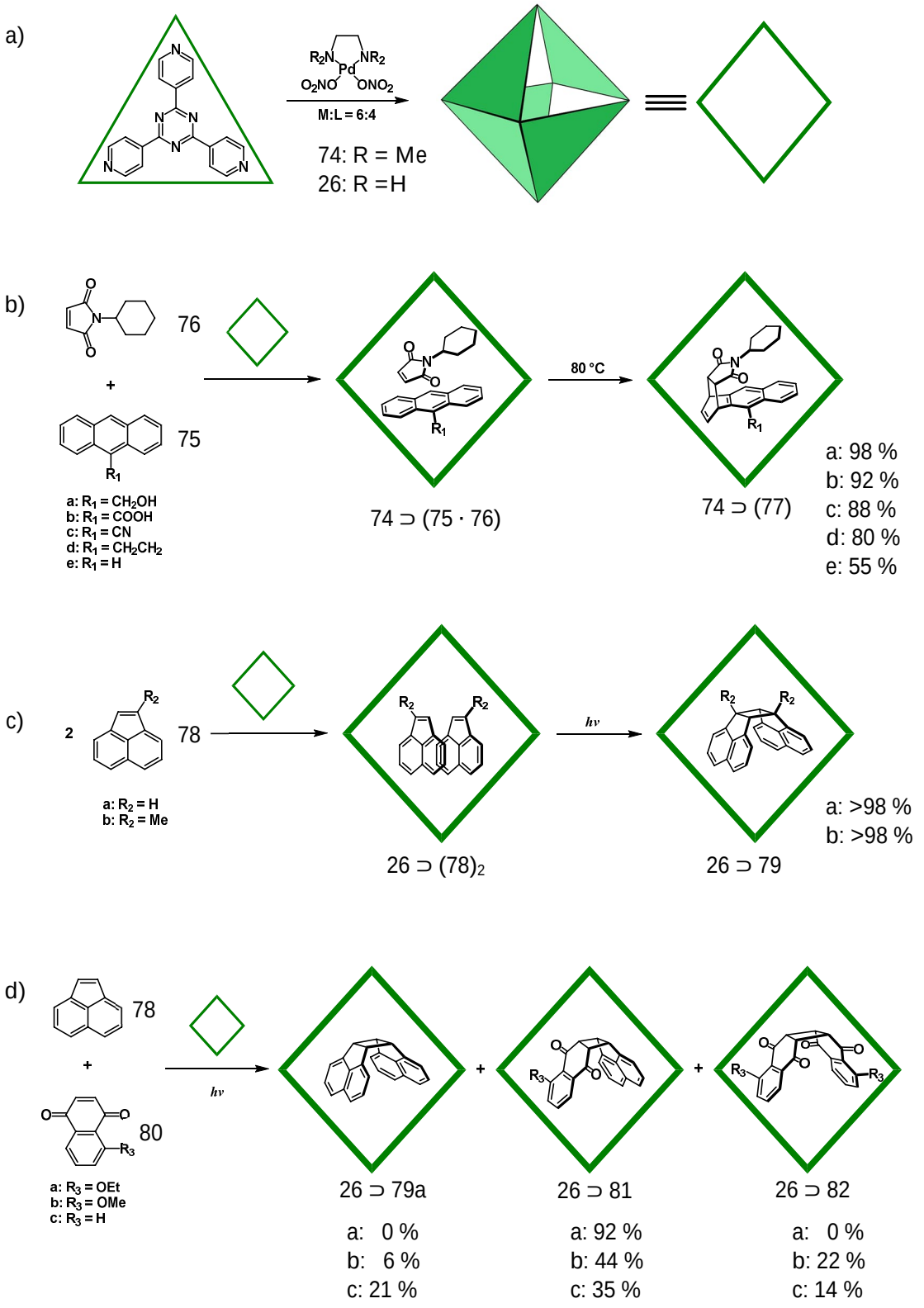

SCHEME 41 a) Schematic representation of hosts 74 and 26, b) Diels-Alder reaction between anthracenes and maleimides, c) [2+2] photodimerization and d) [2+2] cross-photodimerization between olefins.

4.4 Drug delivery

Zheng *et al*. demonstrated that host 26' (structurally similar to 26 except Pt was used instead of Pd) can act as a drug delivery system.[143] Cytotoxic adamantylplatinum(IV) prodrug 83, which has low solubility in water, becomes readily soluble once mixed with host 26' in water at 80 °C with sonication (Scheme 42). The change in solubility is explained by the encapsulation of hydrophobic adamantyl moiety inside the hydrophobic cavity of the host. The host-quest complex 26' ⊃ $(83)_4$ was shown to display micromolar potency against human cancer cell lines A549 (lung cancer), A2780 (ovarian cancer) and A2780CP70 (ovarian cancer resistant to cisplatin). The cytotoxicity against these cancer cell lines were comparable to cisplatin and in the case of A2780CP70, the uptake of host 26' ⊃ $(83)_4$ was 10 times greater when compared to 83 or cisplatin alone. In other words, the cytotoxicity of the prodrug was improved due to high cellular uptake of the cationic cage. Reduction of the complex 26' ⊃ $(83)_4$ releases cisplatin, 1-adamantylamine and succinic acid molecules as the prodrug 83 reacts with ascorbic acid inside cancer cells. This in turn directly delivers cisplatin inside the cancer cell and prompts apoptosis of these cancer cells.

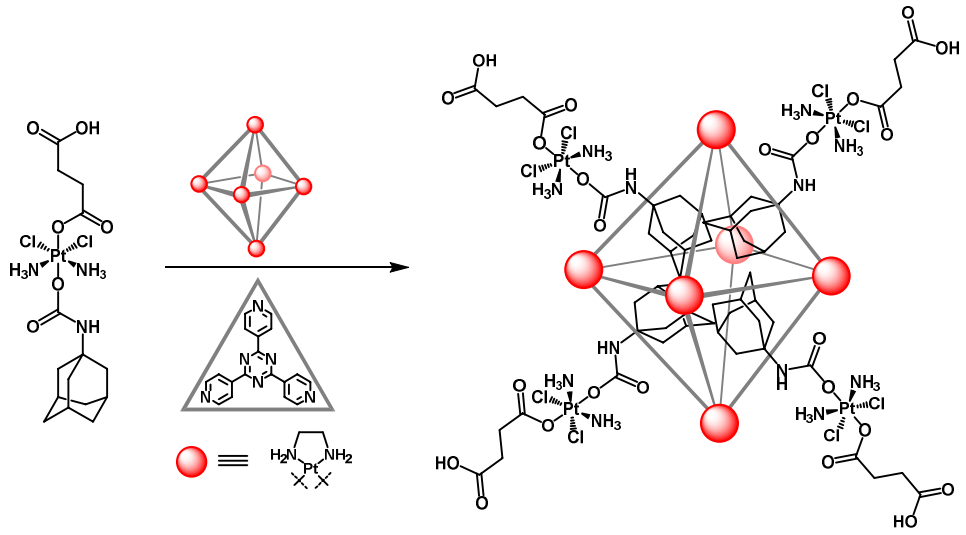

SCHEME 42 Schematic representation of host 26' and host-guest complex 26' ⊃ $(83)_4$.

5 EXPERIMENTAL SECTION

5.1 Aim of the Work

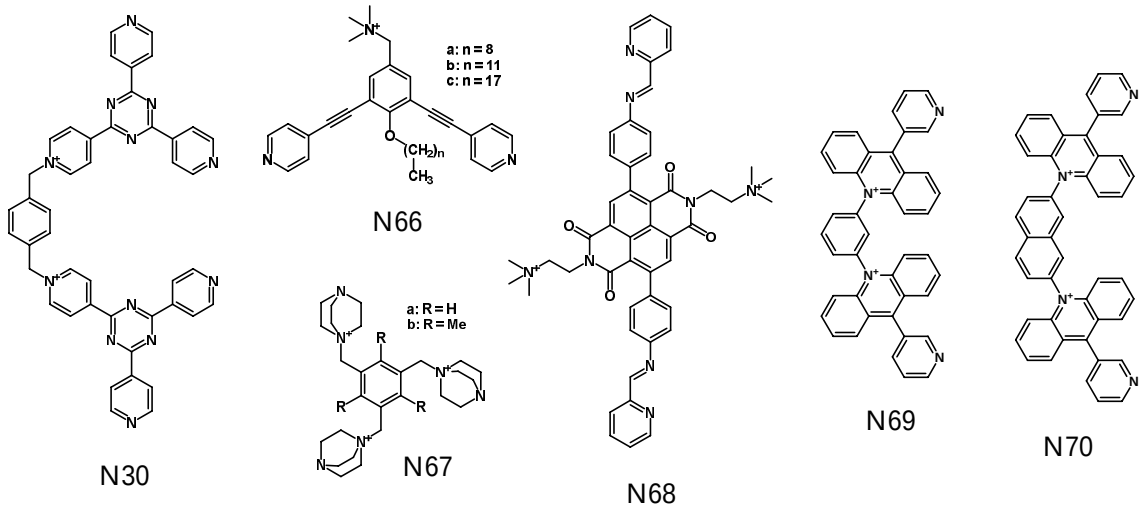

FIGURE 25 Cationic ligands used to obtain MOPs; N30[83]: M_4L_2 open octahedron, N66[144]: $M_{12}L_{24}$ spherical cage; N67[13,14] and N68[145]: M_4L_6 tetrahedron, N69 and N70: M_2L_4 capsule[146].

Though a large number of different kinds of MOPs have been obtained utilizing neutral or negatively charged (anionic) ligands, assemblies obtained by positively charged (cationic) ligands are exceedingly rare. In fact, the ligands presented in figure 25 are essentially (almost) all of the cationic ligands that have been utilized in the creation of MOPs. Generally, cationic ligands contain one or more +1-valent nitrogen atoms, achieved *via* quaternization of either tertiary or aromatic amines, which creates a permanent localized positive charge to the ligand structure. This means that cationic ligands are organic salts and thus offers an opportunity for cation-anion interactions and even for potential anion encapsulation. Furthermore, as cationic ligands are organic salts, the solubility of

mentioned ligands can be relatively easily modified via a simple ion exchange of the counterions and this, in turn, means that the same ligand can be utilized in different solvent environments. Contrastingly modifying the solubility of neutral ligands requires structural changes to the ligand skeleton itself, so in that sense cationic ligands can be more easily optimized to be more suitable components for obtaining MOPs.

The main issue with cationic ligands is that their use will always increase the number of counterions needed for balancing out the total charge of the obtained assembly. For example, let's examine a simple tetrahedral M_4L_6 assembly utilizing unprotected M^{II} metal nodes and either neutral or ±2-valent ligands: with cationic L^{2+} ligands the total charge of the assembly is 20+, whereas with neutral ligands (L^0) the total charge of the assembly arises from metal nodes alone, and equals to 8+. On the contrary, anionic ligands (L^{2-}) act as a counterion themselves and the total charge is thereby 4–, and if M^{III} was used instead of M^{II}, the assembly would have total charge of zero (net-neutral complex). So, the number of single-charge counterions required to balance out the total charge of the assembly is 20, 8 and 4 for cationic, neutral and anionic ligands respectively. Now, anionic ligands do require counterions to balance out the negative charge they possess, but said negative charge is usually formed by deprotonated hydroxy or carboxyl groups and thereby (some) anionic ligands can also exist in neutral protonated forms. Furthermore, the metal nodes will act as counterion for anionic ligands and will balance out the negative charge at least partially thereby reducing the number of counterions required.

Previously it was shown that tricationic ligand N67 yielded M_6L_4 tetrahedra when paired with unprotected metal nodes (Figure 26a) which in some cases formed a pseudo-octahedral disorder where two tetrahedra were disordered in a 0.5 : 0.5 ratio with overlaying Cu^{II} nodes (Figure 26b).[13] Based on those findings current work aimed to create true octahedral cationic assemblies and other MOPs by using a tripodand tricationic ligand where 1,4-diazabicyclo[2.2.2]octane (DABCO) arms were replaced with longer bipyridinium moieties. The main focus of this study was to examine the obtained assemblies in the solid state by single-crystal X-ray crystallography but were also studied in solution with nuclear magnetic resonance spectroscopy (NMR) and thermal analysis to reveal their thermal stability and free solvent content.

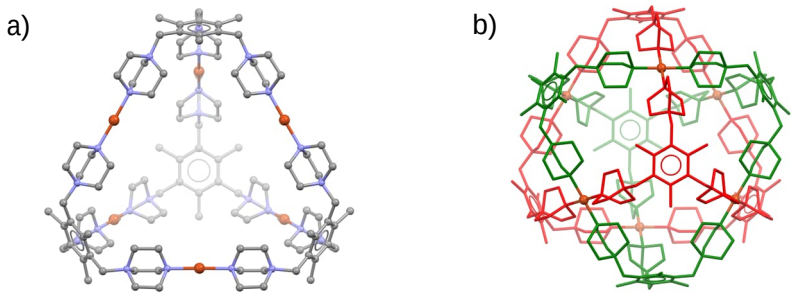

FIGURE 26 a) $[Cu_6(N67b)_4]^{24+}$ tetrahedra and b) pseudo-octahedral disorder. Hydrogens, anions, and solvents omitted for clarity.

5.2 About crystallization techniques

Since the single-crystal X-ray diffraction (SCXRD) is the main characterization method for the crystalline assemblies obtained, it is important to take a look at the most important part of SCXRD, this being crystallization of compounds. Obtaining a good-quality single crystal is a vital part of achieving a high-quality crystal structure, as a poor-quality crystal will effectively give rise to poor reflection data and thus a low-quality crystal structure.[147–149] The process of crystallization involves two main processes: *nucleation* and consequential *crystal growth*, both of which have generally the same optimal conditions. For nucleation to occur, one must "persuade" molecules of the target compound to form a regular three-dimensional arrangement by stacking together *i.e.* undergo a phase transfer from a liquid (or gaseous) phase to a solid state. Now ideally, the crystallization solvent would only contain desired compound and solvent, but usually, this is not the case. Instead, the mother liquid contains not only the desired compound, but also precursor compounds and in some cases side products.

Nucleation process can be spontaneous (primary nucleation) or it can be induced by crystals of solute (secondary nucleation).[150–152] Primary nucleation can further be subcategorized to homogenous (without the presence of foreign surface) or heterogenous (with the presence of foreign surface) nucleation, with foreign surface being, for example, particles of dust. In solution, the driving force towards nucleation is the concentration of desired compound in said solution, and in theory, the crystallization starts when the concentration of the desired compound is higher than the solubility of this compound is in the solvent. However, in practice, things are not so straightforward because, generally speaking, the crystallization is kinetically hindered and there exists a metastable state between the solution and solid phase (Figure 27).

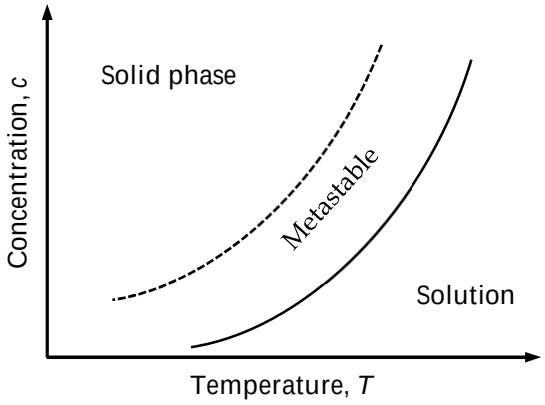

FIGURE 27 Schematic representation of metastable state, where solid line represents point of supersaturation and dotted line represents moment of crystallization.

As the concentration of the desired compound in the solution increases it will reach the point of supersaturation, which typically increases the rate of nucleation drastically. This metastable state resides between point of supersaturation and moment of crystallization, making it a kind of crystal nursery where the solute is on the verge of going through a phase transition. In this state forming aggregates are too small to initiate nucleation and are likely to re-dissolve back to the mother liquid, and beyond this state nucleation and subsequential crystal growth is initiated. A gradual transition from the metastable state to crystalline state leaves ample time for good-quality single crystals to grow to a desirable size. In fact, it may be possible to obtain a high-quality single crystal by placing a tiny seed crystal to a solution in this metastable state. In order to trigger the nucleation, one would need to somehow transfer the solution to the metastable phase by reaching the point of supersaturation. Few of the most common crystallization methods are discussed below.

The easiest way to obtain the state of supersaturation is to leave solution to freely evaporate to increase the concentration of the compound in the solution. The rate of evaporation can be controlled, to a point, by varying the opening of the container but this method is a pretty inefficient way of producing good-quality single crystals. The main problem with this method is the potential dying-out of crystals when the solvent evaporates to (near) dryness, causing the crystals to become cracked or encrusted. The other issue is that if the evaporation is too rapid, too much nucleation will occur at once leading to packing defects and crystals too small for successful structure analysis. To make this method a useful form of crystallization, a slowly evaporating solvent, *i.e.* one with a higher boiling point, should be chosen and the process of evaporation should be closely monitored and controlled.

Another method to obtain a supersaturated solution is to utilize the fact that many compounds are typically more soluble in hot solutions rather than in cold solutions. In this method, in high temperatures a near-saturated solution is prepared and this solution is then allowed to cool down to room temperature or even below that, and this should initiate the crystallization process. Crystals that start growing in higher temperatures are frequently either twinned or contain some static disorder due to being separated by a small energy difference between several metastable conformations existing at the same time. This does lead to more disordered and defected packing of crystal lattice, lowering the quality of crystals. Mirroring the first method, if the cooling down process is too rapid, small or poor-quality crystals will form or the compound will simply precipitate out as a fine powder. For this method to produce good-quality single crystals, the cooling of solution should happen at a constant rate uniformly throughout the solution. Achieving that can be difficult though not impossible.

Typically, the best method to obtain a concentrated solution of MOPs is to use binary solvent systems utilizing an *antisolvent*, a solvent in which the compound is either insoluble or the solubility is negligible. The most common type of binary solvent system is yielded by isothermal distillation, a method more commonly known as *vapor diffusion*. This is achieved by placing an open or loosely covered a small vial containing the solution inside a tightly closed larger vial or container in which the antisolvent is added (Figure 28). The antisolvent, having lower boiling point than the solution, will evaporate and then diffuses slowly as the vapor phase into the solution thus reducing the solubility of the compound or the complexation reactants in the solution. The great advantage of this method is its relative slow rate of diffusion, versatility and controllability with the main restriction being that the solvent and antisolvent need to be immiscible.

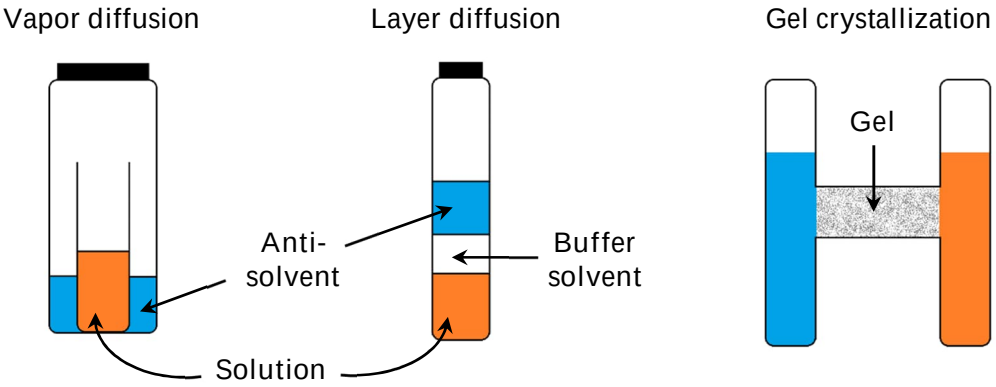

FIGURE 28 Simple binary solvent setups.

A variation of this method is the layer diffusion, in which the solution is layered inside a vial and then antisolvent is carefully layered on top of the solution, and then the two solvents are allowed to mix naturally. It is possible to slow down this mixing by adding a buffer solvent (typically pure solvent used in solution) between the two layers (Figure 28). This method is more time-consuming and requires that the used solvents are carefully chosen with their densities kept in mind.

Another variation of the diffusion method is the *gel crystallization* technique. In this method the solution and the antisolvent are separated by a layer of gel, through which the solvents will slowly diffuse, creating a very fine concentration gradient (Figure 28). The possibility to change the porosity and the thickness of the gel layer makes this method highly customizable and thus creating several variables to fine-tune to achieve high-quality crystallization.

It is noteworthy that these solvent-based methods are not excluding each other but can indeed work in tandem for further increase the change of crystallization. For example, vapor diffusion can be performed in subambient temperatures to slow down the diffusion process and so (sometimes) improve the crystallization process and the quality of crystals. The more time one spends

in optimizing the crystallization conditions and monitoring the crystal growth, the chances of obtaining a good or high-quality crystals will increase. The most important part is patience, as once the crystallization conditions have been set it is important to disturb the vials as little as possible so that the crystal growth can occur without interference. Also, some compounds, such as 3D-MOFs, are formed *in situ* from solution and once formed are insoluble in essentially everything and thereby cannot be recrystallized using the above-mentioned techniques, if at all.

Crystals for compounds that are obtained utilizing precursors which have negligible solubility in ambient temperature and / or pressure are achieved using hydro- or solvothermal methods. In this method a mixture of solvent(s), potential ligand and metal salts are sealed tightly inside, for example, teflon-lined stainless-steel autoclave. The autoclave is then heated to a certain temperature often above the boiling point of the used solvent(s) and held at that temperature for several days. After slowly cooling back down to ambient temperatures, the autoclave is opened, and its contents are examined for crystals. Due to high temperature / pressure forming inside the container it is possible to use materials that in ambient conditions are insoluble or weakly soluble in solvents used. Though this method is often based on trial-and-error, it is possible to obtain structures that would be otherwise impossible to achieve if attempted at ambient conditions. This method is favored in MOF crystallization but is also viable method for crystallizing MOPs.

Non-solvent based crystallization methods such as melt crystallization or sublimation, are typically not useful technique for SCC crystallization as these methods rely on the compound's ability to undergo solid-liquid-solid or solid-gaseous-solid phase transfers, of which SCCs typically cannot. This is due to the simple fact that SCCs are often ionic compounds of organic ligands and metal ions, and this sequentially makes SCCs to be organic salts. These compounds generally don't sublimate, but instead will decompose upon reaching certain temperature threshold. For similar reason, melt crystallization is not viable method as the decomposition of SCCs occurs simultaneously as the compound undergoes solid-liquid phase transfer. The non-solvent crystallization methods are useful methods for obtaining solvent-free precursor compounds with high purity, as long as they can undergo required phase transitions without thermal decomposition.

5.3 Syntheses and methods

Starting materials were obtained from standard commercial sources such as Sigma-Aldrich, Merck, Apollo Scientific and TCI, and used without further purification unless mentioned otherwise.

5.3.1 Synthesis of ligands

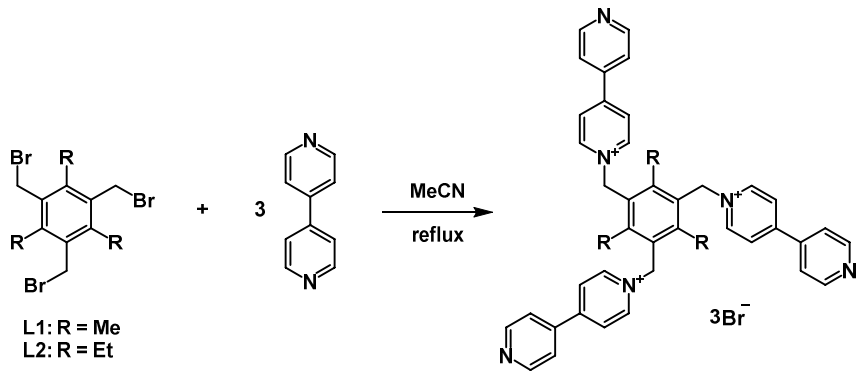

SCHEME 43 General synthesis route of L·Br_3.

Cationic ligand (L1)·Br_3 was synthesized by using a modified procedure of the one published by Belcher *et al*.[153] 2,4,6-tris(bromomethyl)mesitylene (1.00 g, 2.51 mmol) in 100 ml of acetonitrile was added to a solution of 4,4'-bipyridine (3.91 g, 25.06 mmol) in 50 ml of acetonitrile (MeCN) with vigorous stirring and the solution was refluxed for 24 hours. The yellow precipitate was isolated by filtration from a cooled solution, washed three times with 20 ml of MeCN and three times with 50 ml of diethyl ether (Et_2O) and dried *in vacuo*. Yield 1.995 g, 91.72 %. Anal. Calc. for [(L1)·Br_3] · 2 H_2O $C_{42}H_{43}N_6O_2Br_3$: C, 55.83; H, 4.80; N, 9.30. Found: C, 9.67; H, 4.78; N, 9.67%. ^{1}H NMR (D_2O, 300 MHz, δ/ppm): 8.96 (m, 6H, bpy), 8.86 (m, 6H, bpy), 8.52 (m, 6H, bpy), 8.00 (m, 6H, bpy), 6.28 (s, 6H, CH_2N^+), 2.48 (s, 9H, Me).

Cationic ligand (L2)·Br_3 was synthesized similarly as (L1)·Br_3 by using 1,3,5-tris(bromomethyl)-2,4,6-triethylbenzene (1.50 g, 3.40 mmol), 4,4'-bipyridine (3.19 g, 20.41 mmol) and the solution was refluxed for 18 hours. The yellow precipitate was isolated by filtration, washed three times with 20 ml MeCN and 50 ml Et_2O and dried *in vacuo*. Yield 2.950 g, 95.36 %. Anal. Calc.for [(L2)·Br_3] · 1.5 H_2O $C_{45}H_{48}N_6O_{1.5}Br_3$: C, 57.71; H, 5.17; N, 8.97. Found: C, 57.92; H, 5.17; N, 8.87%. ^{1}H NMR (D_2O, 300 MHz, δ/ppm): 9.00 (m, 6H, bpy), 8.86 (m, 6H, bpy), 8.56 (m, 6H, bpy), 7.99 (m, 6H, bpy), 6.25 (s, 6H, CH_2N^+), 2.85 (m, 6H, CH_2Me), 1.06 (s, 9H, Me).

5.3.1.1 Anion exchanges for L·Br_3 salts

Synthesis of L·$(PF_6)_3$. 1.000 g (L1: 1.15 mmol, L2: 1.10 mmol) of L·Br_3 was dissolved in 50 ml deionized water and saturated water solution of ammonium hexafluorophosphate was added dropwise while stirring until no further precipitation occurred. After 30 min of stirring the white product was collected by filtration, washed with water and finally dried *in vacuo*. Yield (L1)·$(PF_6)_3$: 1.120g, 91.42 %. Anal. Calc. for [(L1)·$(PF_6)_3$] · 2 H_2O $C_{42}H_{43}N_6O_2P_3F_{18}$: C, 45.91; H, 3.94; N, 7.65. Found: C, 46.08; H, 3.81; N, 7.61%. ^{1}H NMR ($(CD_3)_2SO$, 300 MHz, δ / ppm): 8.96 (m, 6H, bpy), 8.88 (m, 6H, bpy), 8.45 (m, 6H, bpy), 7.99 (m, 6H, bpy), 6.11 (s, 6H, CH_2N^+), 2.35 (s, 9H, Me).

Yield (L2)·$(PF_6)_3$: 1.157g, 95.25 %. Anal. Calc. for [(L2)·$(PF_6)_3$] · 2 H_2O $C_{45}H_{50}N_6O_{2.5}P_3F_{18}$: C, 47.01; H, 4.38; N, 7.31. Found: C, 47.20; H, 4.30; N, 7.05%. ^{1}H NMR (CD_3CN, 300 MHz, δ / ppm): 8.85 (m, 6H, bpy), 8.72 (m, 6H, bpy), 8.40 (m, 6H, bpy), 7.79 (m, 6H, bpy), 5.95 (s, 6H, CH_2N^+), 2.62 (m, 6H, CH_2Me), 1.06 (m, 9H, Me).

Synthesis of L·$(NTf_2)_3$. 0.947 g (3.30 mmol) of lithium bistrifluoromethyl-sulfonylimide ($LiNTf_2$) in 10 ml of water was added dropwise to a solution of 0.500 g (0.55 mmol) of (L2)·Br_3 in 50 ml water with vigorous stirring. The stirring was continued for 1 h after which the white product was collected by filtration, washed with water and dried *in vacuo.* Yield 0.810g, 97.56 %. Anal. Calc. for [(L2)·$(NTf_2)_3$] · 1.5 H_2O $C_{51}H_{48}N_9O_{13.5}S_6F_{18}$: C, 39.84; H, 3.15; N, 8.20. Found: C, 39.85; H, 3.05; N, 8.14%. ^{1}H NMR (CD_3CN, 300 MHz, δ / ppm): 8.86 (m, 6H, bpy), 8.66 (m, 6H, bpy), 8.33 (m, 6H, bpy), 7.79 (m, 6H, bpy), 5.93 (s, 6H, CH_2N^+), 2.63 (m, 6H, CH_2Me), 1.00 (m, 9H, Me).

5.3.2 Preparation of non-commercially available metal salts

$Ni(NCS)_2$ was prepared according to a literary method.[154] $NiCl_2$ · 6 H_2O (0.95 g, 7.33 mmol) dissolved in 1 ml of deionized water and diluted to a volume of 10 ml with glacial acetic acid (HOAc). The prepared mixture was added at room temperature to a solution of ammonium thiocyanate (0.70 g, 9.2 mmol) dissolved in 2 ml of HOAc with constant stirring which was continued 3 hours after the addition. The yellow-green precipitate was isolated by filtration, washed with 1:10 H_2O:HOAc solution and dried *in vacuo*. Yield 0.49 g, 85.78 %.

$Ni(NO_3)_2$ · 2.5 H_2O was obtained by heating $Ni(NO_3)_2$ · 6 H_2O to 65 °C (mp. 56.7 °C) and keeping the liquid salt in that temperature. The forming solid crust was occasionally mixed into the liquid salt until only the solid phase remained. The obtained pale green solid was then grounded to fine powder and dried *in vacuo*. The obtained salt was a mixture of $Ni(NO_3)_2$ tetra- and dihydrates and was determined to contain 2.5 water molecules, according to thermogravimetry and powder diffraction analyses (see Appendix 1).

$[Ni(MeCN)_6](PF_6)_2$. 1.62 g (8.78 mmol) of KPF_6 in 40 ml MeCN was added to a solution of 1.00 g (4.39 mmol) of $Ni(NO_3)_2 \cdot 2.5\ H_2O$ in 60 ml of MeCN and the mixture was stirred for two hours. Precipitated KNO_3 was filtered off and $[Ni(MeCN)_6](PF_6)_2$ was crystallized from the solution as purple-blue crystals by slow vapor diffusion of $CHCl_3$, and subsequently recrystallized from MeCN in the same manner. The compound was verified by single crystal X-ray diffraction (see Appendix 2) and the crystals of $[Ni(MeCN)_6](PF_6)_2$ were stable for several months. Once powdered, the compound (partially) decomposes slowly over time releasing corrosive products as a result.

5.3.3 Preparation of stock solutions

10 mmol L^{-1} solutions of $(L1)\cdot(PF_6)_3$, $(L2)\cdot(PF_6)_3$ and $(L2)\cdot(NTf_2)_3$ were prepared by dissolving 200 μmol (173.50, 181.92 and 220.95 mg respectively) of appropriate ligand into 20 ml of MeCN. 7.5 mmol L^{-1} solutions of individual metal salts were prepared by dissolving 75 μmol of $Cu(NO_3)_2{\cdot}3H_2O$ (18,12 mg), $Cu(ClO_4)_2{\cdot}6H_2O$ (27.79 mg), $Ni(NO_3)_2{\cdot}2.5H_2O$ (17.08 mg), $NiCl_2$ (9.72 mg), $NiBr_2$ (16.39 mg), $Ni(NCS)_2$ (13.11 mg), $Zn(NO_3)_2{\cdot}6H_2O$ (22.31 mg), $Zn(ClO_4)_2{\cdot}6H_2O$ (27.93 mg), $ZnCl_2$ (10.22 mg), $ZnBr_2$ (16.89 mg) or ZnI_2 (23.94 mg) in 10 ml of either MeOH, EtOH or MeCN depending on solubility. 13.33 mmol L^{-1} solutions of zinc(II) halides were prepared by dissolving 133.33 μmol of $ZnCl_2$ (18.17 mg), $ZnBr_2$ (30.02 mg) or ZnI_2 (42.56 mg) in 10 ml of either EtOH or MeCN. 13.33 mmol L^{-1} $Zn(I_3)_2$ solution was prepared by mixing MeCN solution containing 67.67 mg (266.66 μmol) of I_2 with MeCN solution containing 18.17 mg (133.33 μmol) of ZnI_2, in such a manner, that the final volume was 10 ml. 1 mmol L^{-1} solution of KPF_6 was prepared by dissolving 10 μmol (1.84 mg) of KPF_6 in 10 ml of MeCN. Due to NiI_2, NiF_2 and ZnF_2 possess negligible solubility in the solvents utilized, they were excluded from the study, though assemblies containing Ni–I moiety were obtained during post-synthetic anion exchange made with NH_4I (see section 6.2.11).

5.3.4 General preparation and crystallization of assemblies

M_6L_8 assemblies were prepared by mixing 0.5 ml of 10 mmol L^{-1} ligand solution with 0.5 ml of 7.5 mmol L^{-1} M^{II} salt solution at room temperature, and the mixture was then left to stand for one hour unless otherwise specified. M_4L_3 assemblies were prepared by mixing 0.5 ml of 10 mmol L^{-1} solution of $L\cdot(PF_6)_3$, 0.5 ml of 13.33 mmol L^{-1} Zn^{II} halide solution and 0.5 ml of 1 mmol L^{-1} KPF_6 solution. After standing one hour at room temperature, the solution was filtered through Celite® S to remove any insoluble byproducts (mainly potassium and ligand halides). M_5L_4 was prepared by mixing 0.5 ml of 13.33 mmol L^{-1} $Zn(I_3)_2$ solution with 0.5 ml of 10 mmol L^{-1} $L\cdot(PF_6)_3$, solution, and after standing one hour at room temperature, the solution was filtered through Celite® S to remove any insoluble byproducts (mainly potassium and ligand halides). Crystals suitable for X-ray diffraction were obtained via slow vapor diffusion of either dichloromethane (DCM), chloroform, Et_2O or ethyl acetate (EtOAc) unless otherwise specified.

5.3.5 NMR

^{1}H NMR samples were measured using Bruker Avance III HD 300 or Bruker Avance III 500 spectrometer at 30 °C. Samples of ligands were prepared *in situ* and measured within 5 minutes of preparation whereas samples of M_6L_8 assemblies were either prepared *in situ* from starting materials or from single crystals obtained *via* vapor diffusion crystallization and measured a few hours after preparation.

5.3.6 Thermogravimetry

PerkinElmer STA 6000 TG/DSC simultaneous thermal analyzer was used to analyze the samples, typically over a temperature range of 20–800 °C with heating rate of 10 °C min^{-1}. The thermal stability measurements were conducted in an open platinum crucible under either air or N_2 atmosphere with a gas flow rate of 40 ml min^{-1}. The weight was calibrated at ambient temperature using a steel ball bearing with a standardized reference weight of 55.98 mg (provided by the manufacturer). The melting point onsets of indium and aluminum (Perkin Elmer standards with mp. values of 156.60 °C and 660.1 °C, respectively) were used to calibrate the device temperature and the heat flow was calibrated using the standard enthalpy of fusion of indium (28.45 J g^{-1}). Samples, 5–10 mg by weight, were prepared before measurement at ambient temperature and dried beforehand by either keeping them in a constant 1 × 10^{-6} bar vacuum overnight or under a nitrogen atmosphere for three days unless otherwise specified.

5.3.7 X-Ray Crystallography

Single crystal diffraction data were collected using a Rigaku Oxford Diffraction SuperNova Dual-source X-ray diffractometer, with Mo and Cu radiation hi-flux microfocus sources (Mo K_α, λ = 0.71073 Å and Cu K_α, λ = 1.54184 Å) and an Atlas CCD detector installed. Cu radiation was used for all the obtained compounds throughout this work except in case of $[Ni(MeCN)_6](PF_6)_2$. To achieve diffraction data suitable for structure determination, numerous crystals per compound were screened under the microscope and during pre-experiment (unit cell indexing step) runs. In the case of larger assemblies, the diffraction data acquisition pushed the equipment close to the operational extremes as required data collection times lasted typically two days and occasionally upwards to five days with an achievable data redundancy of at most 2. Crystals were held at a constant temperature of –173.15, –153.15 or –150.15 °C during data collection using a liquid nitrogen cooled Oxford Cryostream 700 device. The CrysAlisPro software package (ver. no. 171.38.43, 171.39.43c, 171.40.67a, 171.41.112a and 171.42.49) was used to conduct data collection and reduction and to apply numeric absorption corrections (Gaussian grid) that were based on the multifaceted crystal models.

Within the OLEX^2 structure solution and refinement program (ver. nos. 1.3 and 1.5), all structures were solved using SHELXT[155] and refined using SHELXL[156] least-squares full-matrix minimization on $|F|^2$. All non-hydrogen atoms were refined anisotropically (as long as allowed by disorder) and hydrogen atoms were calculated isotropically using the standard OLEX^2 riding model (for aromatic hydrogen atoms and –CH_2– groups: U_{iso} = 1.2x of the parent atom, and for other groups: U_{iso} = 1.5x of the parent atom). Occupancies of disordered moieties were determined using free variables in the refinement. In case of severe disorder, the structure was examined in lower symmetry (when enough data was available) and the nature of the disorder was applied back in original symmetry. Electron density from severely disordered solvents (*e.g.* water, acetonitrile, chloroform, 1,4-dioxane, ethyl acetate) was first examined and then removed on the final refinement of the structure using the OLEX^2 solvent mask (SM) tool. On a case-by-case basis, some better-defined solvent molecules were excluded from solvent masking, to demonstrate typical locations and orientations they possessed. The removed electron density was not taken into account when determining the chemical formula.

Powder diffraction patterns were collected by PANalytical X'Pert Pro alpha 1 diffractometer from gently mortar grounded dried single crystal samples in the Bragg–Brentano geometry using a sealed tube X-ray Cu tube with a Johansson monochromator (Cu$K\alpha_1$ λ = 1.5406 Å; at 45 kV and 40 mA). Data were routinely collected from samples prepared on a spinning concave zero background (ZBC) silicon disc with an X'Celerator detector over a 2θ-range of 3–70°. The step size (2θ) and time per step were respectively 0.167° and 180 s. All of the M_6L_8 samples measured turned out to be amorphous (Figure 29) suggesting that the crystalline structure collapses during the drying process, and so further powder diffraction studies of obtained structures were deemed to be unnecessary.

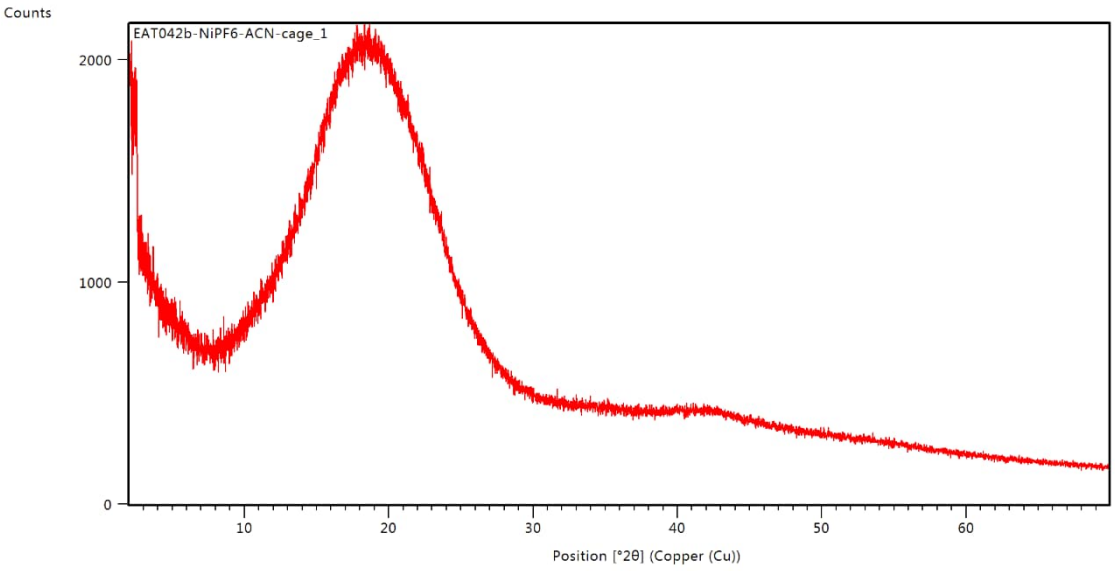

FIGURE 29 Example of measured powder diffraction pattern of a M_6L_8 assembly.

6 RESULTS AND DISCUSSION

6.1 Structural description of ligands

The ligand L comprises of three cationic bipyridinium ‘arms’ linked either *via* a mesitylene (1,3,5-trimethylbenzene) core (L1) or 1,3,5-triethylbenzene core (L2), possessing either ‘bowl’-shaped *syn*-conformation in case of ligands L·Br_3 and L·$(PF_6)_3$ or ‘chair’-shaped *anti*-conformation in case of ligand (L2)·$(NTf_2)_3$ (Figure 30). In *syn*-conformation one of the counter anions is entrapped within the bowl-like structure while the rest are located in proximity to the cationic regions of the ligand but outside of the bowl. In the case of L2 the ethyl-groups are typically oriented at the opposite side of the benzene ring with respect to the bpy-arms, likely to minimize the energy in the conformation and due the steric hindrance ensued by the plausible all substituents in *syn*-conformation.

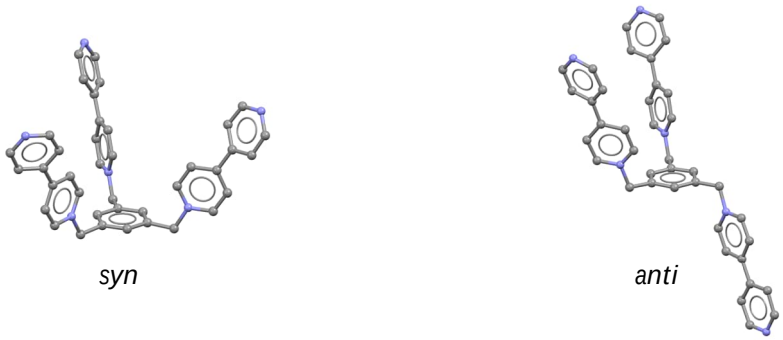

FIGURE 30 *syn*- and *anti*-conformations of ligand L. Hydrogen atoms, counter anions and core substituents (Me or Et -groups) omitted are for clarity.

(L1)·Br_3, crystallized from slightly wet MeOH solution *via* dichloromethane (DCM) vapor diffusion, exhibits a triclinic space group $P\bar{1}$ (a = 10.7684(10) Å, b = 11.6237(8) Å, c = 18.1308(13) Å, α = 95.087(6)°, β = 103.175(7)°, γ = 104.053(7)°, V = 2118.5(3) Å^3, Z = 2) containing three water and one DCM molecules with the ligand in *syn*-conformation and three bromide anions. In crystal lattice, the ligand (L1)·Br_3 orientates to a loose dimeric 'capsules' with one of the bromide anions (Br1) resides within the bowl of the ligand while the two remaining bromide anions are outside the capsule (Figure 31a). Br1 is located 4.5057(13) Å above and slightly off-center of benzene core (Br1-Centroid-projection point angle 81.79° and Br1-Centroid distance 4.5522(12) Å). In loose capsule, Br1 atoms are separated by a distance of 5.6053(8) Å from their 'mirror twin' (Figure 31a-b). The Br1 also participates in a short hydrogen / halogen bond network between two ligands and two water molecules, namely between atoms N4···O1···Br1···O2···N6, while the remaining two bromide ions are interacting with the third water molecule, Br2···O3···Br3, as shown in Figure 31c. Only one solvent molecule is disordered (water containing atom O2) over three positions with approximately 0.33 occupancies each. The bend angles of the bpy arms are between 114.45–115.43° and the zero-valent nitrogen atoms of the bpy arms are approximately equally apart, with the distance between them being 11.844–13.664 Å. The rings containing zero-valent nitrogen atoms are rotated between 23.84–33.68° from the planes of the rings containing +1-valent nitrogen atoms. Crystallographic data for (L1)·Br_3 is presented in Appendix 8 Table A7.

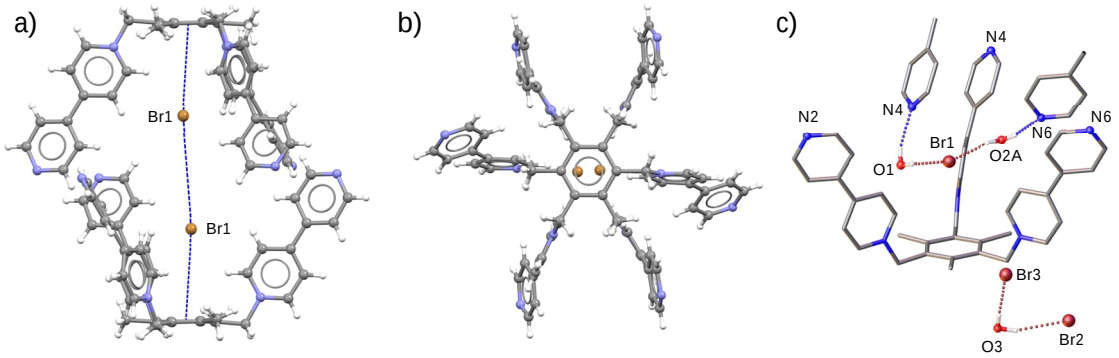

FIGURE 31 a) Encapsulated Br1-anions, b) Off-set of Br1 atoms and c) Hydrogen / halogen bonding within (L1)·Br_3. Only relevant atoms are shown.

(L1)·$(PF_6)_3$, crystallized from MeCN solution *via* Et_2O vapor diffusion, exhibits in a polar orthorhombic space group $Pna2_1$ (a = 30.3451(6) Å, b = 11.1987(2) Å, c = 27.2537(6) Å, $\alpha = \beta = \gamma$ = 90°, V = 9261.5(3) Å^3, Z = 4) containing two crystallographically distinct cations both in *syn*-conformation, six hexafluorophosphate anions and one MeCN molecule with 0.50 occupancy. The packing of the ligand molecules is similar to one observed in the structure of hydrated (L2)·$(PF_6)_3$ · 3 H_2O, reported by Belcher *et al.*[153], even though that one crystallizes in monoclinic space group $P2_1/c$.

In crystal lattice, the cationic ligand (L1)·$(PF_6)_3$ exhibits an interdigitated packing in which two of bpy arms have come closer together (7.083–7.296 Å *cf.* 14.004–14.595 Å) and are partially 'sandwiching' the third bpy arm from another ligand molecule (Figure 32a-b). Entrapped anions lie 5.057-5.197 Å from the centroid of the benzene core (Figure 32c) and are surrounded by bpy arms. The bend angles of the bpy arms are between 112.44–114.92° while the zero-valent pyridine rings are rotated between 23.98–33.69° from the planes of the +1-valent pyridinium rings. One of the PF_6^- anions is disordered over two overlapping positions with approximately 0.68 and 0.32 occupancies respectively. Crystallographic data for (L1)·$(PF_6)_3$ is presented in Appendix 8 Table A7.

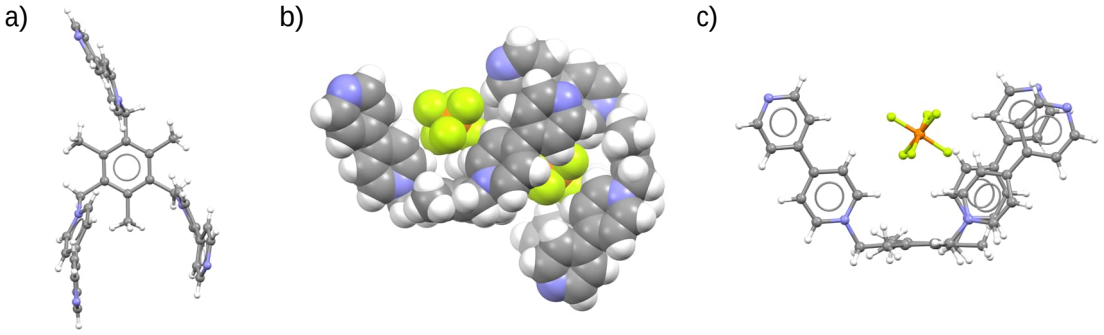

FIGURE 32 a) Twisting of bpy arms, b) Interdigitated packing, and c) anion encapsulated to a ligand bowl. Only relevant atoms are shown.

(L2)·Br_3, crystallized from dry methanol solution via Et_2O vapor diffusion, exhibits a polar orthorhombic space group $Pna2_1$ (a = 23.6932(3) Å, b = 11.1282(2) Å, c = 19.2861(3) Å, $\alpha = \beta = \gamma$ = 90°, V = 5085.02(14) Å^3, Z = 4) containing one crystallographically distinct cation in *syn*-conformation, three bromide anions and five MeOH molecules. The obtained structure differs from the one previously reported by Belcher *et al*.[153] as that one was obtained from different solvent environment. The entrapped bromide anion Br1 is disordered over two positions with equal occupancies of 0.50 each and resides 4.198(2) Å (Br1a) and 4.634(2) Å (Br1b) from the centroid of the benzene core (Figure 33a). One of the two other bromide anions Br2 is also similarly disordered over two positions with approximately 0.75 and 0.25 occupancies each, while the final bromide anion (Br3) is not disordered. Three out of five MeOH molecules are not disordered, while one has its OH-group disordered over two orientations with approximately 0.50 occupancies each. The final MeOH molecule is disordered over two locations with approximately 0.75 and 0.25 occupancies and additionally the MeOH with 0.75 occupancy has further disordered OH-groups over two orientations with approximately 0.50 and 0.25 occupancies respectively. Disordered solvents are located within a cavity surrounded by ligands and share the cavity with bromide anions as shown in Figure 33b.

The bend angles of the bpy arms are between 113.43–115.19° and the zero-valent pyridine ring is rotated between 27.50–45.91° from the plane of the pyridinium ring. Similarly to (L1)·$(PF_6)_3$, two of bpy arms have come closer together (9.769 Å *cf.* 13.132–13.906 Å), but not as much as in (L1)·$(PF_6)_3$. Crystallographic data for (L2)·Br_3 is presented in Appendix 8 Table A7.

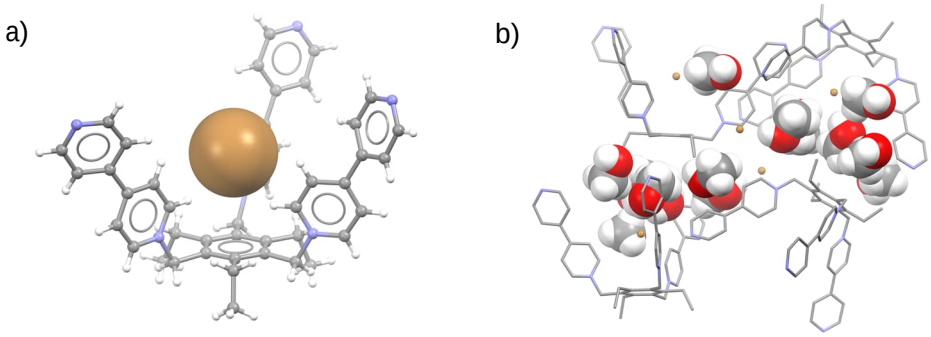

FIGURE 33 a) Anion inside the bowl and b) disordered methanol cavity. Only relevant atoms are shown.

(L2)·$(PF_6)_3$, crystallized from MeCN solution *via* EtOAc vapor diffusion and exhibits in a highly symmetrical hexagonal space group $P6_3$ ($a = b = 11.9234(3)$ Å, $c = 19.9434(4)$ Å, $\alpha = \beta = 90°$, $\gamma = 120°$, $V = 2455.44(10)$ Å^3, $Z = 2$) containing one crystallographically distinct cation, three hexafluorophosphate anions and one disordered MeCN molecule. The structure is practically the same as the one reported by Belcher *et al*.[153] Entrapped anion lays 4.944(3) Å from the centroid of the benzene core (Figure 34a), while the bend angles of the bpy arms are 115.7(3)°. The zero-valent pyridine ring is rotated 38.11° from the plane of the pyridinium ring and are equally 13.021(6) Å apart. Anions are sandwiched between two cations or are located in a pocket containing two anions and MeCN molecule (Figure 34b-c). MeCN molecule is disordered over three positions all sharing the nitrogen atom. Crystallographic data for (L1)·Br_3 is presented in Appendix 8 Table A7.

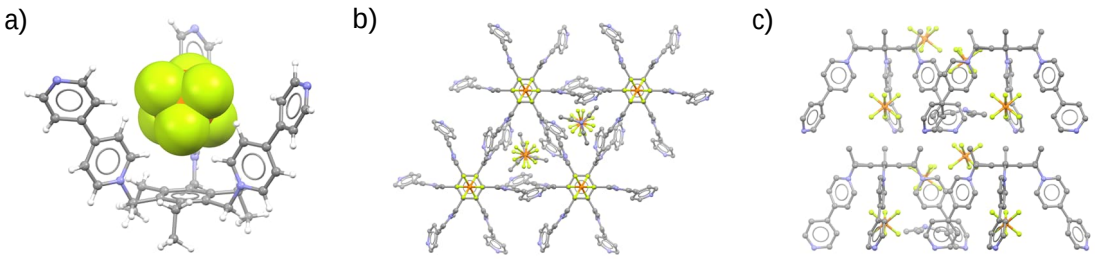

FIGURE 34 a) Encapsulation of PF_6^- anion and crystal packing of (L2)·$(PF_6)_3$ viewed along the crystallographic b) *c*-axis and c) *a*-axis. In b) and c) hydrogen atoms are omitted for clarity.

(L2)·(NTf_2)$_3$ turned out to be a challenging compound to crystallize; evaporation of (L2)·(NTf_2)$_3$ solutions would only yield amorphous powder, whereas diffusion methods would, typically, yield yellow slime or gel instead of single crystals. Eventually, the compound was crystallized from MeCN solution *via* slow THF vapor diffusion as a small, relatively poorly diffracting, colorless rods. Obtained structure exhibits in a monoclinic space group $P2_1/c$ (a = 10.4945(7) Å, b = 27.068(2) Å, c = 22.880(3) Å, $\alpha = \gamma = 90°$, β = 101.995(9)°, V = 6357.7(11) Å^3, Z = 4) containing one crystallographically distinct cation, three NTf_2 anions and one water molecule. Due to the size of the anion, the cation exhibits an *anti*-conformation with bend angles of the bpy arms being 110.27–110.30° for the two on the same side ('up') and 114.52° for the one on the opposite side ('down') of the core benzene ring. All ethyl groups are orientated on the same side as the 'down' bpy arm (Figure 35a). For the *up*-arms, the zero-valent pyridine rings are rotated 26.92–30.20° from the plane of the pyridinium ring, while the *down*-arm is nearly planar with rotation being 4.24°. In the crystal lattice the packing of ligands is dominated by π–π stacking between bpy arms (Figure 35b) and that, along with *anti*-conformation, produces cavities (Figure 35c) where majority of the anions and solvent molecules reside. Crystallographic data for (L2)·(NTf_2)$_3$ is presented in Appendix 8 Table A7.

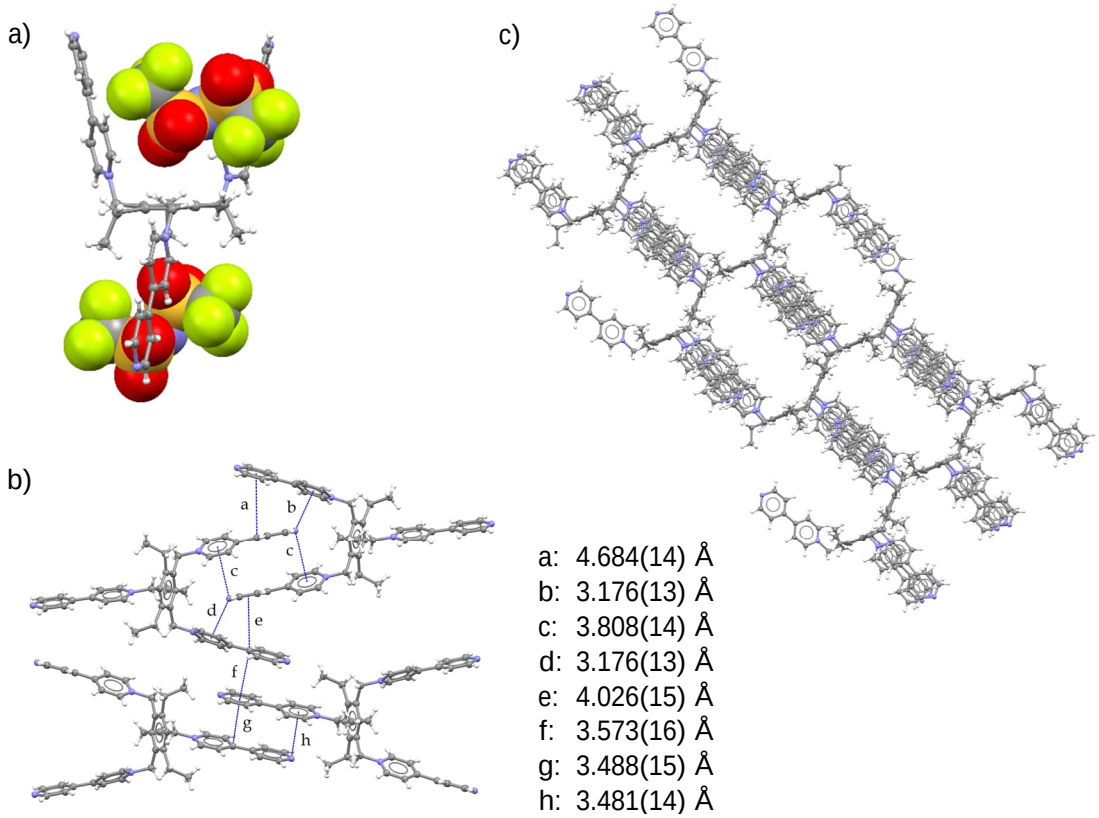

FIGURE 35 a) Ligand in *anti*-conformation and NTf_2 anions near the benzene core, b) packing of bpy arms with selected π–π stacking distances and c) anion cavities viewed along (101) lattice plane. In b) and c), anions and solvent molecules are omitted for clarity.

6.2 M_6L_8 -assemblies

6.2.1 $[Cu_6(L1)_8(MeCN)_{18}(PF_6)_2](PF_6)_{34}$ (C1)

Mixing acetonitrile solutions of $(L1)\cdot(PF_6)_3$ and $Cu(OTf)_2$ in 4:3 ratio followed by slow vapor diffusion of chloroform yielded blue crystals that were highly fragile and spontaneously deteriorated within one minute after removing them from the crystallization solution. X-ray diffraction analysis of mentioned crystals revealed a $[Cu_6(L1)_8(MeCN)_{18}(PF_6)_2](PF_6)_{34}$ (C1) cube-like structure exhibiting in a tetragonal space group *I4/m* ($a = b = 27.5958(2)$ Å, $c = 48.8799(5)$ Å, $\alpha = \beta = \gamma = 90°$, $V = 37\,223.4(5)$ Å^3, $Z = 2$). In this assembly, the mesitylene cores of the ligands act as corner pieces in the cube and metal nodes (L_4M) act as the faces of a cube (Figure 36a). The asymmetric unit consists of one eight of the super cationic (36+) cage unit of C1 and contains two crystallographically distinct Cu^{II} ions (Cu1 and Cu2) each of which exhibit an octahedral coordination geometry where the four equatorial sites are occupied by bpy arms of the ligands (coordinated *via* N-donor atoms) and the two axial sites are occupied by MeCN molecules (Figure 36b). The distances between diagonal Cu^{II} nodes are 24.401(2) Å for d_d(Cu1–Cu1') and 18.358(3) Å for d_d(Cu2–Cu2'), while the distance between nearest Cu^{II} nodes was 15.2677(12) Å for *d*(Cu1–Cu2) and 12.981(2) Å for *d*(Cu2–Cu2) with bridging angles between ligands being 175.9(2)° for ∡(L–Cu1–L) and 173.3(2)° for ∡(L–Cu2–L) with no difference between bridging angles of (L_a–M–L_c) and (L_b–M–L_d). This causes the structure to be squashed from one of its axes (Figure 36c). Two of the ligand's zero-valent pyridine rings are disordered over two orientations with approximate occupancies of 0.50 each and torsion angles of 111.0(4)° and 110.2(4)° between the two orientations.

All ligands of the cage unit are in *syn*-conformation ('bowl') where the bent angles of bpy arms are between 112.87–114.09° and each ligand encapsulates one MeCN molecule and one PF_6^- anion with approximate occupancies of 0.75 and 0.25 respectively (Figure 36d). Encapsulated MeCN is located 3.864(9) Å from benzyl ring centroid to nitrogen of the solvent molecule, whereas encapsulated PF_6^- anion is located 5.019(15) Å from benzyl ring centroid to phosphorus of the anion. The remaining charge of the cationic cage is balanced out *via* exohedral PF_6^- anions, *i.e.* anions located outside the cage, and no triflate anions were observed, though out of the expected 36 anions, only 26 could be assigned. The assembly contains a large amount of, both endo- and exohedral, solvent molecules disordered to a point of which only a few free solvent molecules can be positioned. Overall, 10.9 % of unit cell volume consist of disordered molecules, based on voids calculated in program Mercury[158] (Figure 37a). The missing anions may be disordered among the aforementioned solvent molecules or either metal node or ligand itself (see Section 6.3, p. 132) has (at least partially) underwent a reduction which would lower the total charge of the supercationic cage-unit. This, in turn, would lower the number of counterions required to balance out the total charge, but the possibility of reduction was not investigated.

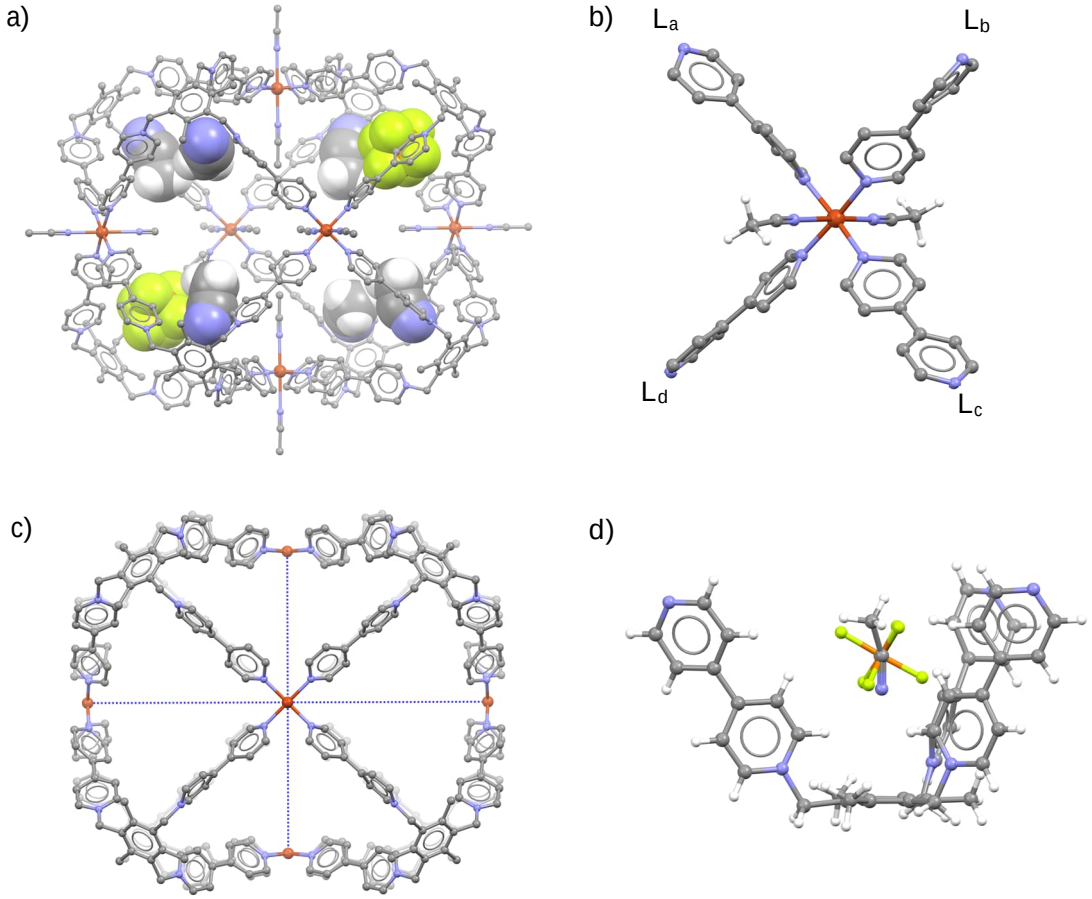

FIGURE 36 a) Structure of C1 cage unit including endohedral MeCN molecules and PF_6^- anions, b) metal node, c) squashed nature of C1 and d) disordered PF_6^- / MeCN inside the bowl of the ligand. Only relevant atoms are shown.

In the crystal lattice, the packing of individual C1 cage units follows the body-centered cubic (BCC) packing model, where one entire C1 cage unit is in the middle of the unit cell and eight C1 other cage units are located in the corners of the unit cell (Figure 37b–c) with exohedral anions and free solvent molecules occupying the space between individual cage-units. Each of the C1 cage units are orientated in the same direction with Cu1 laying parallel with the *c*-axis and Cu2 atoms laying parallel with *ab*-plane. In the lattice, MeCN bonded to Cu1 node are surrounded by four disordered $CHCl_3$ molecules (approx. occup. being 0.45 for each) with the distance of 4.549(15) Å from CH_3 in MeCN to a carbon atom in $CHCl_3$ (Figure 37d). Furthermore, the Cu2 nodes of different C1 cage-units come near to each other, with a distance of 11.723(2) Å between Cu2 atoms and MeCN molecules bonded to those Cu2 nodes come to a distance of 8.95(5) Å measured from carbon in CH_3 to nitrogen atom of the other MeCN molecule. This leaves enough room for one disordered PF_6^- anion to be located between two C1 cage units along the Cu2 plane as shown in Figure 37e-f. Crystallographic data for single crystal X-ray measurement of C1 is presented in Appendix 9 Table A8.

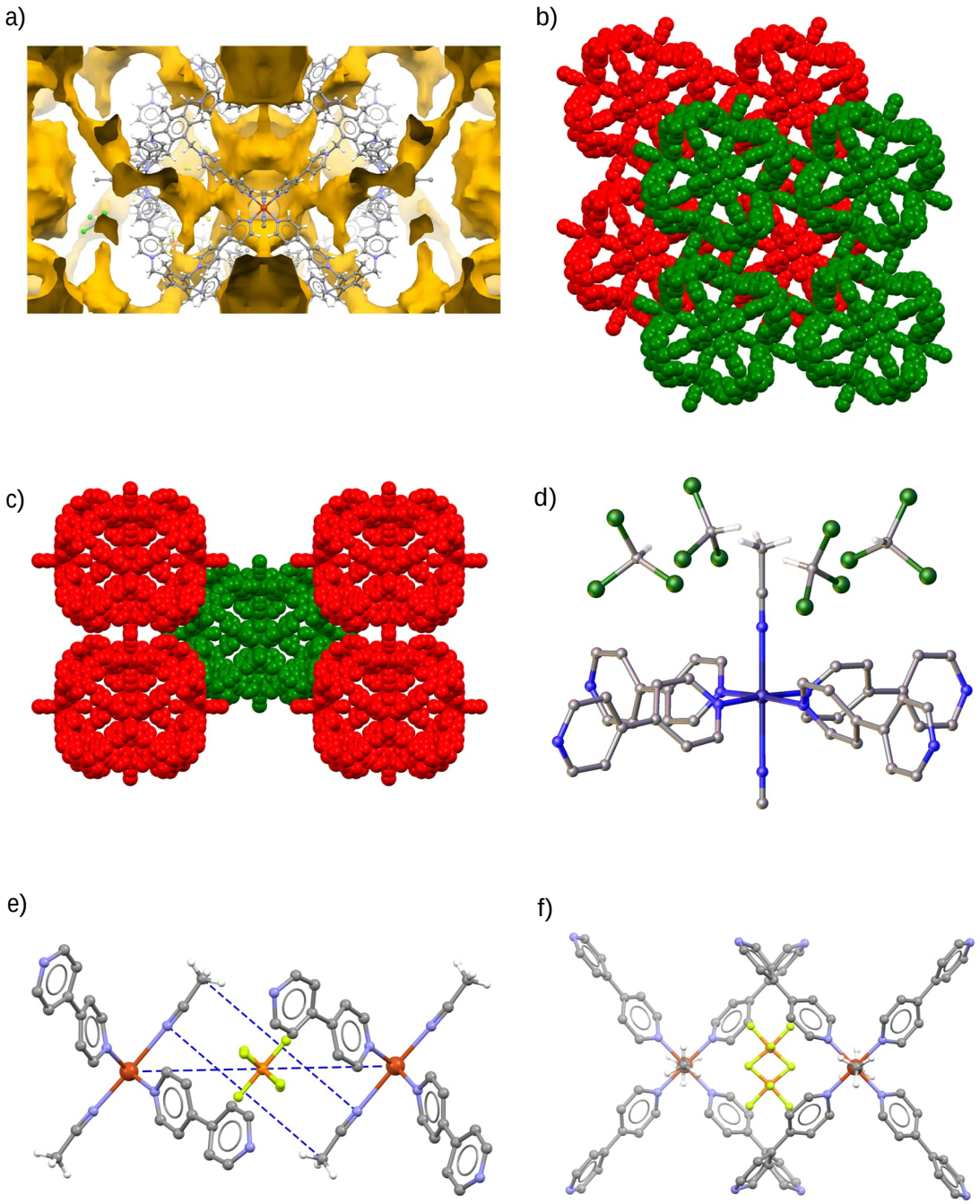

FIGURE 37 a) Solvent accessible surface in the unit cell of C1, b) unit cell packing viewed along the crystallographic *c*-axis, c) along *b*-axis, d) $CHCl_3$ molecules near Cu1 metal nodes and e-f) PF_6^- anions between C1 cage units. Only relevant atoms are shown.

6.2.2 $[Cu_6(L1)_8(MeCN)_7(OH)_7(ClO_4)_6](ClO_4)_{15.5-n}(PF_6)_{7.5+n}$ (C2)

Mixing acetonitrile solutions of $(L1)\cdot(PF_6)_3$ and $Cu(ClO_4)_2\cdot 6\ H_2O$ followed by slow evaporation under 1,4-dioxane yielded blue hexagonal crystals that were similarly fragile and short-lived outside the crystallization solution as compound C1. X-ray diffraction analysis revealed again an analogous cube-like cage structure of $[Cu_6(L1)_8(MeCN)_7(OH)_7(ClO_4)_6](ClO_4)_{15.5-n}(PF_6)_{7.5+n}$ (C2) exhibiting in a monoclinic space group *C*2/*c* (a = 49.8080(12) Å, b = 29.2146(6) Å, c = 55.7326(13) Å, $\alpha = \gamma = 90°$, β = 113.168(3)°, V = 74 557(3) Å^3, Z = 4). The asymmetric unit consists of one-half of a cage-unit of C2 and contains three crystallographic distinct Cu^{II} ions (Cu1, Cu2 and Cu3) with each metal node exhibits in an octahedral coordination geometry where the four equatorial sites are occupied by bpy arms of the ligands, and the two axial sites are occupied by either MeCN molecules or by hydroxide (OH^-) anions (Figure 38a-c). The distances between diagonal Cu^{II} nodes are 21.969(14) Å for d_d(Cu1a–Cu1a'), 20.836(14) Å for d_d(Cu1b–Cu1b'), 20.21(2) Å for d_d(Cu2a–Cu2a'), 19.24(2) Å for d_d(Cu2b–Cu2b'), 21.574(15) Å for d_d(Cu3a–Cu3a)' and 20.486(16) Å for d_d(Cu3b–Cu3b)', while the distances between nearest Cu^{II} nodes varied between 13.600–15.873 Å. The cage unit of C2 is thus more symmetrical than the one observed in C1, despite both containing the same supercationic skeleton of $[Cu_6(L1)_8]^{36+}$. The skeleton of C2 is almost completely disordered over two positions (Figure 38d) with all metal nodes as well as most of the ligand bpy arms being disordered with approximate occupancies of 0.5 each. The disordered Cu^{II} atoms are separated (*i.e.*, the distance between different parts) by a distance of 0.570(12) Å, 0.535(16) Å and 0.548(14) Å for Cu1, Cu2 and Cu3 respectively. Subsequently, the zero-valent N-donor atoms of disordered bpy arms bonded to said metal nodes are separated by an average of 0.633 Å. The bridging angles between bonded ligands are 175.3(8)° / 177.1(8)° for ∡L–Cu1A–L), 177.9(9)° / 178.2(8)° for ∡L–Cu1B–L), 177.2(9)° / 177.3(8)° for ∡L–Cu2A–L), 170.2(9)° / 170.0(8)° for ∡L–Cu2B–L), 175.9(9)° / 174.5(9)° for ∡L–Cu3A–L), and 177.6(10)° / 178.1(10)° for ∡(L–Cu3B–L), presented as $(L_a–M–L_c) / (L_b–M–L_d)$.

All ligands of the cationic cage unit are in *syn*-conformation where the bend angles of bpy arms are between 107.0–120.1° and two of the ligands encapsulate one MeCN molecule each while the remaining six ligands encapsulate one ClO_4^- anion each (Figure 38e-f). Encapsulated MeCN molecule lies 3.643(11) Å from benzyl ring centroid to nitrogen of the solvent molecule, whereas encapsulated ClO_4^- anions are located between 5.016–5.265 Å from benzyl ring centroid to chlorine of the anion. Exohedral anions are a mixture of ClO_4^- and PF_6^- anions, and based on assigned anions and elemental analysis within Olex^2, the ratio of ClO_4^-:PF_6^- is 5:3, which suggests that ClO_4^- is preferred over PF_6^- as the ratio of anions was originally 1:2. Out of expected 36 anions, 33 could be assigned (7x OH^-, 18.5x ClO_4^- and 7.5x PF_6^-) with the remaining three anions most likely being disordered among the large volume of disordered free solvents, consisting of both MeCN and 1,4-dioxane. Overall, 20.8 % of the unit cell volume consists of disordered molecules, based on voids calculated in Mercury (Figure 38g).

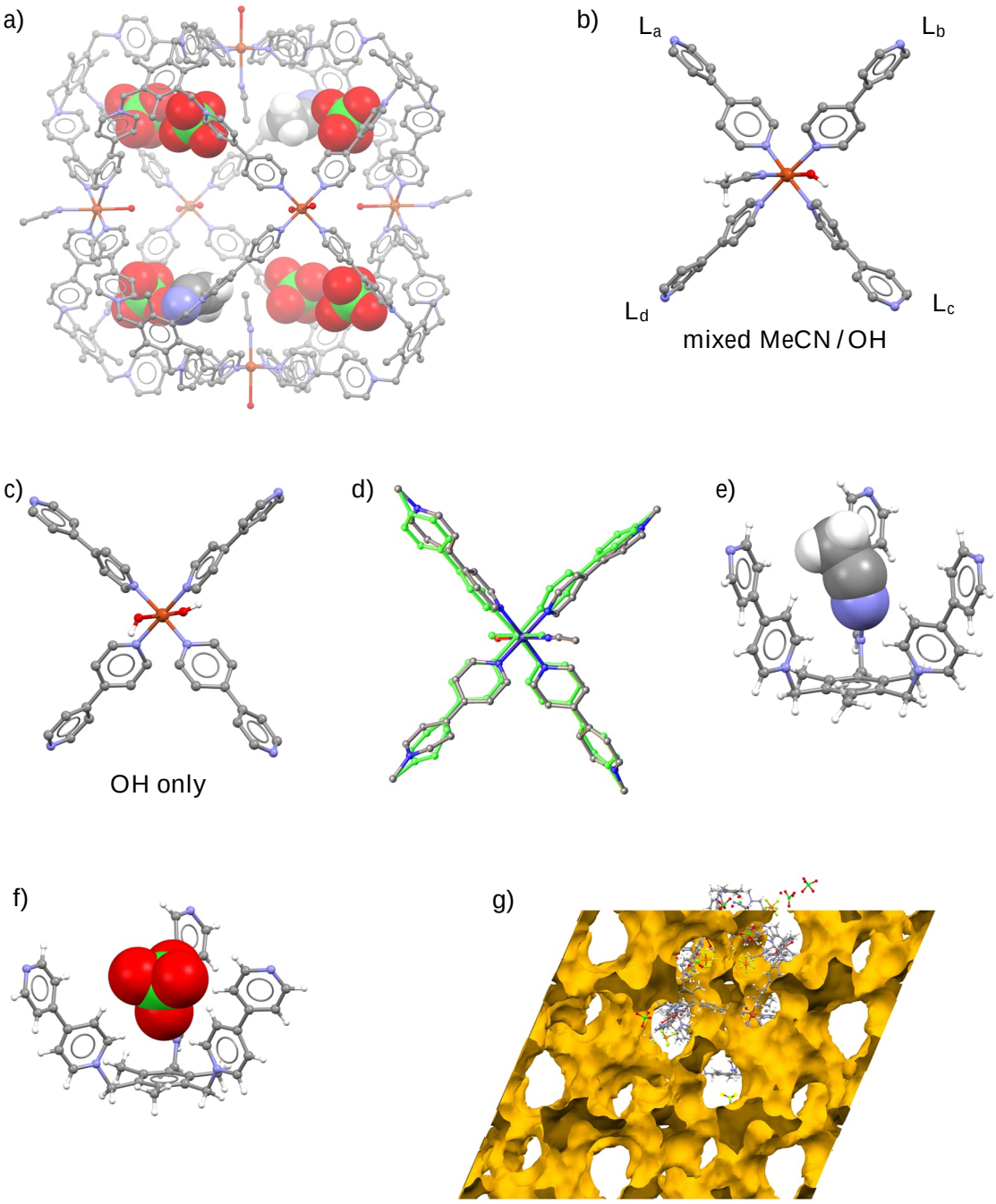

FIGURE 38 a) Structure of C2 cage unit including endohedral ClO_4^- anions and MeCN molecules, b-c) metal nodes, d) disordered nature of metal nodes, e) encapsulated MeCN molecule, f) encapsulated ClO_4^- anion, and g) solvent accessible surface in unit cell of C2. Only relevant atoms are shown.

In the crystal lattice, the individual C2 cage units are packed similar to the face centered cubic (FCC) close-packing model of regular spheres (Figure 39a–c) and unlike in C1, the mesitylene cores of the ligands in C2 come near each other. Subsequently, one of the exohedral ClO_4^- anions is 'trapped' between four C2 cage units, with the average distance from mesitylene core centroid to chloride atom being 4.630 Å. Another disordered perchlorate anion with approximate occupancy of 0.5 is located near the trapped one, with a distance of 6.319(5) Å between the two chloride ions (Figure 39d). The surrounding mesitylene cores are separated between 6.716–8.807 Å, measured from centroid to centroid. Crystallographic data for single crystal X-ray measurement of C2 is presented in Appendix 9 Table A8.

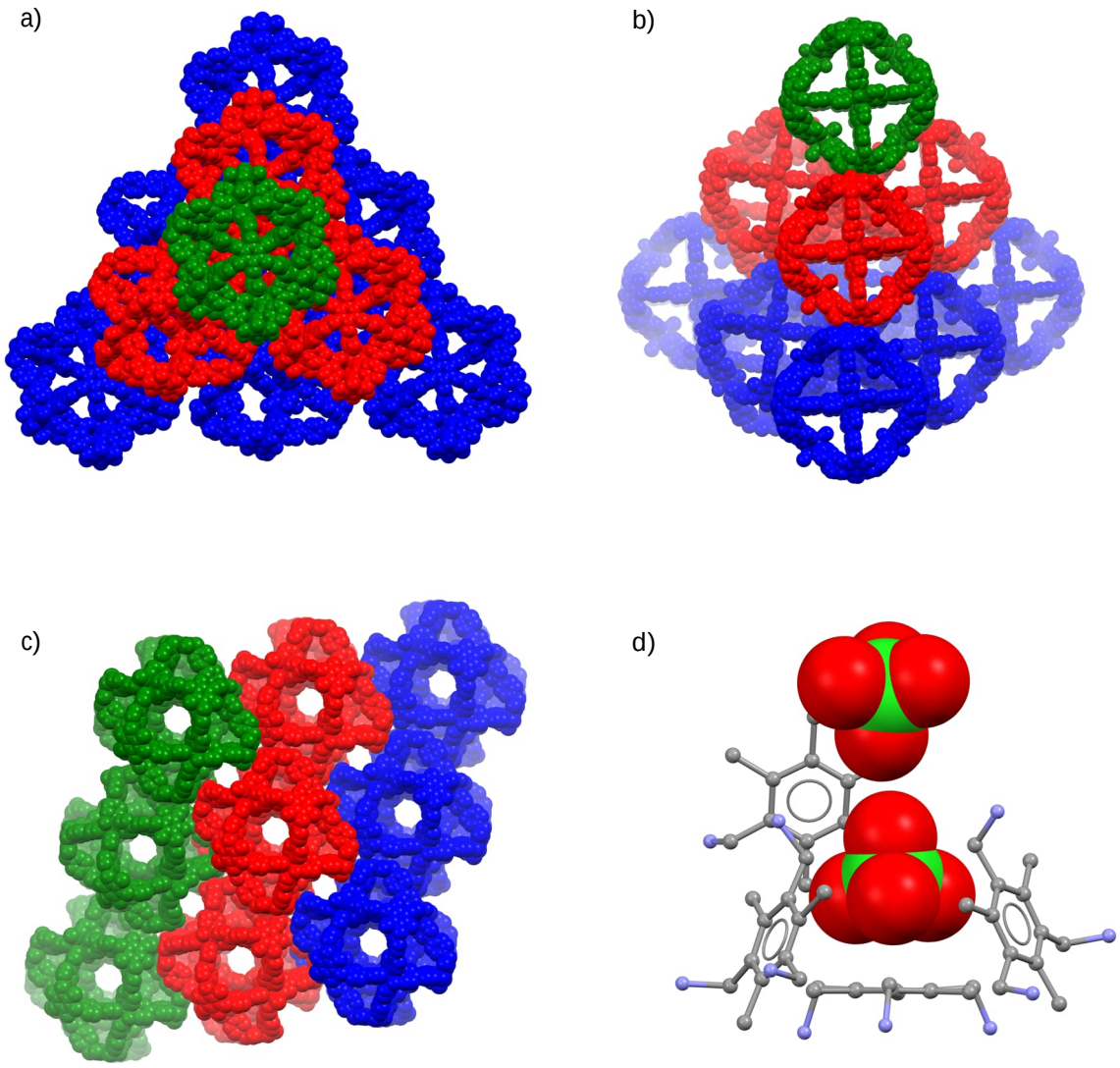

FIGURE 39 a-b) Dense packing of C2 cage units in the crystal lattice, c) packing viewed along (101) lattice plane, and d) trapped ClO_4^- anion surrounded by mesitylene cores of four different cages. Only relevant atoms are shown.

6.2.3 $[Ni_6(L2)_8(MeCN)_{12}(PF_6)_8](PF_6)_{17.5-n}(NO_3)_{10.5+n}$ (C3)

Mixing acetonitrile solutions of $(L2)\cdot(PF_6)_3$ and $Ni(NO_3)_2\cdot 2.5\ H_2O$ in 4:3 ratio followed by slow vapor diffusion of ethyl acetate yields lilac crystals (Figure 40a) and the X-ray diffraction analysis of crystals revealed a $[Ni_6(L2)_8(MeCN)_{12}(PF_6)_8](PF_6)_{17.5-n}(NO_3)_{10.5+n}$ (C3) cube-like structure (Figure 40b) exhibiting in trigonal space group $R\bar{3}$ ($a = b = 58.7031(15)$ Å, $c = 75.1394(14)$ Å, $\alpha = \beta = 90°$, $\gamma = 120°$, $V = 224\ 244(9)$ Å^3, $Z = 12$). The asymmetric unit contains four crystallographically distinct Ni^{II} ions (Ni1–Ni4) each of which exhibits an octahedral coordination geometry where the four equatorial sites are occupied by ligands bpy arms and the two axial sites are occupied acetonitrile molecules (Figure 40c). The asymmetric unit of assembly C3 consists of one-half and one sixth of two individual $[Ni_6(L2)_8(MeCN)_{12}]^{36+}$ cationic cages with slightly different conformation of ethyl-groups: C3–I (Ni1–Ni3) forming from one-half of cage unit, possessing *trans*-conformation of ligand bpy arms and ethyl groups, and C3–II (Ni4) forming from one-sixth of the cage unit, possessing both all-*cis*- and all-*trans*-conformations (in 3:1 ratio) of ligand bpy arms and ethyl groups (Figure 40d-e). Each bowl encapsulates a single PF_6^- anion (Figure 40f) while exohedral anions are a mixture of PF_6^- and NO_3^- anions. Out of expected 36 anions, 33 could be assigned (10.5x NO_3^- and 22.5x PF_6^-) with the remaining three anions most likely being disordered among the large volume of disordered free solvents, with overall 23.1 % of unit cell volume consisting of disordered molecules, based on voids calculated in Mercury (Figure 40g).

Two of the Ni^{II} atoms (Ni2 and Ni4) are disordered over two positions with approximate occupancies of 0.75 and 0.25 for Ni2A and Ni2B respectively, and 0.90 and 0.10 for Ni4A and Ni4B respectively. The two positions are separated with a distance of 0.567(14) Å for *d*(Ni2A–Ni2B) and 0.37(2) Å for *d*(Ni4A–Ni4B). The distances between diagonal Ni^{II} ions in C3–I are 19.411(2) Å for d_d(Ni1–Ni1'), 20.761(7) Å for d_d(Ni2A–Ni2A'), 19.71(3) for d_d(Ni2B–Ni2B') and 21.389(3) Å for d_d(Ni3–Ni3') while in C3–II the diagonal distances are 21.373(6) Å for d_d(Ni4A–Ni4A') and 21.19(7) for d_d(Ni4B–Ni4B') respectively. The distance between nearest Ni^{II} nodes is between 13.649–15.479 Å in C3–I and between 15.03–15.508 Å in C3–II. The bridging angles of bonded ligands in metal nodes were 177.3(3)° / 177.8(2)° for ∡(L–Ni1–L), 175.2(4)° / 177.3(4)° for ∡(L–Ni2A–L), 155.2(8)° / 152.3(7)° for ∡(L–Ni2B–L), 177.8(2)° / 179.0(3)° for ∡(L–Ni3–L), 176.8(2)° / 177.4(3)° for ∡(L–Ni4A–L) and 162.8(12)° / 170.1(18)° for ∡(L–Ni4B–L), presented as $(L_a–M–L_c) / (L_b–M–L_d)$. The bend angles of bpy arms are between 109.6–115.8° in C3–I and between 113.2–117.0° in C3–II, with encapsulated PF_6^- anions lie 4.849–5.198 Å from benzene ring centroid to phosphorus atom. In C3–I, it was not possible to assign the CH_3-atoms of the endohedrally coordinated MeCN molecules, whereas in the case of C3–II it was not possible to assign of the CH_3-atoms of the exohedrally coordinated MeCN molecules. This is due to MeCN being disordered to a point where CH_3-groups could not be identified from the electron density map (or the occupancy would have been minute), and similar disorder was also observed in other M_6L_8 assemblies.

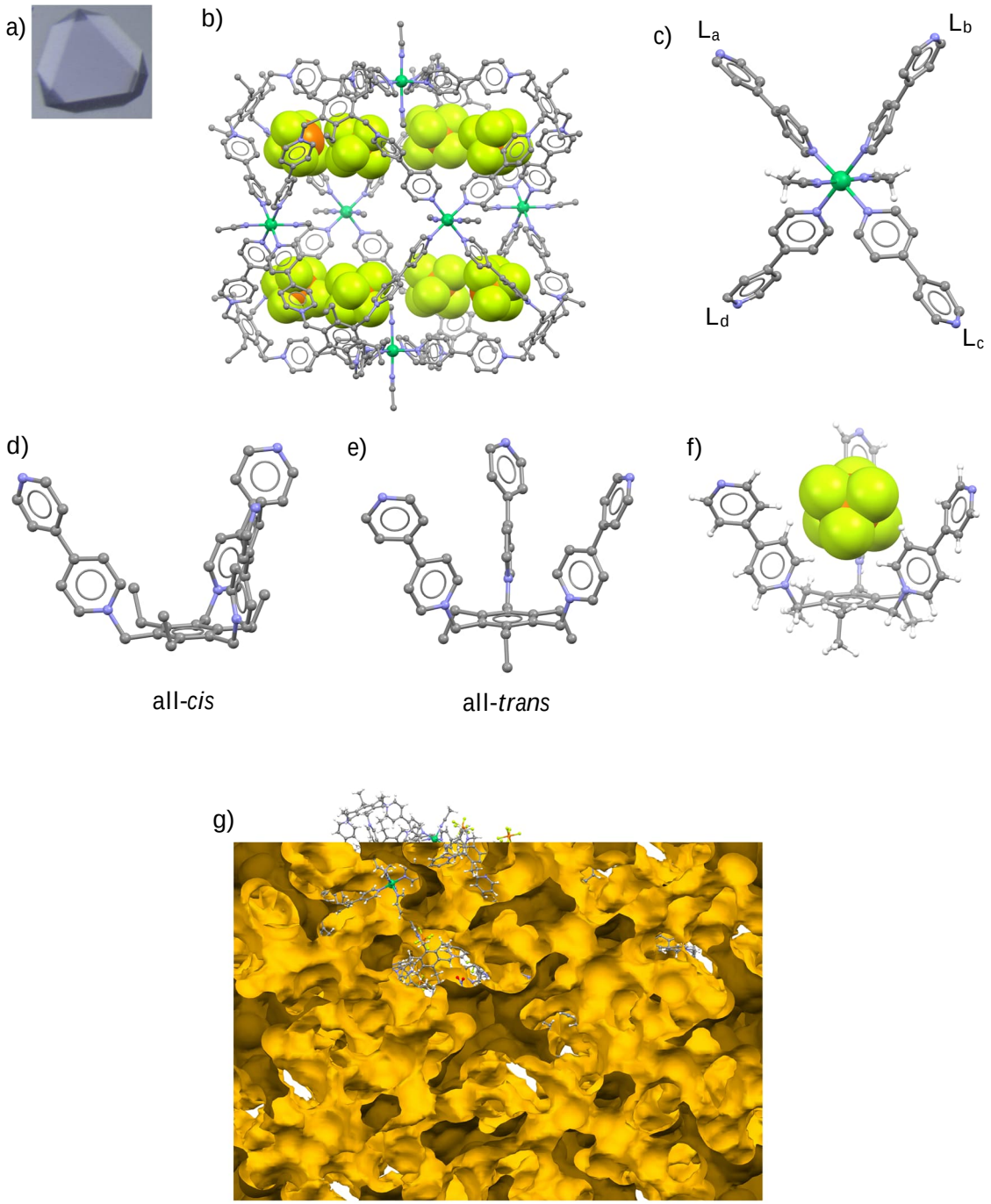

FIGURE 40 a) Crystals of C3, b) structure of C3 cage unit including endohedral anions, c) metal node, d-e) all-*cis*- and all-*trans*-conformations of the ligand, f) encapsulated PF_6^- anion, and g) solvent accessible surface in unit cell of C3. Only relevant atoms are shown.

The unit cell contains 12 C3 cage units, out of which 9 are C3–I cage units and 3 are C3–II cage units. C3–II cage units are located in the corners of the unit cell and along ($\bar{1}11$) lattice plane, while C3–I cage units are filling the rest of the unit cell (Figure 41a-d). In the crystal lattice, individual C3 cage units are following the FCC packing model, similarly to assembly C2 but unlike in C2, the orientation of individual cage units is different. Instead of metal nodes coming near to each other, it is the ligand benzene cores that come near to each other (centroid-centroid distance of 9.9255(2) Å) or exohedral MeCN in Ni1 node comes near one of the benzene cores (centroid to CH_3 distance 3.813(11) Å. Subsequently there are no anions 'trapped' between C3 cage units in a similar fashion as was observed with assembly C2. Crystallographic data for single crystal X-ray measurement of C3 is presented in Appendix 9 Table A8.

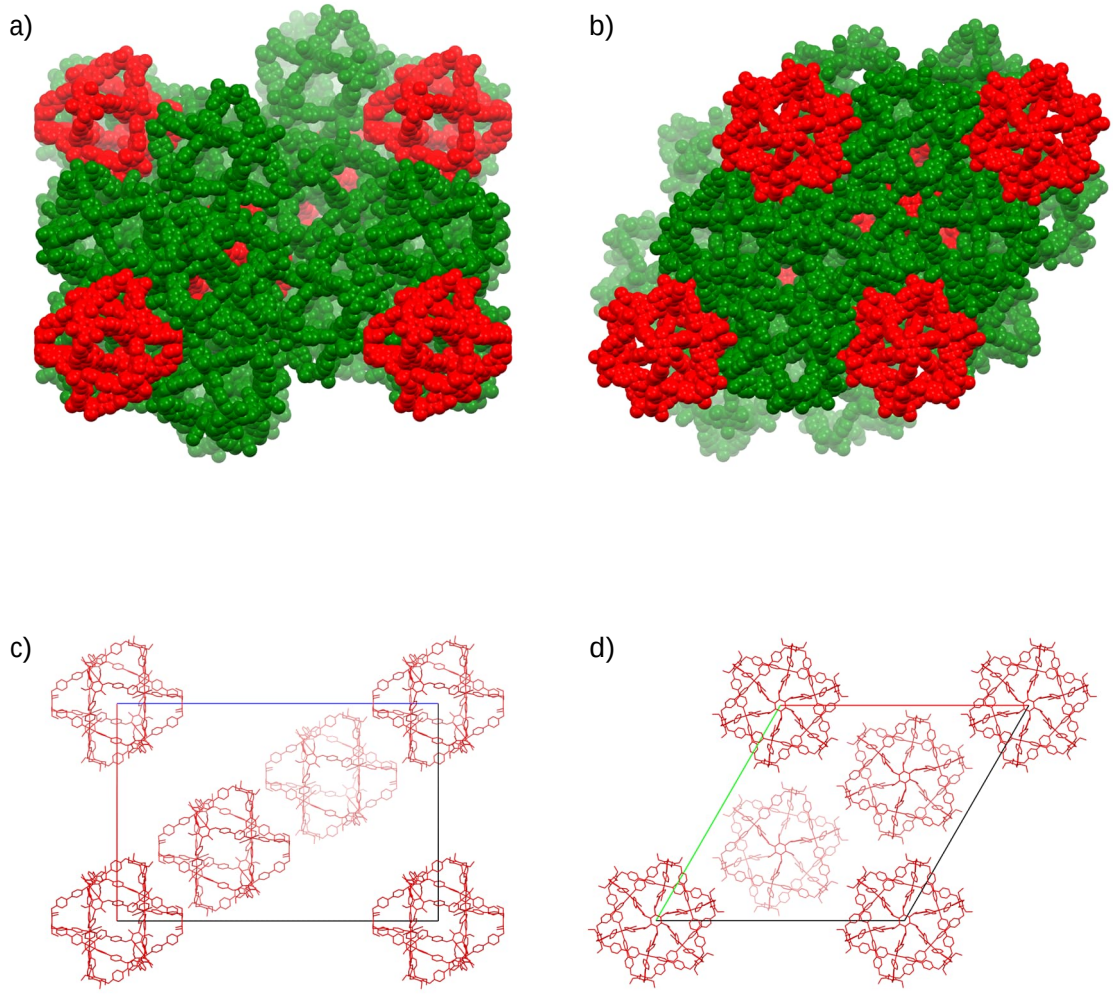

FIGURE 41 Unit cell packing viewed along the crystallographic a) *b*-axis and b) *c*-axis. Locations of C3–II cage units in the unit cell viewed along c) *b*-axis and d) *c*-axis. Green represents cage unit C3–I and red represents cage unit C3–II. Only relevant atoms are shown.

6.2.4 $[Ni_6(L2)_8(MeCN)_{12}(PF_6)_8](PF_6)_{28}$ (C3*)

As observed above, using $Ni(NO_3)_2$ as a source of metal ions, yield an assembly which contains no endohedral nitrate anions. To examine is similar assembly could be obtained nitrate 'free', $Ni(PF_6)_2$ was instead used as a metal source. Mixing acetonitrile solutions of $(L2)\cdot(PF_6)_3$ and $[Ni(MeCN)_6](PF_6)_2$ in 4:3 ratio followed by slow vapor diffusion of ethyl acetate yields lilac crystals and the X-ray diffraction analysis of crystals revealed a $[Ni_6(L2)_8(MeCN)_{12}(PF_6)_8](PF_6)_{28}$ (C3*) cube-like structure (Figure 42a–b) exhibiting monoclinic space group *C*2/*c* (a = 40.9416 (13) Å, b = 45.5508(13) Å, c = 41.8085(15) Å, $\alpha = \gamma = 90°$, β = 90.979(3) °, V = 77 958(4) Å^3, Z = 4). The asymmetric unit contains one-half of the C3* cage unit with three crystallographically distinct Ni^{II} ions (Ni1, Ni2 and Ni3) each of which exhibit an octahedral coordination geometry where the four equatorial sites are occupied by ligands bpy arms and the two axial sites are occupied by MeCN molecules (Figure 42c), with a bond length between 2.025–2.099 Å. The distances between diagonal Ni^{II} ions are 20.121(3) Å for d_d(Ni1–Ni1'), 20.914(3) Å for d_d(Ni2–Ni2'), and 19.644(4) Å for d_d(Ni3–Ni3') respectively, while the distance between nearest Ni^{II} nodes was between 13.716–14.930 Å. The bridging angles between coordinated ligands are 177.6(3)° / 177.6(2)° for ∡(L–Ni1–L), 177.8(3)° / 178.5(4)° for ∡(L–Ni2–L) and 177.5(4)° / 177.7(3)° for ∡(L–Ni3–L), presented as $(L_a–M–L_c) / (L_b–M–L_d)$.

One ligand has one ethyl-group disordered between *cis*- and *trans*-conformations with 0.50 occupancies each, while the rest have all-*trans* conformation with the bent angles of bpy arms being between of 112.48–117.13°. One out of four 'bowls' is occupied by a disordered MeCN molecule and the remaining 'bowls' are occupied by PF_6^- anions. The encapsulated MeCN lies between 3.892(16) Å from benzyl ring centroid to nitrogen of MeCN molecule, whereas encapsulated PF_6^- anions are located between 5.072–5.238 Å from benzyl ring centroid to phosphorus of the anion. In the metal nodes, the CH_3-group of coordinated MeCN molecules can only be assigned with an approximate occupancy of 0.50, while C≡N group has full occupancy. Out of the expected 36 anions, 32 could be assigned and the remaining anions are likely disordered among the large volume of heavily disordered solvent molecules. In fact, no free solvent molecules could be assigned with a reliable degree of accuracy (0.25 occupancy was generally used as a cut limit for the refinement of solvent positions), and 22.6 % of the unit cell volume remains unassigned according to solvent accessible surface calculated in Mercury, as shown in Figure 42d.

In the crystal lattice, individual C3* cage units are following the FCC packing model, similarly to assemblies C2 and C3. Each of the C3* cage units are orientated in the same direction with Ni1 and Ni2 atoms are laying parallel with the *ac*-plane, while Ni3 atoms laying parallel with *b*-axis (Figure 42e). The exohedral MeCN bonded to Ni3 nodes are surrounded by PF_6^- anions with distance between 4.107–4.829 Å from CH_3 group in MeCN molecule to phosphorus atom in PF_6^- (Figure 42f). Furthermore, both Ni1 and Ni2 nodes come near to their symmetry twins, with distances of 11.859(3)Å and 11.704(3) Å

respectively, and MeCN molecules bonded to those Ni^{II} nodes come to a distance of 8.891(3) Å for Ni1 and 8.82(2) Å for Ni2 respectively. This leaves enough room for one PF_6^- anion to reside (in a special position) between two C3* cage units along the Ni1 and Ni2 planes as shown in Figure 42g. Crystallographic data for single crystal X-ray measurement of C3* is presented in Appendix 9 Table A8.

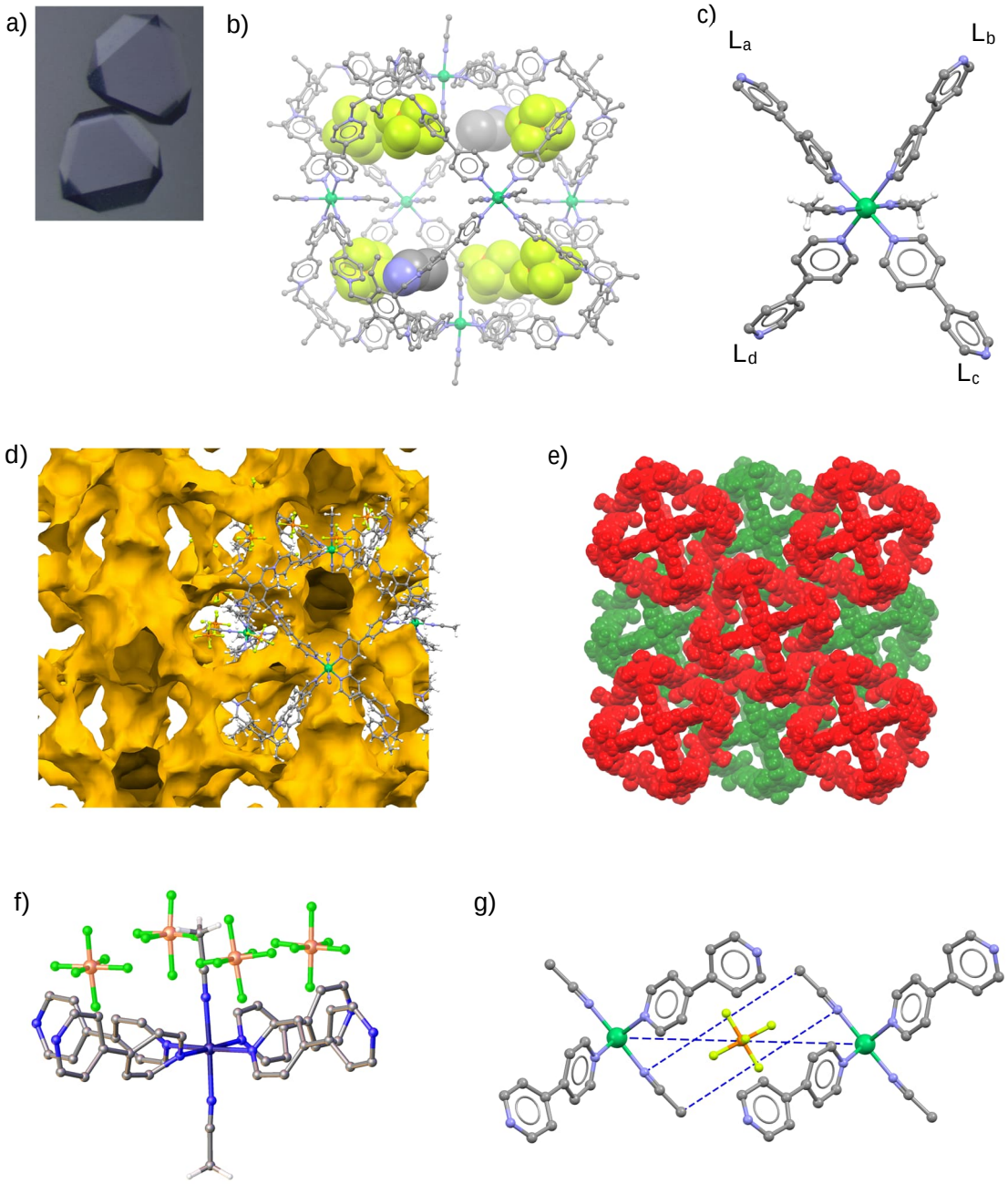

FIGURE 42 a) Crystals of C3*, b) structure of C3* cage unit including encapsulated molecules, c) metal node, d) solvent accessible surface in unit cell of C3*, e) packing viewed the crystallographic along *b*-axis, f) PF_6^- anions near Ni3 metal node and g) PF_6^- anions between C3* cage units. Only relevant atoms are shown.

6.2.5 $[Ni_6(L2)_8Cl_{14}(PF_6)_6](PF_6)_{14-n}Cl_{2+n}$ (C4)

Mixing acetonitrile solution of $(L2)\cdot(PF_6)_3$ and ethanol solution of anhydrous $NiCl_2$ in a 4:3 ratio, followed by slow vapor diffusion of chloroform yields green crystals (Figure 43a) and the X-ray diffraction analysis of crystals revealed a $[Ni_6(L2)_8Cl_{14}(PF_6)_6](PF_6)_{14-n}Cl_{2+n}$ (C4) cube-like structure exhibiting monoclinic space group *C2/c* (a = 40.1388(10) Å, b = 40.1148(9) Å, c = 46.1812(15) Å, $\alpha = \gamma = 90°$, β = 103.279(3)°, V = 72 371(3) Å^3, Z = 4). The asymmetric unit consists of one-half of a C4 cage unit (Figure 43b) and contains three crystallographically distinct Ni^{II} ions (Ni1, Ni2 and Ni3) each of which exhibit an octahedral coordination geometry where the four equatorial sites are occupied by ligands bpy arms and the two axial sites are occupied by chloride anions (Figure 43c). Two of the metal nodes are disordered over two positions each with a separation of 0.460(12) Å for d(Ni1A–Ni1B) and 0.446(7) Å for d(Ni2A–Ni2B) (Figure 43d). The distances between diagonal Ni^{II} ions are 21.682(15) Å for d_d(Ni1A–Ni1A'), 21.067(18) Å for d_d(Ni1B–Ni1B'), 21.034(18) Å for d_d(Ni2A–Ni2A'), 20.860(15) Å for d_d(Ni2B–Ni2B') and 19.385(4) Å for d_d(Ni3–Ni3') respectively, while the distances between nearest Ni^{II} nodes were between 13.960–15.724 Å and the Ni–Cl distances between 2.14–2.692 Å. The bridging angles of bonded ligands in metal nodes are 171.5(5)° / 170.2(5)° for ∡(L–Ni1A–L), 167.3(5)° / 167.6(5)° for ∡(L–Ni1B–L), 163.2(3)° / 174.9(5)° for ∡(L–Ni2A–L), 172.3(3)° / 176.9(5)° for ∡(L–Ni2B–L) and 172.5(3)° / 175.1(3)° for ∡(L–Ni3–L), presented as $(L_a–M–L_c) / (L_b–M–L_d)$.

The bpy arms of the ligands have bend angles between 104.5–117.4° and one of the ligands has a single ethyl group disordered between *cis*- and *trans*-conformations with approximate occupancies of 0.333 and 0.667 respectively, with the *trans*-conformation further disordered over two orientations with 0.333 occupancies each (Figure 43d). In the asymmetric unit, five zero-valent pyridine rings are disordered over two orientations with four having approximate occupancies of 0.50 and 0.50 between orientations and one with approximate occupancies of 0.75 and 0.25 between orientations, with orientations being separated by a torsion angle between 78.6–110.1° (Figure 43d). Additionally, one of the +1-valent pyridine rings including the methylene-bridge between core and bpy arm is disordered over two positions with approximate occupancies of 0.50 each with a separation of 0.578(3) Å between pyridine ring centroids (Figure 43d). One bowl is occupied by PF_6^- anion, while three are occupied by both chloride and PF_6^- anions with approximate occupancies of either 0.50:0.50 (1x) or 0.75:0.25 (2x) for PF_6^-:Cl^-. On average, the C4 cage unit thus encapsulates two chloride and six PF_6^- anions. The chloride anions lie between 3.992–4.146 Å above the benzene ring centroid and encapsulated PF_6^- anions lie between 5.126–5.155 Å from benzene ring centroid to the phosphorus atom.

Out of the required 24 non-coordinated anions, 16.5 could be assigned to a satisfactory level (2x Cl^- and 14.5x PF_6^-), which brings the total negative charge to 28.5 out of 36 required, when the 12 exohedrally coordinated chlorides are included. Two exohedral chloride anions were observed and nearly all of the exohedral PF_6^- anions are disordered with approximate occupancies of either 0.25 or 0.50, while being disordered together with solvent molecules (either MeCN or EtOH) as shown in Figure 43e-f. Additionally, it was possible to assign all of the required fluorine atoms to all of the PF_6^- anions in s satisfactory level. The missing 7.5 anions are most likely disordered among the large volume of disordered free solvents (MeCN, EtOH and $CHCl_3$), with an overall 20.5 % of unit cell volume consisting of disordered molecules based on voids calculated in Mercury (Figure 43g).

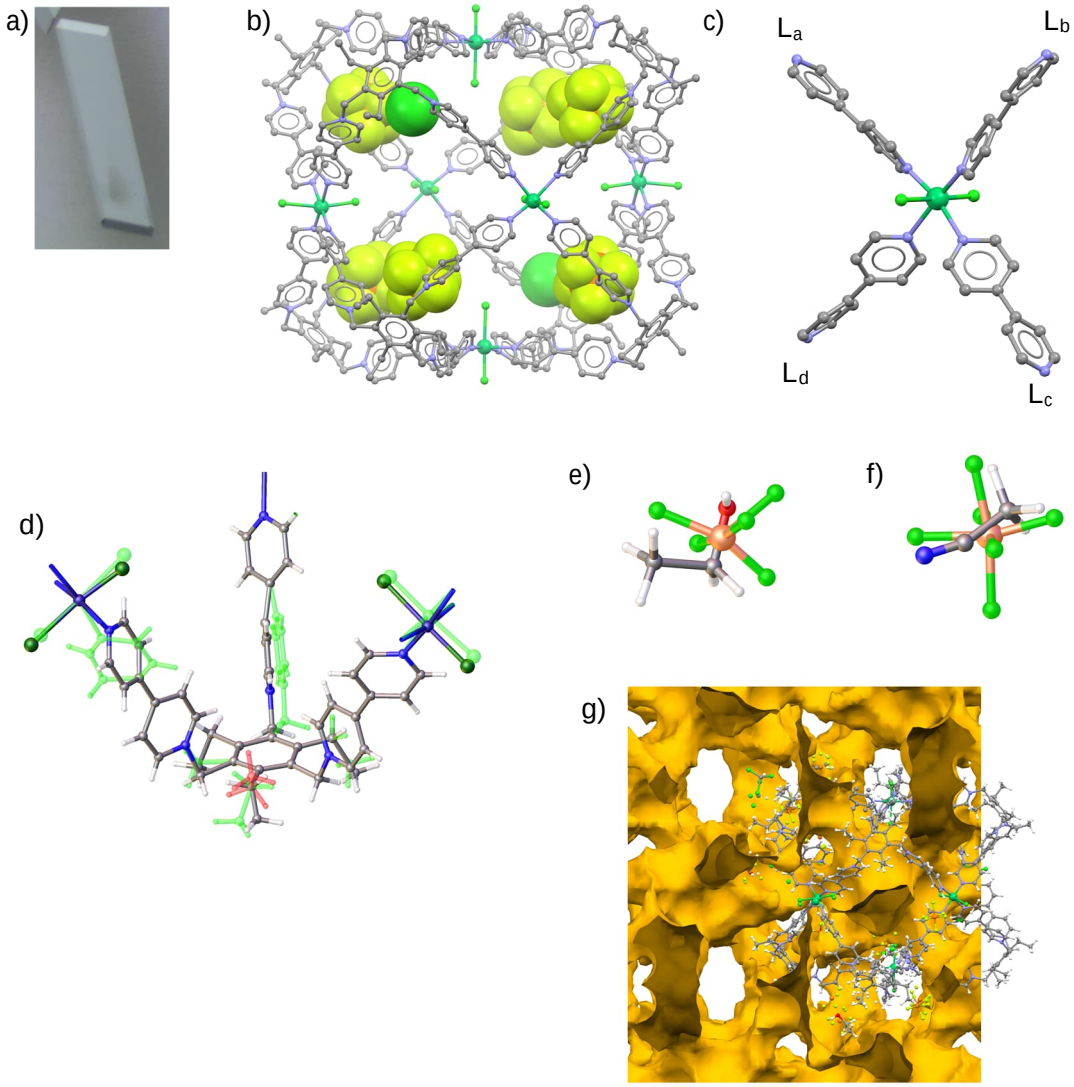

FIGURE 43 a) Crystals of C4, b) structure of C4 cage unit including endohedral anions, c) metal node, d) disorder observed in C4 metal nodes and ligands, e-f) solvent-anion disorder and g) solvent accessible surface in unit cell of C4, Only relevant atoms are presented.

In the crystal lattice, individual C4 cage units are following the FCC packing model, similarly to assemblies C2–C3* (Figure 44a-b). Each of the C4 cage units are orientated in the same direction with Ni3 laying roughly parallel with the (102) lattice plane while Ni1 and Ni2 atoms are laying roughly perpendicular with a said plane. All of the Ni^{II} nodes come near their symmetry twins, with distances of 9.139(18) / 9.13(2) Å for Ni1, 8.677(17) / 8.330(14) for Ni2 and 10.727(3) Å for Ni3, while the exohedrally bonded chloride anions are separated by a distance of 6.80(3) / 6.29(3) Å for Cl1A / Cl1B and 5.38(3) / 5.65(3) Å for Cl3A / Cl3B respectively. In Ni3 node the chloride atoms (Cl5) come near +1-valent pyridine ring with a distance to +1-valent nitrogen being 3.771(12) / 4.235(12) Å for Cl5A / Cl5B. The packing near Ni^{II} nodes is orientated differently than in C1 or C3* and unlike in C1 or C3* there is not enough room for anion to reside between two C4 cage units (Figure 44c–f). Crystallographic data for single crystal X-ray measurement of C4 is presented in Appendix 9 Table A8.

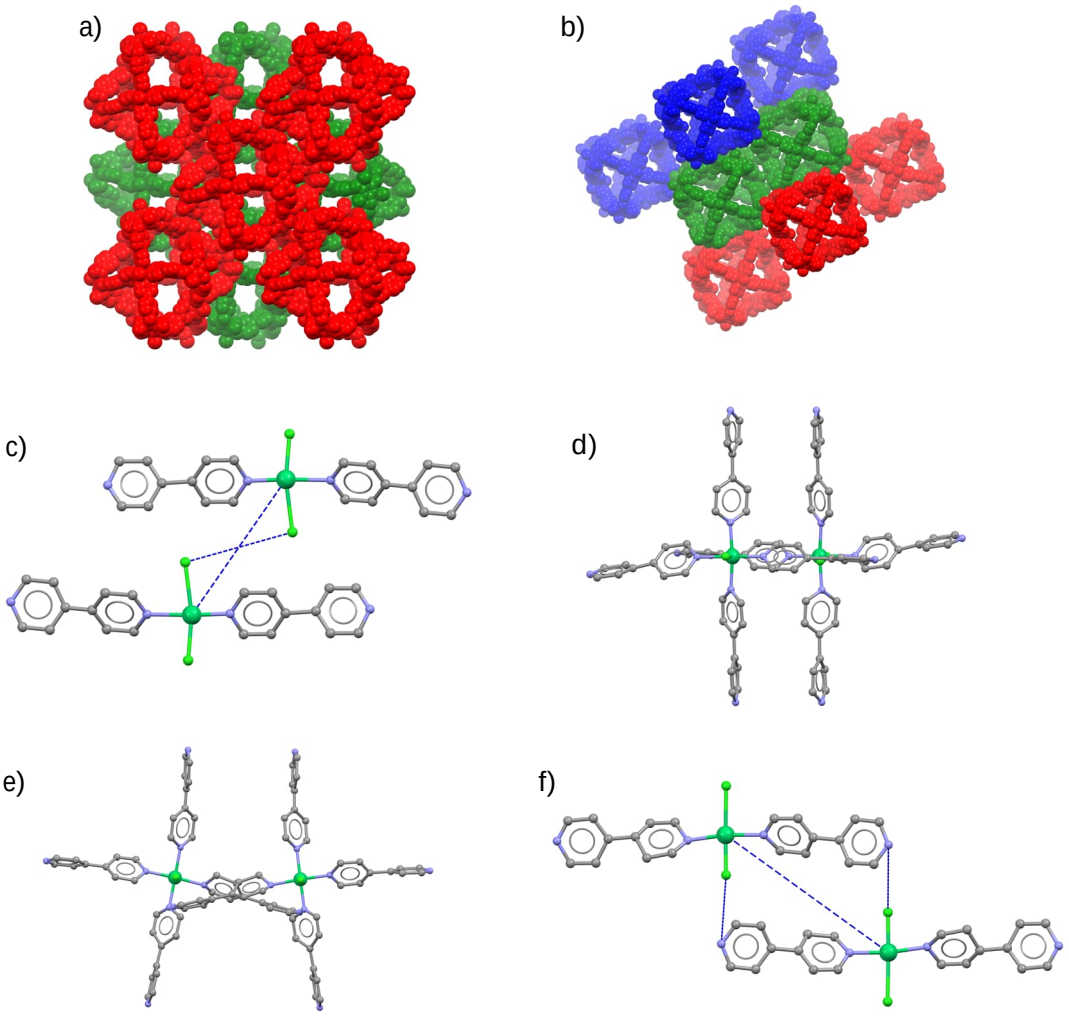

FIGURE 44 Unit cell packing viewed along the crystallographic a) *c*-axis, b) (110) lattice plane, c-d) packing near Ni1 and Ni2 nodes, and e-f) packing near Ni3 nodes. Only relevant atoms are shown.

6.2.6 $[Ni_6(L2)_8(MeCN)_6Br_{13.1}(PF_6)_{0.9}](PF_6)_{22}$ (C5)

Mixing acetonitrile solution of $(L2)\cdot(PF_6)_3$ and ethanol solution of anhydrous $NiBr_2$ in a 4:3 ratio followed by slow vapor diffusion of ethyl acetate yields green-blue crystals (Figure 45a) and the X-ray diffraction analysis of crystals revealed a $[Ni_6(L2)_8(MeCN)_6Br_{13.1}(PF_6)_{0.9}](PF_6)_{22}$ (C5) cube-like structure (Figure 45b) crystallizing in tetragonal space group $P4_2/n$ (a = 41.5335(5) Å, b = 41.5335(5) Å, c = 45.7428(7) Å, $\alpha = \beta = \gamma = 90°$, V = 78 907.7(17) Å^3, Z = 4). Due to high level of disorder it was not possible to determine the structure to a satisfactory level, and therefore the assembly was instead determined in a monoclinic space group $P2/n$ (a = 41.52326(8) Å, b = 45.7321(7) Å, c = 41.5248(7) Å, $\alpha = \gamma = 90°$, β = 90.088(2)°, V = 78 871(2) Å^3, Z = 4). The asymmetric unit contains six crystallographically distinct Ni^{II} ions (Ni1–Ni6) each of which exhibits an octahedral coordination geometry where the four equatorial sites are occupied by ligands bpy arms and the two axial sites are occupied by a single endohedral bromide anion and single exohedral MeCN molecule (Figure 45c). The asymmetric unit of assembly C5 consists of two individual halves of $[Ni_6(L2)_8(MeCN)_6Br_6]^{30+}$ cationic cages with slightly different composition of encapsulated anions: C5–I (Ni1–Ni3) containing 3.64 bromide anions and 0.36 PF_6^- anions, and C5–II (Ni4–Ni6) containing 3.46 bromide anions and 0.54 PF_6^- anions. Beyond that only major difference is that the cationic skeleton of C5–I is less disordered than the one in C5–II.

The distances between diagonal Ni^{II} ions in C5–I are 20.543(3) Å for d_d(Ni1–Ni1'), 20.498(3) Å for d_d(Ni2–Ni2') and 19.561(5) Å for d_d(Ni3–Ni3') while in C5–II the distances are 20.486(3) Å for d_d(Ni4–Ni4'), 20.544(3) Å for d_d(Ni5–Ni5') and 19.551(5) Å for d_d(Ni6–Ni6) respectively. The distance between nearest Ni^{II} nodes was between 13.786–14.538 Å in C5–I and between 13.755–14.591 Å in C5–II. The bridging angles of bonded ligands in metal nodes were 176.5(3)° / 178.0(3)° for ∡(L–Ni1–L), 178.0(3)° / 177.4(3)° for ∡(L–Ni2–L), 177.3(5)° / 176.5(3)° for ∡(L–Ni3–L), 177.1(3)° / 173.2(2)° for ∡(L–Ni4–L), 176.5(3)° / 176.8(3)° for ∡(L–Ni5–L) and 176.8(6)° / 171.9(5)° for ∡(L–Ni6–L), presented as $(L_a–M–L_c)/(L_b–M–L_d)$. The bond distance from Ni^{II} node to endohedrally coordinated bromide anions is between 2.570–2.627 Å, and the exohedrally coordinated MeCN the bond distances vary between 2.093–2.148 Å. The bend angles of bpy arms are between 95.5–121.4 Å and encapsulated bromide anions lie 4.040–5.173 Å above the benzene ring centroid and encapsulated PF_6^- anions lie 4.399–5.462 Å above the benzene ring centroid to the phosphorus atom.

In the asymmetric unit, one of the coordinated bromide anions (Br3) in C5–I is disordered over two locations with approximate occupancies of 0.50 each (Figure 45d), and one of the encapsulated bromide anions is disordered over two positions with approximate occupancies of 0.85 and 0.15 respectively and with a separation of 0.744(15) Å. The two remaining encapsulated anions consist of PF_6^- and bromide anions disordered over the same locations with approximate occupancies of 0.82 for bromide and 0.18 for PF_6^- anions (Figure 45e) in both cases. Additionally, one of the ligands in C5–I has its benzene core, including ethyl

groups and methylene bridges, disordered over two positions with approximate occupancies of 0.50 in each case and separation of 0.682(4) Å between benzene core centroids (Figure 45f). Similarly, in C5–II one of the coordinated bromide anions (Br6) is disordered over two locations with approximate occupancies of 0.50 each and one of the encapsulated bromide anions is disordered over two positions with approximate occupancies of 0.90 and 0.10 respectively and with a separation of 0.823(18) Å. The three remaining encapsulated anions consist of PF_6^- and bromide anions disordered over the same locations with approximate occupancies of 0.85 for bromide and 0.15 for PF_6^- anions in all three cases. Additionally, one of the ligands in C5–II has its benzene core, including ethyl groups, methylene bridges and one of the +1-valent pyridine rings are disordered over two positions with approximate occupancies of 0.50 each and a separation of 0.515(3) Å between benzene core centroids (Figure 46a). Furthermore, another ligand has two of its bpy arms, two of the ethyl groups and the remaining +1-valent pyridine ring disordered over two positions with approximate occupancies of 0.50 in each case (Figure 46b). Finally, in a third ligand one of the zero-valent pyridine rings (the one bonded to Ni6) and one ethyl-group being disordered over two locations with approximate occupancies of 0.50 each (Figure 46c).

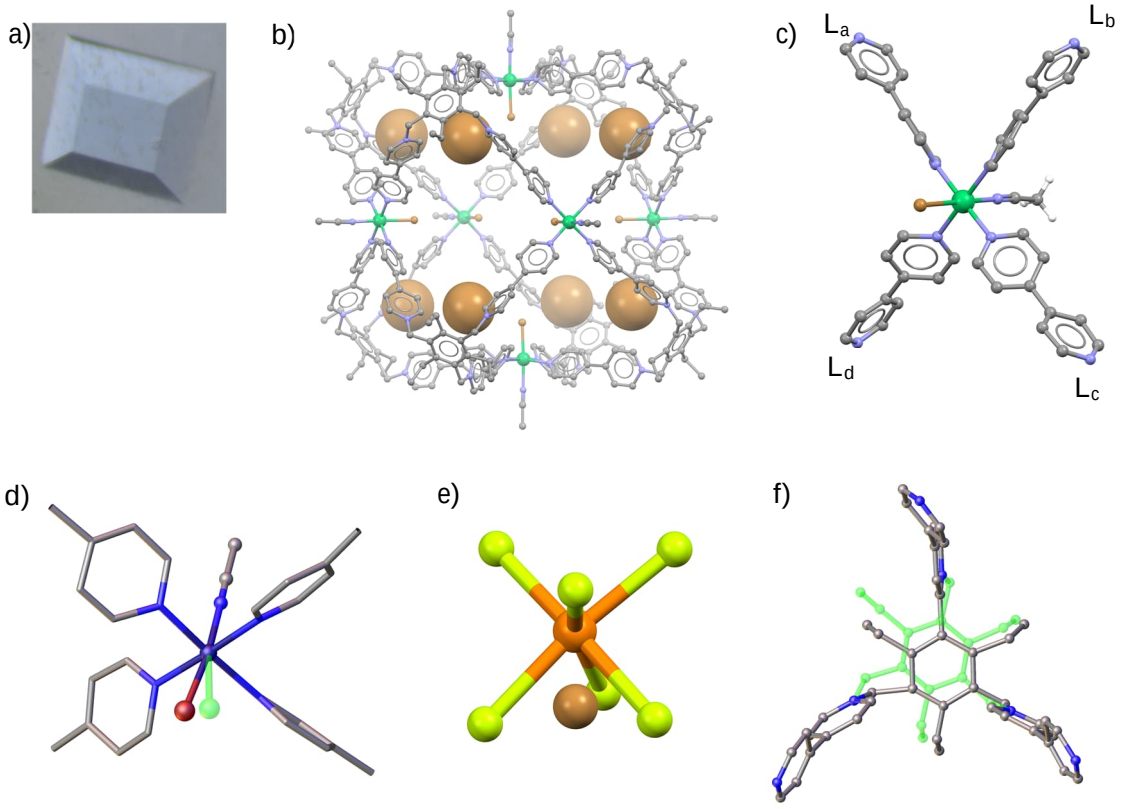

FIGURE 45 a) Crystals of C5, b) structure of C5 cage unit including endohedral bromide anions, c) metal node, disordered d) bromides in metal nodes, e) encapsulated anions, and f) ligand in C5–I. Only relevant atoms are shown.

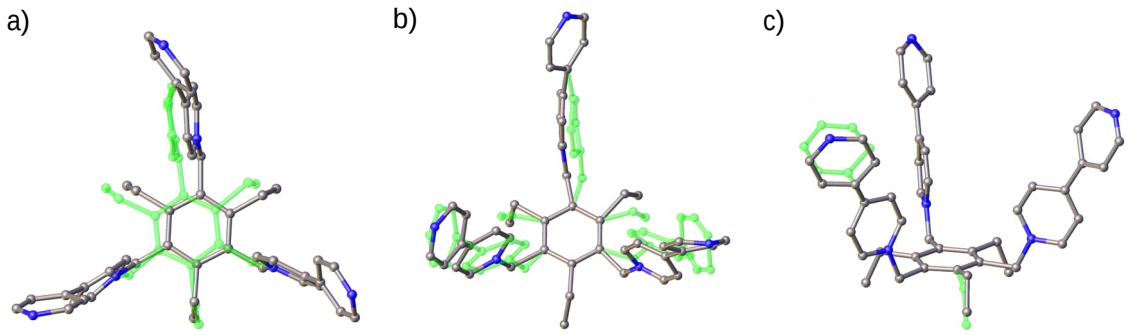

FIGURE 46 Different types of disorder present in the ligands of C5–II assembly. Only relevant atoms are shown.

Out of the required 36 counter anions, 31.25 could be assigned (13.1x Br^- and 18.15x PF_6^-), with no exohedral bromide anions observed. The missing 4.75 anions are thus most likely consisting of highly disordered PF_6^- anions residing among the large volume of disordered endo- and exohedral solvent molecules with overall 28.5 % of unit cell volume consists of disordered molecules based on voids calculated in Mercury (Figure 47a).

In the crystal lattice, individual C5 cage units are following the FCC packing model, similarly to assemblies C2–C4 (Figure 47b-c). Each of the C5 cage units are orientated in the same direction with Ni3 and Ni6 nodes laying parallel with the crystallographic *b*-axis while Ni1, Ni2, Ni4 and Ni5 nodes are laying parallel to *ac*-plane. The exohedral MeCN bonded to Ni3 and Ni6 nodes are surrounded by PF_6^- anions with the distance between 3.795–5.02 Å from CH_3-group in MeCN molecule to phosphorus atom in PF_6^- (Figure 47d). Furthermore, Ni^{II} nodes Ni1, Ni2, Ni4 and Ni5 come near to their symmetry twins, with distances of 11.827(3) Å for Ni1, 11.788(3) Å for Ni2, 11.783(3) Å for Ni4, and 11.841(3) Å for Ni5, with MeCN molecules exohedrally bonded to these Ni^{II} nodes come to a distance of 8.89(2) Å for Ni1, 8.80(4) Å for Ni2, 8.86(2) Å for Ni4 and 8.877(19) Å for Ni5. Similarly, to C1 and C3*, this leaves enough room for one PF_6^- anion to reside (in a special position) between two C5 cage units along the Ni1–Ni2 or Ni4–Ni5 planes as shown in Figure 47e-f. Crystallographic data for single crystal X-ray measurement of C5 is presented in Appendix 9 Table A9.

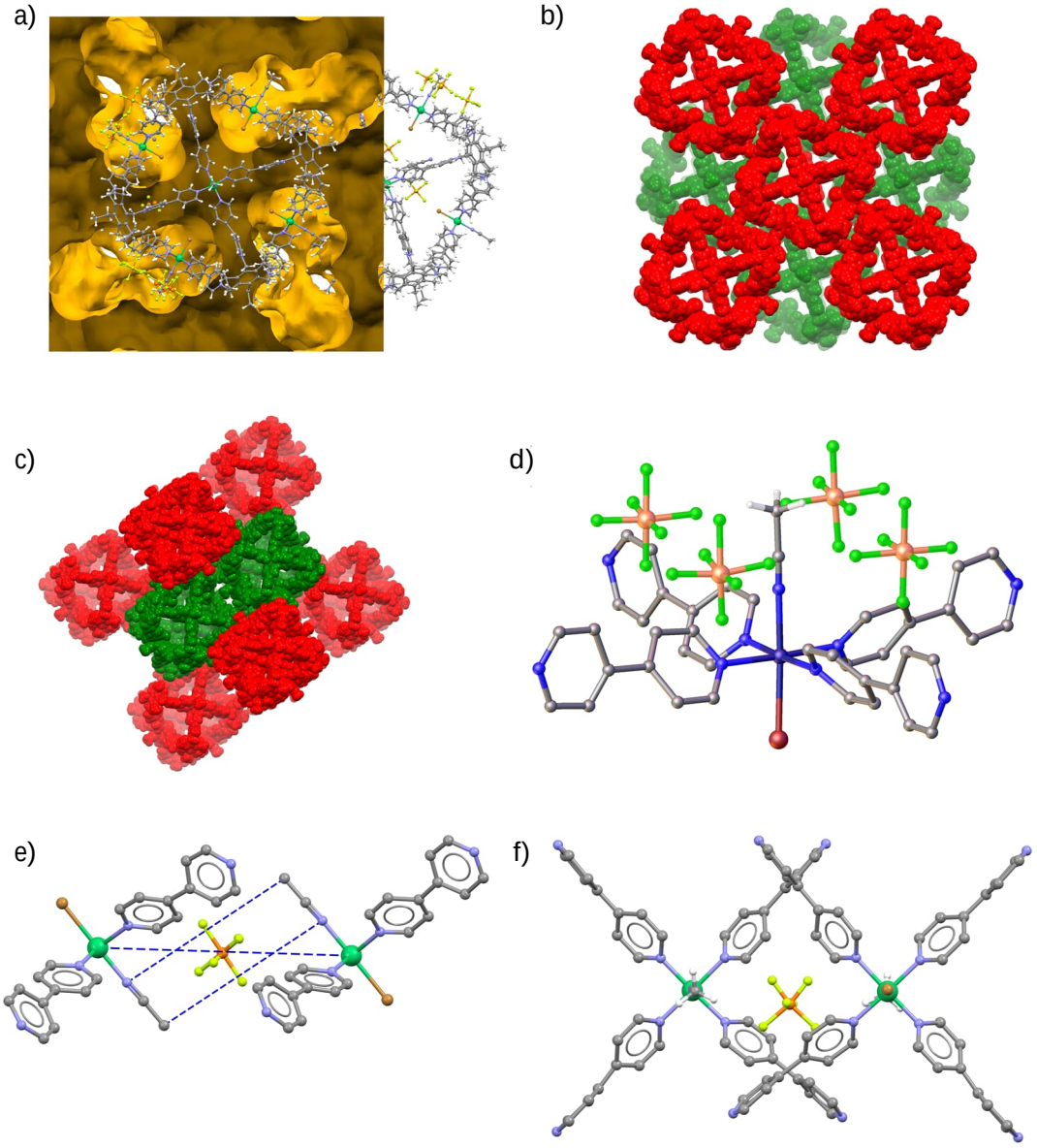

FIGURE 47 a) Solvent accessible surface in the unit cell of C5, packing of C5 cage units viewed along the crystallographic b) b-axis, c) (101) lattice plane, d) PF_6^- anions near Ni3 and Ni6 metal nodes, and e-f) PF_6^- anions between C5 cage units. Only relevant atoms are shown.

6.2.7 $[Ni_6(L2)_8(NCS)_{12}(MeCN)_{5.3}(PF_6)_{2.7}](PF_6)_{21.3}$ (C6)

Mixing acetonitrile solution of $(L2)\cdot(PF_6)_3$ and ethanol solution of $Ni(SCN)_2$ in a 4:3 ratio followed by slow vapor diffusion of ethyl acetate yields blue crystals (Figure 48a) and the X-ray diffraction analysis of crystals revealed a $[Ni_6(L2)_8(NCS)_{12}(MeCN)_{5.3}(PF_6)_{2.7}](PF_6)_{21.3}$ (C6) cube-like structure (Figure 48b) exhibiting in a triclinic space group $P\bar{1}$ (a = 27.88784(5) Å, b = 27.9602(8) Å, c = 29.0693(7) Å, α = 62.560(3)°, β = 70.3815(19)°, γ = 77.8548(19)°, V = 18 900.3(9) Å^3, Z = 1). The symmetric unit contains one-half of the C6 cage unit with three crystallographically distinct Ni^{II} ions (Ni1, Ni2 and Ni3) each of which exhibits an octahedral coordination geometry where the four equatorial sites are occupied by ligands bpy arms and the two axial sites are occupied by thiocyanate anions (Figure 48c), with bond lengths varying between 2.045–2.077 Å. The distances between diagonal Ni^{II} ions are 20.4320(17) Å for d_d(Ni1–Ni1'), 20.0324(17) Å for d_d(Ni2–Ni2'), and 21.3767(17) Å for d_d(Ni3–Ni3') respectively, while the distance between nearest Ni^{II} nodes are between 13.869–15.388 Å. The bridging angles between coordinated ligands are 177.86(11)° / 177.37(14)° for ∡(L–Ni1–L), 174.71(14)° / 178.66(14)° for ∡(L–Ni2–L) and 179.24(12)° / 178.22(14)° for ∡(L–Ni3–L), presented as $(L_a–M–L_c) / (L_b–M–L_d)$.

The ligands possess an all-*trans*-conformation regarding the ethyl-groups, with the bent angles of bpy arms being between of 112.8–115.5°. The 'bowls' are occupied by overlapping MeCN molecules and PF_6^- anions with approximate occupancies of 0.50:0.50, 0.80:0.20 (2x) or 0.55:0.45 ($MeCN:PF_6^-$). These molecules are highly disordered, and it was not possible to assign all of the required atoms to a satisfactory level (Figure 48d). Encapsulated MeCN lies between 3.83–4.000 Å from benzyl ring centroid to nitrogen of MeCN molecule, whereas PF_6^- anions are located between 4.965–5.628 Å from benzyl ring centroid to phosphorus of the anion. In the metal nodes, the exohedral NCS^- anions are near linear (∡(NCS): 179.0(4)°, 177.7(4)° and 178.9(3)° for Ni1, Ni2 and Ni3 respectively) while the bent angle of ∡(Ni–N–S) was 166.21(16)°, 146.32(16)° and 156.39(14)° for Ni1, Ni2 and Ni3 respectively. Contrastingly, the endohedral NCS^- anions are disordered over three orientations in such a manner that the nitrogen atom has a full occupancy, the carbon atom is disordered over two positions with 0.50 approximate occupancies each and the sulphur atom is disordered over three positions with approximate occupancies of 0.50, 0.35 and 0.15 respectively (Figure 48e). No free exo- or endohedral thiocyanate anions were observed.

No considerable disorder was observed in the M_6L_8 skeleton itself, outside single the ethyl-group being disordered over two orientations with approximate occupancies of 0.75 and 0.25 respectively (Figure 48f). All of the expected 36 anions could be assigned (12x NCS^- and 24x PF_6^-), with multiple PF_6^- anions being disordered between themselves or with solvent molecules (Figure 48g–h) and similarly several solvent molecules are disordered among themselves with varying degree of disorder (Figure 48i). Overall, 11.0 % of unit cell volume remains unmodelled according to solvent accessible surface calculated in Mercury as shown in Figure 48j.

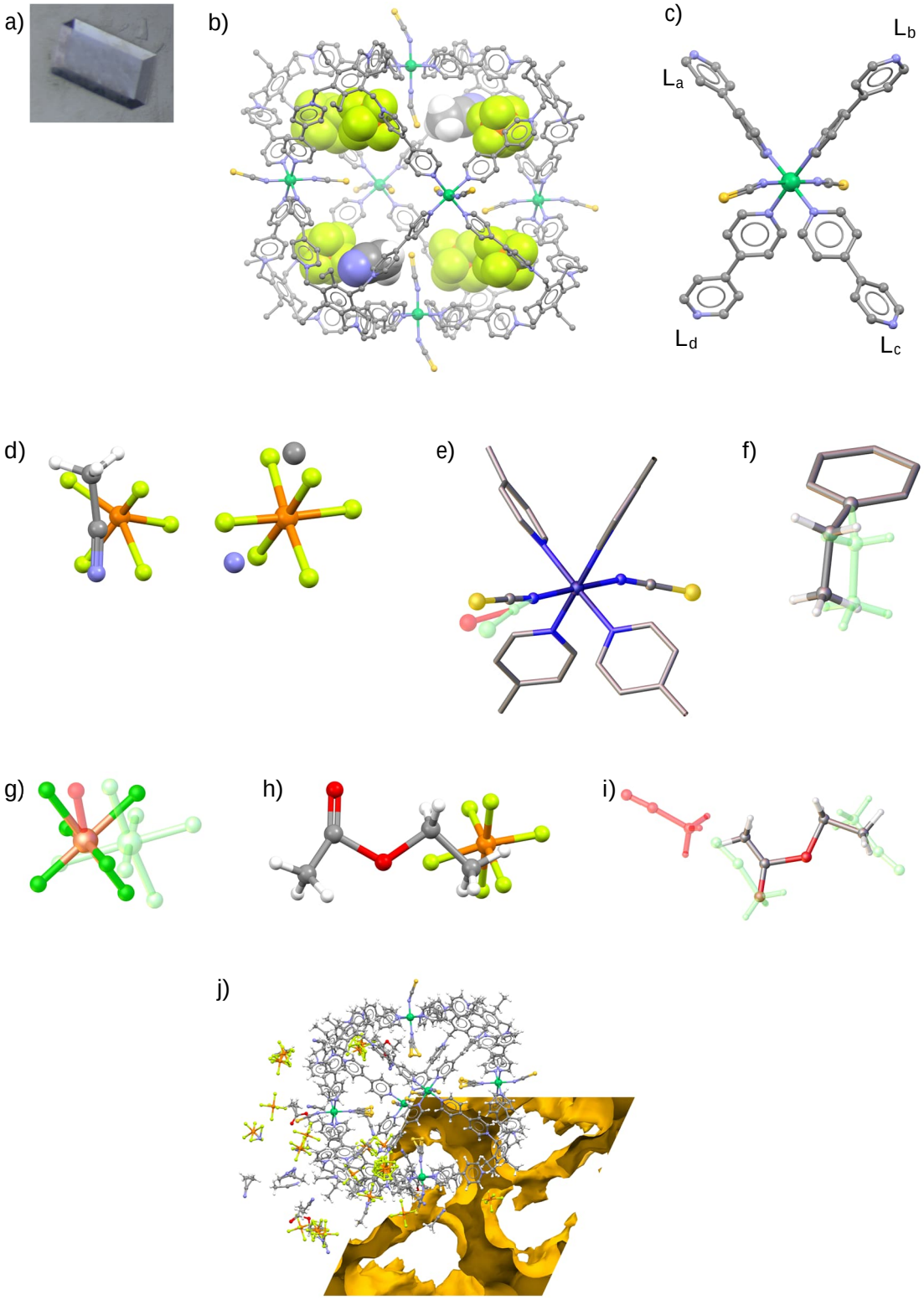

FIGURE 48 a) Crystal of C6, b) structure of C6 cage unit including encapsulated molecules, and c) metal node. Disordered nature of d) encapsulated molecules, e) thiocyanate anions, and f) ethyl-group. Examples of disorder between exohedral g) PF_6^- anions, h) anion-solvent, and i) solvent-solvent overlap, and j) solvent accessible surface in unit cell of C6. Only relevant atoms are shown.

In crystal lattice each corner of the unit cell houses one of the C6 cage units (origin lies middle of the C6 cage unit) and each cage is orientated so that the cage axis formed *via* Ni1-Ni1 is roughly parallel to the crystallographic *b*-axis and axis formed *via* Ni3-Ni3 is roughly parallel to *a*-axis. Individual C6 cage units are following the FCC packing model, similarly to assemblies C2–C5 (Figure 49a-b). Furthermore, Ni^{II} nodes Ni1 and Ni3 come near to their symmetry twins, with distances of 8.4187(14) Å for Ni1 and 7.8078(15) Å for Ni2 with exohedral NCS^- anions bonded to these Ni^{II} nodes being separated by a distance of 5.139(4) Å for Ni1 and 4.968(4) Å for Ni3, measured from sulphur atom to nitrogen atom (Figure 49c-d). Similarly to assembly C4, there is no room for PF_6^- anions to reside between Ni1 or Ni2 nodes. Crystallographic data for single crystal X-ray measurement of C6 is presented in Appendix 9 Table A9.

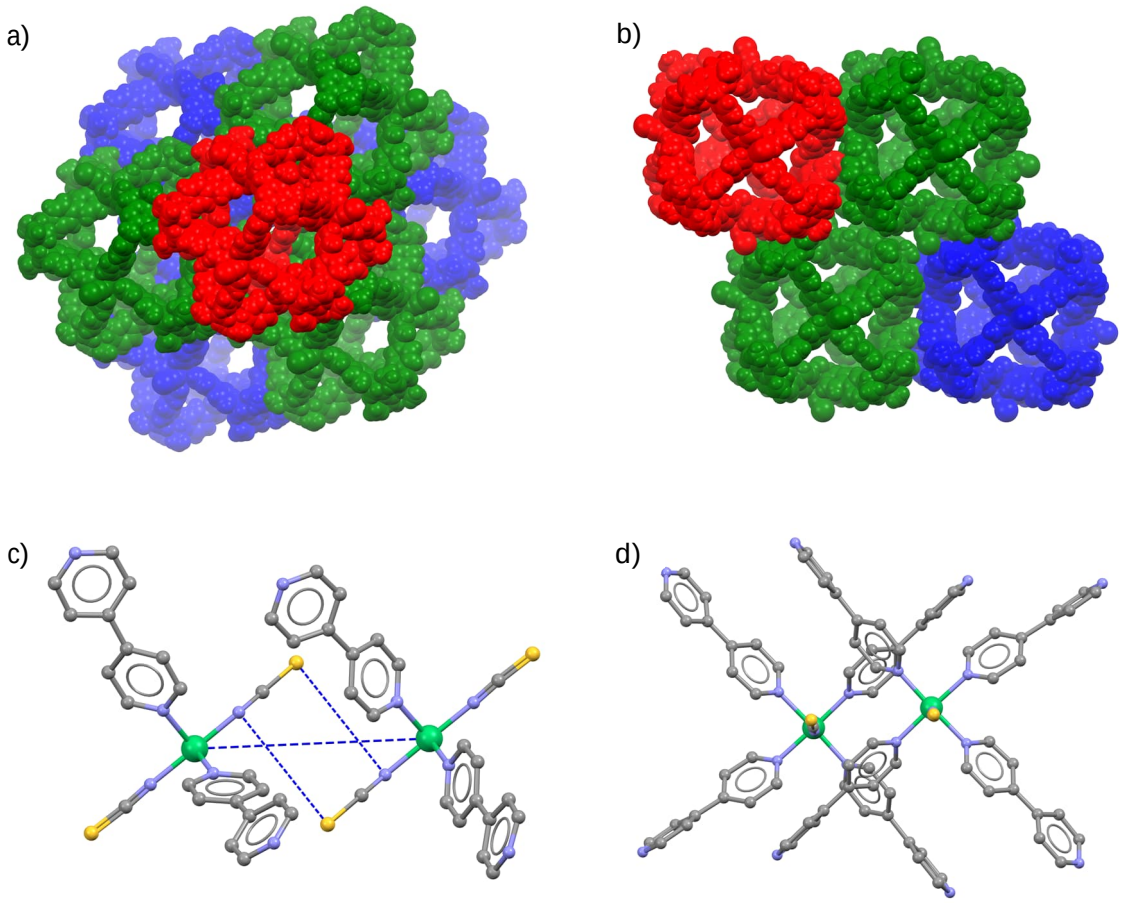

FIGURE 49 a) Unit cell packing viewed along (111) lattice plane, b) unit cell packing viewed along the crystallographic *a*-axis, and c-d) proximity of Ni1 and Ni3 metal nodes in crystal lattice. Only relevant atoms are shown.

6.2.8 $[Ni_6(L2)_8Cl_{20}](NTf_2)_{12}Cl_4$ (C7)

Mixing acetonitrile solution of $(L2)\cdot(NTf_2)_3$ and ethanol solution of anhydrous $NiCl_2$ in a 4:3 ratio followed by slow vapor diffusion of chloroform yielded green crystals and the X-ray diffraction analysis of crystals revealed a $[Ni_6(L2)_8Cl_{20}](NTf_2)_{12}Cl_4$ (C7) cube-like structure (Figure 50a) exhibiting in a trigonal space group $R\bar{3}c$ ($a = b = 31.1670(3)$ Å, $c = 124.0564(10)$ Å, $\alpha = \beta = 90°$, $\gamma = 120°$, $V = 118184.9(19)$ Å^3, $Z = 6$). The asymmetric unit contains one-sixth of the C7 cage unit with one crystallographically distinct Ni^{II} ion, Ni1, exhibiting an octahedral coordination geometry where the four equatorial sites are occupied by bpy arms of ligands, and the two axial sites are occupied by chloride anions (Figure 50b). The bond lengths of d(Ni–Cl) are 2.398(2) Å and 3.4370(18) Å for endo- and exohedral Cl^- anions with ∡(Cl1–Ni1–Cl2) being 178.92(6)°. The distance between diagonal Ni^{II} ions is 20.415(2) Å and the distance between the nearest Ni^{II} nodes varies between 13.9760–14.990 Å, while the bridging angles between bonded ligands are 175.75(19)° and 178.42(12)° for ∡(L_a–Ni1–L_c) and ∡(L_b–Ni1–L_d) respectively. The ligands possess an all-*trans*-conformation regarding the ethyl-groups, with the bent angles of bpy arms being between of 112.9–114.6°. Due to the large size of the bistriflimide anion, NTf_2^-, it does not fit well inside the bowl (see p. 86) and subsequently the bowl is occupied by chloride anion instead. The remaining charge of the cationic cage is balanced out *via* exohedral NTf_2^- and Cl^- anions which exist in 12:3.5 ratio of NTf_2^-:Cl^-, with the missing 0.5 negative charge most likely belonging to highly disordered chloride anion. Overall, the 21.5 % of the unit cell volume remains unmodelled according to solvent accessible surface calculated in Mercury as shown in Figure 50c.

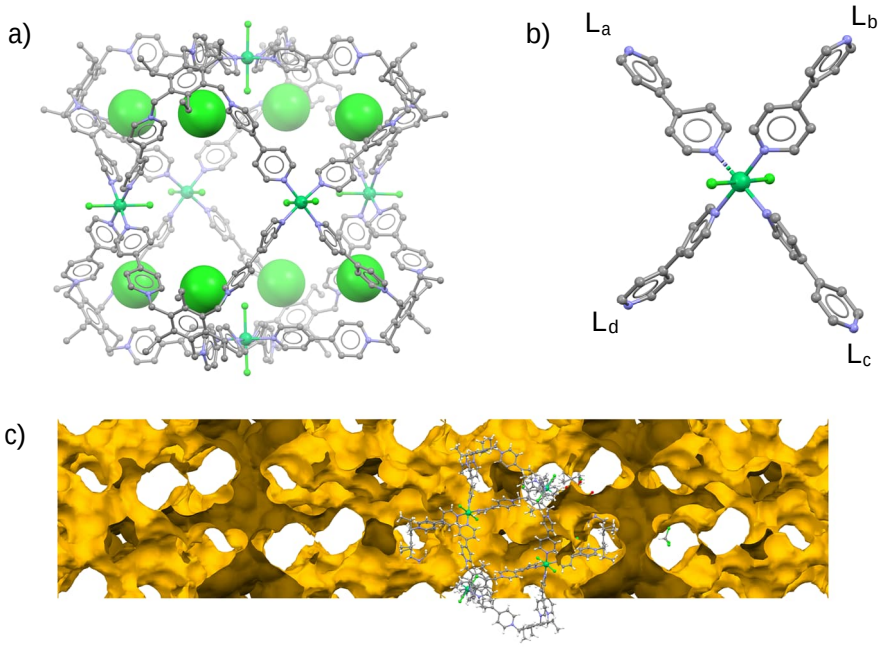

FIGURE 50 a) Structure of C7 cage unit including encapsulated anions, b) metal node, c) solvent accessible surface in unit cell of C7. Only relevant atoms are shown.

In the crystal lattice 1⅔ of NTf_2^- anions are disordered over three locations around a 3-fold rotation axis (symmetry operations –y, x–y, z and –x+y, –x, z) so that the NTF_2^- anion directly above the benzene core of a ligand has approximate occupancy of 0.333 while the two NTf_2^- anions surrounding the benzene core have approximate occupancies of 0.667 (Figure 51a). Additionally, there is one chloride anion disordered over six positions around the 3-fold rotation axis with approximate occupancies of 0.167 each (Figure 51b). One chloroform molecule laying on the 3-fold rotation axis is fulfilled by symmetry and is surrounded by three C7 cage units (Figure 51c) with a distance of 5.2532(4) Å from the benzene ring centroid to the carbon atom of chloroform. On the 3-fold rotation axis two C7 cage units are separated by a distance of 31.0794(3) Å and the space between is occupied by previously mentioned NTf_2^- anions, two $CHCl_3$ molecules, one disordered chloride ion and disordered MeCN molecule (Figure 51d).

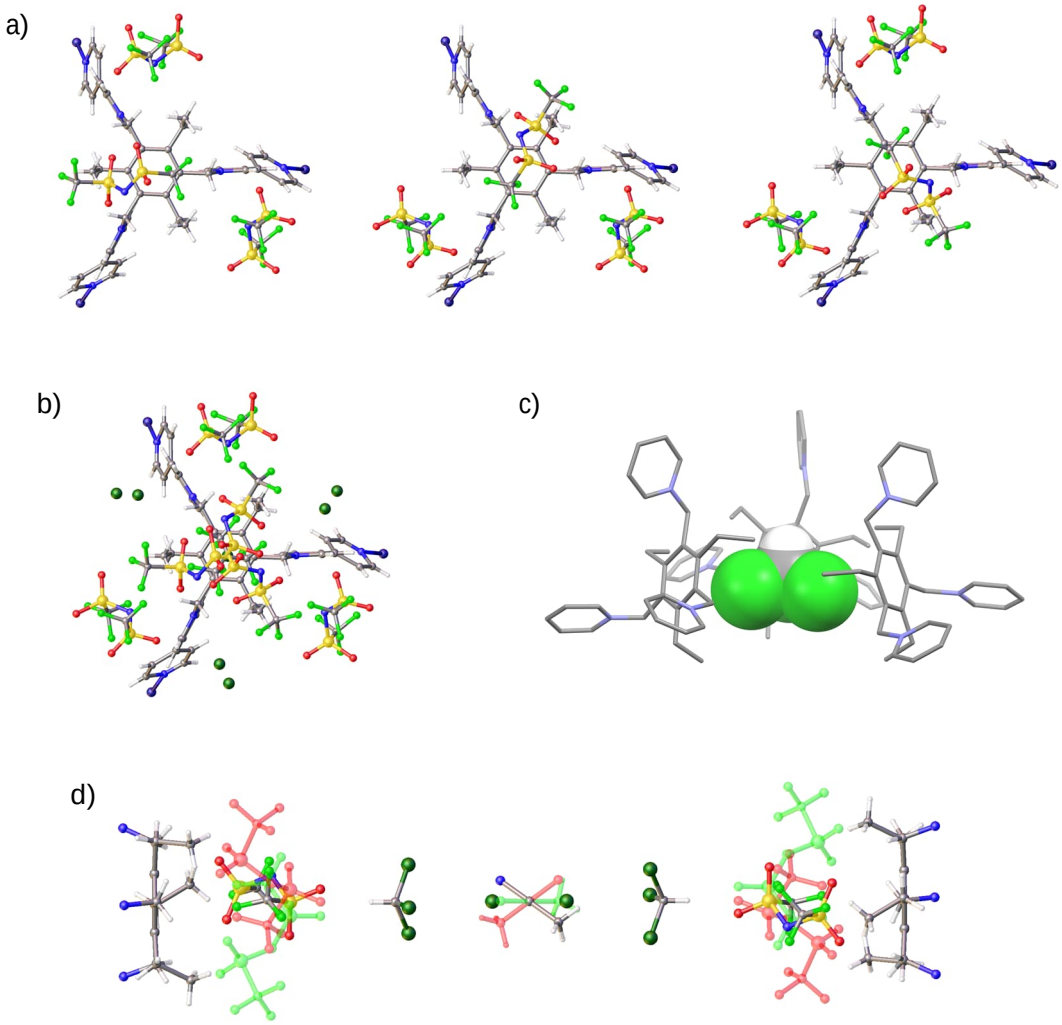

FIGURE 51 a) Three orientations of NTf_2^- anions, b) anions located around a 3-fold rotation axis, c) $CHCl_3$ molecule between C7 cage units, and d) anions and solvents between C7 cage units. Only relevant atoms are shown.

The chloride ion is disordered over two positions with approximate occupancies of 0.25 each and MeCN molecule is disordered over six orientations across a special position with approximate occupancy of 0.083 for N and CH_3 atoms while C is located in a special position with approximate occupancy of 0.50 (Figure 52a). Each zero-valent pyridine ring is disordered over two orientations with approximate occupancies of 0.50 each and torsion angles between different orientations being 73.2–98.5° (Figure 52b). Additionally, the second ligand has the CH_3 of ethyl-group disordered over two orientations with approximate occupancy of 0.50 (Figure 52c). In the crystal lattice, Ni1 metal nodes come near their symmetry twins in different C7 cage units in a similar manner to assembly C4 (Figure 52d), as on all three Ni-Ni axes have a distance between Ni1 nodes being 8.711(3) Å and the distance between chloride atoms being 5.553(2) Å. In the crystal lattice, the individual C7 cage units follow the FCC packing model, similarly to assemblies C2–C6 (Figure 53a–c). Crystallographic data for single crystal X-ray measurement of C7 is presented in Appendix 9 Table A9.

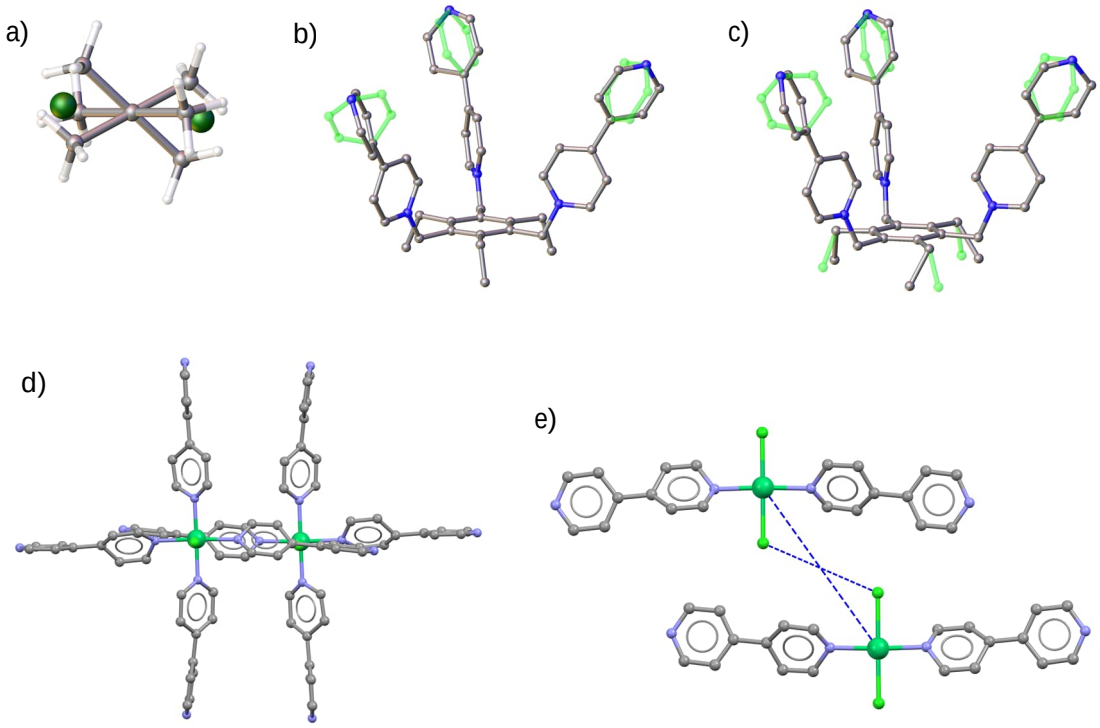

FIGURE 52 a) Disordered MeCN molecule and Cl^- anion with N and CH_3 groups fully overlapped (only CH_3 shown) due to 180° orientational disorder with itself, b-c) disordered observed in the ligands of C7 cage unit, d-e) proximity of Ni1 metal nodes in crystal lattice. Only relevant atoms are shown.

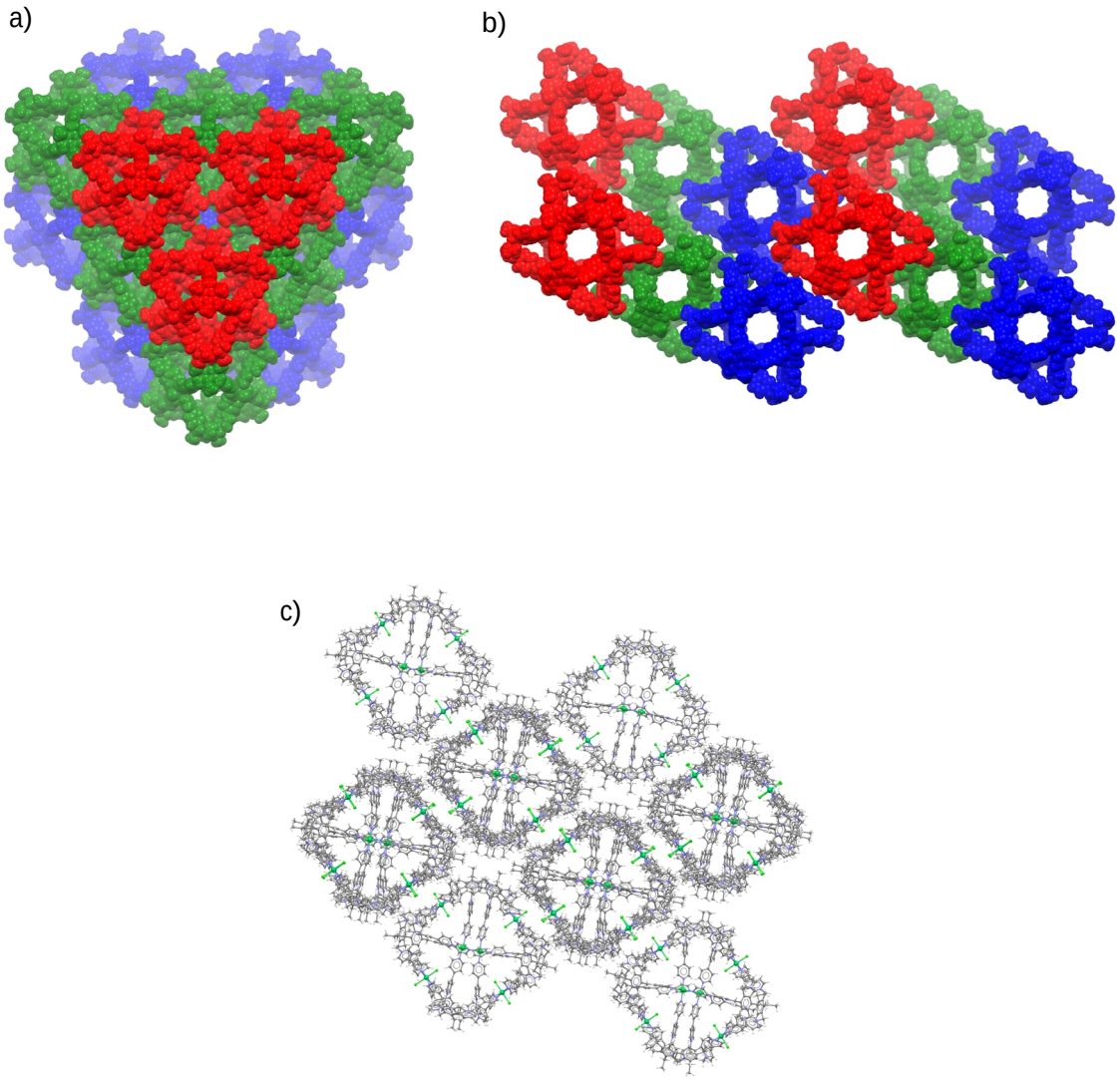

FIGURE 53 a) FCC packing in C7, b) unit cell packing viewed along the crystallographic *b*-axis, and c) unit cell packing viewed along (42$\bar{1}$) lattice plane. Only relevant atoms are shown.

6.2.9 $[Ni_6(L2)_8Br_{14}(MeCN)_6](NTf_2)_{21-n}Br_{1+n}$ (C8)

Mixing acetonitrile solution of $(L2)\cdot(NTf_2)_3$ and anhydrous ethanol solution of anhydrous $NiBr_2$ in a 4:3 ratio followed by slow vapor diffusion of ethyl acetate yields pale blue crystals and the X-ray diffraction analysis of crystals revealed a $[Ni_6(L2)_8Br_{14}(MeCN)_6](NTf_2)_{21-n}Br_{1+n}$ (C8) cube-like structure (Figure 54a) exhibiting in a monoclinic space group *C2/c* (a = 41.0344(6) Å, b = 40.4562(9) Å, c = 49.2477(8) Å, $\alpha = \gamma = 90°$, β = 100.310(2)°, V = 80 436(3) Å^3, Z = 4). The asymmetric unit consists of one-half of a C8 cage unit and contains three crystallographically distinct Ni^{II} ions (Ni1, Ni2 and Ni3) each of which exhibit an octahedral coordination geometry where the four equatorial sites are occupied by ligands bpy arms, the two axial sites are occupied by exohedral bromide anion and either endohedral MeCN molecule or bromide anion with approximate occupancies of 0.75 and 0.25 respectively (Figure 54). The distances between diagonal Ni^{II} ions are 21.263(2) Å for d_d(Ni1–Ni1'), 21.119(2) Å for d_d(Ni2–Ni2') and 20.809(2) Å for d_d(Ni3–Ni3') respectively, while the distance between the nearest Ni^{II} nodes was between 14.673–15.060 Å, the d(Ni–Br) between 2.586–2.710 Å and d(Ni–MeCN) between 1.908–1.990 Å. The bridging angles of bonded ligands in Ni^{II} metal nodes were 179.0(2)° / 178.2(2)° for ∡(L–Ni1–L), 177.8(3)° / 178.6(2)° for ∡(L–Ni2–L), and 177.52(17)° / 177.2(2)° for ∡(L–Ni3–L) respectively, presented as $(L_a–M–L_c) / (L_b–M–L_d)$.

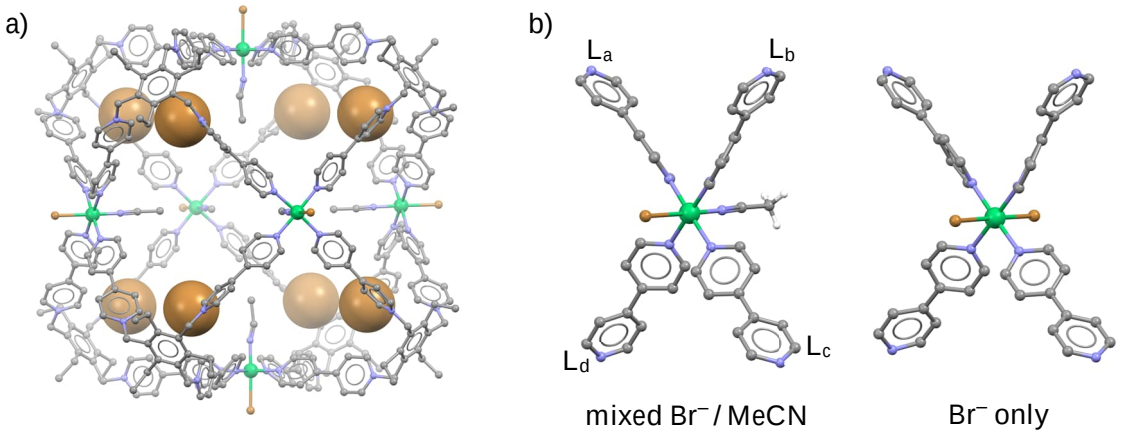

FIGURE 54 a) Structure of C8 cage unit including encapsulated Br^- anions, and b) metal nodes. Only relevant atoms are shown.

All of the ligands possess an all-*trans*-conformation regarding the ethyl-groups, with the bent angles of bpy arms being between of 113.3–115.7°, and the 'bowls' are occupied by Br^- anions laying between 4.201–4.223 Å above the benzyl ring centroid or by MeCN solvent molecules located between 3.170–3.210 Å from benzyl ring centroid to the nitrogen atom of the solvent. Out of expected 36 counter anions, a total of 24 (15x Br^- and 9x NTf_2^-), could be assigned to a satisfactory level, with one of the NTf_2^- anions being disordered to a point, where it was not possible to attain correct geometry nor to assign some of the fluorine or oxygen atoms. A single exohedral bromide anion was observed with the remaining exohedral anions consisting of NTf_2^- anions in 1:9 ratio of Br^-:NTf_2^-. The remaining 12 anions are probably a mixture of both Br and NTf_2 anions being severely disordered among the large volume of disordered free solvents (only one free MeCN molecule could be assigned with an approximate occupancy of 0.25), with overall 25.4 % of unit cell volume consists of disordered molecules based on voids calculated in Mercury (Figure 55).

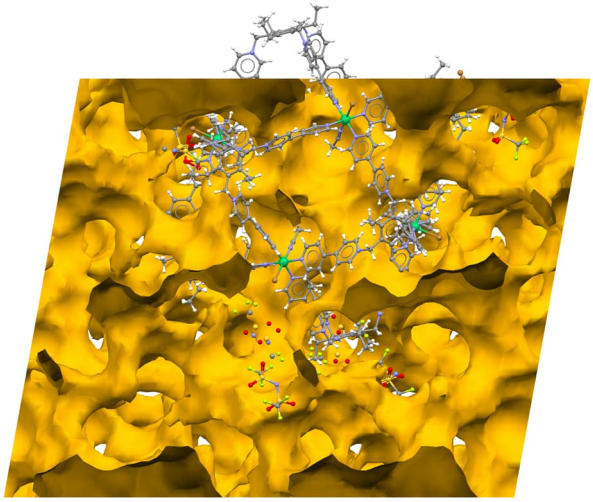

FIGURE 55 Solvent accessible surface in unit cell of C8.

In the crystal lattice, individual C8 cage units are following the FCC packing model, similarly to assemblies C2–C7 (Figure 56a-b). Each of the C8 cage units are orientated in the same direction with Ni3 laying roughly parallel with the (102) lattice plane while Ni1 and Ni2 atoms are laying roughly perpendicular with said plane. All of the Ni^{II} nodes come near their symmetry twins, with distances of 9.009(2) Å for Ni1, 8.969(2) Å for Ni2 and 11.930(3) Å for Ni3, while in the Ni1 and Ni2 nodes, the exohedrally bonded bromide anions are separated by a distance of 5.9427(14) Å for Br1 and 5.7524(16) Å for Br3 respectively (Figure 56c-d). In Ni3 node the bromide atom (Br5) comes near +1-valent pyridine ring with a distance to +1-valent nitrogen being 3.916(6) Å (Figure 56e-f). Crystallographic data for single crystal X-ray measurement of C8 is presented in Appendix 9 Table A9.

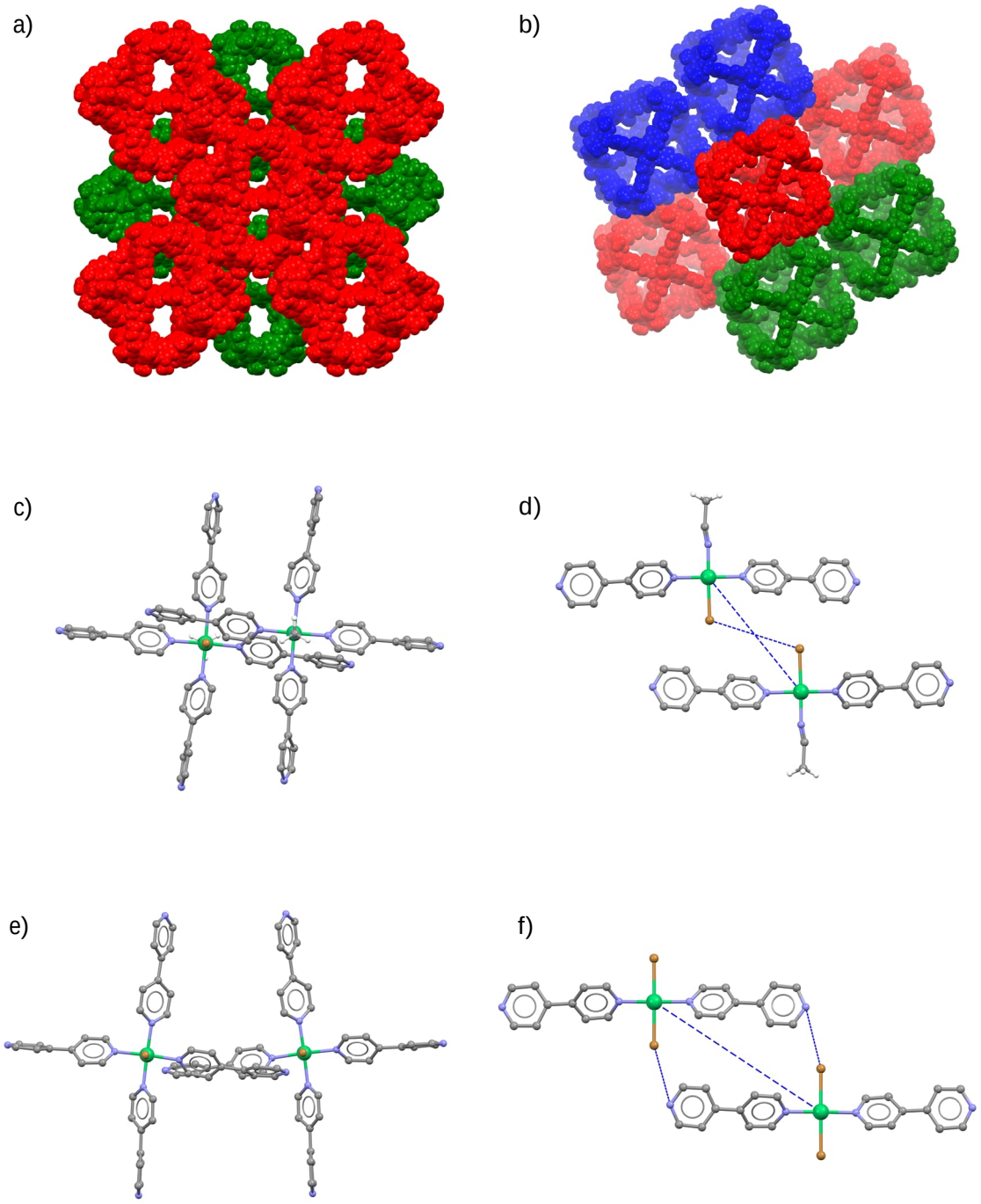

FIGURE 56 Unit cell packing viewed along the crystallographic a) *c*-axis, b) (110) lattice plane, c-d) packing near Ni1 and Ni2 nodes, and e-f) packing near Ni3 nodes. Only relevant atoms are shown.

6.2.10 $[Cu_6(L2)_8(MeCN)_{12}(PF_6)_8](PF_6)_{28}$ (C9)

Refluxing acetonitrile solution of $(L2)\cdot(PF_6)_3$ with an excess solid CuSCN overnight, followed by filtration through Celite® S and slow evaporation under 1,4-dioxane atmosphere yields blue crystals and the X-ray diffraction analysis of crystals revealed a $[Cu_6(L2)_8(MeCN)_{12}(PF_6)_8](PF_6)_{28}$ (C9) cube-like structure (Figure 57a–b). Assembly C9 exhibits in a tetragonal space group *I*4/*m* (a = 29.6094(5) Å, b = 29.6094(5) Å, c = 46.5947(10) Å, $\alpha = \beta = \gamma = 90°$, V = 40 850.3(13) Å^3, Z = 2), but due to the high level of disorder it was not possible to determine the structure to a satisfactory level, and therefore the assembly was instead determined in a monoclinic space group *I*2/*m* (a = 29.124(10) Å, b = 49.5621(13) Å, c = 29.124(10) Å, $\alpha = \gamma = 90°$, β = 90.012(3)°, V = 40851(2) Å^3, Z = 2). Interestingly, C9 possesses Cu^{II} metal nodes rather than Cu^{I}, which means that Cu^{I} must have oxidized during the reflux. Furthermore, if the reaction is done at room temperature, an $(M_1L_1)_n$ 1D-MOF is obtained (see Appendix 3) instead of M_6L_8 assembly.

The asymmetric unit of C9 contains one-fourth of the cage unit with three crystallographically distinct Cu^{II} ions (Cu1, Cu2 and Cu3) residing disordered in special positions with Cu1 and Cu2 being disordered over three positions with approximate occupancies of 0.50:0.25:0.25 respectively for both nodes, whereas Cu3 is disordered over six positions with approximate occupancies of 0.25:0.25:0.125:0.125 respectively (Cu3C and Cu3D reside in two positions fulfilled by symmetry). Each metal node exhibits an octahedral coordination geometry where the four equatorial sites are occupied by ligands bpy arms and the two axial sites are occupied by MeCN molecules (Figure 57c). The coordination bond length between Cu^{II} nodes and MeCN varies between 2.220–2.64 Å, measured from disordered metal node centroid to nitrogen of the MeCN molecule. The distances between diagonal Cu^{II} ions are 20.557(4) Å for d_d(Cu1A–Cu1A'), 21.41(2) Å for d_d(Cu1B–Cu1B'), 19.634(19) Å for d_d(Cu1C–Cu1C'), 20.599(4) Å for d_d(Cu2A–Cu2A'), 19.671(18) Å for d_d(Cu2B–Cu2B'), 21.48(2) Å for d_d(Cu2C–Cu2C'), 20.80(3) Å for d_d(Cu3A–Cu3A'), 19.05(2) Å for d_d(Cu3B–Cu3B'), 20.16(4) Å for d_d(Cu3C–Cu3C'), and 20.16(4) Å for d_d(Cu3D–Cu3D') respectively, while the distance between nearest Cu^{II} nodes was between 13.81–14.97 Å. The bridging angles between coordinated ligands in Cu1 and Cu2 nodes are 176.9(2)° for ∡(L–Cu1A–L), 157.6(6)° for ∡(L–Cu1B–L), 151.7(5)° for ∡(L–Cu1C–L), 177.1(3)° for ∡(L–Cu2A–L), 151.4(5)° for ∡(L–Cu2B–L) and 157.9(6)° for ∡(L–Cu2C–L) with no difference between $(L_a–M–L_c)$ / $(L_b–M–L_d)$, whereas in Cu3 node the bridging angles are 175.8(7)° / 173.8(8)° for ∡(L–Cu3A–L) and 165.1(9)° / 164.1(10)° for ∡(L–Cu3A–L), 147.1(8)° / 145.8(7)° for ∡(L–Cu3B–L), 169(3)° / 163(2)° for ∡(L–Cu3C–L) and 162(2)° / 166(3)° for ∡(L–Cu3D–L) presented as $(L_a–M–L_c)$ / $(L_b–M–L_d)$. All of the ligands possess an all-*trans*-conformation regarding the ethyl-groups, with the bent angles of bpy arms being between of 111.3–116.6°. The 'bowls' are occupied by PF_6^- anions with a distance between 5.207–5.216 Å from benzyl ring centroid to phosphorus of the anion.

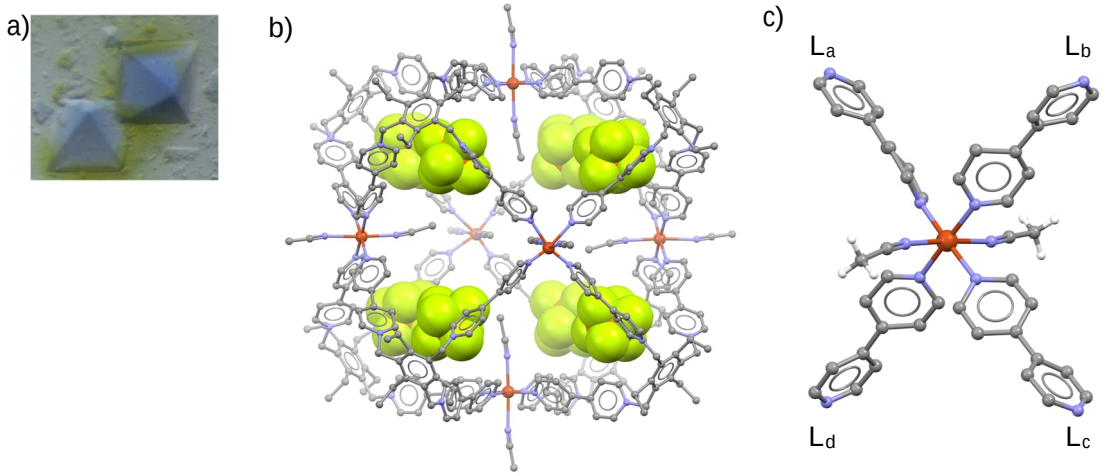

FIGURE 57 a) Crystals of C9, b) structure of C9 cage unit including encapsulated PF_6^- anions, and c) metal node. Only relevant atoms are shown.

One of the ligands has two ethyl groups and two +1-valent pyridine rings disordered over two positions, and additionally two zero-valent pyridine rings disordered over two orientations with approximate occupancies of 0.50 each. The +1-valent pyridine rings are separated by distances 0.293(8) Å and 0.556(9) Å, while the torsion angles between zero-valent pyridine rings are 111.3(4)° and 79.2(5)° (Figure 58a). Another ligand has all ethyl groups and one zero-valent pyridine ring disordered over two positions and two +1-valent pyridine rings disordered over two orientations disordered with approximate occupancies of 0.50 each. The +1-valent pyridine rings are separated by a distance of 0.336(4) Å, while the torsion angles between zero-valent pyridine rings are 65.9(3)° and 77.7(5)° (Figure 58b).

Out of the required 36 counter anions, 30 PF_6^- anions could be assigned, and only a few of the fluorides on PF_6^- anions could not be assigned due to disordered nature of exohedral anions. Furthermore, no free solvent could be assigned, which leaves 22.5 % of the unit cell unassigned (Figure 58c), according to solvent accessible voids calculated in Mercury. The missing anions are most likely disordered among the said unassigned volume and likely consist of PF_6^- anions. Interestingly no coordinated, encapsulated or free thiocyanate anions were observed in the assembly C9, and similarly, no thiocyanate anions were observed in Cu^I–MOF M1. Thus indicating that SCN^- is not preferred in Cu^{II} or Cu^I metal coordination over MeCN solvent molecules or as counter anion for ligands over PF_6^- anions, when paired with (L2)·$(PF_6)_3$ ligand, although it might be possible that very few seriously disordered SCN^- anion exists among the disordered solvent volume.

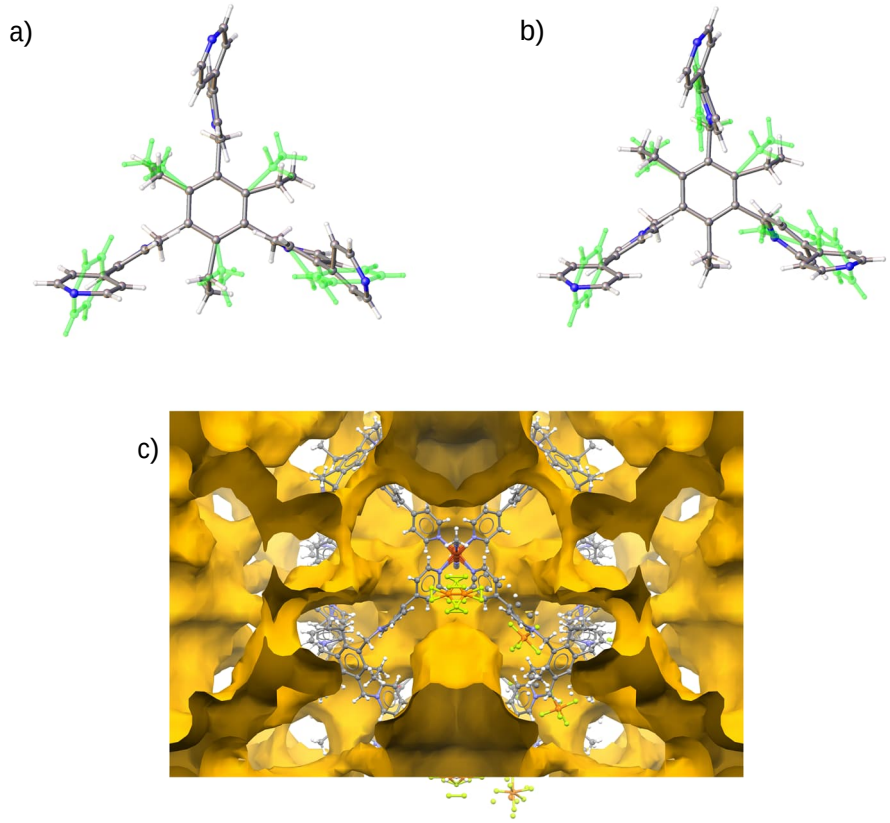

FIGURE 58 a-b) The disorder observed among ligands, and c) solvent accessible surface in unit cell of C9. Only relevant atoms are shown.

In the crystal lattice, the C9 cage unit follows the same BCC packing motif observed in C1, where one entire C9 cage unit is in the middle of the unit cell and eight C9 cage units are located in the corners of the unit cell (Figure 59a–b) with exohedral anions and free solvent molecules occupy the remaining space. Each of the C9 cage units are orientated in the same direction with Cu3 laying parallel with the *b*-axis and Cu1 and Cu2 atoms laying parallel with *ac*-plane. In the lattice, MeCN bonded to Cu3 node is surrounded by four PF_6^- anions (P3 and P4, two of each) molecules with the distance of 4.643–4.649 Å from CH_3-group in MeCN molecule to phosphorus atom in PF_6^- (Figure 59c). Furthermore, the Cu1 and Cu2 nodes come near to each other's symmetry equivalents in different C9 cage units, with separation between metal nodes being 11.952(7) Å for *d*(Cu1A–Cu1A') and 11.936(6) for *d*(Cu2A–Cu2A'), respectively. Accordingly, the distance from a nitrogen atom of MeCN molecule to carbon atom in methyl group of the opposing MeCN molecule (see Figure 59d-e) is either 8.765(16) Å or 8.92(3) Å for MeCN bonded to Cu1 and Cu2 respectively. This leaves enough room for one disordered hexafluorophosphate anion between two C9 cage units along the Cu2 plane as shown in Figure 59d-e. Crystallographic data for single crystal X-ray measurement of C9 is presented in Appendix 9 Table A9.

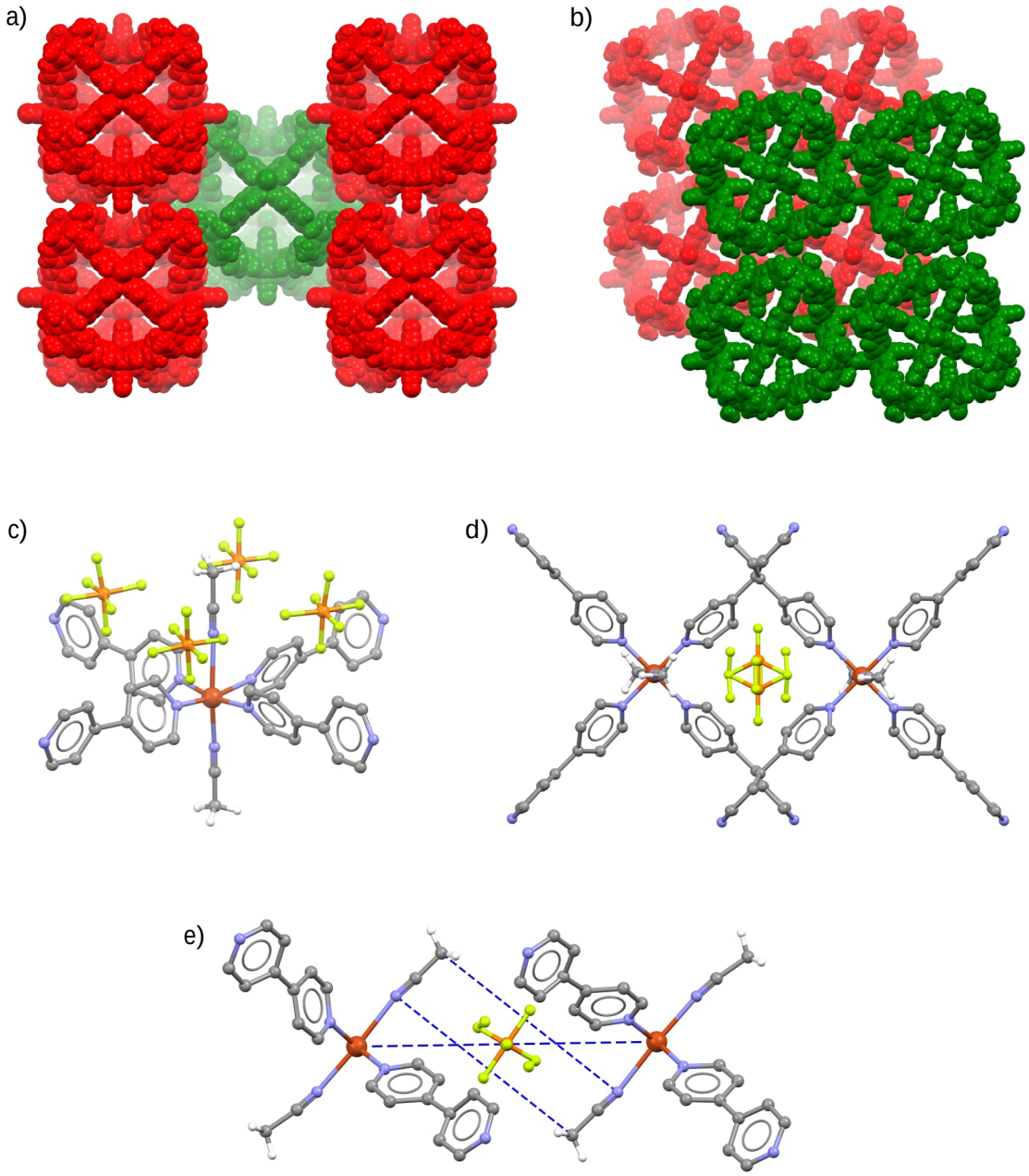

FIGURE 59 a) Unit cell packing viewed along the crystallographic *a*-axis, b) unit cell packing viewed along *b*-axis, c) PF_6^- molecules near Cu3 metal nodes and d-e) PF_6^- anions between C9 cage units. Only relevant atoms are shown.

6.2.11 Post-synthetic anion exchange studies

Assemblies C3–C8 possess the same supercationic $[Ni_6(L2)_8]^{36+}$ skeleton, with the similar skeleton also obtained with Cu^{II} (C9) or by pairing Cu^{II} with L1 (C1 and C2). Looking at assemblies C1–C9, it would seem so that the same $[M_6L_8]^{36+}$ motif is achieved regardless of counter anions of utilized metal or ligand salts with the main differences between assemblies rising from the solvent and/or anion molecules that are either coordinated to the metal node or encapsulated within the cage unit itself. With the knowledge that the $Ni(NCS)_2$ salt was prepared from $NiCl_2$ *via* anion exchange with NH_4NCS (see section 5.3.2), it might be then possible to exchange the chloride anions located in the axial binding sites of the metal node of C4 cage unit to thiocyanate anions with addition of NH_4NCS.

To test this postulation, first a 2 ml MeCN/MeOH solution of C4 with a concentration of 1.25 mmol L^{-1} was prepared and this solution was left in a closed vial for two days to maximize the formation of C4. Then a stoichiometric amount (2.284 mg, 30 μmol) of NH_4NCS dissolved in 0.5 ml of methanol was added to solution of C4. Following the addition, the green color of C4 solution turned towards greyish-green and slow vapor diffusion of $CHCl_3$ yielded blueish crystals. X-ray diffraction analysis of said crystals revealed a new compound (C10, see Appendix 4) which had both Cl^- and NCS^- anions bonded to the axial sites of the metal nodes. Thus, indicating that it would be possible to exchange, at least partially, the atoms or molecules coordinated in axial positions in the coordination sphere of Ni^{II} node. This then led to the question of whether or not it would be possible to obtain one or more compounds via a simple anion exchange, *e.g.* by first preparing compound C3*, which only has MeCN molecules in axial positions, and then adding suitable ammonium salt to exchange these to chloride, bromide or thiocyanate anions to obtain the same structural motifs as described for C4–C6 (Scheme 44).

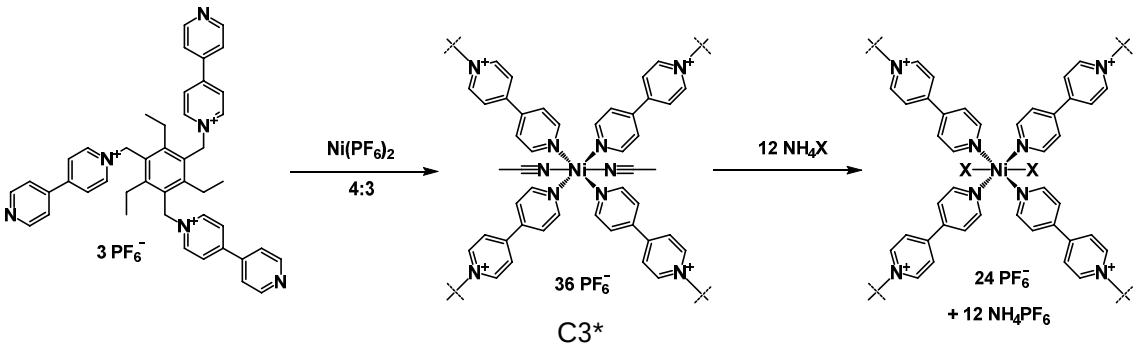

SCHEME 44 Potential post-synthetic route for modification of metal nodes in C3* cage unit. X represents halide or NCS^- anion.

To examine this possibility, three 2 ml MeCN solutions of C3* with a concentration of 1.25 mmol L^{-1} (15 μmol of Ni^{II}) were prepared and these were left in closed vials for two days to maximize the formation of C3* in solution. Next stoichiometric amounts of NH_4Cl (1.605 mg, 30 μmol), NH_4Br (2.938 mg, 30 μmol) and NH_4NCS (2.284 mg, 30 μmol) dissolved in 0.5 ml of MeOH were added respectively to three vials containing acetonitrile solution of C3*. With addition of ammonium salt solution, the lilac color of C3* solution changed almost immediately to color corresponding to that observed earlier with C4, C5 or C6 containing solutions shown in Figure 60. Crystallization of these complexation solutions yielded crystals that closely matched both visually and by unit cell determination to the characterized crystal structures of C4–6.

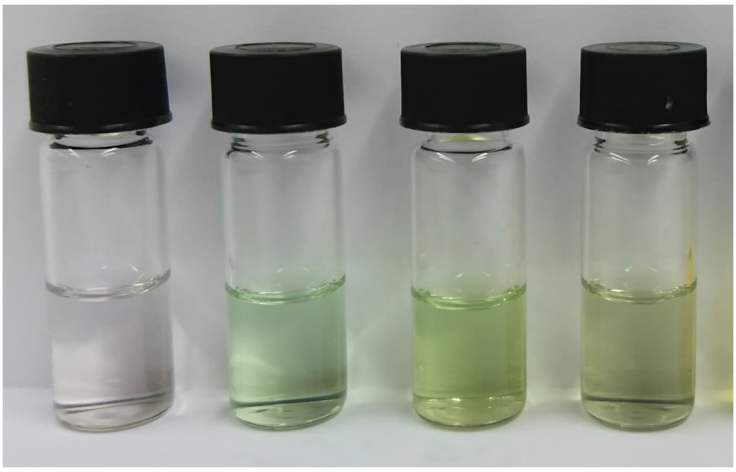

C3* C4 C5 C6

FIGURE 60 1.25 mmol L^{-1} solutions of M_6L_8 assemblies C3*–C6.

Despite the observations made it was not yet ascertained that these post-synthetically prepared ‘new’ compounds were the exact replicas of previously afforded M_6L_8 assemblies, as made by simply adding stoichiometric amounts of ammonium salts to replicate the original structures with equivalent molar ratios of respective anion types. The main issue is that despite compounds C4–C6 starting with same the metal-halide (M:X) ratios of 6:12, the ratio in single crystal structure is different; 6:16 in C4, 6:13.25 in C5 and 6:12 in C6. Additionally, the metal nodes in C4 and C6 have the composition of NiL_4X_2, while in C5 it is $NiL_4(MeCN)X$ and the bowls encapsulate X^- / PF_6^- in C4, X in C5 and MeCN / PF_6^- in C6. In principle, by extrapolating from the structures made *via* metal salt complexation (C1–C9), by varying the amount of ammonium salt added, *i.e.* adding NH_4X in 6:1, 8:1, 12:1, 14:1 or 20:1 molar ratios (NH_4X:M_6L_8), it should be possible to obtain assemblies with eight different idealized anion compositions, as shown in Table 4.

TABLE 4 Idealized cage compositions.

Type	*exo*	*endo*	bowl	Composition	Cage:X:A
1	MeCN	MeCN	A^-	$[M_6L_8(MeCN)_{12}]^{36+} \supset (8\ A^-)$	1:0:8
2	MeCN	MeCN	X^-	$[M_6L_8(MeCN)_{12}]^{36+} \supset (8\ X^-)$	1:8:0
3	MeCN	X^-	A^-	$[M_6L_8(MeCN)_6X_6]^{30+} \supset (8\ A^-)$	1:6:8
4	X^-	MeCN	A^-	$[M_6L_8(MeCN)_6X_6]^{30+} \supset (8\ A^-)$	1:6:8
5	MeCN	X^-	X^-	$[M_6L_8(MeCN)_6X_6]^{30+} \supset (8\ X^-)$	1:14:0
6	X^-	MeCN	X^-	$[M_6L_8(MeCN)_6X_6]^{30+} \supset (8\ X^-)$	1:14:0
7	X^-	X^-	A^-	$[M_6L_8X_{12}]^{24+} \supset (8\ A^-)$	1:12:8
8	X^-	X^-	X^-	$[M_6L_8X_{12}]^{24+} \supset (8\ X^-)$	1:20:0

A represents PF_6^- or ClO_4^- and X represents halide or NCS^- anion

However, the problem arises with the uncertainty of the outcome, as with addition of NH_4X, *e.g.* in a 12:1 ratio, can lead to the formation of any of the eight possible assemblies with varying yields and/or possible mixed combinations. Due to somewhat limited availability of data collection time, the relatively long crystallization time and typically a minimum of 48 hours of data recording time to achieve a single-crystal structure of M_6L_8 assemblies, it was simply not feasible to measure all the possible combinations of NH_4X with described molar ratios within the scope of this dissertation. Instead to see what effect the addition of different molar ratios of NH_4X has on the system it was decided to simplify the test by choosing a single ammonium halide salt with two different molar ratios.

Nickel iodide was originally considered one of the metal sources in creation of possible metal-organic assemblies, but due to negligible solubility to everything else but water, NiI_2 was excluded from plausible metal sources as so far no M_6L_8 assemblies could be crystallized from solutions containing water. Therefore, when deciding on which ammonium halide would be used in post-synthetic anion exchange, ammonium iodide (NH_4I) was chosen as this would potentially create new Ni_6L_8 assemblies. Two different stoichiometric amounts of NH_4I, 8:1 and 20:1, were chosen; using 8:1 would in theory yield type 2, 3 or 4 assemblies (Table 4) with excess NH_4I left behind in types 3 and 4, and 20:1 would have enough iodide to either fully replace all MeCN and PF_6^- molecules within the bowl (Type 8) or subsequently form any of the other six types containing halide anions. The 12:1 stoichiometry (Type 7), which would be equivalent of using NiI_2, was not chosen, in order to create a larger difference between the two different stoichiometric amounts used.

First two 2 ml MeCN solutions of C3* with a concentration of 1.25 mmol L^{-1} were prepared as previously mentioned and stoichiometric amounts of NH_4I in 8:1 ratio (2.899 mg, 20 μmol) and 20:1 ratio (7.247 mg, 50 μmol) were dissolved in 0.5 ml of methanol. Upon addition of colorless methanolic solution of NH_4I, the lilac color of the solution containing the assembly C3* turned into yellow (Figure 61a), and slow vapor diffusion of EtOAc yielding yellow crystals in both cases (Figure 61b-c). X-ray diffraction analysis of said crystals revealed that the two different NH_4I stoichiometries used produced assemblies with different iodide concentrations. In case of 8:1 ratio of NH_4I:C3*, the obtained assembly C11 contains 5.3 iodide atoms; 1.5 endohedrally coordinated to metal node, 2 encapsulated within the cage unit and 1.8 as free exohedral anions (see Appendix 5). Comparatively, in case of 20:1 ratio of NH_4I:C3*, the obtained assembly C12 contains 21.33 iodide atoms; 3.75 endohedrally coordinated to metal node, 4.25 encapsulated within the cage unit and 13.33 as free exohedral anions (see Appendix 6).

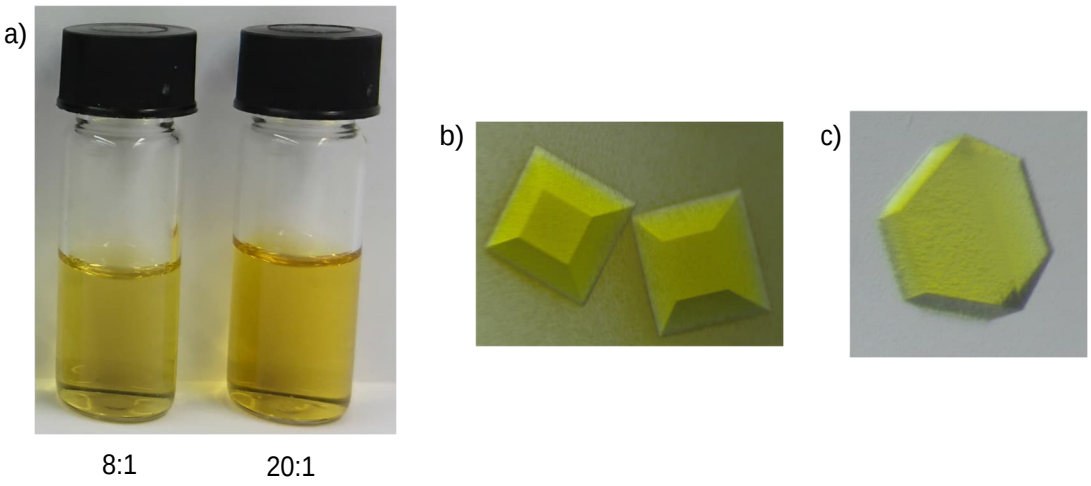

FIGURE 61 a) Solutions of assembly C3* after addition of NH_4I, b) crystals obtained from 8:1 ratio of NH_4I:C3*, and c) crystals obtained from 20:1 ratio of NH_4I:C3*.

This brief anion exchange test therefore shows the plausibility to exchange the solvent molecules filling the axial sites of the metal nodes, the anions encapsulated within the cage and / or the exohedral free anions. It also shows that simply adding the 'correct' amount of halide anions to the solution containing C3* cage unit may not produce the idealized cage composition as 8:1 (as NH_4I:C3*) addition produced an assembly (C11) with I^-:C3* ratio of 5.63:1 while 20:1 addition produced an assembly (C12) with I^-:C3* ratio of 21.33:1. More over while majority of iodide anions in C11 are endohedral, in C12 the majority of iodide anions are exohedral. Together with anion compositions of assemblies C4–C6, there seem to be different preferences whether Cl^-, Br^-, I^- or NCS^- anions are coordinated to metal nodes, encapsulated within a cage unit or remain free exohedral anions. And so, even though the aforementioned additions of NH_4I,

NH_4Br and NH_4NCS to the solution containing C3* produced crystals with same unit cells as the ones obtained using $NiCl_2$, $NiBr_2$ or $Ni(SCN)_2$, the actual anion composition might be completely different. Thus, more detailed post-synthetic anion exchange study would be necessary to conclusively determine of how controllable the introduction of anions into axial sites of metal nodes is, and how to control the exchange of the encapsulated anions.

6.2.12 ^{1}H NMR studies of C3* assembly

Lilac crystals of assembly C3* were isolated from the crystallization solution, rinsed with acetonitrile, and dried overnight under N_2-stream to obtain opaque pale blue pseudocrystals of C3*. A sample of mentioned crystals was dissolved in deuterated acetonitrile (CD_3CN) and ^{1}H NMR spectrum was measured the next day at 30 °C using Bruker Avance III 500 spectrometer and the obtained spectrum was compared to that of non-coordinated starting ligand (L2)·$(PF_6)_3$ as shown in Figure 62. The ^{1}H NMR spectra (Bruker Avance III HD 300) of a free ligand (L2)·$(PF_6)_3$ shows clear peaks reminiscent of the ones reported by Belcher *et al*.[153] together with a peak at 2.14 ppm attributed to water due to slightly wet CD_3CN solvent. Comparatively, the ^{1}H NMR spectra of C3* shows a clear change in chemical shifts related to aromatic bpy protons H_1–H_4 with the pattern of peaks indicating the presence of a single complex. The presence of residual free ligand peaks is likely due to minor decomposition of C3* during the drying process and water peak around 2.14 ppm is due to wet CD_3CN solvent. Additionally, peaks for EtOAc (H_a–H_c) are also present, with a peak for CH_3CO (H_a) overlapping with both CD_3CN residual signal and free CH_3CN signal. The spectrum of C3* shows broadening and loss of multiplicity for all peaks related to ligand L2 (H1–H7), but not with peaks related to EtOAc or free ligand, while the two peaks closest to Ni^{II} node have drastically moved downfield and appear as board low-intensity peaks around 39.1 ppm and 37.4 ppm respectively. This shift to downfield and broadening of ^{1}H signals is characteristic of six-coordinated paramagnetic Ni^{II} complexes.[159,160] Overall, this indicates that once crystalized, assembly C3* can be redissolved while attaining the $[Ni_6(L2)_8]^{36+}$ moiety in solution.

Though immediate color change occurs when ligand solution is mixed with the metal salt solution, indicating that the M_6L_8 assemblies form almost instantaneously upon mixing said solutions, it is not guaranteed that the formation of M_6L_8 is similarly instantaneously complete. To test this, ^{1}H NMR spectra were measured from *in situ* prepared sample of C3* by first dissolving (L2)·$(PF_6)_3$ and $[Ni(MeCN)_6](PF_6)_2$ individually in CD_3CN and these solutions were then mixed 5 minutes before the ^{1}H NMR measurement was performed. The measured spectrum (Figure 63) shows similar ^{1}H signal broadening and shift to downfield as observed with crystallized C3*, indicating that the formation of C3* cage unit in solution is rather quick, but not complete as the signals of free ligand are present with a larger concentration than compared to ones observed in the spectrum of crystallized C3*.

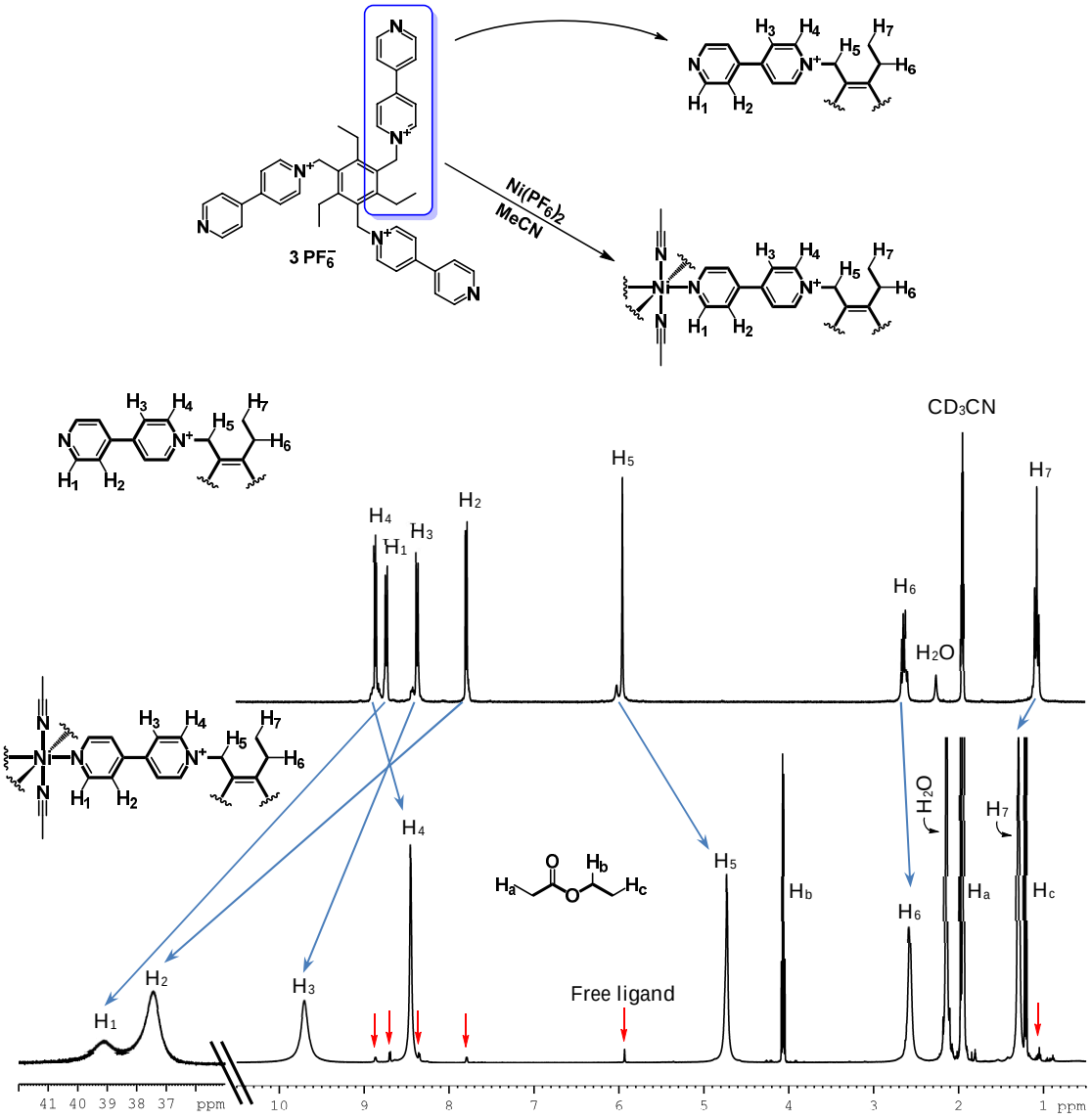

FIGURE 62 Comparison of ^{1}H NMR spectra of the free ligand (L2)·$(PF_6)_3$ (300 MHz) with complex C3* (500 MHz) in CD_3CN.

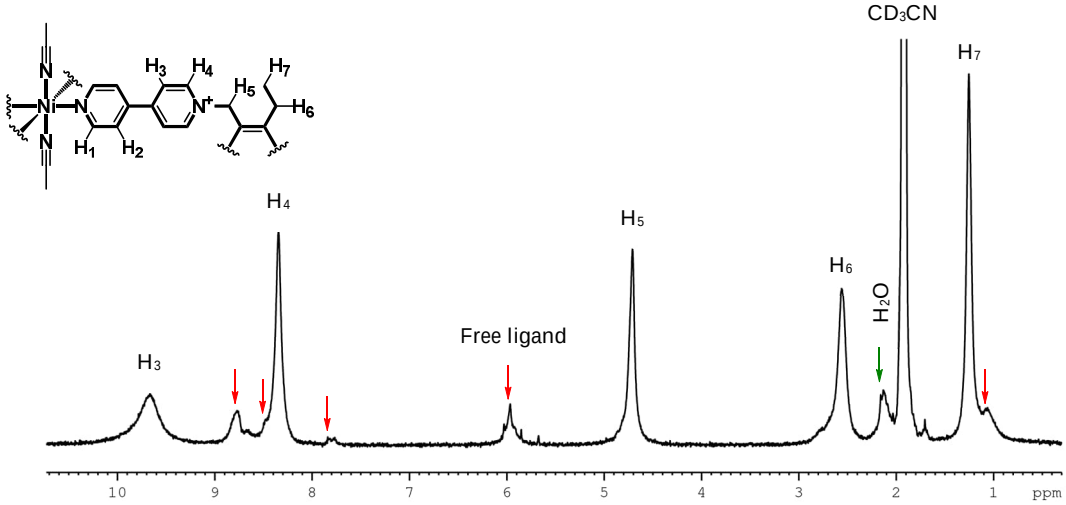

FIGURE 63 ^{1}H NMR spectrum of the *in situ* prepared complex C3* (300 MHz) in CD_3CN.

6.2.13 Summary of M_6L_8 assemblies

The aforementioned crystalline assemblies C1–C12 possess, in general, identical structural geometry regarding to the supercationic $[M_6L_8]^{36+}$, where M is either Cu^{II} or Ni^{II}, with the main physical differences being the axially coordinated solvent molecules and/or anions in the metal nodes and the composition of encapsulated anions or solvents. Each assembly possesses a *syn*-conformation regarding the bpy arms of the ligands utilized and the average bend angles of bpy arms were; C1: 113.5 ± 0.6°, C2: 114.1 ± 3.5° (*c.f.* free (L1)·$(PF_6)_3$: 113.5 ± 1.1°), C3: 113.5 ± 2.0°, C3*: 114.7 ± 1.4°, C4: 112.9 ± 3.1°, C5: 112.1 ± 5.5,° C6: 114.2 ± 0.7°, C9: 113.6 ± 2.2°, C10: 114.0 ± 1.1°, C11: 114.9 ± 2.3°, C12: 115.5 ± 6.4° (*c.f.* free (L2)·$(PF_6)_3$: 115.7°), C7: 113.5 ± 0.8° and C8: 114.4 ± 0.9° (*c.f.* free (L2)·$(NTf_2)_3$: 112.9±1.1°). Typically, two or four of the bpy arms (out of 24 total) have a larger bend angle than the rest in order to accommodate the formation of the M_6L_8 assembly. The general compositions of the obtained assemblies are described in Table 5. All attempts of using L·Br_3 as a starting ligand yielded no crystals likely due to their sparing to negligible solubility to solvents used in the crystallizations, as L·Br_3 are essentially only soluble in water and methanol. In water, no complexation occurs and even with the obtained assemblies, water causes rapid decomposition of the structures by dissolving the metal cation as an aqua ion, and in a high enough concentration, water causes the hydrophobic L·$(PF_6)_3$ or (L2)·$(NTf_2)_3$ to precipitate out of the solution. In contrast, reacting the methanolic solution of L·Br_3 with a metal salt, leads to immediate precipitation of near insoluble powder-like substance. For these reasons L·$(PF_6)_3$ or (L2)·$(NTf_2)_3$ were used in constructing obtained M_6L_8 assemblies.

TABLE 5 General composition of obtained M_6L_8 assemblies.

Name	Metal salt	Ligand	M_{ax}(endo)[a]	M_{ax}(exo)[a]	bowl[a]	exo anion(s)[a]
C1	$Cu(OTf)_2$	(L1)·$(PF_6)_3$	MeCN	MeCN	PF_6^- / MeCN	PF_6^-
C2	$Cu(ClO_4)_2$	(L1)·$(PF_6)_3$	MeCN	MeCN	ClO_4^- / MeCN	ClO_4^- / PF_6^-
C3	$Ni(NO_3)_2$	(L2)·$(PF_6)_3$	MeCN	MeCN	PF_6^-	PF_6^- / NO_3^-
C3*	$Ni(PF_6)_2$	(L2)·$(PF_6)_3$	MeCN	MeCN	PF_6^-	PF_6^-
C4	$NiCl_2$	(L2)·$(PF_6)_3$	Cl^-	Cl^-	PF_6^- / Cl^-	PF_6^- / Cl^-
C5	$NiBr_2$	(L2)·$(PF_6)_3$	Br^-	MeCN	Br^- / PF_6^-	PF_6^-
C6	$Ni(NCS)_2$	(L2)·$(PF_6)_3$	NCS^-	NCS^-	MeCN / PF_6^-	PF_6^-
C7	$NiCl_2$	(L2)·$(NTf_2)_3$	Cl^-	Cl^-	Cl^-	NTf_2^-
C8	$NiBr_2$	(L2)·$(NTf_2)_3$	Br^- / MeCN	Br^-	Br^-	NTf_2^- / Br^-
C9	CuNCS	(L2)·$(PF_6)_3$	MeCN	MeCN	PF_6^-	PF_6^-
C10	$NiCl_2$	(L2)·$(PF_6)_3$	NCS^- / Cl^-	NCS^- / Cl^-	Cl^- / PF_6^-	PF_6^- / Cl^-
C11	$Ni(PF_6)_2$	(L2)·$(PF_6)_3$	MeCN	I^-	PF_6^- / I^-	PF_6^-
C12	$Ni(PF_6)_2$	(L2)·$(PF_6)_3$	MeCN	I^-	I^- / PF_6^-	I^- / PF_6^-

[a]Major / Minor

When Cu^{II} was used as a metal node (C1 and C2) the obtained crystals were fragile and, after they were removed from the crystallization solution, would spontaneously crumble into a fine powder within a minute scale, and thus lose their single crystal nature. In fact the decomposition was visibly noticeable as a flow of solvent emerging out from crystal to Fomblin® Y oil, under which the crystals were prepared for the data collection. Interestingly in the compound C1, even though $Cu(OTf)_2$ was used in the preparation of said compound, no triflate anions were present as neither endo- or exohedral anions but instead all the determined anions comprised of PF_6^- anions. This would suggest that PF_6^- is preferred counter anion over triflate both in- and outside the cage. Therefore the formation of the C1 assembly has PF_6^- as a limiting factor controlling the yield depending on the amount of (L1)·$(PF_6)_3$ available. The opposite occurs when $Cu(ClO_4)_2$ is used as the majority of the counter anions appeared to be perchlorates, which then causes the formation of C2 thus be dependent on the amount of $Cu(ClO_4)_2$ present. ClO_4^- is seemingly also preferred over PF_6^- as an endohedral anion. Albeit, why only ¾ of ligand bowls are occupied by anions and the ¼ by a MeCN molecule remains a mystery, as there should be no steric or chemical hindrances forcing the ¼ of the bowls to be left without an anion. The C1 is clearly compressed from one of its axes (18.358(3) Å vs. 24.401(2) Å) while the C2 is more symmetrical and maybe this has something to do with preferred location of the counter anions either in- or outside the cage. In order to stabilize the Cu^{II} structures, various solvent combinations were tried but none of the solvents tested improved the stability of the obtained crystals, so the starting

ligand was changed from methyl substituted core (L1) to ethyl substituted core (L2), to see whether that would 'force' the bowl to be more favorable for forming a cage structure by being preferably in *syn*-conformation. Though (L2)·$(PF_6)_3$ paired with $Cu(OTf)_2$ yielded blue crystals, these were also highly fragile and would crumble within one or two minutes, and no crystals suitable for structure analysis were obtained despite of numerous attempts.

For the above-said reasons, in further studies, the metal node was switched from Cu^{II} to Ni^{II}, as Ni^{II} seemed to form more stable octahedral assemblies than Cu^{II} did. Due to the poor solubility of $Ni(OTf)_2$ in the solvents used, $Ni(NO_3)_2$ was chosen instead, as metal ion source for the complexation reactions, due to its better solubility. Commercially available $Ni(NO_3)_2$·6 H_2O was first dehydrated to $Ni(NO_3)_2 \cdot 2.5\ H_2O$ before its use (afforded as a fine powder), in order to minimize the amount of water in the reaction. The obtained structure C3 was analogous with the previously obtained Cu^{II} assemblies, and the crystals were sturdier and had a longer lifespan outside crystallization solution than Cu^{II} assemblies. The compound C3, as described earlier is comprised of two slightly different assemblies (C3–I and C3–II, see section 6.2.3) that showed somewhat more symmetrical cage geometry than in the case of C1. Albeit $Ni(NO_3)_2$ was used in the reaction, no nitrate anions were present inside the cage, nor were they bonded to metal node itself like nitrate frequently tends to do. However, nitrate anions were located outside the cage unit as a minority while PF_6^- represents the majority of the exohedral anions. This is likely due to the physical shape of the nitrate anion as it is planar whereas PF_6^- and ClO_4^- are spherical, which makes them fit more ideally inside the bowl. A completely nitrate free C3 assembly can be obtained by first performing anion change between KPF_6 to $Ni(NO_3)_2$ to afford $Ni(PF_6)_2$. Based on the structure determination the nitrate-free assembly C3* proved to be structurally almost identical to compound C3, except for the absence of nitrate anions.

Next it was examined if it would be possible to form a M_6L_8 assembly with a metal salt without weakly or non-coordinating counter anion, thus it was decided to replace $Ni(PF_6)_2$ with nickel(II) halides. Of the available halides chloride and bromide proved to be soluble in the used solvents and were also stable enough for the reaction (NiI_2 tends to degrade over time to nickel(II) oxide and elemental iodine). It was also decided to prepare $Ni(SCN)_2$ as an alternative metal salt as it shows similar reactions like halides (NCS^- is defined as pseudohalide). Moreover, it is similar in size to MeCN molecule and provides both nitrogen and sulfur as a binding site. Anhydrous $NiCl_2$ and $Ni(SCN)_2$ mixed with (L2)·$(PF_6)_3$ both yielded compounds C4 and C6 respectively, that were similar to C3* in the sense that all the axial binding sites of node metal (endo and exo) were occupied by the same type of secondary ligands and the bowl encapsulated (predominantly) a PF_6^- anion. Since the axial positions of metal nodes are occupied by anions in case of C4 and C6, instead of MeCN molecules as in cages C1–C3*, the overall charge of the supercationic M_6L_8 assembly was reduced from 36+ to 24+, and a result number of exohedral anions is less than in C1–C3*. The ligand bowls of the cage unit in C4 is occupied by chloride and PF_6^-

anions sharing the site (one in 0.5:0.5, and two in 0.25:0.75 occupancy), except in the case of two of the ligands bowls wherein PF_6^- resides alone. The endohedral anion ratio of 6:2, in favor of PF_6^- indicates that PF_6^- is preferred over chloride. Chloride is observed also as an exohedral anion, in turn suggesting that at least some competition exists between PF_6^- and chloride anions. On the other hand, in C6 no thiocyanate anions were detected outside the metal nodes, so it can be assumed that the PF_6^- is the preferred counter anion over thiocyanate. With thiocyanate being observed only as a coordinated anion, the formation of C6 was not dependent on NCS^- anion, as the required amount of NCS^- anions for metal node is reached with metal salt alone. Furthermore, when NH_4NCS was introduced to the solution containing C4 cage unit, the chlorides residing on the axial sites of the metal node, were exchanged partially to thiocyanate anions (C10), and once again no free thiocyanate anions were observed. Thus suggesting, that PF_6^- and chloride anions are preferred free counter anions over thiocyanate, whereas thiocyanate is preferred as a coordinating anion over chloride (and MeCN solvent molecule).

Mixing anhydrous $NiBr_2$ with $(L2)\cdot(PF_6)_3$ yielded the compound C5, which had different secondary ligands bonded to axial positions of metal nodes (MeCN in exo- and Br^- in endohedral position) in addition to bromides occupying the bowls. The compound C5 is therefore the first cage unit showing asymmetrical ligand configuration on its metal node. The existence of bromide within the bowls instead of PF_6^-, suggests that bromide is preferred as an endohedral counter anion over PF_6^-. As the compound C5 has 14 bromide ions compared to 12 that were introduced with $NiBr_2$, bromide deficit likely reason why exohedral position of metal node is occupied by MeCN molecule instead of bromide, as there are seemingly no steric hindrances against both axial positions in the metal node to be occupied by bromide anion. Similar asymmetric metal nodes were obtained with the post-synthetic anion exchange studies when NH_4I was introduced to the solution of C3* producing assemblies C11 and C12, in which the endohedrally coordinated MeCN molecules were (at least partially) substituted with iodide anions (see section 6.2.11). Now this is not truly one-to-one comparison as the compound C11 only has, on average, 1.5 iodide anions coordinated to metal nodes, and C12 has 3.75 iodide anions coordinated to metal nodes. Additionally, both PF_6^- and iodide are occupying the bowls, often sharing the site instead of only encapsulating either one of the anions.

To examine what effect a larger counter anion may have on forming the M_6L_8 cage unit, $(L2)\cdot(NTf_2)_3$ was reacted with anhydrous $NiCl_2$ and $NiBr_2$. Two slightly different compounds were formed: C7 wherein both axial sites as well as ligand bowls are occupied by chlorides, and C8 which possesses partially asymmetrical metal nodes while ligand bowls are encapsulating bromides. Interestingly, albeit the metal nodes in C8 and C5 cage units have the same composition of $NiBr(MeCN)L_4$, in C5 the bromide is coordinated endohedrally, whereas in C8 it is coordinated exohedrally to the metal node. Also, in C8 cage unit one-fourth of the metal nodes are symmetrical, wherein both axial sites are filled with bromides. Because counter anion introduced with the ligand (NTf_2^-)

is too large to fit inside the bowl, the interiors of both cages were occupied by the only alternative left; the halide anions originating from the metal salt. This shows that it is still possible to achieve M_6L_8 assembly while using a counter anion too big for the bowl, as long as there was a viable anion type present in the system which fits to the ligand bowl.

With the success of all these different Ni^{II} assemblies, it was briefly returned to Cu-based structures, but instead of using Cu^{II} salts, copper(I) thiocyanate was used in hopes to stabilize the assembly. Refluxing acetonitrile solution of $(L2)\cdot(PF_6)_3$ with the excess of solid CuSCN overnight followed by filtration and crystallization yielded a similar M_6L_8 assembly as before. Rather than the expected Cu^{I} complex, careful structural analysis revealed that the obtained compound (C9) was indeed a Cu^{II} complex. The emergence of Cu^{I}–MOF (see Appendix 3) when the same reaction was performed at room temperature further indicates that a redox-reaction must have occurred during the reflux. Furthermore, the crystals of C9 were far more stable than the other Cu^{II} based cage structures (C1 and C2) and in fact the crystals were stable for days outside crystallization solvent. Crystals previously obtained from pairing $(L2)\cdot(PF_6)_3$ with Cu^{II} OTf^-, NO_3^- or ClO_4^-, were similarly fragile to crystals of C1 and C2, so it is possible that (even though not present in the structure) SCN^- 'guides' the cage formation towards more stable Cu^{II} assembly. This might be due to systems aversion towards the SCN^- anion, whereas there is seemingly some preference towards *e.g.* ClO_4^-, as observed with C2. This competition between PF_6^- and different anions then creates instability within crystalline Cu^{II} assemblies when paired with ligands L1 or L2.

Looking at the obtained structures it comes clear that the metal node can exhibit four different conformations regarding what is bonded to the axial sites: type A, where both sites are filled by a MeCN molecule; type B, where exohedral site is filled by a MeCN molecule and endoheral site is filled by a halide or thiocyanate anion; type C, where exohedral site is filled by a halide or thiocyanate anion and endoheral site is filled by a MeCN molecule, and finally type D, where both sites are filled by a halide or thiocyanate anions (Figure 64). According to preliminary anion exchange tests (see section 6.2.11) it proved possible to change (to a certain extent) the secondary component bonded to the axial sites of the metal nodes as well as MeCN molecules are interchangeable with halide or NCS^- anions either asymmetrically (endo- or exoheral site) or fully. To what extent this mechanism can be controlled, was not examined further in the context of this study.

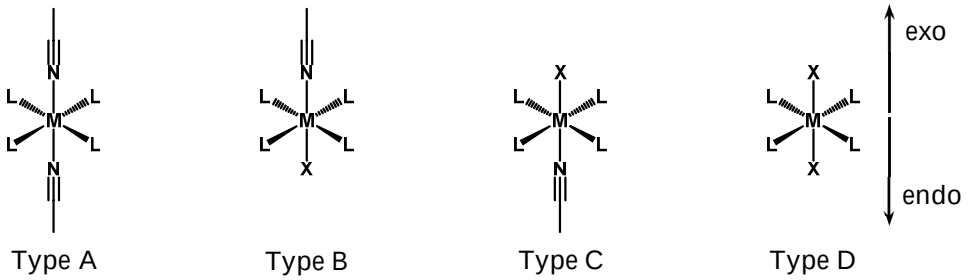

FIGURE 64 Possible conformations around M^{2+}-node, where X is a halide or thiocyanate.

The observed metal nodes are relatively rare according to the Cambridge Structural Database (CSD)[161,162], as of version 2021.3.0, there are 313 crystal structures which contain Ni^{II}–Type A, B, C or D metal nodes in combination with pyridine-ring moiety as the N-donor ligand. The number of crystal structures drops to 258 when chelating ligands are excluded and none of the reported structures contain Type B or C metal nodes. Overall, there are 3 Type A and 246 Type D (6x F^-, 26x Cl^-, 11x Br^-, 3x I^- and 209x NCS^-) Ni^{II} metal node containing structures. Comparatively, if X is defined as *any*, then the number of reported NiX_2L_4 type of structures increases to 1721. Similarly, there are 84 crystal structures, which contain Cu^{II}–Type A, B, C or D metal nodes in combination with pyridine-ring moiety as the N-donor ligand. The number of crystal structures drop to 28 when chelating ligands are excluded and none of the reported structures contain Type B or C metal nodes. Overall, there are 2 Type A and 63 Type D (12x Cl^-, 4x Br^-, 2x I^- and 7x NCS^-) Cu^{II} metal node containing structures. Comparatively, if *X* is defined as *any*, then the number of reported CuX_2L_4 type of structures increases to 1201.

The assemblies C1–C12 are relatively uniform regarding their size despite possessing different asymmetric unit cells (containing between one-eight and two-thirds of the cage unit) as shown in Table 6. This can also be observed with the packing of different assemblies, *e.g.* most aforementioned M_6L_8 assemblies, regardless of the space group they crystallize, follow some of the packing motifs of regular spheres. For example, assemblies C1, C9 and C11 follow the body-centered cubic packing model, and in fact when the unit cell packings of said assemblies are overlaid, the packings are almost indistinguishable as shown in Figure 65a. Contrastingly, assemblies C3 and C12 (like most of the obtained assemblies) follow the face centered cubic close-packing model od regular spheres, and when overlaid, the unit cell packings of C3 and C12 are a close resemblance, albeit the orientation of individual cage units are different.

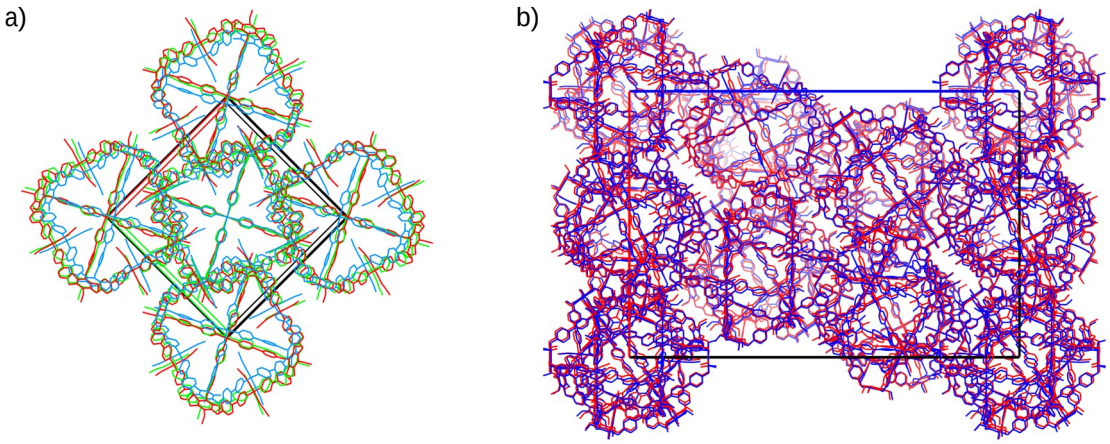

FIGURE 65 a) Overlay of unit cell packings of cage units C1 (blue), C9 (red) and C11 (green) viewed along the crystallographic *b*-axis for C1 and C11 and along –*b*-axis for C9. b) Overlay of unit cell packings of cage units C3 (red) and C12 (blue) viewed along *b*-axis.

TABLE 6 Comparison of M_6L_8 assemblies.

Name	Space group	Volume / Å^3	d_d(M–M) / Å	d(M–M) / Å	∡(L–M–L) / °
C1	*I*4/*m*	37 223.4(7)	19.039 ± 1.180	14.505 ± 1.126	174.6 ± 1.6
C2	*C*2/*c*	74 557(3)	20.719 ± 0.981	14.673 ± 0.552	175.8 ± 2.9
C3	$R\bar{3}$	224 244(12)	20.896 ± 0.731	14.865 ± 0.608	171.6 ± 9.5
C3*	*C*2/*c*	77 958(4)	20.226 ± 0.642	14.300 ± 0.472	177.8 ± 0.4
C4	*C*2/*c*	72 371(3)	20.806 ± 0.853	14.628 ± 0.535	171.2 ± 4.2
C5	*P*2/*n*	78 871(2)	20.197 ± 0.497	14.275 ± 0.322	175.6 ± 2.6
C6	$P\bar{1}$	18 900.3(9)	20.232 ± 0.283	14.659 ± 0.564	177.7 ± 1.6
C7	$R\bar{3}c$	118 185(10)	20.415 ± 0.000	14.430 ± 0.480	177.1 ± 1.9
C8	*C*2/*c*	80 436(3)	21.064 ± 0.232	14.895 ± 0.136	178.0 ± 0.7
C9	*I*2/*m*	40 851(2)	20.352 ± 0.778	14.402 ± 0.320	162.4 ± 8.9
C10	$P\bar{1}$	20 323.9(7)	20.716 ± 0339	14.647 ± 0.266	178.3 ± 0.8
C11	*I*4/*m*	38 948.1(19)	20.899 ± 0.749	14.600 ± 0.219	170.2 ± 7.5
C12	$R\bar{3}$	227 364(12)	20.259 ± 0.643	14.671 ± 0.418	175.4 ± 1.6

Measured values are reported as average and standard deviation

One of the common features of all of these M_6L_8 assemblies is their large interior cavity and according to structures obtained by single crystal X-ray diffraction this cavity is seemingly empty; beyond the anions and solvents bonded to endohedral positions and those occupying within the bowls, there is seemingly nothing inside the cage. Obviously, it is not completely empty as it would be an impossibility but crystallographically speaking these cages are empty as there are no distinct electron density maximums that can be assigned reliably to any atom or groups of atoms forming sensible molecules. To a lesser extent similar issue occurs also outside the cage, as some of the structures are 'missing' anions balancing out the supercationic M_6L_8 cage. Also, most of the solvent molecules are similarly 'missing' even though according to thermogravimetrical data, these structures contain anywhere from 10 to 30 % solvent by weight. Depending on the structure the cage interior is more or less negatively charged due to the large number of anions encapsulated in the bowls and those bonded to endohedral positions, so it is unlikely that the missing anions would lie inside the cage. The interior of the cage is most likely filled with free solvent molecules that is severely disordered throughout the interior void. Essentially with the equipment and time available it was not possible to obtain high-quality structural data that would determine the location of missing anions, and even if there would have been, it is entirely possible that the missing anions are simply so disordered among the solvent volume that their exact locations will remain uncertain regardless of equipment of measurement parameters. As an interesting comparison, unit cells of the obtained M_6L_8 assemblies are by volume larger than some small proteins *e.g.* plant protein crambin: $V \approx 16814$ Å^3 (monoclinic space group $P2_1$)[163] and on par with *e.g.* maltose-binding protein found in some bacteria: $V \approx 91737$ Å^3 (triclinic space group $P1$)[164] or $V \approx 313714$ Å^3 (trigonal space group $P3_2$)[165].

6.3 Unexpected color changes on M_6L_8 cage structures

Interestingly it was noticed that during the SCXRD measurement crystals of M_6L_8 structures had changed color to either opaque purple or red depending on the metal salt used (Figure 66). Reindexing the unit cell immediately after the data collection showed no changes in the unit cell parameters before and after the color change and thus indicating no structural changes large enough for altering the unit cell parameters occurred. The corresponding color change was not observed during the SCXRD measurements of pure ligands $L{\cdot}Br_3$, $L{\cdot}(PF_6)_3$, or $(L2){\cdot}(NTf_2)_3$, though this might also be due to relatively quick measurement times compared to measuring times of M_6L_8 assemblies (1-3 hours *cf.* 48 hours) as color change with M_6L_8 crystals was not imminent but occurred slowly within several hours.

To figure out whether the color change was an effect of thermochromism or caused by the X-ray radiation, a crystal of C3* was left overnight under the cryo-stream at –153.15 °C, during which time no color change was observed, suggesting that the change is thereby induced by X-ray radiation. The use of Mo-radiation instead of Cu-radiation yielded no noticeable color change in a crystal of C3* implying that the color change is induced by the wavelenght corresponding to Cu-radiation. Due to the nature of the obtained crystals, it was not possible to perform SCXRD measurements at room temperature but removing crystals from the cryostream caused the crystals to revert to the original color within few seconds, suggesting that this state is not stable above cryogenic temperatures.

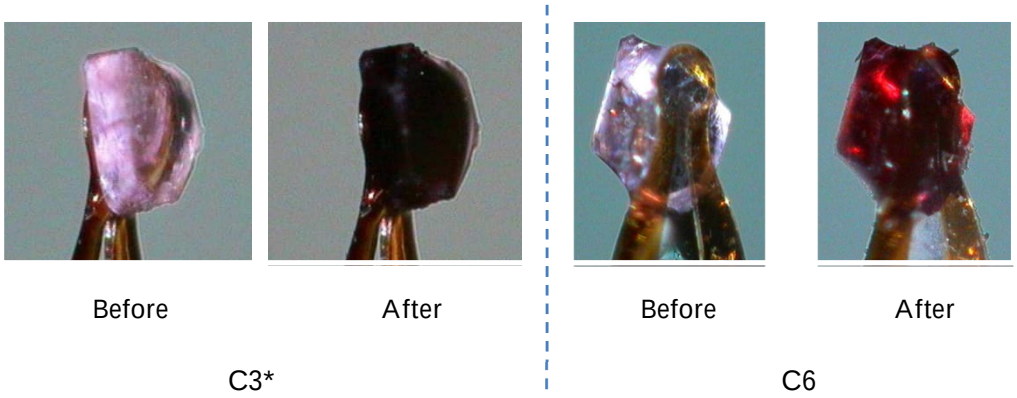

FIGURE 66 Color changes observed during SCXRD measurements.

The next step was to examine whether color change was a unique attribute of the Ni^{II}-based coordination cages. Analogous M_6L_8 structure was prepared by reacting $(L2)\cdot(PF_6)_3$ with $[Pd(MeCN)_4](BF_4)_2$ in MeCN followed by slow vapor diffusion of $CHCl_3$ which yielded small fragile colorless crystals. X-ray diffraction analysis revealed a M_6L_8 cubic cage like structure of $[Pd_6(L2)_8(BF_4)_4(PF_6)_4](PF_6)_{26-n}(BF_4)_{2+n}$ (C12, see Appendix 6) which also underwent a color change during the measurement. While the cationic cage of compound C12 is analogous to Ni^{II}-assemblies there are no axial solvent molecules or anions bonded in the metal nodes due to the square planar nature of Pd^{II} nodes. Later similar color change was observed during the SCXRD data collection on $Zn_4L_3X_7$ type of dimeric capsules (see section 6.4.), which contain tetrahedral metal nodes instead of octahedral ones. These observations further indicate that the phenomenon is not unique to Ni^{II}-compounds but is instead a property of the ligand while interacting with a metal cation.

Diquaternized bipyridine derivatives, also called viologens, are known to be able to undergo two one-electron redox reactions to afford colored radical cation, and neutral species forming a colorless dication (Scheme 45a).[166] Similarly, light irradiation can cause a charge transfer between viologen and counter anion to yield a radical cation (Scheme 45b).[167] The color of radical cation is intensive, owing to charge transfer between the +1-valent and zero-valent nitrogen atoms, whereas the color of neutral species is less intensive due to lack of aforementioned charge transfer. A similar effect can also be observed in a metal-organic donor-acceptor dyads, using metal ion with monoquaternized bpy (MQ^+) ligands, where the color change arises from low-lying metal-ligand charge transfer (MLCT) states. This involves electron transfer between *d* (M) → π^* (MQ^+) and occurs in cryogenic temperatures.[168] Although the tripodal ligands L1 and L2 are tricationic, the bpy arms of the ligands can locally be considered as MQ^+ 'ligands'. In that sense, each ligand essentially forms three M···MQ^+ types of interactions when binding to a metal node, and so the M_6L_8 assembly would contain 24 M···MQ^+ interactions.

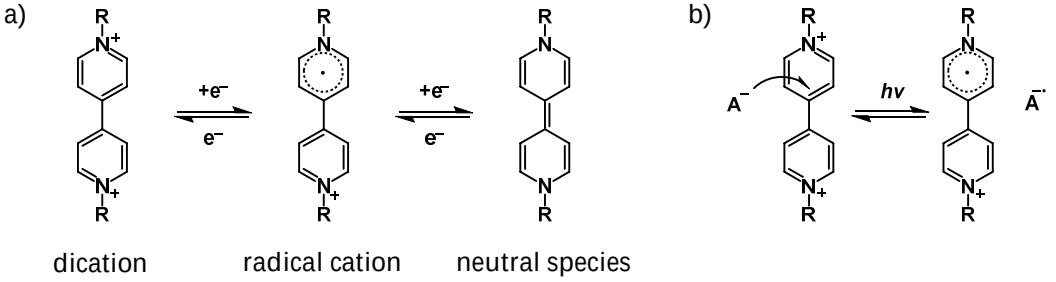

SCHEME 45 a) Viologen electrochromic redox couples, and b) photochromic cycle. R represents any type of organic substituent.

According to the CSD, the only crystal structures containing the tripodal moiety of L are the ligands originally reported by Belcher *et al*.[153] and a $[Pd_6L_8](NO_3)_{36}$ complex by Roy *et al*.[169], a structure similar to ones obtained in this dissertation, was acquired by using ligand (L1)·$(NO_3)_3$. Neither of these papers make any notion regarding the color of the crystals changing during the SCXRD measurement, which is likely due to Belcher *et al*. only reporting non-complexed ligands whereas Roy *et al*. used synchrotron radiation for structure determination. Due to a lack of time and available instruments, this phenomenon was not investigated further during this work.

6.4 Dimeric capsules

6.4.1 M_4L_3 assemblies

6.4.1.1 $[Zn_4(L2)_3Cl_7](PF_6)_{10}$ (D1)

With the successful creation of Ni_6L_8 assemblies, the metal node was switched to Zn^{II} to see whether it also could form M_6L_8 assemblies. This was first attempted by pairing $(L2)\cdot(PF_6)_3$ with $Zn(NO_3)_2$, $Zn(OTf)_2$ or $Zn(ClO_4)_2$ in various solutions, but despite several attempts in different crystallization conditions, no crystals with high enough quality for single crystal X-ray structure determination were obtained. Unit cell determinations of obtained crystals suggested that the crystallized assemblies would most likely be large structures on par with obtained Ni_6L_8 assemblies. Following this, Zn^{II} halides (Cl^-, Br^- or I^-) were paired with $(L2)\cdot(PF_6)_3$ and this gave rise to a completely unprecedented type of cage-like structures. Mixing acetonitrile solution of $(L2)\cdot(PF_6)_3$ and ethanol solution of $ZnCl_2$ in 4:3 metal-ligand ratio with one equivalent of KPF_6 present, followed by slow vapor diffusion of ethyl acetate, yielded clear needle-like crystals. X-ray diffraction analysis of these crystals revealed a tricyclic M_4L_3 complex of $[Zn_4(L2)_3Cl_7](PF_6)_{10}$ (D1) that forms dimeric capsules in crystal lattice as shown in Figure 67.

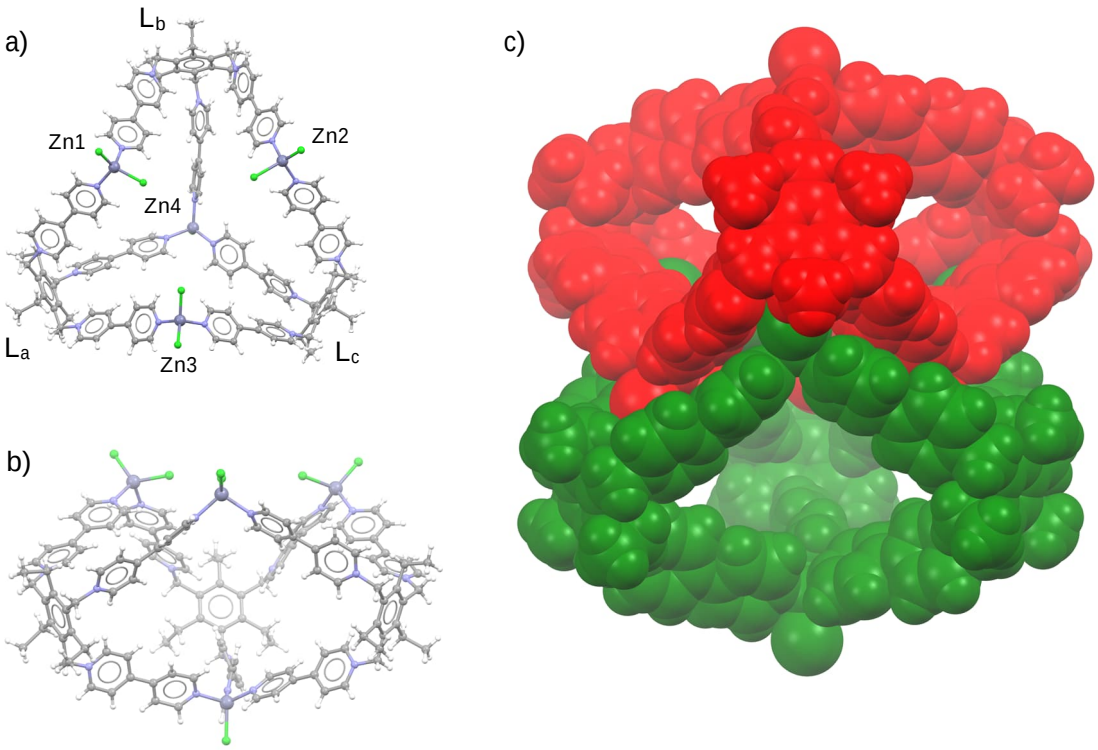

FIGURE 67 Tricyclic compound D1 and its dimeric capsule. a) Top view of monomer, b) side view of monomer and c) dimeric capsule. Free anions and solvent molecules are omitted for clarity.

Compound D1 crystallizes in triclinic space group $P\bar{1}$ (a = 22.1367(3) Å, b = 22.8679(3) Å, c = 25.2691(4) Å, α = 112.6862(13)°, β = 101.4546(13)°, γ = 90.1222(12)°, V = 11 523.1(3) Å^3, Z = 2) and each asymmetric unit holds entire $[Zn_4(L2)_3Cl_7](PF_6)_{10}$ entity together with four MeCN molecules and one ethyl acetate molecule with approximate occupancy of 0.25. Compound D1 is tricyclic and shaped like a three spiked crown with two different conformations present for Zn^{II} metal nodes: three of which Zn^{II} is bonded with two ligands and two chloride anions (type A, Zn1–3), and one Zn^{II} is bonded with three ligands and one chloride anion (type B, Zn4) as shown in Figure 68a-b. One of the ethyl groups of the ligand is disordered over three orientations between *cis*- and *trans*-conformations: two *cis*-conformations with approximate occupancies of 0.30 (C54) and 0.35 (C53), and one *anti*-conformation with approximately 0.35 (C55) occupancy (Figure 68c). Additionally in one ligand, three pyridine rings of the bpy arms are disordered over two orientations with approximately 0.50 occupancies each, and the two orientations are separated by 42.30°, 35.22° and 25.98° torsion angles between the planes of pyridine rings containing nitrogen atoms N8, N9 and N11 respectively (Figure 68d). The chloride anions bonded to metal nodes Zn1 (Cl1 and Cl2) and Zn2 (Cl3 and Cl4) are disordered over two orientations with approximately 0.50 occupancies for both metal nodes (Figure 68e). The different orientations correspond to the angle of ∡(Cl–Zn–Cl); 122.0(3)° for ∡(Cl1A–Zn1–Cl2A), 128.3(4)° for ∡(Cl1B–Zn1–Cl2B), 116.56(14)° for ∡(Cl3A–Zn2–Cl4A) and 122.93(14)° for ∡(Cl3B–Zn2–Cl4B). A molecule of ethyl acetate with approximate occupancy of 0.25 is sharing the same site with one PF_6^- anion (P5, occup. 0.50) and one MeCN solvent molecule (N167, occup. 0.75), as shown in Figure 68f. Four PF_6^- anions (P1A, P1B, P5 and P7) have occupancies of 0.50 each, with P1A and P1B being located next to each other.

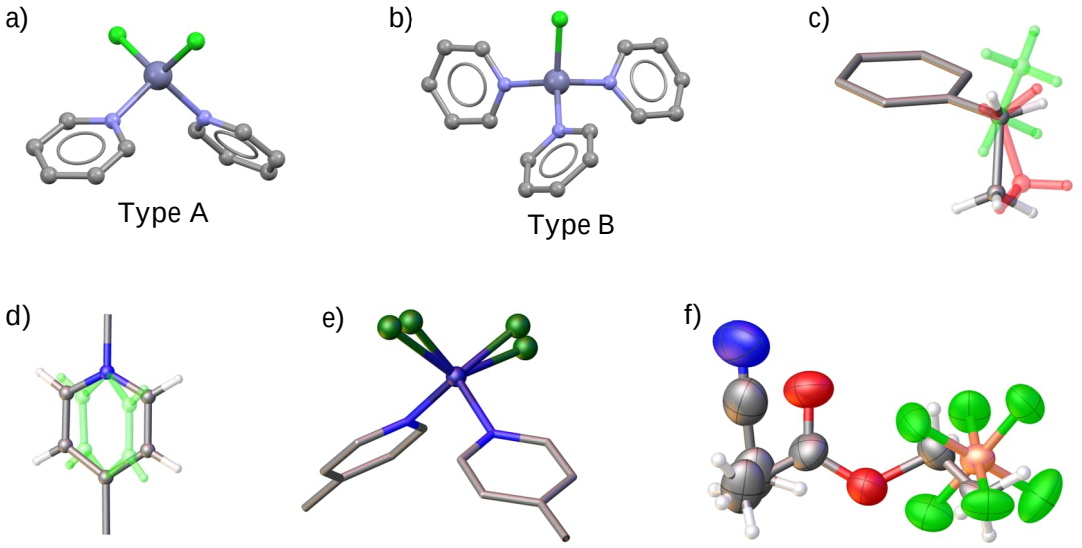

FIGURE 68 a,b) Different conformations of Zn^{II} nodes, c) disordered ethyl group, d) disordered bpy arm, e) disordered chloride anions and f) solvent-anion overlap. Only relevant atoms are shown and for d) and e) only one example is presented.

The distances between type A Zn^{II} nodes are 11.7649(11) Å for *d*(Zn1-Zn2), 13.2767(9) Å for *d*(Zn2-Zn3) and 11.6796(10) Å for *d*(Zn1-Zn3) respectively. While the distance between type A and B Zn^{II} nodes is between 14.163–14.423 Å. Moreover the distance between type B Zn^{II} ions in the formed dimer is 23.4519(12) Å. The type A Zn^{II} nodes have bridging angles of 103.66(14)° for ∡(L_a–Zn1–L_b), 106.29(13)° for ∡(L_b–Zn2–L_c) and 104.51(13)° for ∡(L_a–Zn3–L_c) respectively with the Zn–Cl distance varying between 2.025–2.356 Å. Ligands bpy arms have a bend angle between 112.28–114.54° and interestingly the bowls are occupied by MeCN molecules instead of PF_6^- anions. This can be expected to arise by the dimeric nature of this compound; in the dimeric capsule the crown 'spikes' interlock causing the outermost chloride atoms, bonded to type A Zn^{II} ions, to come close to the two of the +1-valent nitrogen atoms (3.699–4.659 Å) in the bowl. This in turn would cause major steric hindrances for type A Zn^{II} nodes, if the bowls were occupied by PF_6^- anions instead of MeCN molecules. Due to highly disordered solvent molecules inside the dimeric capsule, only one of the three encapsulated MeCN molecule was able to be assigned properly, and is located 4.318(6) Å above the centroid of the benzene ring. According to voids calculated in Mercury, 9.6 % of the unit cell volume of D1 is unassigned solvent molecules. In the dimeric capsule, the overlapping bpy arms are rotated around 120° respectively to each other with the centroid-centroid distances of overlapping pyridine rings being between 3.574–3.779 Å. In the dimeric capsule, the innermost chloride anions bonded in type A Zn^{II} nodes (*e.g.* *d*(Cl2A–Cl4A)) are separated by a distance between 5.483–6.340 Å, while the diagonal distances (*e.g.* d_d(Cl6–Cl6')) are between 8.450–12.022 Å.

In the crystal lattice type B metal nodes come near to their symmetry twin with the distance between Zn4–Zn4' being 4.6184(9) Å, Cl7–Cl7' being 3.826(2) Å and Zn4–Cl7' being 3.6148(12) Å (Figure 69a), with an inversion center located in the halfway from one Zn4 to another. Similarly, the disordered ethyl groups come near to each other with the distance between methyl-carbons (C53) being 2.51(4) Å. The dimeric capsule has a vaguely octahedral shape (when considering benzene cores of the ligands as vertices in the octahedron, Figure 69b) and the packing of compound D1 resembles the dense packing of octahedra (Figure 70a-b). Crystallographic data for single crystal X-ray measurement of D1 is presented in Appendix 10 Table A10.

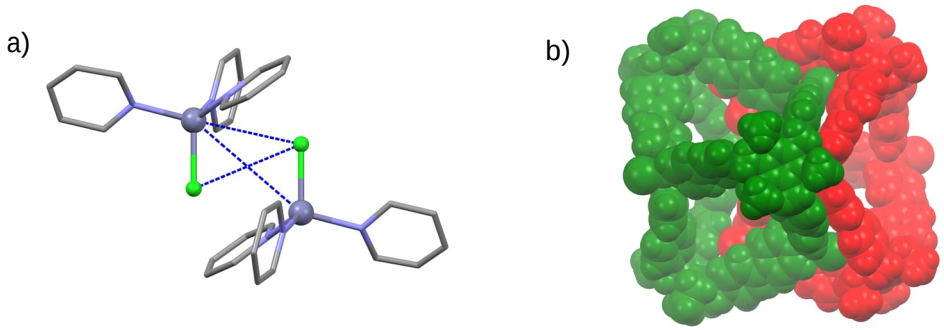

FIGURE 69 a) Close proximity of type B Zn^{II} nodes in the packing of D1, b) octahedral nature of D1 dimer, viewed along octahedral 'vertex'. Only relevant atoms are shown.

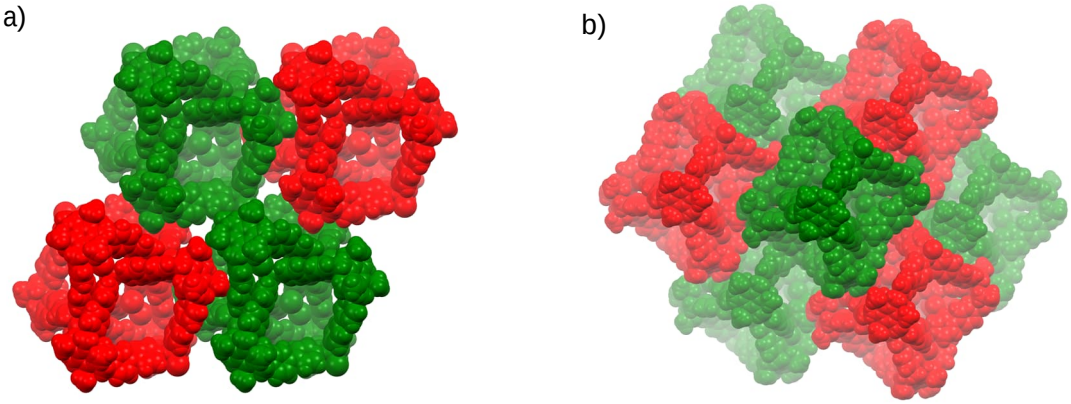

FIGURE 70 Packing of compound D1, viewed a) along the crystallographic *a*-axis and b) along (111) lattice plane. Free anions and solvents omitted for clarity.

6.4.1.2 $[Zn_4(L2)_3Br_7](PF_6)_{10}$ (D2)

Compound D2 was prepared similarly to D1 by using $ZnBr_2$ instead of $ZnCl_2$ and possesses the same topology as D1 with coordinated bromide anions instead of chloride anions (Figure 71). Compound D2 crystallizes as colorless needle-like crystals in triclinic space group $P\bar{1}$ (a = 22.4439(4) Å, b = 25.3852(5) Å, c = 26.1323(4) Å, α = 61.3103(19)°, β = 72.1709(15)°, γ = 84.7924(16)°, V = 12 405.4 Å^3, Z = 2) and each asymmetric unit holds the entire $[Zn_4(L2)_3Br_7](PF_6)_{10}$ entity together with seven MeCN molecules and two EtOAc molecule. Four of the MeCN molecules have approximate occupancies of 0.50 occupancies each, while the remaining have full occupancy and EtOAc molecules have similarly approximate occupancies of 0.50 each. Additionally, one of the PF_6^- anions (P4) is disordered over two positions with approximately 0.50

occupancies each. Furthermore, PF_6^- anions P6 and P11 have occupancies of 0.50, with P11 laying in a special position. The bromide anions bonded to metal nodes Zn1 (Br1 and Br2) and Zn2 (Br3 and Br4) are disordered over two orientations with approximate occupancies of 0.90 and 0.10 in both metal nodes. The different positions of disordered bromide anions correspond to the angle of ∡(Br–Zn–Br); 119.43(6)° for ∡(Br1A–Zn1–Br2A), 116.1(3)° for ∡(Br1B–Zn1–Br2B), 119.06(5)° for ∡(Br3A–Zn2–Br4A) and 122.3(3)° for ∡(Br3B–Zn2–Br4B) respectively. The distances between type A Zn^{II} nodes are 11.9619(10) Å for *d*(Zn1-Zn2), 11.4261(10) Å for *d*(Zn2-Zn3) and 11.3696(9) Å for *d*(Zn1-Zn3) respectively, while the distance between type A and B Zn^{II} nodes is between 14.673–16.014 Å. Moreover, the distance between type B Zn^{II} nodes in the formed dimer is 25.5650(14) Å making compound D2 slightly more elongated than compound D1.

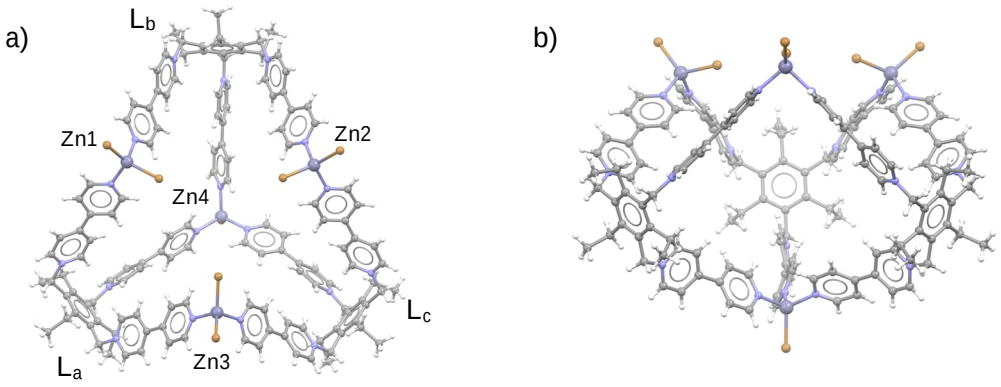

FIGURE 71 Tricyclic compound D2. a) Top view of monomer and b) side view of monomer. Free anions and solvent molecules are omitted for clarity.

The type A Zn^{II} nodes have bridging angles of 104.95(13)° (L_a–Zn1–L_b), 106.47(13)° (L_b–Zn2–L_c) and 95.72(12)° (L_a–Zn3–L_c) respectively with the Zn–Br distance varying between 2.274–2.599 Å. Ligands bpy arms have a bend angle between 112.56–115.32° and while the bowls are occupied by MeCN molecules, the rest of the interior free space is occupied by disordered EtOAc molecules. Due to highly disordered solvent volume, only two of the encapsulated MeCN molecules were able to be assigned properly. According to voids calculated in Mercury, 9.8 % of the unit cell volume of D2 is unassigned solvent molecules. In the dimeric capsule, the overlapping bpy arms are rotated around 120° respectively to each other with the centroid-centroid distances of pyridine rings being between 3.607–3.707 Å. The innermost bromide anions of type A Zn^{II} node (*e.g.* *d*(Br2A–Br4A)) are separated by a distance between 4.721–5.818 Å, while the diagonal distances (*e.g.* d_d(Br6–Br6')) are between 8.943–9.926 Å. The distance from outermost bromide atoms in type A metal node to ligands +1-valent nitrogen atoms varies between 3.714–5.042 Å.

In the crystal lattice type B metal nodes come near to the benzene core of L_c, with the distance between Br7 and one of the methylene-bridges (C103) being 3.581(4) Å. Subsequently, the bpy arm between L_c and Zn4 is facing itself from another dimer, with the separation between pyridine-ring centroids being 5.210(3) Å, as shown in Figure 72a. The benzene cores of ligands L_a and L_b are also pointing roughly towards the type B metal node, with separations of 9.3532(15) Å and 11.0044(14) Å respectively. The packing of D2 dimers is similar to the packing observed in compound D1, but the individual dimeric capsules are orientated differently to pack together more densely than compound D1 (Figure 72b-c). Crystallographic data for single crystal X-ray measurement of D2 is presented in Appendix 10 Table A10.

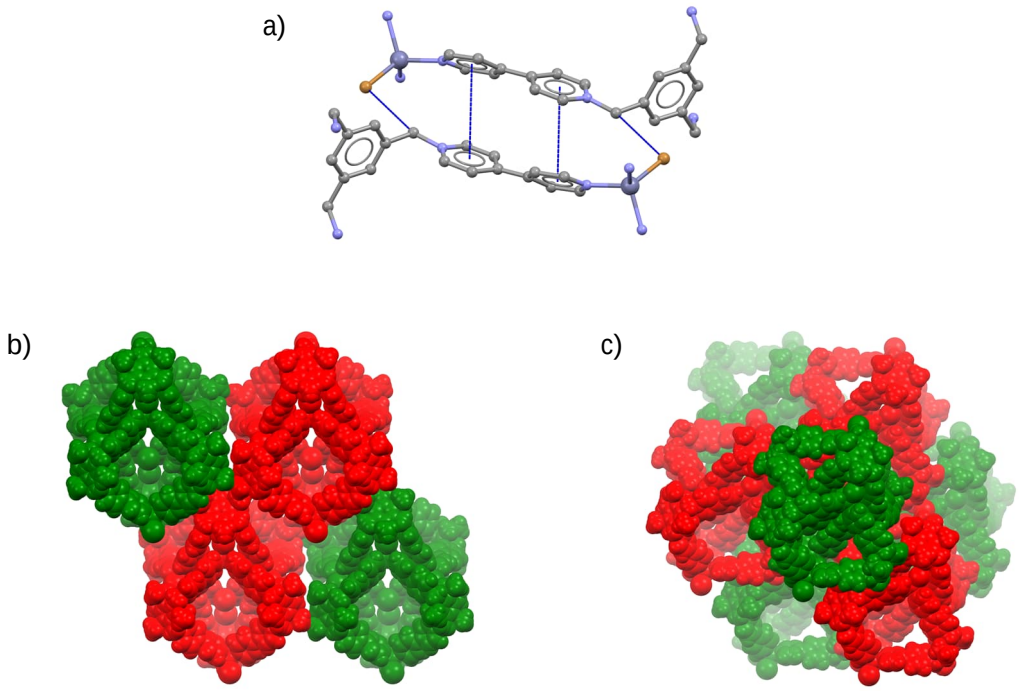

FIGURE 72 a) Close proximity of bpy arms in packing of compound D2. Packing of compound D2, viewed b) along the crystallographic *a*-axis and c) along (111) lattice plane. Free anions and solvent molecules are omitted for clarity.

6.4.1.3 $[Zn_4(L2)_3I_7](PF_6)_{10}$ (D3)

Compound D3 was prepared similarly to D1 by using ZnI_2 instead of $ZnCl_2$, and possesses the same topology as D1 with iodide anions instead of chloride anions (Figure 73). Compound D3 crystallizes as yellow needle-like crystals in monoclinic space group $P2_1/c$ (a = 22.6771(4) Å, b = 45.8546(8) Å, c = 25.7178(5) Å, $\alpha = \gamma = 90°$, β = 100.7886(18)°, V = 26 269.9(8) Å^3, Z = 4) and each asymmetric unit holds the entire $[Zn_4(L2)_3I_7](PF_6)_{10}$ entity together with 6.5 MeCN molecules and 1.25 EtOAc molecules. Two of the MeCN molecules have full occupancy, while the remaining 4.5 are disordered and have either 0.50 (6 locations) or 0.25 (6 locations) occupancies. The 1.25 EtOAc molecules are also disordered, consisting of one with 0.5 occupancies and three with 0.25 occupancies. One of the pyridine rings of bpy arms in L_c is disordered over two orientations with approximately 0.50 occupancies each, and the two orientations are separated by 25.59° torsion angle between the planes of pyridine rings containing nitrogen atom N8. Additionally, Zn1 metal node and iodine atoms bonded to it (I1 and I2) are disordered over two orientations with approximately 0.50 occupancies each. The different positions of disordered iodide anions correspond to the angle of ∡(I–Zn–I); 121.7(4)° for ∡(I1A–Zn1A–I2A) and 116.5(3)° for ∡(I1B–Zn1B–I2B). One of the PF_6^- anions (P1) is disordered over three positions with approximate occupancies of 0.40, 0.35 and 0.25 respectively for P1A, P1B and P1C, with distance between P1A and P1B being 3.928(15) Å and 1.031(17) Å between P1B and P1C. Another PF_6^- anion (P2) is disordered over two positions, with approximate occupancies of 0.75 and 0.25 respectively for P2A and P2B, and the distance between P2A and P2B is 2.150(13) Å. Furthermore PF_6^- anions P3, P4 and P10 are disordered over two orientations each, with approximate occupancies of 0.50 for all.

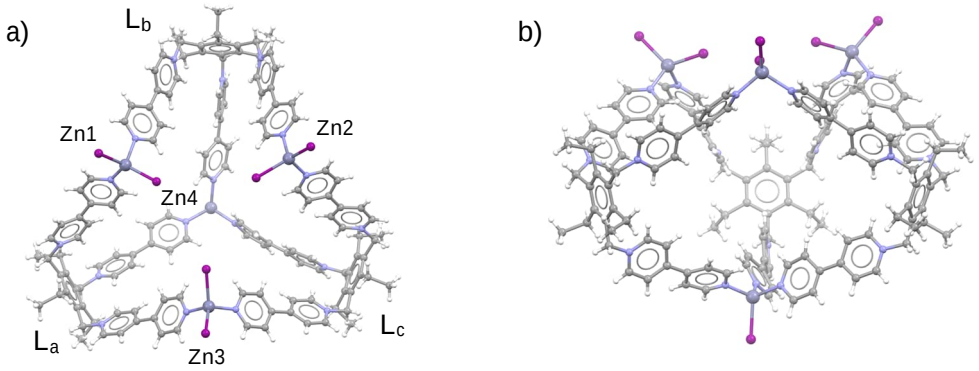

FIGURE 74 Tricyclic compound D3. a) Top view of monomer and b) side view of monomer. Free anions and solvent molecules are omitted for clarity.

The distances between type A Zn^{II} nodes are 10.970(9) Å for *d*(Zn1A-Zn2), 10.906(8) Å for *d*(Zn1B-Zn2), 11.2313(13) Å for *d*(Zn2-Zn3), 11.194(5) Å for *d*(Zn1A-Zn3) and 10.870(5) Å *d*(Zn1B-Zn3) respectively, while the distances between type A and B Zn^{II} nodes are between 14.755–15.958 Å. Moreover the distance between type B Zn^{II} nodes in the formed dimer is 26.3570(18) Å, which makes compound D3 slightly more elongated than compounds D1 and D2. The type A Zn^{II} nodes have bridging angles of 101.8(4)° for ∡(L_a–Zn1A–L_b), 99.4(4)° for ∡(L_a–Zn1B–L_b), 97.7(2)° for ∡(L_b–Zn2–L_c) and 105.6(2)° for ∡(L_a–Zn3–L_c) respectively with the Zn–I distance varying between 2.465–2.565 Å. Ligands bpy arms have a bend angle between 112.20–116.04° and while the bowls are occupied by MeCN molecules, the rest of the interior free space is occupied by disordered EtOAc molecules. Although MeCN molecules can be assigned to each bowl, only one has full occupancy and the remaining two have occupancies of 0.50 each. Out of expected 10 PF_6^- anions, 9.5 could be assigned with the remaining 0.5 PF_6^- anion being disordered among unassigned solvent molecules. According to voids calculated in Mercury, 6.2 % of the unit cell volume of D3 is unassigned solvent molecules. In the dimeric capsule, the overlapping bpy arms are rotated around 120° respectively to each other with the centroid-centroid distances of pyridine rings being between 3.763–3.873 Å. The innermost iodide anions of type A Zn^{II} node (*e.g.* *d*(I2A–I4)) are separated by a distance between 4.598–4.971 Å, while the diagonal distances (*e.g.* d_d(I6–I6')) are between 7.983–8.566 Å. The distance from outermost iodide atoms in type A metal node to ligands +1-valent nitrogen atoms is between 3.915–4.663 Å.

In crystal lattice type B metal node comes near to one of the +1-valent nitrogen atom (N5) in ligand L_b, with distance between I7 and +1-valent nitrogen N5 being 3.500(2) Å. In addition type B metal node also comes near to one of the ethyl-groups in ligand L_c, with distance between I7 and C53 being 4.048(8) Å (Figure74a). The dimeric capsules of D3 are orientated in two different layers (red and green in Figure 74b–d) with the orientations of different layers following the symmetry element $2_1/c$. Viewing the packing along the crystallographic *c*-axis, two out of three cycles in D3 monomers are aligned creating solvent-anion cavities through the crystal lattice. Crystallographic data for single crystal X-ray measurement of D3 is presented in Appendix 10 Table A10.

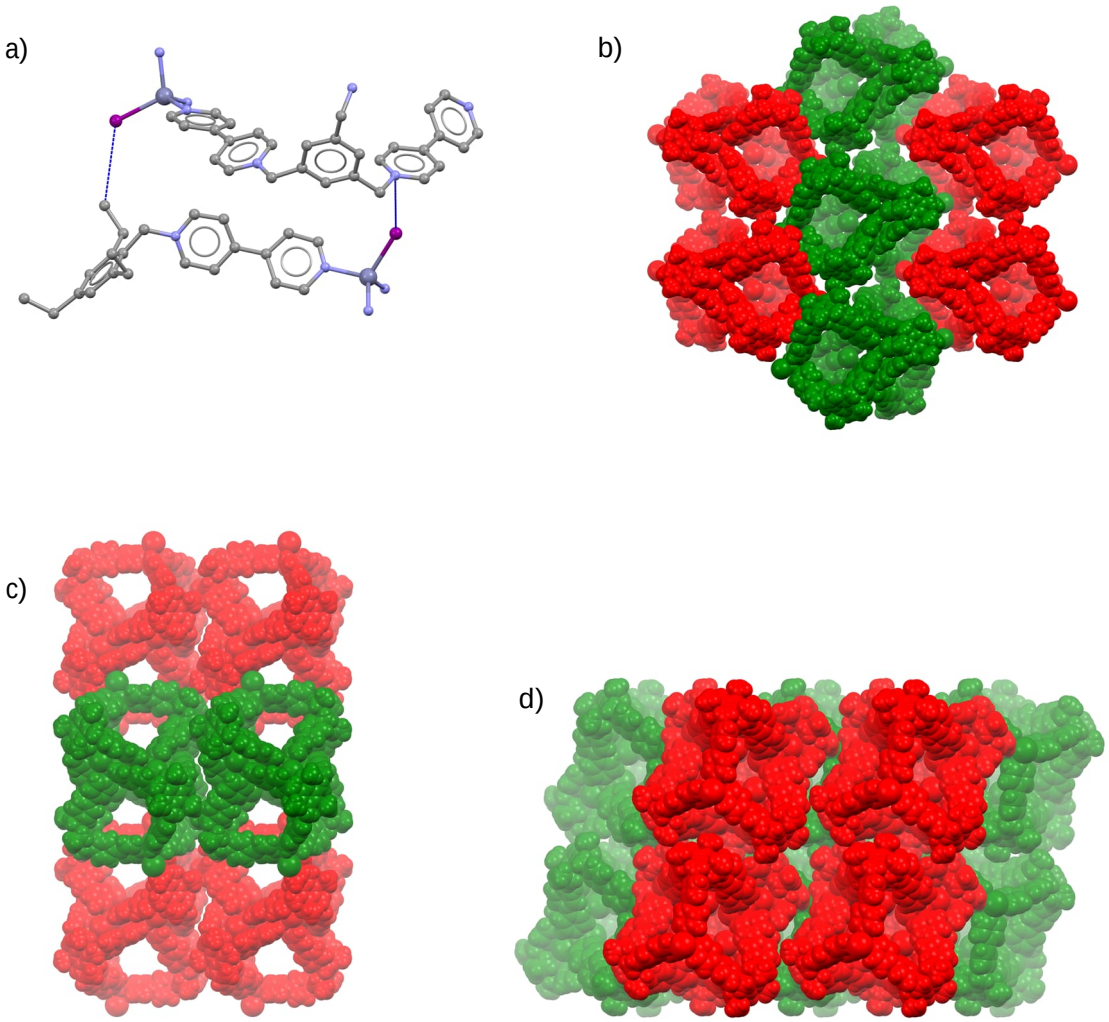

FIGURE 75 Close proximity of type B metal nodes and packing of compound D3, viewed along the crystallographic a) *a*-axis, b) *c*-axis and d) *b*-axis. Free anions and solvent molecules are omitted for clarity.

6.4.1.4 $[Zn_4(L1)_3I_7](PF_6)_{10}$ (D4)

Despite several attempts, no crystals suitable for X-ray diffraction analysis were obtained when $(L1)\cdot(PF_6)_3$ was paired with either $ZnCl_2$ or $ZnBr_2$ but pairing $(L1)\cdot(PF_6)_3$ with ZnI_2 followed by slow vapor diffusion of ethyl acetate yielded yellow needle-like crystals. The compound D4 crystallizes in triclinic space group $P\bar{1}$ (a = 22.7773(3) Å, b = 23.3081(4) Å, c = 24.5807(4) Å, α = 102.8010(10)°, β = 109.0290(10)°, γ = 93.0280(10)°, V = 11 918.8(3) Å^3, Z = 2) and each asymmetric unit holds the entire $[Zn_4(L2)_3I_7](PF_6)_{10}$ entity together with five MeCN molecules and one EtOAc molecule with approximate occupancy of 0.50 (Figure 75). Four of the MeCN molecules are approximate occupancies of 0.50 each while the remaining one has full occupancy. One of the PF_6^- anions (P1) is disordered over two locations with approximate occupancies of 0.75 and 0.25 respectively for P1A and P1B, and the distance between P1A and P1B is 2.28(2) Å. Additionally PF_6^- anions P1A and P1B are sharing one of the fluoride atoms, namely F6. Another PF_6^- anion (P9) is disordered over two positions, with approximate occupancies of 0.75 and 0.25 respectively for P9A and P9B.

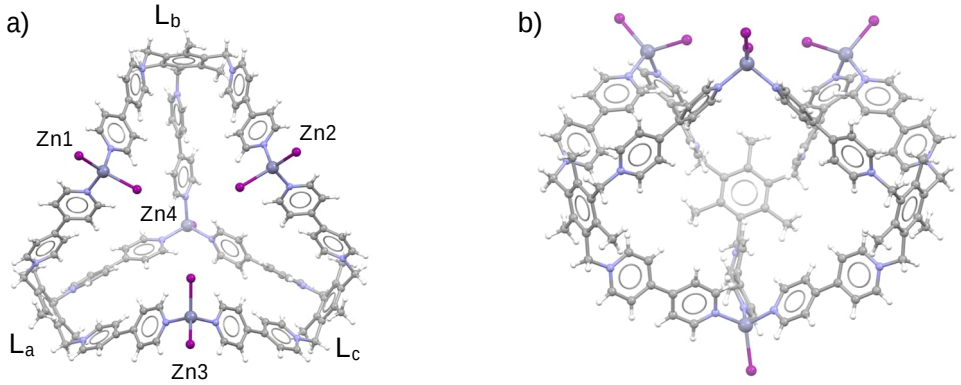

FIGURE 76 Tricyclic compound D4. a) Top view of monomer and b) side view of monomer. Free anions and solvent molecules are omitted for clarity.

The distances between type A Zn^{II} nodes are 10.801(2) Å for d(Zn1-Zn2), 10.876(2) Å for d(Zn2-Zn3) and 10.836(3) Å for d(Zn2-Zn3), while the distance between type A and B Zn^{II} nodes is between 15.930–16.020 Å. Moreover the distance between type B Zn^{II} nodes in the formed dimer is 28.093(3) Å, which makes compound D4 slightly more elongated than compounds D1–D3. The type A Zn^{II} nodes have bridging angles of 100.2(4)° for ∡(L_a–Zn1–L_b), 99.3(3)° for ∡(L_a–Zn2–L_b) and 100.1(3)° for ∡(L_b–Zn3–L_c) respectively with the Zn–I distance varies between 2.512–2.560 Å. Ligands bpy arms have a bend angle between 111.96–116.40° and while the bowls are occupied by MeCN molecules, the rest of the interior free space is occupied by disordered EtOAc molecules. MeCN molecules can be assigned to two of the bowls with occupancies of 0.50 each. Out of the expected 10 PF_6^- anions, 8.5 could be assigned with the remaining 1.5 PF_6^-

anions being disordered among unassigned solvent molecules. According to voids calculated in Mercury, 12.5 % of the unit cell volume of D4 is unassigned solvent molecules. In the dimeric capsule, the overlapping bpy arms are rotated around 120° respectively to each other with the centroid-centroid distances of pyridine rings being between 3.748–3.856 Å. The innermost iodide anions of type A Zn^{II} node (*e.g.* *d*(I2–I4)) are separated by a distance between 4.657–4.746 Å, while the diagonal distances (*e.g.* d_d(I6–I6')) are between 8.053–8.142 Å. The distance from outermost iodide atoms in type A metal node to ligands +1-valent nitrogen atoms is between 4.030–4.422 Å.

In crystal lattice type B metal nodes come to proximity with the distance between *d*(Zn4–Zn4') being 6,172(4) Å, *d*(I7–I7') being 5.200(2) Å and *d*(Zn4–I7') being 5.124(2) Å (Figure 76a), with an inversion center located in the halfway from one Zn4 to another. The methylene-bridges of bpy arm in L_b come to proximity with the distance between methylene-carbons *d*(C52–C52') being 3.89(2) Å. Similarly methyl-bridges C21 (L_a) and C74 (L_b) come to close proximity with a distance of 4.185(16) Å (Figure 76b). In crystal lattice the dimeric capsules in D4 are packed in identical layers loosely following the packing of octahedra, similarly to D1 but the packing model of D4 dimeric capsules is less dense (Figure 76c-d). Crystallographic data for single crystal X-ray measurement of D4 is presented in Appendix 10 Table A10.

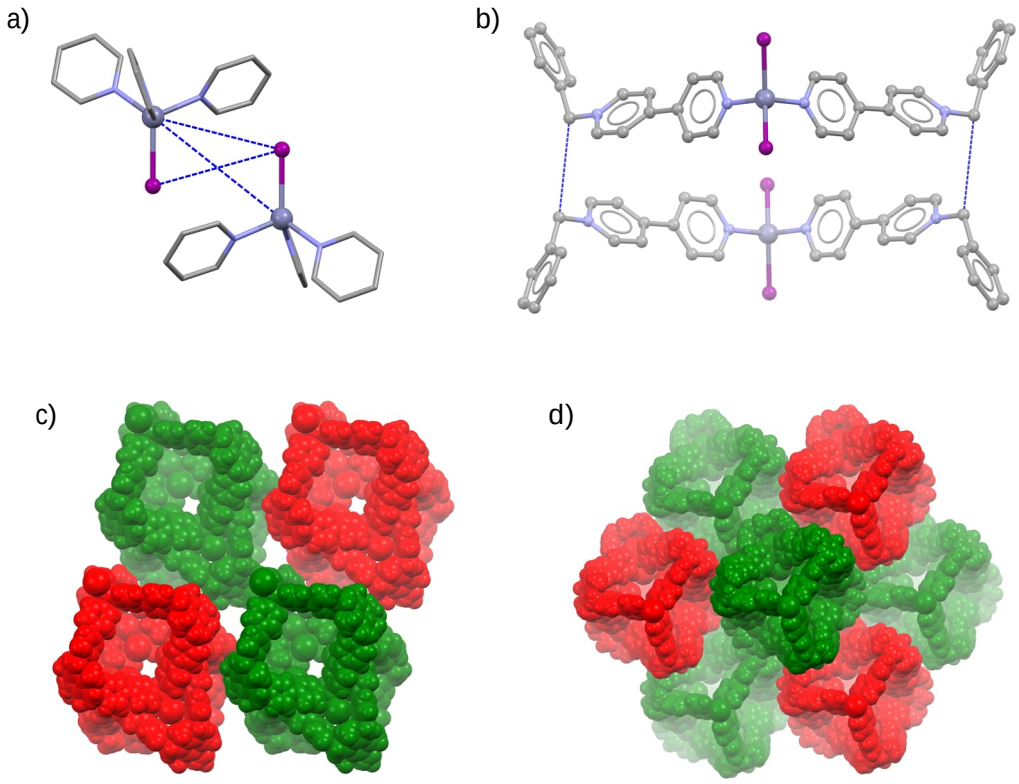

FIGURE 77 Close proximity of a) type B Zn^{II} nodes and b) methylene bridges in the packing of compound D4. Packing of compound D4, viewed c) along the crystallographic *a*-axis and d) along (111) lattice plane. Free anions and solvent molecules are omitted for clarity.

6.4.2 Summary of M_4L_3 dimeric capsules

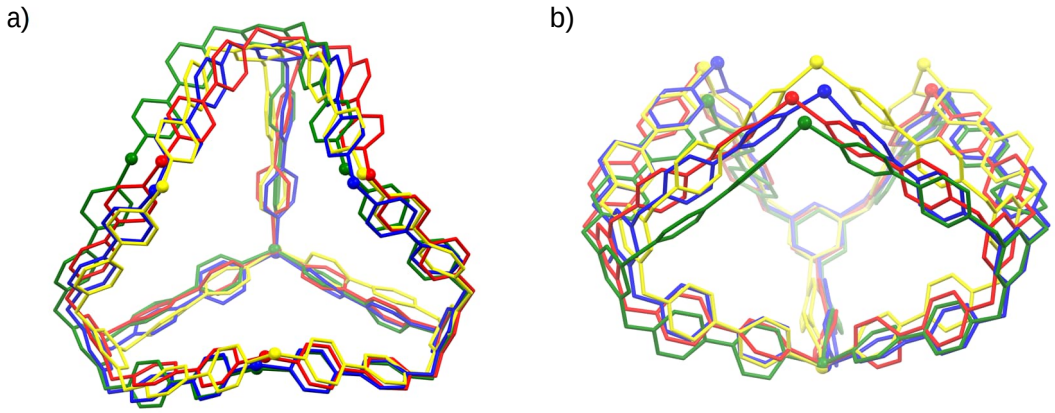

FIGURE 77 Overlay of M_4L_3 assemblies, a) top view of monomers, b) side view of monomers. Green: D1, Red: D2, Blue: D3 and Yellow: D4. Hydrogen atoms, solvent molecules, anions, Me and Et groups omitted are for clarity.

All M_4L_3 dimeric capsules have a generic composition of $[Zn_4L_3X_7](PF_6)_{10}$, where X is either Cl^-, Br^- or I^-. The overlays of cationic cage units of assemblies D1–D4 are depicted in Figure 77 and the obtained structures are relatively the same size and contain similar distances and bond angles as shown in Table 7. In general, the crystals of the assemblies D1–4 were more stable than crystals of M_6L_8 assemblies. This was seen from the crystals under Fomblin® Y oil within which the crystals remained suitable for X-ray diffraction for hours and in some cases, even for days after separation from crystallization solution. Albeit aforesaid assemblies can be obtained by mixing 10 mmol L^{-1} ligand solution and 7.5 mmol L^{-1} ZnX_2 solution (M:L = 3:4), the reaction was revised to be better suited for the formation of M_4L_3 assemblies by increasing the concentration of ZnX_2 solution to 13.33 mmol L^{-1} thus better matching the metal-ligand ratio of the end products (M:L = 4:3). Similarly, higher yield and better-quality crystals were obtained when 1 molar equivalent of KPF_6 was added to the reaction mixture. In the absence of KPF_6, the complexation reaction of M_4L_3 assemblies is PF_6^- poor and so the excess ligand precipitates during the crystallization process as LX_3 along with excess ZnX_2 (Equation 1). This can be avoided by the aforementioned introduction of KPF_6 into the system, in which case, precipitated KX can be filtered out before crystallization of the M_4L_3 assemblies (Equation 2).

$$3\,L(PF_6)_3 + 4\,ZnX_2 \rightarrow \frac{9}{10}[L_3Zn_4X_7](PF_6)_{10} + \frac{3}{10}\,LX_3 + \frac{2}{5}ZnX_2 \quad (1)$$

$$3\,L(PF_6)_3 + 4\,ZnX_2 + KPF_6 \rightarrow [L_3Zn_4X_7](PF_6)_{10} + KX \quad (2)$$

TABLE 7 Selected distances and angles of dimeric M_3L_4 capsules.

Compound	D1	D2	D3	D4
d(Zn–Zn)[a] / Å	12.240 ± 0.898	11.586 ± 0.327	11.034 ± 0.167	10.838 ± 0.038
d(Zn–Zn4)[b] / Å	14.335 ± 0.149	15.127 ± 0.769	15.117 ± 0.565	15.972 ± 0.045
d(Zn4–Zn4') / Å	23.452 ± 0.000	25.565 ± 0.000	26.357 ± 0.000	28.093 ± 0.000
d_d(Zn–Zn')[c] / Å	14.202 ± 1.279	13.477 ± 0.403	12.781 ± 0.276	12.587 ± 0.022
∡(L–Zn–L)[d] / °	104.8 ± 1.3	102.38 ± 5.85	101.13 ± 3.42	99.87 ± 0.49
d(Bz–Bz) / Å	19.115 ± 0.197	18.447 ± 1.020	18.342 ± 0.824	17.921 ± 0.080
$d(X^-–N^+)$ / Å	4.122 ± 0.348	4.247 ± 0.496	4.252 ± 0.270	4.253 ± 0.167
d(π–π) / Å	3.667 ± 0.093	3.644 ± 0.049	3.819 ± 0.086	3.786 ± 0.054
d(X–X) / Å	5.912 ± 0.288	5.352 ± 0.361	4.750 ± 0.176	4.697 ± 0.115
d_d(X–X)[c] / Å	10.287 ± 1.457	9.398 ± 0.532	8.246 ± 0.241	8.095 ± 0.045

[a]Between Type A, [b]between Type A and B, [c]diagonal, [d]Type A, presented as average ± standard deviation

Comparing the distances between metal nodes in different dimeric capsules, it can be noted that while the distance between type A metal nodes (*d*(Zn–Zn)) decreases, the distance between type B metal nodes (*d*(Zn4–Zn4)) increases following the series D1 < D2 < D3 < D4. Similarly, the angle between type A metal nodes and ligands (∡(L–Zn–L)) is decreasing following the same series (Table 7). On the other hand, the distance between type A and B metal nodes (*d*(Zn–Zn4)) and the distance between centroids of the benzene cores of the ligands (*d*(Bz–Bz)), follows the series D1 < D2 ≈ D3 < D4. This can be explained, at least partially, by the ionic radius of the corresponding halide anion in the series. The ionic radius increases in the series Cl^- < Br^- < I^-, and so halide anions force ligands to adapt to steeper bond angles to accommodate larger anions. Similarly, as the ionic radius of halide anion increases, the distance between halide anions in type A metal nodes and +1-valent nitrogen atoms in ligand bpy arms also increases. These changes combined are causing the dimeric capsule to become more elongated while becoming narrower as the ionic radius of implemented halide anion increases. The increasing ionic radius of halide anions does not, however, explain the variation seen in ∡(L–Zn–L) bend angles between different metal nodes as the difference between highest and lowest bend angle (Δ°) is 2.63° for D1, 10.75° for D2, 7.90° for D3 and 0.90° for D4. Typically one of the type A metal nodes have a steeper bend angle, while the other two are relatively similar, which causes a visible twisting of the monomer skeleton (Figure 77a). Interestingly assembly D4 is the most symmetrical out of all M_4L_3 dimeric assemblies possessing the lowest differences between aforementioned distances and angles of individual metal nodes and ligands. This would indicate that the M_4L_3 assemblies D1–D3 are more sterically restricted, due to ligands containing triethylbenzene core than D4 which contains ligands with trimethylbenzene core. This, in combination with halides anionic radius, could explain the differences witnessed with ∡(L–Zn–L) bend angles.

The $M_4L_3X_7$ dimeric capsules of monomers D1–4 are seemingly held together by two different simultaneous interactions, namely π–π -interactions between overlapping bpy arms, and electrostatic interactions between halides in type A metal nodes and +1-valent bpy arms of the ligands. The pyridine rings coordinated to type A Zn^{II} nodes in individual monomers overlap upon formation of the dimeric capsule (Figures 78a–b) with ring centroid-centroid distance (d(π–π), Table 7) being on average 3.667 Å, 3.644 Å, 3.803 Å and 3.786 Å for D1, D2, D3 and D4 respectively. The overlapping bpy arms are rotated approximately 120° respectively to Zn–bpy coordination bond with pyridine rings have near face-to-face alignment and almost parallel ring planes. Janiak[164] has suggested that, in metal-ligand complexes with aromatic nitrogen-containing heterocycles, π–π -interactions typically occur up to ring centroid-centroid distance of 3.8 Å. This is usually accompanied by a ring displacement angle (centroid-centroid offset) of around 20° but (near) perfect face-to-face is also possible, though exceedingly rare. The centroid-centroid distances observed in M_4L_3 assemblies are near the upper limit for Janiak's suggestion which would indicate that there is, to an extent, still a π–π -interaction between bpy arms of the dimeric capsule, though one of the rarer varieties.

The other potential interaction, electrostatic interaction, occurs between halides in type A metal nodes and +1-valent bpy arms of the ligands. In dimeric capsules D1–D4, outermost halide anions bonded to each type A metal nodes are nested near two +1-valent nitrogen atoms in each of the ligands as follows: Zn1 near L_c, Zn2 near L_a and Zn3 in near L_b (Figure 78c). The average distances from halide anion to +1-valent nitrogen atoms ($d(X^-–N^+)$, Table 7) are 4.115 Å, 4.247Å, 4.252 Å and 4.253 Å for assemblies D1, D2, D3 and D4 respectively. Again, the observed trend of increasing distances can be partially explained by the increasing ionic radius of halide anion in question. The difference between the longest and the shortest distance (Δ*d*) being 0.960 Å, 1.328 Å, 0.748 Å and 0.390 Å for assemblies D1, D2, D3 and D4 respectively is likely due to the twisted nature of each assembly, along with steric hindrances forcing to slightly different orientations in each nest. The proximity of halide anion to +1-valent nitrogen atoms together with previously observed anion binding affinity of the ligand bowl, suggests that electrostatic interaction is present between the aforementioned system. Overall, each dimeric capsule is held together, or at least its formation is guided by, six electrostatic interactions together with an additional six π–π -interactions.

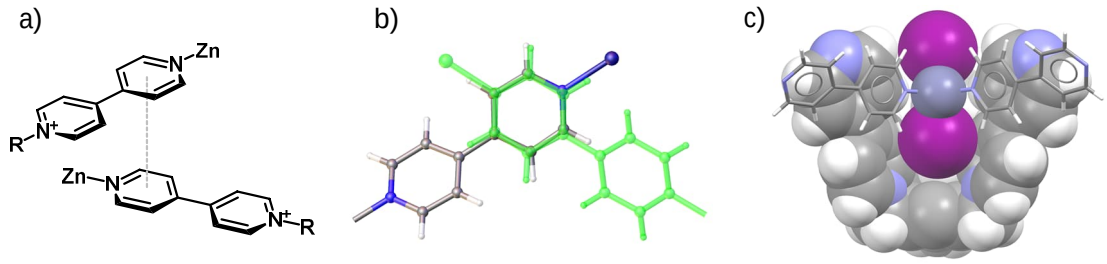

FIGURE 78 a) Representation of π–π –interactions, b) top view of overlapping bpy arms and c) nesting location of halide anions near +1-valent nitrogen atoms.

In the dimeric capsules, the innermost halide atoms coordinated in type A Zn^{II} nodes are separated on average by 5.912 Å for D1, 5.352 Å for D2, 4.750 Å for D3 and 4.697 for D4, while the diagonal distance on average is 10.287 Å for D1, 9.398 Å for D2, 8.246 Å for D3 and 8.095 Å for D4 respectively (d(X–X) and d_d(X–X), Table 7). This essentially creates a 'ring' of halide atoms in the middle of the dimeric capsule as shown in Figure 79. Outside the steric hindrance caused by the formation of dimeric capsule itself, this ring is also most likely the reason why there are no PF_6^- anions inside the M_4L_3 assembly; if PF_6^- would be located within the bowl, the proximity to the halide atom would cause severe repulsion between two anions.

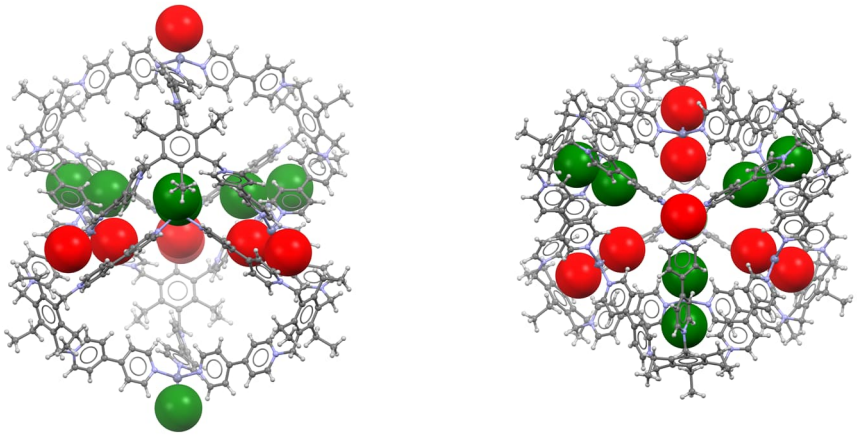

sideview top view

FIGURE 79 Halide 'ring' within dimeric capsules: a) sideview and b) top view.

Finally, to emphasize how unique the $M_4L_3X_7$ assemblies are, according to CSD only 192 structures contain tetrahedral type B Zn^{II} metal node (L_3ZnX) with N-donor ligands. Out of these structures only three utilized pyridine derivatives as ligands, and each of the said three examples are heterometallic compounds. Additionally, although numerous examples of assemblies containing the type A (L_2ZnX_2) tetrahedral node exists, there is only one reported structure containing both type A and B zinc nodes in the same assembly: a boron imidazolate based 2D-MOF.[165] This makes assemblies D1–4 completely previously unreported type of assembly.

6.4.3 M_5L_4 assembly

Compound D5 was obtained by mixing acetonitrile solutions of $Zn(I_3)_2$ and $(L2)\cdot(PF_6)_3$ followed by slow vapor diffusion of diethyl ether. X-ray diffraction analysis reveals that compound D5 crystallizes in tetragonal space group *P4/nnc* ($a = b = 27.4251(2)$ Å, $c = 44.1104(5)$ Å, $\alpha = \beta = \gamma = 90°$, $V = 33\,177.0(5)$ Å^3, $Z = 4$), but due to the high level of disorder, it was not possible to determine the structure to a satisfactory level. The structure was first examined in triclinic space group $P\bar{1}$ to assess the disordered nature of the assembly, though there was not enough data to completely solve the structure in the triclinic space group. Eventually the structure was determined in monoclinic space group *P2/n* ($a = 27.4114(3)$ Å, $b = 27.4257(3)$ Å, $c = 44.0965(5)$ Å, $\alpha = \gamma = 90°$, $\beta = 90.0050(10)°$, $V = 33\,150.7(6)$ Å^3, $Z = 4$) and each asymmetric unit holds the entire M_5L_4 entity of $[Zn_5(L2)_4I_8(H_2O)(MeCN)](PF_6)_{7.8}(I_3)_{6.2}$ together with several disordered MeCN solvent molecules. Similarly to M_4L_3 assemblies, M_5L_4 assembly D5 forms a dimeric capsule, but the compound is tetracyclic and shaped like a four spiked crown (Figure 80). Unlike originally intended, the type A Zn^{II} nodes do not contain $L_2Zn(I_3)_2$ moieties but instead, the node is the same as in D3 and D4 (L_2ZnI_2). Furthermore, instead of type B nodes, compound D5 possesses an additional type C node: an octahedral node where Zn^{II} is bonded with four ligands, one endohedral water molecule and one exohedral MeCN molecule as shown in Figure 81.

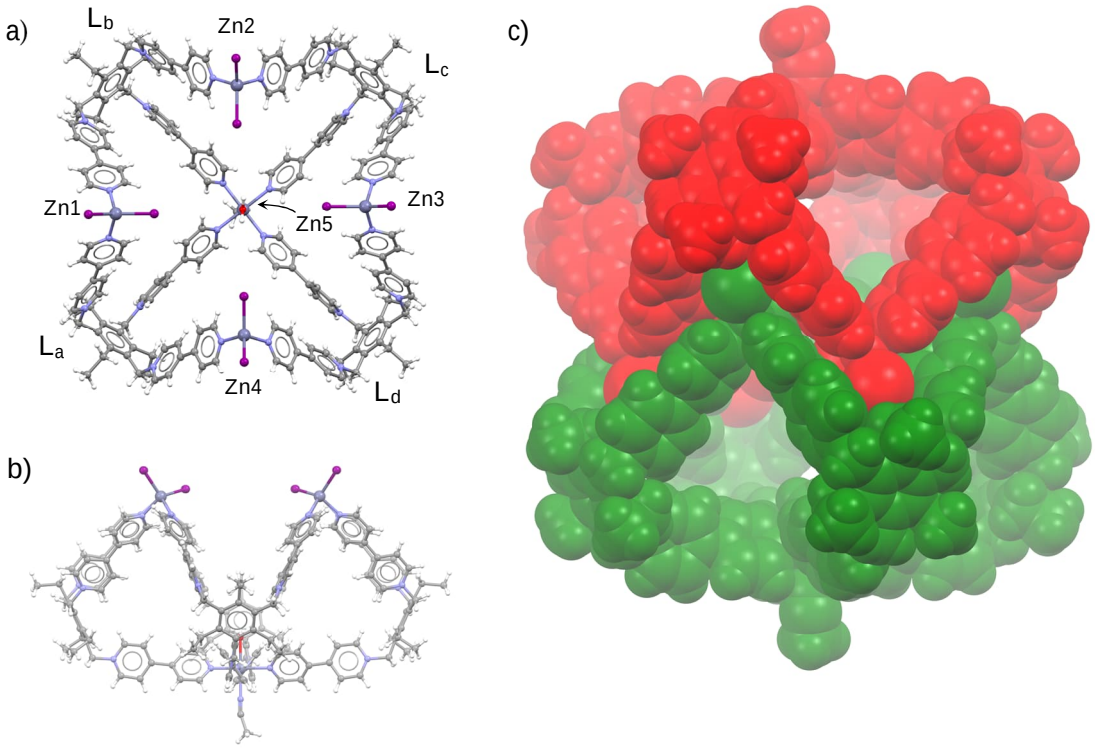

FIGURE 80 Tetracyclic compound D5 and its dimeric capsule. a) Top view of monomer, b) side view of monomer and c) dimeric capsule. Free anions and solvent molecules are omitted for clarity.

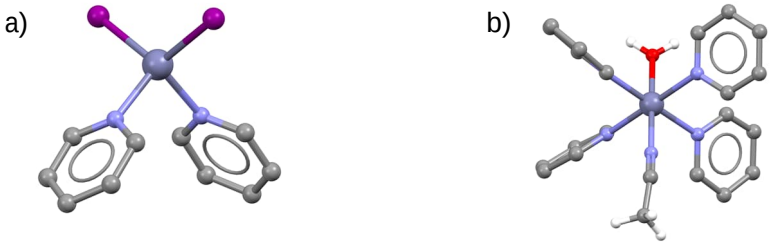

FIGURE 81 Metal nodes present in compound D5: a) type A node and b) type C node. Only relevant atoms are shown.

The distances between type A Zn^{II} ions are 11.359(3) Å for *d*(Zn1-Zn2), 11.360(3) Å for *d*(Zn2-Zn3), 11.358(3) Å for *d*(Zn3-Zn4) and 11.360(3) Å for *d*(Zn1-Zn4) respectively, while the distance between type A and C Zn^{II} ions is between 14.662–14.667 Å and the distance between type C Zn^{II} ions in the formed dimer is 22.827(4) Å making compound D5 slightly shorter than compounds D1–4. The type A Zn^{II} nodes have bridging angles of 94.9(4)° for ∡(L_a–Zn1–L_b), 95.0(4)° for ∡(L_b–Zn2–L_c), 94.6(4)° for ∡(L_c–Zn3–L_d) and 94.7(4)° for ∡(L_d–Zn4–L_a), while bridging angle for type C is 179.1(4)° for both ∡(L_a–Zn5–L_c) and ∡(L_b–Zn5–L_d). The Zn–I distance varies between 2.536–2.542 Å, while the distance from Zn5 to water molecule is 2.193(9) Å and the distance to the nitrogen atom of coordinated MeCN molecule is 2.204(10) Å. Ligands bpy arms have a bend angle between 111.67–114.92° and similar to M_4L_3 assemblies the bowls are occupied by MeCN molecules. Due to the highly disordered nature of solvent molecules in D5 the encapsulated MeCN molecules located between 4.13–4.70 Å above the benzene cores of the ligands. The encapsulated MeCN molecules are disordered with approximate occupancies varying from 0.25 to 1 depending on the molecule and the level of disorder. Some of the MeCN molecules were so disordered that, even though each atom could be assigned, anisotropic refinement could not be performed on them. According to voids calculated in Mercury, 17.8 % of the unit cell volume of D5 is unassigned solvent molecules. In the dimeric capsule, the overlapping bpy arms are rotated around 120° respectively to each other with the centroid-centroid distances of pyridine rings being between 3.638–3.860 Å. The innermost iodide anions of type A Zn^{II} node (*e.g.* I(I2H–I4H)) are separated by a distance between 4.931–5.194 Å, while the diagonal distances (*e.g.* d_d(I4H–I7H)) are between 11.099–11.097 Å. The distance from outermost iodide atoms in type A metal nodes to ligands +1-valent nitrogen atoms is between 4.365–4.439 Å. Similarly to M_4L_3 assemblies, larger dimeric capsule D5 is also seemingly held together by a combination of electrostatic and π–π -interactions with eight of each present in the assembly.

The total positive charge of the M_5L_4 assembly is 22+, which is balanced out with eight iodide anions coordinated to type A Zn^{II} nodes and the remaining positive charge (14+) is balanced out with a mixture of exohedral I_3^- and PF_6^- anions. In fact, four of the PF_6^- anions are disordered with I_3^- anions in approximately 0.95 and 0.05 occupancies respectively and they also share a site with one MeCN molecule (Figure 82a). The solvent molecules in question are

disordered with approximate occupancies between 0.25 and 0.50. Remaining four PF_6^- anions are heavily disordered to a point where it was not feasible to assign all the required fluoride atoms to each of the disordered phosphorus atom (Figure 82b), as some of PF_6^- anions were disordered over a special position. Additionally, four of the I_3^- anions are disordered over two orientations with approximate occupancies of 0.50 for each while sharing the middle iodine atom with full occupancy (Figure 82c). The remaining two I_3^- anions are located in a I_3-pseudoring around exohedral MeCN molecule in type C Zn^{II} node, and so the total composition of counter anions is 7.8 PF_6^- anions and 6.2 I_3^- anions. Locations of I_3^- anions are shown Figure 82d–e.

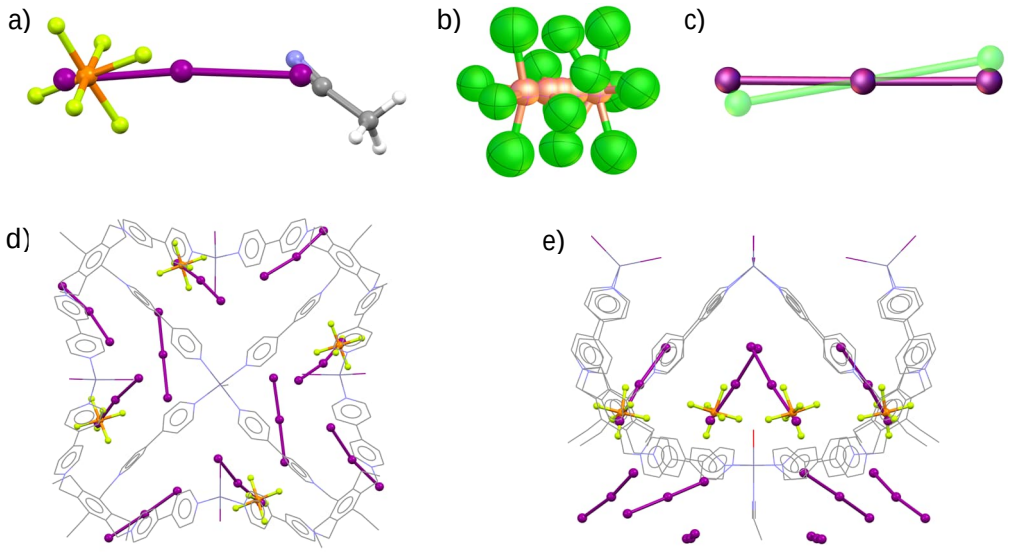

FIGURE 82 Examples of disordered a) PF_6^- / I_3^- / MeCN, b) PF_6^- anion and c) I_3^- anion. Locations of I_3^- anions: d) top view and e) side view. Only relevant atoms are shown.

The I_3-pseudo-ring consist of two I_3^- anions that are disordered over six positions, with approximate occupancies of 0.249, 0.242, 0.167, 0.166, 0.091 and 0.085 respectively for each position (Figure 83a). The two I_3^- anions are separated by a distance of 8.250–9.352 Å between middle iodine atoms and in the crystal lattice two I_3-pseudo-rings are facing each other with distance between two pseudo-rings being ≈12 Å. Furthermore, in crystal lattice four PF_6^- anions (two distinct anions P3 and P7, fulfilled via symmetry) are located between two of the I_3-pseudo-rings forming a highly unusual anion-anion-anion sandwich-like (a^3s) structure as shown in Figure 83b–c. The PF_6^- anions themselves are highly disordered with phosphorus atoms laying midway between the two pseudo-rings, while the PF_6^- anions are separated by ≈7 Å between the nearest anions and ≈10 Å diagonally. Beyond assigned PF_6^- anions, no additional electron density was observed between I_3-pseudo-rings, so the remaining ‘empty’ space consists of most likely of extremely disordered solvent molecules.

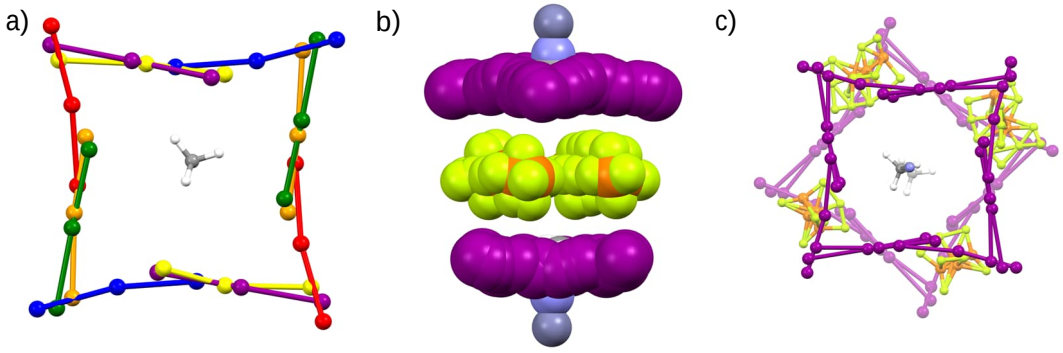

FIGURE 83 a) Disordered I_3^- pair in I_3-pseudo-ring with each color presenting different orientation, b) side view of a^3s-like structure and c) top view of a^3s-like structure.

In crystal lattice, Zn5 metal nodes of the dimeric capsules are orientated parallel to *c*-axis, while Zn1–Zn4 nodes lay on the *ab*-plane. The dimeric capsule of D5 has relatively spherical shape and the packing of dimeric capsules resembles that of body-centered cubic packing of spheres (Figure 84a). On *ab*-plane each dimeric capsule is on the same layer with separation between Zn5 atoms being 27.411(3) Å parallel to *a*-axis and 27.114(3) Å parallel to *b*-axis. Each identical layer (red and green in Figure 84a) is separated by 21.270(4) Å measured from one Zn5 atom to another. In the "middle" layer (blue in Figure 84b), located between the two identical layers, houses dimeric capsules which are rotated 90° along the *c*-axis compared to ones in identical layers. The leftover space located between individual dimeric capsules is occupied by counter anions and solvent molecules. Crystallographic data for single crystal X-ray measurement of D5 is presented in Appendix 10 Table A10.

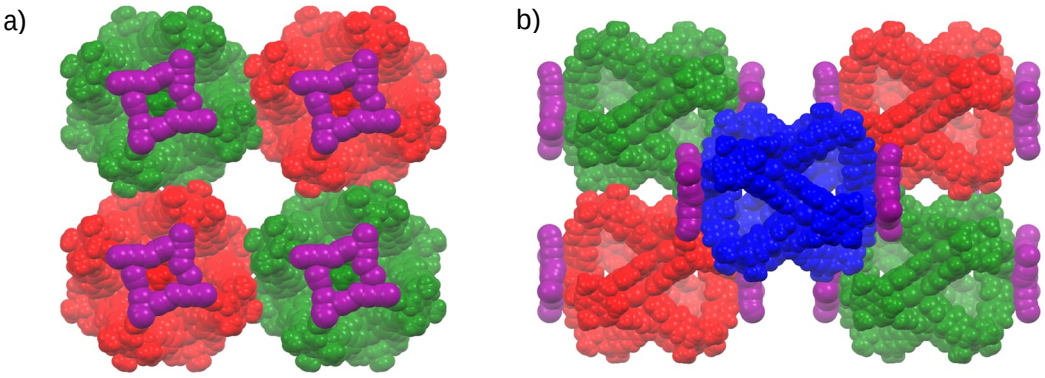

FIGURE 84 Packing of compound D5, viewed a) along the crystallographic *c*-axis and b) along *b*-axis. Solvent molecules and free anions (expect I_3-pseudo-rings) are omitted for clarity.

6.5 Thermogravimetry

Thermal stability of the utilized ligands, L·Br_3, L·$(PF_6)_3$ and (L2)·$(NTf_2)_3$, as well as selected M_6L_8 and M_4L_3 assemblies were briefly studied and compared. The L1 ligand salts have onset decomposition temperatures of 254.90 °C for (L1)·Br_3 and 197.61 °C for (L1)·$(PF_6)_3$, while L2 ligand salts have onset decomposition temperatures of 253.66 °C for (L2)·Br_3, 200.69 °C for (L2)·$(PF_6)_3$ and 307.41 °C for (L2)·$(NTf_2)_3$. The near-equal thermal decomposition temperatures between L1 and L2 bromide (254.90 °C *cf.* 253.66 °C) and hexafluorophosphate (197.61 °C *cf.* 200.61 °C) salts would indicate that neither trimethyl- nor triethylbenzene core of the respective ligands increases or diminishes the thermal stability of the said ligands. In the case of both L1 and L2 ligands, the bromide salts are more thermally stable than PF_6^- salts, whereas (L2)·$(NTf_2)_3$ salt has a higher decomposition temperature than either (L2)·Br_3 or (L2)·$(PF_6)_3$. Thus the thermal stability of the utilized ligands can be organized into the following series: (L1)·Br_3 ≈ (L2)·Br_3 < (L1)·$(PF_6)_3$ ≈ (L2)·$(PF_6)_3$ < (L2)·$(NTf_2)_3$.

Bromide and PF_6^- salts of both L1 and L2 ligands undergo an exothermic decomposition, with 2–3 overlapping reactions, which ends around 320 °C for both bromide salts and around 333 °C for both PF_6^- salts. This is then followed by more gradual exothermic step, which ends around 545 °C in case of (L1)·Br_3 and around 700 °C in case of (L2)·Br_3 and L·$(PF_6)_3$ salts. Contrastingly the (L2)·$(NTf_2)_3$ salt undergoes a multi-step exothermic decomposition with several overlapping reactions, which end around 490 °C and is followed by more energetic exothermic overlapping reactions, which end around 620 °C. The selected comparison of thermographs of L1 and L2 ligand salts are presented in Figures 85a and 85b respectively, while full TG/DSC graphs are presented in Appendix 13 and decomposition temperatures are also presented in Table 8.

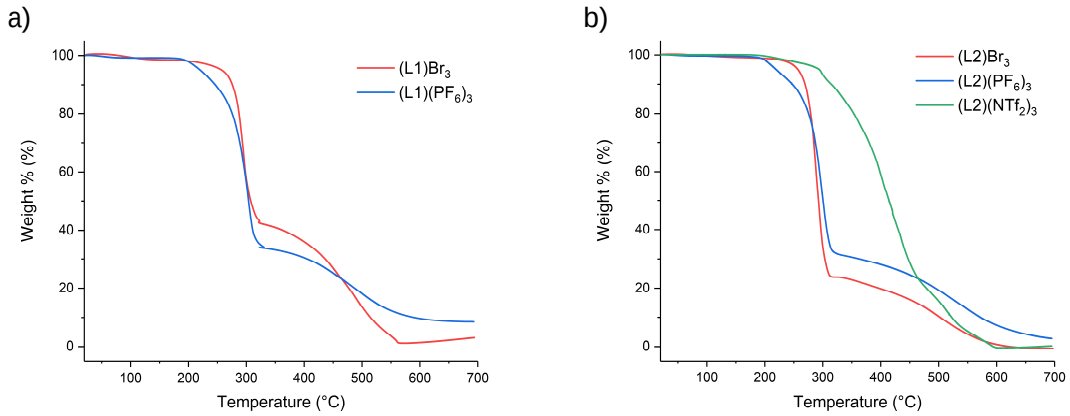

FIGURE 85 Comparison of a) L1 ligand salts and b) L2 ligand salts.

TABLE 8 Extrapolated onset temperatures for thermal decomposition

Compound	Onset (°C)	Compound	Onset (°C)
(L1)·Br_3	254.90	C4 ($NiCl_2$, dry)	274.25
(L2)·Br_3	197.61	C5 ($NiBr_2$, dry)	276.44
(L1)·$(PF_6)_3$	253.66	C6 ($Ni(SCN)_2$, dry)	274.03
(L2)·$(PF_6)_3$	200.69	D1 ($ZnCl_2$, dry)	291.73
(L2)·$(NTf_2)_3$	307.41	D2 ($ZnBr_2$, dry)	296.46
C3* ($Ni(PF_6)_2$, fresh)	289.53	D3 (ZnI_2, dry)	294.50
C3* ($Ni(PF_6)_2$, dry)	293.07		

As mentioned previously, obtained M_6L_8 assemblies contain a large amount of solvent within the crystal lattice, and this can also be observed in the thermographs of said assemblies. For example, when 'fresh' crystals of C3* ($Ni(PF_6)_2$) were measured almost immediately after removal from the crystallization solvent, nearly 28.8 % mass loss was observed before thermal decomposition occurred (Figure 86a, C3* fresh). Furthermore, a rapid mass loss was observed during the premeasurement one-minute stabilization period as volatile solvents (MeCN and EtOAc) were evaporating from the crystal surfaces. This is also reflected in the actual measurement as a starting weight-% (wt.-%) of 96.5 % and quick mass loss of around 20 % occurring between 20–80 °C. Comparatively, crystals of C3* which dried under N_2 flow prior to thermal stability measurement, showed only around 8.5 % mass loss before thermal decomposition (Figure 86a, C3* N_2 dry) and no rapid mass loss was observed during the stabilization period.

The fresh sample had a slightly lower decomposition temperature, 289.53 °C, than the N_2 dried sample, 293.07 °C, though this can be explained by observer error. More importantly, the decomposition occurs at, roughly 90 °C, a higher temperature than in non-coordinated starting ligand (L2)·$(PF_6)_3$ (Figure 86b). In both cases (fresh and N_2 dry C3*) the thermal decomposition occurs around 290 °C, which is nearly 100 °C higher than non-coordinated (L2)·$(PF_6)_3$ (Figure 86b), indicating that coordination with Ni^{II} metal ions increases the thermal stability of ligand (L2)·$(PF_6)_3$. Similar decomposition temperatures were also observed with M_6L_8 assemblies C4–C6 (around 275 °C) and with dimeric capsules D1–D3 (around 294 °C), comparison of which are shown Figures 86c and 86d respectively and presented in Table 8. This would then indicate that if Ni^{II} node contains one or more coordinated anion, the decomposition temperature is lower than if only MeCN is coordinated to the metal node. The thermal decomposition of M_6L_8 assemblies follow the similar two-step decomposition route as observed with ligand (L2)·$(PF_6)_3$.

In the case of the dimeric capsules, $Zn_4L_3X_7$, the decomposition temperatures are around 20 °C higher than what was observed with M_8L_6 assemblies and seemingly different halides have relatively similar decomposition temperatures. The decomposition also occurs differently than in M_6L_8 assemblies; the decomposition in $M_4L_3X_7$ is, generally speaking, a one-step process. Whether the slightly higher decomposition temperature can be attributed to the use of Zn^{II} halides, to the different metal-organic skeletons, to the different types of metal nodes (octahedral in Ni^{II} *cf.* tetrahedral in Zn^{II}) or for some other reason cannot be stated at this point.

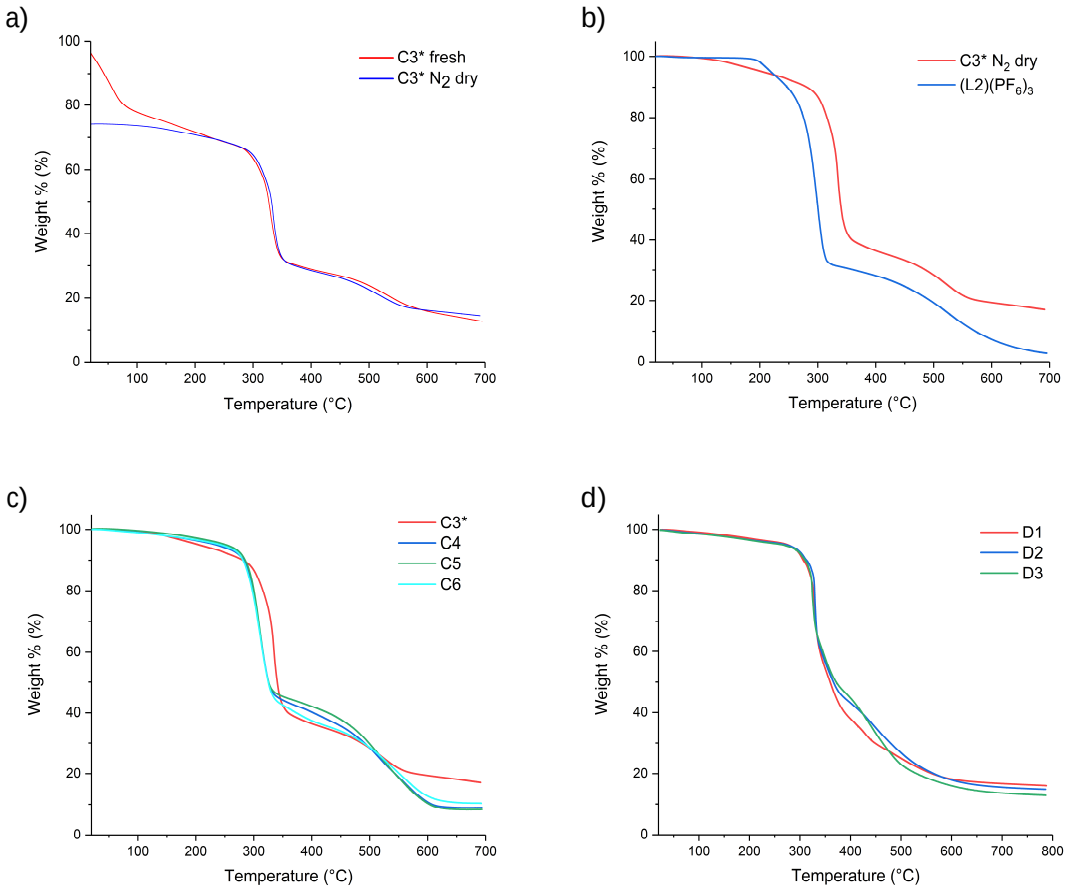

FIGURE 86 Comparison of a) fresh and dry C3* assemblies, b) dry C3* assembly and ligand (L2)·$(PF_6)_3$, c) selected M_6L_8 assemblies and d) selected M_4L_3 dimeric capsules.

7 CONCLUSIONS

In conclusion, this thesis describes the synthesis of two similar tripodal tricationic N-donor ligands L1 and L2, based on bipyridinium moiety, and studies of their utilization as a building unit for the creation of cationic metal-organic polyhedra when paired with various metal salts. The obtained assemblies were crystallized, characterized and their structure was examined, and briefly subjected for post-synthetic modification involving anion exchange in solution.

Firstly, ligand L1 was reacted with copper(II) triflate and copper(II) perchlorate, which resulted in two similar $Cu_6(L1)_8$ assemblies, C1 and C2. The crystalline products proved to be highly fragile, and their crystallinity rapidly degraded after separation from crystallization solution. Despite numerous attempts, no tested solution combination could prevent this degradation of crystallinity, so the ligand was switched to potentially more rigid L2. Alas, the obtained crystals remained highly fragile, so the metal source was switched from Cu^{II} based to Ni^{II} based, in hopes to achieve more stable crystalline structures. When paired with $Ni(NO_3)_2$, $Ni_6(L2)_8$ assembly C3 possesses a similar metal node as C1 ($ML_4(MeCN)_2$) was obtained, but more importantly the crystals of C3 were more stable outside the crystallization solution than the crystals of either C1 or C2. Following this discovery, nickel(II) salts were used as a metal source and four other $Ni_6(L2)_8$ assemblies C3* ($Ni(PF_6)_2$), C4 ($NiCl_2$), C5 ($NiBr_2$) and C6 ($Ni(SCN)_2$) were synthesized. All these assemblies contain a similar supercationic $[Ni_6(L2)_8]^{36+}$ skeleton, with main structural differences rising from metal-coordinated solvents or anions as well as from encapsulated anions. Then, the counter anions of ligand L2 were exchanged to larger NTf_2^- anions, in order to study what effect does a less well encapsulating anion has on the formation metal-ligand assemblies. When reacted with $NiCl_2$ and $NiBr_2$, two new $Ni_6(L2)_8$ assemblies C7 and C8 were achieved, with different halide compositions, compared to once obtained using PF_6^- as the counter anion for ligand L2. Thus, showing that the $[Ni_6(L2)_8]^{36+}$ can be formed as long as suitable counter anions can be encapsulated.

With this success possibility for copper assemblies were re-examined by utilizing copper(I) as a metal ion source instead of copper(II). Reacting CuNCS with (L2)·$(PF_6)_3$ yielded a $Cu_6(L2)_8$ assembly C9, reminiscent of the C1 assembly previously obtained using (L1)·$(PF_6)_3$, and while the obtained crystals were more stable than the ones from the previous Cu–assemblies, the C9 cage unit did not contain Cu^{I} metal nodes, but Cu^{II} metal nodes instead. Interestingly, no SCN^- anions were observed in assembly C9.

Returning to Ni-assemblies, it was examined if it would be possible to exchange solvent molecules or anions coordinated to the metal nodes by introducing a competing anion to the solution once the cage had formed. This was first implemented by introducing NCS^- anions to a solution of C4, to potentially exchange axial chloride anions of C4 to NCS^- anions and obtain assembly C6 by a post-synthetic method. After crystallization, it was revealed, that the obtained assembly C10 had a vastly different anion composition than C6; although both contain NCS^- anions within the metal node, C10 encapsulated mostly chloride anions, whereas C6 encapsulates mostly MeCN solvent molecules. After this, a completely new anion, iodide, was introduced to a solution of C3* (which contains no axial anions) in two different concentrations. This resulted in the formation of assemblies C11 and C12, both of which contain iodide, but in different molar ratios. This, in combination with assembly C10, indicate that it is possible to modify the metal node and the anion composition of the cage interior. Further studies are required to determine to what extent is the exchange controllable.

Secondly, with the succession of Ni^{II}-based assemblies, it was examined what effect would a metal preferring a tetragonal coordination geometry over octahedral one, and to test this zinc(II) was selected and reacted with L·$(PF_6)_3$. Though most zinc(II) salts provided no single crystals suitable for structure analysis, zinc(II) halides (Cl^-, Br^-, I^-) yielded completely new type of dimeric capsules containing $Zn_4L_3X_7$ moieties. These as-of-yet reported dimeric capsules are formed from two interlocking $Zn_4L_3X_7$ moieties, and the dimer is seemingly held together by a combination of electrostatic and π–π interactions. Furthermore, a larger $Zn_5L_4I_8$ dimeric capsule was obtained when (L2)·$(PF_6)_3$ was paired with $Zn(I_3)_2$, and this assembly additionally contains a unique triple-anion sandwich-like structure, where PF_6^- anions are ‘sandwiched’ between two disordered layers of triiodide.

The existence of M_6L_8 assembly C3* in solution was verified by *in situ* preparation and by redissolving the crystals of C3*. This suggests that the almost instantaneous color change, which occurs when ligand and metal salt solutions are mixed, is indicating the formation of other M_6L_8 assemblies in solutions also occur relatively quickly. The existence of a soluble cage unit gives rise for potential host-quest chemistry applications for M_6L_8 assemblies. The large interior space of the aforementioned supercationic M_6L_8 assemblies should be suitable for encapsulating anionic quests other than the counter anions provided by the ligand or by the metal source. Contrastingly, after encapsulating smaller

anions, the now mostly negatively charged interior, might be capable of hosting cationic guests.

An interesting observation during this study was the color changing behavior under X-ray radiation. This phenomenon, which is most probably a property of the ligand while interacting with metal, merits further investigation for the underlying mechanism of the color change observed.

In conclusion, the results presented here demonstrate that multivalent cationic N-donor ligands based on bipyridinium moieties are capable of forming self-assembling stable supercationic (36+) cages with various metal sources, while attaining the general M_6L_8 assembly. Each M_6L_8 assembly containing Ni^{II} or Cu^{II} metal nodes exhibits octahedral coordination geometry, where two axial sites are either pointing inward (endohedral) or outward (exohedral) of the cage interior. These sites, occupied by either solvent molecules or anions, can be to an extent be switched to another anion either by changing the original metal source or by introducing a new anion post-assembly to the system. Additionally, each M_6L_8 cage unit is capable of encapsulating up to eight anions within the interior cavity of the cage unit. Although it is possible to exchange these encapsulated anions, further research is needed to optimize the procedure. The potentially customizable interior of these M_6L_8 assemblies offers a new way of creating, for example, anion, solvent or dye capturing compounds. Furthermore, the cationic tripodal ligands form the similar types of assemblies (M_6L_8) when paired with octahedrally coordinating (Cu^{II} and Ni^{II}) or square-planar (Pd^{II}) metals, while also be capable to form new type of assemblies ($M_4L_3X_7$ or $M_5L_4X_8$) when paired with tetrahedrally coordinating metal (Zn^{II}). These new dimeric capsules possess the unique combination of different metal-ligand coordination types, never reported before.

REFERENCES

1. Lehn, J.-M., Supramolecular Chemistry – Scope and Perspectives Molecules, Supermolecules, and Molecular Devices (Nobel Lecture), *Angew. Chemie Int. Ed. English*, 1988, *27*, 89–112.

2. Kyba, E. P.; Helgeson, R. C.; Madan, K.; Gokel, G. W.; Tarnowski, T. L.; Moore, S. S. and Cram, D. J., Host-guest complexation. 1. Concept and illustration, *J. Am. Chem. Soc.*, 1977, *99*, 2564–2571.

3. Cram, D. J., The Design of Molecular Hosts, Guests, and Their Complexes (Nobel Lecture), *Angew. Chemie Int. Ed. English*, 1988, *27*, 1009–1020.

4. Lehn, J.-M., Toward complex matter: Supramolecular chemistry and self-organization, *Proc. Natl. Acad. Sci.*, 2002, *99*, 4763–4768.

5. Fischer, E., Einfluss der Configuration auf die Wirkung der Enzyme, *Berichte der Dtsch. Chem. Gesellschaft*, 1894, *27*, 2985–2993.

6. Lichtenthaler, F. W., 100 Years “Schlüssel-Schloss-Prinzip”: What Made Emil Fischer Use this Analogy?, *Angew. Chemie Int. Ed. English*, 1995, *33*, 2364–2374.

7. Steed, J. W. and Atwood, J. L., *Supramolecular Chemistry: Second Edition*, John Wiley and Sons, Wiltshire, UK, 2009.

8. Emsley, J., Very strong hydrogen bonding, *Chem. Soc. Rev.*, 1980, *9*, 91.

9. Metrangolo, P.; Murray, J. S.; Pilati, T.; Politzer, P.; Resnati, G. and Terraneo, G., Fluorine-Centered Halogen Bonding: A Factor in Recognition Phenomena and Reactivity, *Cryst. Growth Des.*, 2011, *11*, 4238–4246.

10. McNaught, A. D. and Wilkinson, A., *Compendium of Chemical Terminology, 2nd ed. (the ‘Gold Book’)*, 2nd edition, Blackwell Scientific Publications, Oxford, 1997.

11. Constable, E. C., Novel oligopyridines for metallosupramolecular chemistry, *Pure Appl. Chem.*, 1996, *68*, 253–260.

12. Peuronen, A.; Lehtimäki, E. and Lahtinen, M., Self-Assembly of Water-Mediated Supramolecular Cationic Archimedean Solids, *Cryst. Growth Des.*, 2013, *13*, 4615–4622.

13. Peuronen, A.; Forsblom, S. and Lahtinen, M., Sterically controlled self-assembly of tetrahedral M_6L_4 cages via cationic N-donor ligands, *Chem. Commun.*, 2014, *50*, 5469–5472.

14. Turunen, L.; Peuronen, A.; Forsblom, S.; Kalenius, E.; Lahtinen, M. and Rissanen, K., Tetrameric and Dimeric [N···I⁺···N] Halogen-Bonded Supramolecular Cages, *Chem. - A Eur. J.*, 2017, *23*, 11714–11718.

15. Shengzhong, L. I. U.; Ying-Jie, L. U.; Kappes, M. M. and Ibers, J. A., The structure of the C_{60} molecule: X-ray crystal structure determination of a twin at 110 K, *Science (80-.).*, 1991, *254*, 408–410.

16. Rafie, K.; Lenman, A.; Fuchs, J.; Rajan, A.; Arnberg, N. and Carlson, L. A., The structure of enteric human adenovirus 41 – A leading cause of diarrhea in children, *Sci. Adv.*, 2021, *7*, eabe0974.

17. Nemecek, D.; Boura, E.; Wu, W.; Cheng, N.; Plevka, P.; Qiao, J.; Mindich, L.; Heymann, J. B.; Hurley, J. H. and Steven, A. C., Subunit folds and maturation pathway of a dsRNA virus capsid, *Structure*, 2013, *21*, 1374–1383.

18. Holden, A., *Shapes, Space, and Symmetry*, Columbia University Press, New York, 1971.

19. Vukičević, D. and Balaban, A. T., Note on ordering and complexity of Platonic and Archimedean polyhedra based on solid angles, *J. Math. Chem.*, 2008, *44*, 725–730.

20. Johnson, N. W., Convex Polyhedra with Regular Faces, *Can. J. Math.*, 1966, *18*, 169–200.

21. Golgberg, M. A., A Class of Multi-Symmetric Polyhedra, *Tohoku Math. J.*, 1937, 104–108.

22. Hart, G., Goldberg polyhedra. In: *Shaping Space: Exploring Polyhedra in Nature, Art, and the Geometrical Imagination*, Springer New York, New York, 2013, pp. 125–138.

23. Dutour, M. and Deza, M., Goldberg-Coxeter construction for 3- and 4-valent plane graphs, *Electron. J. Comb.*, 2004, *11*, R20–R20.

24. Haynes, W. M. and Lide, D. R., Eds., *CRC Handbook of Chemistry and Physics, 93rd Edition*, Boca Raton, 2012.

25. Bethe, H., Termaufspaltung in Kristallen, *Ann. Phys.*, 1929, *395*, 133–208.

26. Zuckerman, J. J., Crystal field splitting diagrams, *J. Chem. Educ.*, 1965, *42*, 315.

27. Griffith, J. S. and Orgel, L. E., Ligand-field theory, *Q. Rev. Chem. Soc.*, 1957, *11*, 381.

28. Roche, S.; Haslam, C.; Heath, S. L. and Thomas, J. A., Self-assembly of a supramolecular cube, *Chem. Commun.*, 1998, 1681–1682.

29. Leininger, S.; Fan, J.; Schmitz, M. and Stang, P. J., Archimedean solids: transition metal mediated rational self-assembly of supramolecular-truncated tetrahedra., *Proc. Natl. Acad. Sci. U. S. A.*, 2000, *97*, 1380–4.

30. Olenyuk, B.; Whiteford, J. A.; Fechtenkötter, A. and Stang, P. J., Self-assembly of nanoscale cuboctahedra by coordination chemistry, *Nature*, 1999, *398*, 796–799.

31. Olenyuk, B.; Levin, M. D.; Whiteford, J. A.; Jeffrey E. Shield and Stang, P. J., Self-Assembly of Nanoscopic Dodecahedra from 50 Predesigned Components, *J. Am. Chem. Soc.*, 1999, *121*, 10434–1435.

32. Kuehl, C. J.; Yamamoto, T.; Seidel, S. R. and Stang, P. J., Self-Assembly of Molecular Prisms *via* an Organometallic 'Clip', *Org. Lett.*, 2002, *4*, 913–915.

33. Enders, M.; Görling, B.; Braun, A. B.; Seltenreich, J. E.; Reichenbach, L. F.; Rissanen, K.; Nieger, M.; Luy, B.; Schepers, U. and Bräse, S., Cytotoxicity and NMR Studies of Platinum Complexes with Cyclooctadiene Ligands, *Organometallics*, 2014, *33*, 4027–4034.

34. Braga, D., Crystal engineering, Where from? Where to?, *Chem. Commun.*, 2003, *3*, 2751–2754.

35. Li, H.; Davis, C. E.; Groy, T. L.; Kelley, D. G. and Yaghi, O. M., Coordinatively Unsaturated Metal Centers in the Extended Porous Framework of $Zn_3(BDC)_3{\cdot}6CH_3OH$ (BDC = 1,4-benzenedicarboxylate), *J. Am. Chem. Soc.*, 1998, 120, 2186–2187.

36. Chui, S. S. Y.; Lo, S. M. F.; Charmant, J. P. H.; Orpen, A. G. and Williams, I. D., A chemically functionalizable nanoporous material $[Cu_3(TMA)_2(H_2O)_3]_n$, *Science (80-.).*, 1999, *283*, 1148–1150.

37. Eddaoudi, M.; Kim, J.; Wachter, J. B.; Chae, H. K.; O'Keeffe, M. and Yaghi, O. M., Porous Metal−Organic Polyhedra: 25 Å Cuboctahedron Constructed from 12 $Cu_2(CO_2)_4$ Paddle-Wheel Building Blocks, *J. Am. Chem. Soc.*, 2001, *123*, 4368–4369.

38. Moulton, B.; Lu, J.; Mondal, A. and Zaworotko, M. J., Nanoballs: nanoscale faceted polyhedra with large windows and cavities, *Chem. Commun.*, 2001, 863–864.

39. Gosselin, E. J.; Rowland, C. A.; Balto, K. P.; Yap, G. P. A. and Bloch, E. D., Design and Synthesis of Porous Nickel(II) and Cobalt(II) Cages, *Inorg. Chem.*, 2018, *57*, 11847–11850.

40. Rowland, C. A.; Lorzing, G. R.; Gosselin, E. J.; Trump, B. A.; Yap, G. P. A.; Brown, C. M. and Bloch, E. D., Methane Storage in Paddlewheel-Based Porous Coordination Cages, *J. Am. Chem. Soc.*, 2018, *140*, 11153–11157.

41. Young, M. D.; Zhang, Q. and Zhou, H.-C., Metal–organic polyhedra constructed from dinuclear ruthenium paddlewheels, *Inorganica Chim. Acta*, 2015, *424*, 216–220.

42. Park, J.; Perry, Z.; Chen, Y.-P.; Bae, J. and Zhou, H.-C., Chromium(II) Metal–Organic Polyhedra as Highly Porous Materials, *ACS Appl. Mater. Interfaces*, 2017, *9*, 28064–28068.

43. Li, J.-R.; Timmons, D. J. and Zhou, H.-C., Interconversion between Molecular Polyhedra and Metal−Organic Frameworks, *J. Am. Chem. Soc.*, 2009, *131*, 6368–6369.

44. Li, J.-R.; Yakovenko, A. A.; Lu, W.; Timmons, D. J.; Zhuang, W.; Yuan, D. and Zhou, H.-C., Ligand Bridging-Angle-Driven Assembly of Molecular Architectures Based on Quadruply Bonded Mo−Mo Dimers, *J. Am. Chem. Soc.*, 2010, *132*, 17599–17610.

45. Li, J.-R. and Zhou, H.-C., Metal-Organic Hendecahedra Assembled from Dinuclear Paddlewheel Nodes and Mixtures of Ditopic Linkers with 120 and 90° Bend Angles, *Angew. Chemie Int. Ed.*, 2009, *48*, 8465–8468.

46. Brückner, C.; Powers, R. E. and Raymond, K. N., Symmetry-Driven Rational Design of a Tetrahedral Supramolecular Ti_4L_4 Cluster, *Angew. Chemie Int. Ed.*, 1998, *37*, 1837–1839.

47. Caulder, D. L.; Powers, R. E.; Parac, T. N. and Raymond, K. N., The Self-Assembly of a Predesigned Tetrahedral M4L6 Supramolecular Cluster, *Angew. Chemie Int. Ed.*, 1998, *37*, 1840–1843.

48. Hong, C. M.; Morimoto, M.; Kapustin, E. A.; Alzakhem, N.; Bergman, R. G.; Raymond, K. N. and Toste, F. D., Deconvoluting the Role of Charge in a Supramolecular Catalyst, *J. Am. Chem. Soc.*, 2018, *140*, 6591–6595.

49. Pluth, M. D.; Johnson, D. W.; Szigethy, G.; Davis, A. V.; Teat, S. J.; Oliver, A. G.; Bergman, R. G. and Raymond, K. N., Structural Consequences of Anionic Host−Cationic Guest Interactions in a Supramolecular Assembly, *Inorg. Chem.*, 2009, *48*, 111–120.

50. Johnson, D. W. and Raymond, K. N., The self-assembly of a $[Ga_4L_6]^{12-}$ tetrahedral cluster thermodynamically driven by host-guest interactions, *Inorg. Chem.*, 2001, *40*, 5157–5161.

51. Clegg, J. K.; Lindoy, L. F.; Moubaraki, B.; Murray, K. S. and McMurtrie, J. C., Triangles and tetrahedra: metal directed self-assembly of metallo-supramolecular structures incorporating bis-β-diketonato ligands, *Dalt. Trans.*, 2004, 2417–2423.

52. Clegg, J. K.; Li, F.; Jolliffe, K. A.; Meehan, G. V. and Lindoy, L. F., An expanded neutral M_4L_6 cage that encapsulates four tetrahydrofuran molecules, *Chem. Commun.*, 2011, *47*, 6042.

53. Constable, E. C., Expanded ligands – An assembly principle for supramolecular chemistry, *Coord. Chem. Rev.*, 2008, *252*, 842–855.

54. Whitesides, G. M. and Grzybowski, B., Self-assembly at all scales, *Science (80-.).*, 2002, 295, 2418–2421.

55. Swiegers, G. F. and Malefetse, T. J., Classification of Coordination Polygons and Polyhedra According to Their Mode of Self-Assembly, *Chem. - A Eur. J.*, 2001, *7*, 3636–3643.

56. Fujita, M.; Umemoto, K.; Yoshizawa, M.; Fujita, N.; Kusukawa, T. and Biradha, K., Molecular paneling *via* coordination, *Chem. Commun.*, 2001, 509–518.

57. Fujita, M., Molecular Paneling Through Metal-Directed Self-Assembly. In: *Molecular Self-Assembly Organic Versus Inorganic Approaches*, Springer Berlin Heidelberg, 2007, pp. 177–201.

58. Yan, Y.; Huang, J. and Tang, B. Z., Kinetic trapping – a strategy for directing the self-assembly of unique functional nanostructures, *Chem. Commun.*, 2016, *52*, 11870–11884.

59. Varela, A. E.; England, K. A. and Cavagnero, S., Kinetic trapping in protein folding, *Protein Eng. Des. Sel.*, 2019, *32*, 103–108.

60. Fujita, D.; Yokoyama, H.; Ueda, Y.; Sato, S. and Fujita, M., Geometrically Restricted Intermediates in the Self-Assembly of an $M_{12}L_{24}$ Cuboctahedral Complex, *Angew. Chemie Int. Ed.*, 2015, *54*, 155–158.

61. Jacopozzi, P. and Dalcanale, E., Metal-Induced Self-Assembly of Cavitand-Based Cage Molecules, *Angew. Chemie (International Ed. English)*, 1997, *36*, 613–615.

62. Fochi, F.; Jacopozzi, P.; Wegelius, E.; Rissanen, K.; Cozzini, P.; Marastoni, E.; Fisicaro, E.; Manini, P.; Fokkens, R. and Dalcanale, E., Self-assembly and anion encapsulation properties of cavitand-based coordination cages, *J. Am. Chem. Soc.*, 2001, *123*, 7539–7552.

63. Kobayashi, K.; Yamada, Y.; Yamanaka, M.; Sei, Y. and Yamaguchi, K., Complete selection of a self-assembling homo- or hetero-cavitand cage *via* metal coordination based on ligand tuning, *J. Am. Chem. Soc.*, 2004, *126*, 13896–13897.

64. Haino, T.; Kobayashi, M.; Chikaraishi, M. and Fukazawa, Y., A new self-assembling capsule via metal coordination, *Chem. Commun.*, 2005, 2321–2323.

65. Pirondini, L.; Bertolini, F.; Cantadori, B.; Ugozzoli, F.; Massera, C. and Dalcanale, E., Design and self-assembly of wide and robust coordination cages, *Proc. Natl. Acad. Sci. U. S. A.*, 2002, *99*, 4911–4915.

66. Pinalli, R.; Boccini, F. and Dalcanale, E., Cavitand-Based Coordination Cages: Achievements and Current Challenges, *Isr. J. Chem.*, 2011, *51*, 781–797.

67. Paul, R. L.; Bell, Z. R.; Jeffery, J. C.; McCleverty, J. A. and Ward, M. D., Anion-templated self-assembly of tetrahedral cage complexes of cobalt(II) with bridging ligands containing two bidentate pyrazolyl-pyridine binding sites., *Proc. Natl. Acad. Sci. U. S. A.*, 2002, *99*, 4883–8.

68. Fleming, J. S.; Mann, K. L. V.; Carraz, C.-A.; Psillakis, E.; Jeffery, J. C.; McCleverty, J. A. and Ward, M. D., Anion-Templated Assembly of a Supramolecular Cage Complex, *Angew. Chemie Int. Ed.*, 1998, *37*, 1279–1281.

69. Bell, Z. R.; Harding, L. P. and Ward, M. D., Self-assembly of a molecular M8L12 cube having S6 symmetry, *Chem. Commun.*, 2003, *3*, 2432–2433.

70. Suzuki, K.; Tominaga, M.; Kawano, M. and Fujita, M., Self-assembly of an M_6L_{12} coordination cube, *Chem. Commun.*, 2009, 1638.

71. Tominaga, M.; Suzuki, K.; Kawano, M.; Kusukawa, T.; Ozeki, T.; Sakamoto, S.; Yamaguchi, K. and Fujita, M., Finite, Spherical Coordination Networks that Self-Organize from 36 Small Components, *Angew. Chemie Int. Ed.*, 2004, *43*, 5621–5625.

72. Sun, Q.-F.; Iwasa, J.; Ogawa, D.; Ishido, Y.; Sato, S.; Ozeki, T.; Sei, Y.; Yamaguchi, K. and Fujita, M., Self-assembled $M_{24}L_{48}$ polyhedra and their sharp structural switch upon subtle ligand variation., *Science*, 2010, *328*, 1144–7.

73. Bunzen, J.; Iwasa, J.; Bonakdarzadeh, P.; Numata, E.; Rissanen, K.; Sato, S. and Fujita, M., Self-Assembly of $M_{24}L_{48}$ Polyhedra Based on Empirical Prediction, *Angew. Chemie Int. Ed.*, 2012, *51*, 3161–3163.

74. Yokoyama, H.; Ueda, Y.; Fujita, D.; Sato, S. and Fujita, M., Finely Resolved Threshold for the Sharp $M_{12}L_{24}$ / $M_{24}L_{48}$ Structural Switch in Multi-Component M_nL_{2n} Polyhedral Assemblies: X-ray, MS, NMR, and Ultracentrifugation Analyses, *Chem. - An Asian J.*, 2015, *10*, 2292–2295.

75. Fujita, D.; Ueda, Y.; Sato, S.; Yokoyama, H.; Mizuno, N.; Kumasaka, T. and Fujita, M., Self-Assembly of $M_{30}L_{60}$ Icosidodecahedron, *Chem*, 2016, *1*, 91–101.

76. Fujita, D.; Ueda, Y.; Sato, S.; Mizuno, N.; Kumasaka, T. and Fujita, M., Self-assembly of tetravalent Goldberg polyhedra from 144 small components, *Nature*, 2016, *540*, 563–566.

77. Sun, Q.-F.; Murase, T.; Sato, S. and Fujita, M., A Sphere-in-Sphere Complex by Orthogonal Self-Assembly, *Angew. Chemie Int. Ed.*, 2011, *50*, 10318–10321.

78. Fujita, M.; Oguro, D.; Miyazawa, M.; Oka, H.; Yamaguchi, K. and Ogura, K., Self-assembly of ten molecules into nanometre-sized organic host frameworks, *Nature*, 1995, *378*, 469–471.

79. Ibukuro, F.; Kusukawa, T. and Fujita, M., A thermally switchable molecular lock. Guest-templated synthesis of a kinetically stable nanosized cage, *J. Am. Chem. Soc.*, 1998, *120*, 8561–8562.

80. Kusukawa, T. and Fujita, M., Self-assembled M_6L_4-type coordination nanocage with 2,2′-bipyridine ancillary ligands. Facile crystallization and X-ray analysis of shape-selective enclathration of neutral guests in the cage, *J. Am. Chem. Soc.*, 2002, *124*, 13576–13582.

81. Fang, Y.; Murase, T.; Sato, S. and Fujita, M., Noncovalent Tailoring of the Binding Pocket of Self-Assembled Cages by Remote Bulky Ancillary Groups, *J. Am. Chem. Soc.*, 2013, *135*, 613–615.

82. Yoshizawa, M.; Kusukawa, T.; Kawano, M.; Ohhara, T.; Tanaka, I.; Kurihara, K.; Niimura, N. and Fujita, M., Endohedral clusterization of ten water molecules into a 'molecular ice' within the hydrophobic pocket of a self-assembled cage, *J. Am. Chem. Soc.*, 2005, *127*, 2798–2799.

83. Cai, L.-X.; Li, S.-C.; Yan, D.-N.; Zhou, L.-P.; Guo, F. and Sun, Q.-F., Water-Soluble Redox-Active Cage Hosting Polyoxometalates for Selective Desulfurization Catalysis, *J. Am. Chem. Soc.*, 2018, *140*, 4869–4876.

84. Fujita, M.; Yu, S.-Y.; Kusukawa, T.; Funaki, H.; Ogura, K. and Yamaguchi, K., Self-Assembly of Nanometer-Sized Macrotricyclic Complexes from Ten Small Component Molecules, *Angew. Chemie Int. Ed.*, 1998, *37*, 2082–2085.

85. Yu, S.-Y.; Kusukawa, T.; Biradha, K. and Fujita, M., Hydrophobic Assembling of a Coordination Nanobowl into a Dimeric Capsule Which Can Accommodate up to Six Large Organic Molecules, *J. Am. Chem. Soc.*, 2000, *122*, 2665–2666.

86. Takeda, N.; Umemoto, K.; Yamaguchi, K. and Fujita, M., A nanometre-sized hexahedral coordination capsule assembled from 24 components, *Nature*, 1999, *398*, 794–796.

87. Umemoto, K.; Tsukui, H.; Kusukawa, T.; Biradha, K. and Fujita, M., Molecular Paneling by Coordination: An $M_{15}L_6$ Hexahedral Molecular Capsule having Clefts for Reversible Guest Inclusion, *Angew. Chemie Int. Ed.*, 2001, *40*, 2620–2622.

88. Yamanoi, Y.; Sakamoto, Y.; Kusukawa, T.; Fujita, M.; Sakamoto, S. and Yamaguchi, K., Dynamic assembly of coordination boxes from (en)Pd(II) unit and a rectangular panel-like ligand: NMR, CSI-MS, and X-ray studies, *J. Am. Chem. Soc.*, 2001, *123*, 980–981.

89. Fujita, N.; Biradha, K.; Fujita, M.; Sakamoto, S. and Yamaguchi, K., A Porphyrin Prism: Structural Switching Triggered by Guest Inclusion, *Angew. Chemie Int. Ed.*, 2001, *40*, 1718–1721.

90. Caskey, D. C.; Yamamoto, T.; Addicott, C.; Shoemaker, R. K.; Vacek, J.; Hawkridge, A. M.; Muddiman, D. C.; Kottas, G. S.; Michl, J. and Stang, P. J., Coordination-driven face-directed self-assembly of trigonal prisms. Face-based conformational chirality, *J. Am. Chem. Soc.*, 2008, *130*, 7620–7628.

91. Bar, A. K.; Chakrabarty, R.; Mostafa, G. and Mukherjee, P. S., Self-Assembly of a Nanoscopic $Pt_{12}Fe_{12}$ Heterometallic Open Molecular Box Containing Six Porphyrin Walls, *Angew. Chemie Int. Ed.*, 2008, *47*, 8455–8459.

92. Hiraoka, S.; Harano, K.; Shiro, M.; Ozawa, Y.; Yasuda, N.; Toriumi, K. and Shionoya, M., Isostructural Coordination Capsules for a Series of 10 Different d^5–d^{10} Transition-Metal Ions, *Angew. Chemie Int. Ed.*, 2006, *45*, 6488–6491.

93. Fujita, M.; Nagao, S. and Ogura, K., Guest-Induced Organization of a Three-Dimensional Palladium(II) Cagelike Complex. A Prototype for 'Induced-Fit' Molecular Recognition, *J. Am. Chem. Soc.*, 1995, *117*, 1649–1650.

94. Chand, D. K.; Biradha, K.; Fujita, M.; Sakamoto, S. and Yamaguchi, K., A molecular sphere of octahedral symmetry, *Chem. Commun.*, 2002, 2486–2487.

95. Sun, W.-Y.; Fan, J.; Okamura, T.; Xie, J.; Yu, K.-B. and Ueyama, N., Self-Assembly of Frameworks with Specific Topologies: Construction and Anion Exchange Properties of M_3L_2 Architectures by Tripodal Ligands and Silver(I) Salts, *Chem. - A Eur. J.*, 2001, *7*, 2557–2562.

96. Meng, W.-L.; Fan, J.; Okamura, T.; Kawaguchi, H.; Lv, Y.; Sun, W.-Y. and Ueyama, N., Molecular Cage, One-Dimensional Tube and Two-Dimensional Polycatenane obtained from Reactions of Flexible Tripodal Ligand 1,3,5-Tris(imidazol-1-ylmethyl)-2,4,6-trimethylbenzene with Copper Salts, *Zeitschrift für Anorg. und Allg. Chemie*, 2006, *632*, 1890–1896.

97. Fan, J.; Sun, W.-Y.; Okamura, T.; Xie, J.; Tang, W.-X. and Ueyama, N., First example of a dumbbell-like architecture containing M_3L_2 cages and terephthalate anions, *New J. Chem.*, 2002, *26*, 199–201.

98. Liu, H. K. and Tong, X., Assembly of supermolecular complexes from the tripodal ligand titmb: assembly of a large M_6L_8 cage from 14 components, *Chem. Commun.*, 2002, *2*, 1316–1317.

99. Hong, M.; Zhao, Y.; Su, W.; Cao, R.; Fujita, M.; Zhou, Z. and Chan, A. S. C., A nanometer-sized metallosupramolecular cube with O_h symmetry, *J. Am. Chem. Soc.*, 2000, *122*, 4819–4820.

100. Baxter, P.; Lehn, J.-M.; DeCian, A. and Fischer, J., Multicomponent Self-Assembly: Spontaneous Formation of a Cylindrical Complex from Five Ligands and Six Metal Ions, *Angew. Chemie Int. Ed. English*, 1993, *32*, 69–72.

101. Baxter, P. N. W.; Lehn, J.-M.; Kneisel, B. O.; Baum, G. and Fenske, D., The Designed Self-Assembly of Multicomponent and Multicompartmental Cylindrical Nanoarchitectures, *Chem. - A Eur. J.*, 1999, *5*, 113–120.

102. Baxter, P. N. W.; Lehn, J.-M.; Baum, G. and Fenske, D., The Design and Generation of Inorganic Cylindrical Cage Architectures by Metal-Ion-Directed Multicomponent Self-Assembly, *Chem. - A Eur. J.*, 1999, *5*, 102–112.

103. Kumazawa, K.; Biradha, K.; Kusukawa, T.; Okano, T. and Fujita, M., Multicomponent Assembly of a Pyrazine-Pillared Coordination Cage That Selectively Binds Planar Guests by Intercalation, *Angew. Chemie Int. Ed.*, 2003, *42*, 3909–3913.

104. Yoshizawa, M.; Nakagawa, J.; Kumazawa, K.; Nagao, M.; Kawano, M.; Ozeki, T. and Fujita, M., Discrete Stacking of Large Aromatic Molecules within Organic-Pillared Coordination Cages, *Angew. Chemie Int. Ed.*, 2005, *44*, 1810–1813.

105. Yamauchi, Y.; Yoshizawa, M. and Fujita, M., Engineering stacks of aromatic rings by the interpenetration of self-assembled coordination cages, *J. Am. Chem. Soc.*, 2008, *130*, 5832–5833.

106. Ono, K.; Yoshizawa, M.; Kato, T. and Fujita, M., Three-metal-center spin interactions through the intercalation of metal azaporphines and porphines into an organic pillared coordination box, *Chem. Commun.*, 2008, 2328.

107. Yamauchi, Y.; Yoshizawa, M.; Akita, M. and Fujita, M., Engineering double to quintuple stacks of a polarized aromatic in confined cavities, *J. Am. Chem. Soc.*, 2010, *132*, 960–966.

108. Zheng, Y. R.; Zhao, Z.; Wang, M.; Ghosh, K.; Pollock, J. B.; Cook, T. R. and Stang, P. J., A facile approach toward multicomponent supramolecular structures: Selective self-assembly via charge separation, *J. Am. Chem. Soc.*, 2010, *132*, 16873–16882.

109. Wang, M.; Zheng, Y. R.; Ghosh, K. and Stang, P. J., Metallosupramolecular tetragonal prisms via multicomponent coordination-driven template-free self-assembly, *J. Am. Chem. Soc.*, 2010, *132*, 6282–6283.

110. Wang, M.; Zheng, Y.-R.; Cook, T. R. and Stang, P. J., Construction of Functionalized Metallosupramolecular Tetragonal Prisms via Multicomponent Coordination-Driven Self-Assembly, *Inorg. Chem.*, 2011, *50*, 6107–6113.

111. Wang, M.; Lan, W.-J.; Zheng, Y.-R.; Cook, T. R.; White, H. S. and Stang, P. J., Post-Self-Assembly Covalent Chemistry of Discrete Multicomponent Metallosupramolecular Hexagonal Prisms, *J. Am. Chem. Soc.*, 2011, *133*, 10752–10755.

112. Zhao, Z.; Zheng, Y.-R.; Wang, M.; Pollock, J. B. and Stang, P. J., Construction of Hexagonal Prisms of Variable Size *via* Coordination-Driven Multicomponent Self-Assembly, *Inorg. Chem.*, 2010, *49*, 8653–8655.

113. Campbell, V. and Nitschke, J., Complex Systems from Simple Building Blocks via Subcomponent Self-Assembly, *Synlett*, 2008, *2008*, 3077–3090.

114. Nitschke, J. R., Construction, Substitution, and Sorting of Metallo-organic Structures *via* Subcomponent Self-Assembly, *Acc. Chem. Res.*, 2007, *40*, 103–112.

115. Nitschke, J. R., Mutual Stabilization between Imine Ligands and Copper(I) Ions in Aqueous Solution, *Angew. Chemie Int. Ed.*, 2004, *43*, 3073–3075.

116. Sarma, R. J.; Otto, S. and Nitschke, J. R., Disulfides, Imines, and Metal Coordination within a Single System: Interplay between Three Dynamic Equilibria, *Chem. - A Eur. J.*, 2007, *13*, 9542–9546.

117. Mal, P.; Schultz, D.; Beyeh, K.; Rissanen, K. and Nitschke, J. R., An Unlockable-Relockable Iron Cage by Subcomponent Self-Assembly, *Angew. Chemie Int. Ed.*, 2008, *47*, 8297–8301.

118. Meng, W.; Breiner, B.; Rissanen, K.; Thoburn, J. D.; Clegg, J. K. and Nitschke, J. R., A Self-Assembled M_8L_6 Cubic Cage that Selectively Encapsulates Large Aromatic Guests, *Angew. Chemie Int. Ed.*, 2011, *50*, 3479–3483.

119. Bilbeisi, R. A.; Clegg, J. K.; Elgrishi, N.; Hatten, X. de; Devillard, M.; Breiner, B.; Mal, P. and Nitschke, J. R., Subcomponent Self-Assembly and Guest-Binding Properties of Face-Capped $Fe_4L_4^{8+}$ Capsules, *J. Am. Chem. Soc.*, 2012, *134*, 5110–5119.

120. Smulders, M. M. J.; Jiménez, A. and Nitschke, J. R., Integrative Self-Sorting Synthesis of a $Fe_8Pt_6L_{24}$ Cubic Cage, *Angew. Chemie Int. Ed.*, 2012, *51*, 6681–6685.

121. Ziegler, M.; Brumaghim, J. L. and Raymond, K. N., Stabilization of a Reactive Cationic Species by Supramolecular Encapsulation, *Angew. Chemie*, 2000, *39*, 4119–4121.

122. Brumaghim, J.; Michels, M. and Raymond, K., Hydrophobic Chemistry in Aqueous Solution: Stabilization and Stereoselective Encapsulation of Phosphonium Guests in a Supramolecular Host, *European J. Org. Chem.*, 2004, *2004*, 4552–4559.

123. Brumaghim, J.; Michels, M.; Pagliero, D. and Raymond, K., Encapsulation and Stabilization of Reactive Aromatic Diazonium Ions and the Tropylium Ion Within a Supramolecular Host, *European J. Org. Chem.*, 2004, *2004*, 5115–5118.

124. Dong, V. M.; Fiedler, D.; Carl, B.; Bergman, R. G. and Raymond, K. N., Molecular Recognition and Stabilization of Iminium Ions in Water, *J. Am. Chem. Soc.*, 2006, *128*, 14464–14465.

125. Fiedler, D.; Bergman, R. G. and Raymond, K. N., Stabilization of reactive organometallic intermediates inside a self-assembled nanoscale host, *Angew. Chemie - Int. Ed.*, 2006, *45*, 745–748.

126. Mal, P.; Breiner, B.; Rissanen, K. and Nitschke, J. R., White Phosphorus Is Air-Stable Within a Self-Assembled Tetrahedral Capsule, *Science (80-.).*, 2009, *324*, 1697–1699.

127. Riddell, I. A.; Smulders, M. M. J.; Clegg, J. K. and Nitschke, J. R., Encapsulation, storage and controlled release of sulfur hexafluoride from a metal-organic capsule, *Chem. Commun.*, 2011, *47*, 457–459.

128. Preston, D.; Lewis, J. E. M. and Crowley, J. D., Multicavity $[Pd_nL_4]^{2n+}$ Cages with Controlled Segregated Binding of Different Guests, *J. Am. Chem. Soc.*, 2017, *139*, 2379–2386.

129. Glasson, C. R. K.; Clegg, J. K.; McMurtrie, J. C.; Meehan, G. V.; Lindoy, L. F.; Motti, C. A.; Moubaraki, B.; Murray, K. S. and Cashion, J. D., Unprecedented encapsulation of a $[Fe^{III}Cl_4]^-$ anion in a cationic $[Fe^{II}_4L_6]^{8+}$ tetrahedral cage derived from 5,5‴-dimethyl-2,2′:5′,5″:2″,2‴-quaterpyridine, *Chem. Sci.*, 2011, *2*, 540–543.

130. Kishi, N.; Li, Z.; Sei, Y.; Akita, M.; Yoza, K.; Siegel, J. S. and Yoshizawa, M., Wide-Ranging Host Capability of a Pd^{II}-Linked M_2L_4 Molecular Capsule with an Anthracene Shell, *Chem. - A Eur. J.*, 2013, *19*, 6313–6320.

131. Yamashina, M.; Akita, M.; Hasegawa, T.; Hayashi, S. and Yoshizawa, M., A polyaromatic nanocapsule as a sucrose receptor in water, *Sci. Adv.*, 2017, *3*, e1701126.

132. Yamashina, M.; Matsuno, S.; Sei, Y.; Akita, M. and Yoshizawa, M., Recognition of Multiple Methyl Groups on Aromatic Rings by a Polyaromatic Cavity, *Chem. - A Eur. J.*, 2016, *22*, 14147–14150.

133. Freye, S.; Engelhard, D. M.; John, M. and Clever, G. H., Counterion Dynamics in an Interpenetrated Coordination Cage Capable of Dissolving AgCl, *Chem. - A Eur. J.*, 2013, *19*, 2114–2121.

134. Freye, S.; Michel, R.; Stalke, D.; Pawliczek, M.; Frauendorf, H. and Clever, G. H., Template control over dimerization and guest selectivity of interpenetrated coordination cages, *J. Am. Chem. Soc.*, 2013, *135*, 8476–8479.

135. Cullen, W.; Misuraca, M. C.; Hunter, C. A.; Williams, N. H. and Ward, M. D., Highly efficient catalysis of the Kemp elimination in the cavity of a cubic coordination cage, *Nat. Chem.*, 2016, *8*, 231–236.

136. Hastings, C. J.; Bergman, R. G. and Raymond, K. N., Origins of Large Rate Enhancements in the Nazarov Cyclization Catalyzed by Supramolecular Encapsulation, *Chem. - A Eur. J.*, 2014, *20*, 3966–3973.

137. Hart-Cooper, W. M.; Clary, K. N.; Toste, F. D.; Bergman, R. G. and Raymond, K. N., Selective monoterpene-like cyclization reactions achieved by water exclusion from reactive intermediates in a supramolecular catalyst, *J. Am. Chem. Soc.*, 2012, *134*, 17873–17876.

138. Zhao, C.; Sun, Q. F.; Hart-Cooper, W. M.; Dipasquale, A. G.; Toste, F. D.; Bergman, R. G. and Raymond, K. N., Chiral amide directed assembly of a diastereo- and enantiopure supramolecular host and its application to enantioselective catalysis of neutral substrates, *J. Am. Chem. Soc.*, 2013, *135*, 18802–18805.

139. Jiao, J.; Li, Z.; Qiao, Z.; Li, X.; Liu, Y.; Dong, J.; Jiang, J. and Cui, Y., Design and self-assembly of hexahedral coordination cages for cascade reactions, *Nat. Commun.*, 2018, *9*, 1–8.

140. Yoshizawa, M.; Tamura, M. and Fujita, M., Diels-alder in aqueous molecular hosts: Unusual regioselectivity and efficient catalysis, *Science (80-.).*, 2006, *312*, 251–254.

141. Yoshizawa, M.; Takeyama, Y.; Kusukawa, T. and Fujita, M., Cavity-Directed, Highly Stereoselective [2+2] Photodimerization of Olefins within Self-Assembled Coordination Cages, *Angew. Chemie Int. Ed.*, 2002, *41*, 1347–1349.

142. Yoshizawa, M.; Takeyama, Y.; Okano, T. and Makoto, F., Cavity-Directed Synthesis within a Self-Assembled Coordination Cage: Highly Selective [2+2] Cross-Photodimerization of Olefins, *J. Am. Chem. Soc.*, 2003, *125*, 3243–3247.

143. Zheng, Y. R.; Suntharalingam, K.; Johnstone, T. C. and Lippard, S. J., Encapsulation of Pt(IV) prodrugs within a Pt(II) cage for drug delivery, *Chem. Sci.*, 2015, *6*, 1189–1193.

144. Suzuki, K.; Iida, J.; Sato, S.; Kawano, M. and Fujita, M., Discrete and Well-Defined Hydrophobic Phases Confined in Self-Assembled Spherical Complexes, *Angew. Chemie Int. Ed.*, 2008, *47*, 5780–5782.

145. Lu, Z.; Ronson, T. K. and Nitschke, J. R., Reversible reduction drives anion ejection and C60 binding within an $Fe^{II}_4L_6$ cage, *Chem. Sci.*, 2020, *11*, 1097–1101.

146. Yazaki, K.; Sei, Y.; Akita, M. and Yoshizawa, M., Polycationic-Shelled Capsular and Tubular Nanostructures and Their Anionic-Guest Binding Properties, *Chem. - A Eur. J.*, 2016, *22*, 17557–17561.

147. Müller, P., Practical suggestions for better crystal structures, *Crystallogr. Rev.*, 2009, *15*, 57–83.

148. Spingler, B.; Schnidrig, S.; Todorova, T. and Wild, F., Some thoughts about the single crystal growth of small molecules, *CrystEngComm*, 2012, *14*, 751–757.

149. Davey, R. and Garside, J., *From Molecules to Crystallizers - An Introduction to Crystallization*, 1st edition, Oxford University Press, New York, 2000.

150. Beckmann, D. W., Ed., *Crystallization: Basic Consepts and Industrial Applications*, Wiley-VCH Verlag, Weinheim, Germany, 2013.

151. Desiraju, G. R.; Vittal, J. J. and Ramanan, A., *Crystal Engineering: A Textbook*, World Scientific, Singapore, 2011.

152. Coquerel, G., Crystallization of molecular systems from solution: Phase diagrams, supersaturation and other basic concepts, *Chem. Soc. Rev.*, 2014, 43, 2286–2300.

153. Belcher, W. J.; Fabre, M.; Farhan, T. and Steed, J. W., Pyridinium CH···anion and π-stacking interactions in modular tripodal anion binding hosts: ATP binding and solid-state chiral induction, *Org. Biomol. Chem.*, 2006, *4*, 781–786.

154. Sarma, K. P. and Poddar, R. K., A convenient method of preparing nickel(II) thiocyanate and its use in synthesis, *Transit. Met. Chem.*, 1984, *9*, 135–138.

155. Dolomanov, O. V.; Bourhis, L. J.; Gildea, R. J.; Howard, J. A. K. and Puschmann, H., OLEX2: a complete structure solution, refinement and analysis program, *urn:issn:0021-8898*, 2009, *42*, 339–341.

156. Sheldrick, G. M., SHELXT - Integrated space-group and crystal-structure determination, *Acta Crystallogr. Sect. A Found. Crystallogr.*, 2015, *71*, 3–8.

157. Sheldrick, G. M., Crystal structure refinement with SHELXL, *Acta Crystallogr. Sect. C Struct. Chem.*, 2015, *71*, 3–8.

158. MacRae, C. F.; Sovago, I.; Cottrell, S. J.; Galek, P. T. A.; McCabe, P.; Pidcock, E.; Platings, M.; Shields, G. P.; Stevens, J. S.; Towler, M. and Wood, P. A., Mercury 4.0: from visualization to analysis, design and prediction, *urn:issn:1600-5767*, 2020, *53*, 226–235.

159. Olatunde, A. O.; Dorazio, S. J.; Spernyak, J. A. and Morrow, J. R., The NiCEST approach: Nickel(II) ParaCEST MRI contrast agents, *J. Am. Chem. Soc.*, 2012, *134*, 18503–18505.

160. Bertini, I.; Turano, P. and Vila, A. J., Nuclear Magnetic Resonance of Paramagnetic Metalloproteins, *Chem. Rev.*, 1993, *93*, 2833–2932.

161. Groom, C. R.; Bruno, I. J.; Lightfoot, M. P. and Ward, S. C., The Cambridge Structural Database, *urn:issn:2052-5206*, 2016, *72*, 171–179.

162. Bruno, I. J.; Cole, J. C.; Edgington, P. R.; Kessler, M.; Macrae, C. F.; McCabe, P.; Pearson, J. and Taylor, R., New software for searching the Cambridge Structural Database and visualizing crystal structures, *urn:issn:0108-7681*, 2002, *58*, 389–397.

163. Schmidt, A.; Teeter, M.; Weckert, E. and Lamzin, V. S., Crystal structure of small protein crambin at 0.48 Å resolution, *Acta Crystallogr. Sect. F Struct. Biol. Cryst. Commun.*, 2011, *67*, 424–428.

164. Sharff, A. J.; Rodseth, L. E.; Spurlino, J. C. and Quiocho, F. A., Crystallographic Evidence of a Large Ligand-Induced Hinge-Twist Motion between the Two Domains of the Maltodextrin Binding Protein Involved in Active Transport and Chemotaxis, *Biochemistry*, 1992, *31*, 10657–10663.

165. Telmer, P. G. and Shilton, B. H., Structural studies of an engineered zinc biosensor reveal an unanticipated mode of zinc binding, *J. Mol. Biol.*, 2005, *354*, 829–840.

166. Monk, P. M. S., *The Viologens: Physicochemical Properties, Synthesis and Applications of the Salts of 4,4'-Bipyridine*, 1st edition, Wiley, Chichester, UK, 1999.

167. Papadakis, R., Mono- and Di-Quaternized 4,4′-Bipyridine Derivatives as Key Building Blocks for Medium- and Environment-Responsive Compounds and Materials, *Mol. 2020, Vol. 25, Page 1*, 2019, *25*, 1.

168. Shen, Y.; Walters, K. A.; Abboud, K. and Schanze, K. S., Intramolecular charge transfer in pyridinium-substituted Ru-polypyridine complexes, *Inorganica Chim. Acta*, 2000, *300–302*, 414–426.

169. Roy, B.; Zangrando, E. and Mukherjee, P. S., Self-assembly of a redox active water soluble Pd_6L_8 'molecular dice', *Chem. Commun.*, 2016, *52*, 4489–4492.

170. Janiak, C., A critical account on π-π stacking in metal complexes with aromatic nitrogen-containing ligands, *J. Chem. Soc. Dalt. Trans.*, 2000, 3885–3896.

171. Wen, T. and Zhang, J., Rational design of metal boron imidazolate cages to frameworks, *Inorganica Chim. Acta*, 2017, *460*, 89–92.

APPENDIX

Appendix 1. Characterization of $Ni(NO_3)_2 \cdot 2.5\ H_2O$.

In order to determinate the amount of water remaining in $Ni(NO_3)_2 \cdot x\ H_2O$, obtained by drying $Ni(NO_3)_2 \cdot 6\ H_2O$, the pale green solid was analyzed with powder X-ray diffraction and TG / DSC.

Thermal degradation / decomposition of $Ni(NO_3)_2 \cdot 6\ H_2O$ is generally agreed to proceed stepwise through tetra- and dihydrates followed by complicated reactions leading eventually to NiO.[1] No anhydrous $Ni(NO_3)_2$ phase occurs, instead degradation of $Ni(NO_3)_2 \cdot 2\ H_2O$ leads to formation of alkaline $Ni_x(NO_3)_y(OH)_z$ species with varying compositions. Similarly the phase before NiO can be Ni_2O_3, Ni_3O_4 or mixture of both depending on conditions and time. The measured decomposition of $Ni(NO_3)_2 \cdot x\ H_2O$ shows three distinct steps with second and third step being amalgamation of multiple overlapping reactions (Figure A1). As $Ni(NO_3)_2 \cdot x\ H_2O$ is obtained by drying hexahydrate form, no tetrahydrate phase is observed, and instead the first step corresponds to formation of dihydrate phase, while the second step results an alkaline species and third step yields the oxide species. With second phase, assumedly, corresponding to dihydrate species, the first step should be removal of water alone. The observed mass loss of 4.159 % therefore corresponds to removal of around 0.5 water molecules, which would indicate that the composition of the semi-dehydrated salt is $Ni(NO_3)_2 \cdot 2.5\ H_2O$.

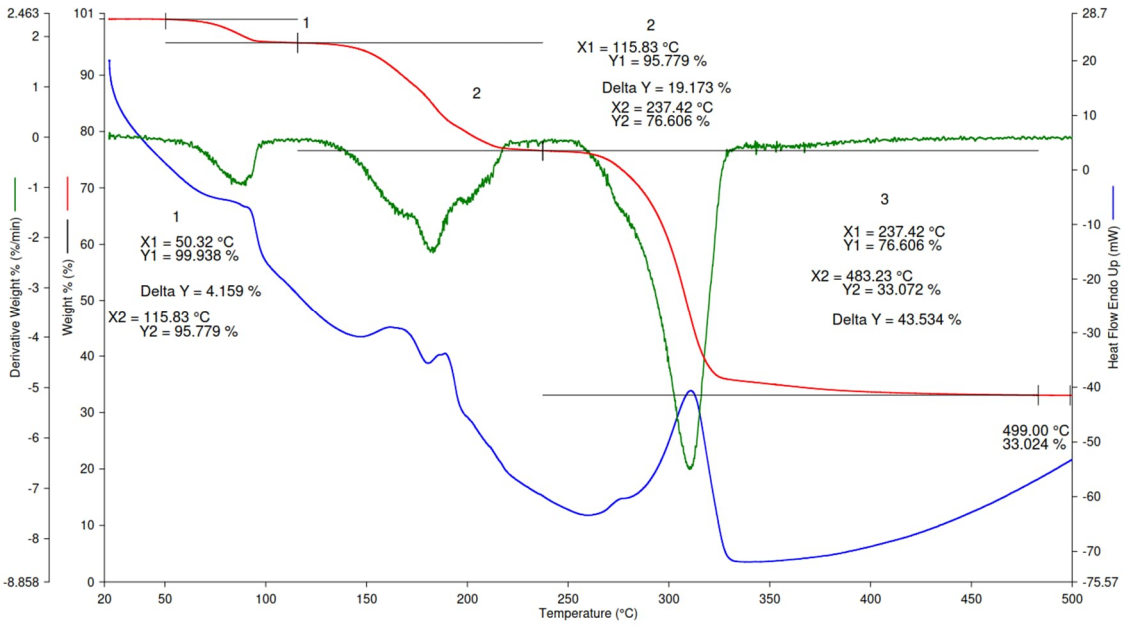

FIGURE A1 Thermal decomposition of $Ni(NO_3)_2 \cdot x\ H_2O$ under nitrogen atmosphere.

The measured powder X-ray diffraction pattern was compared in HighScore program[2] to previously reported[3] nickel(II) salts and was found to correlate with both $Ni(NO_3)_2$ tetra- and dihydrates[4,5] (Figure A2). So instead of obtaining pure tetra- or dihydrate, by drying of the hexahydrate salt, the salt is a mixture of both $Ni(NO_3)_2 \cdot 4\ H_2O$ and $Ni(NO_3)_2 \cdot 2\ H_2O$. According to semi-quantitative analysis, based on, RIR (Reference Intensity Ratio), performed in HighScore, the ratio between $Ni(NO_3)_2$ tetra- and dihydrates is 30:70. This indicates that the composition of obtained dried salt $Ni(NO_3)_2 \cdot x\ H_2O$ is in reality approximately $[Ni(H_2O)_4]_{0.3}[Ni(H_2O)_2]_{0.7}(NO_3)_2$, or if using calculated average level of hydration, around $Ni(NO_3)_2 \cdot 2.6\ H_2O$. This also correlates with the level of hydration observed with TG / DSC, and so the obtained salt $Ni(NO_3)_2 \cdot x\ H_2O$ was deemed to be equivalent for that of hemi(pentahydrate), $Ni(NO_3)_2 \cdot 2.5\ H_2O$, and treated as such moving forward.

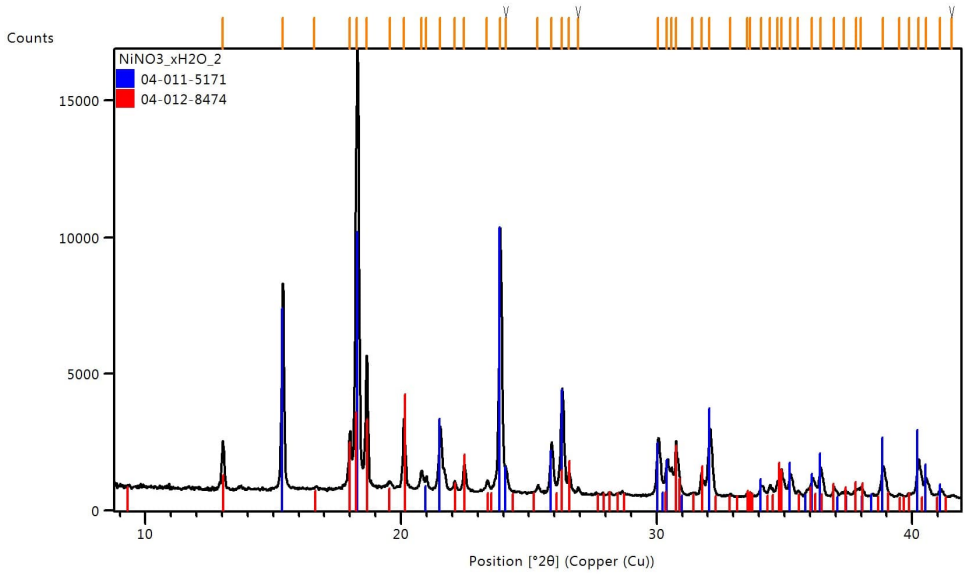

FIGURE A2 Powder X-ray diffraction pattern of $Ni(NO_3)_2 \cdot x\ H_2O$ in comparison with tetrahydrate and dihydrate salts of $Ni(NO_3)_2$, marked by red and blue coloured line bars, respectively.

1. Brockner, W.; Ehrhardt, C. and Gjikaj, M., Thermal decomposition of nickel nitrate hexahydrate, $Ni(NO_3)_2 \cdot 6H_2O$, in comparison to $Co(NO_3)_2 \cdot 6H_2O$ and $Ca(NO_3)_2 \cdot 4H_2O$, *Thermochimica Acta*, 2007, *1*, 64–68.
2. The HighScore suite, T. Degen, M. Sadki, E. Bron, U. König, G. Nénert; *Powder Diffraction* 29 S2, 2014, S13-S18.
3. International Centre for Diffraction Data, ICDD-PDF4+, Release 2021, 12 Campus Boulevard, Newton Square, Pennsylvania USA, 2021
4. Milinski N. and Ribár B., The crystal structure of nickel nitrate dihydrate, $Ni(NO_3)_2 \cdot 2\ H_2O$, *Zeitschrift für Kristallographie - Crystalline Materials*, 1976, *144*, 126-132.
5. Morosin B. and Haseda T., Crystal structure of the β form of $Ni(NO_3)_2 \cdot 4\ H_2O$, *Acta Crystallogr., Sect. B: Struct. Crystallogr. Cryst. Chem.*, 1979, *35*, 2856-2858.

Appendix 2. Structural description of $[Ni(MeCN)_6](PF_6)_2$.

Crystallization of acetonitrile solution of $Ni(PF_6)_2$ via slow vapor diffusion of chloroform yielded purple-blue crystals and X-ray diffraction analysis of crystals revealed a structure of $[Ni(MeCN)_6](PF_6)_2$ (Figure A3a). Compound crystallizes in a trigonal space group $R\bar{3}$ ($a = b = 11.0545(5)$ Å, $c = 16.5827(8)$ Å, $\alpha = \beta = 90°$, $\gamma = 120°$, $V = 1754.95(18)$ Å^3, $Z = 3$). The asymmetric unit contains one crystallographically distinct Ni^{II} atom in a special position (Occup.: 0.16667), one MeCN molecule with full occupancy and one third of a PF_6^- anion with phosphorus atom located in a special position (Occup.: 0.3333) and two fluoride atoms with full occupancy. The $Ni\cdots NCCH_3$ bond distance is 2.062(3) Å and the angle from nickel to CH_3, ∡(Ni–N–CH_3), is 174.64(16)° while the acetonitrile itself is near-linear with ∡(N–C–CH_3) being 179.2(4)°. In crystal lattice, the PF_6^- anions are located between $[Ni(MeCN)_6]^{2+}$ units following order $Ni\cdots PF_6\cdots PF_6\cdots Ni$, which lies parallel to the crystallographic *c*-axis (Figure A3b–c), while similar packing along *a* and *b*-axis is blocked by overlapping MeCN molecules. The distance from Ni^{II} to phosphorus atom in PF_6^- is 5.4548(14) Å, while distance between two PF_6 anions is 5.673(3) Å measured from phosphorus to phosphorus. The $[Ni(MeCN)_6]^{2+}$ units are packed in a three-dimensional 'framework', where methyl ends of MeCN come to close proximity of neighboring Ni^{II} ions with distance between Ni^{II} atoms being 8.4432(2) Å (Figure A3d). The crystallographic data of $[Ni(MeCN)_6](PF_6)_2$ is presented in Table A1.

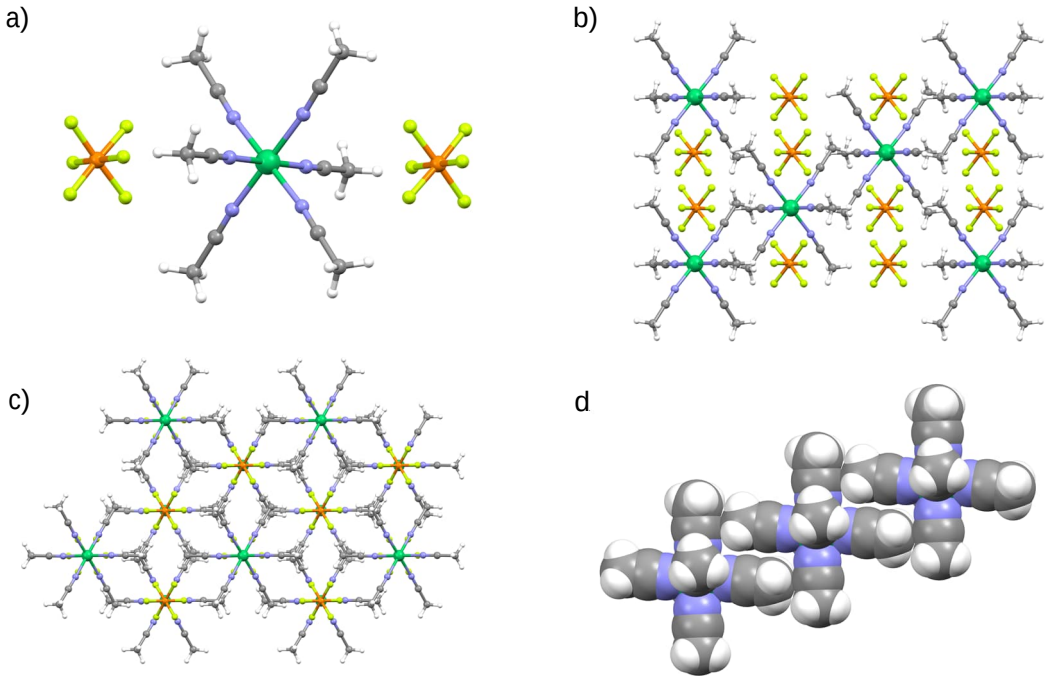

FIGURE A3 a) $[Ni(MeCN)_6](PF_6)_2$, b) packing viewed along *b*-axis, c) packing viewed along the crystallographic *c*-axis and d) close packing of $[Ni(MeCN)_6]^{2+}$ units (only one dimension is shown).

Table A1. Crystallographic data for $[Ni(MeCN)_6](PF_6)_2$.

Compound	$[Ni(MeCN)_6](PF_6)_2$
Empirical formula	$C_{12}H_{18}F_{12}N_6NiP_2$
Formula weight	594.96
Temperature / K	120.00(10)
Crystal system	trigonal
Space group	*R*-3
a / Å	11.0545(5)
b / Å	11.0545(5)
c / Å	16.5827(8)
α / °	90
β / °	90
γ / °	120
Volume / Å^3	1754.95(18)
Z	3
ρ_{calc} g / cm^3	1.689
μ / mm^{-1}	1.073
F(000)	894.0
Crystal size / mm^3	0.245 × 0.142 × 0.129
2Θ range for data collection / °	4.914 to 58.634
Reflections collected	2825
Independent reflections	958 [R_{int} = 0.0222, R_{sigma} = 0.0224]
Data / restraints / parameters	958 / 12 / 52
GooF on F^2	1.073
Final *R* indexes [$I \geq 2\sigma(I)$]	R_1 = 0.0636, wR_2 = 0.1822
Final *R* indexes [all data]	R_1 = 0.0653, wR_2 = 0.1846
Largest diff. peak / hole / e Å^{-3}	1.88 / -0.86

Appendix 3. Structural description of [Cu(L2)(MeCN)]$(PF_6)_4$ (M1)

Acetonitrile solution of (L2)·$(PF_6)_3$ was stirred overnight at room temperature in the presence of excess solid CuSCN, after which any solids were filtered off. Slow vapor diffusion of $CHCl_3$ yielded orange-yellow crystals and the X-ray diffraction analysis revealed a [Cu(L2)(MeCN)]$(PF_6)_4$ (M1) 1D-MOF structure exhibiting a triclinic space group $P\bar{1}$ (a = 11.0322(5) Å, b = 18.9657(11) Å, c = 19.3071(9) Å, α = 92.132(4)°, β = 91.364(4)°, γ = 93.169(4)°, V = 4029.4(4) Å^3, Z = 2). Asymmetric unit holds of one whole ligand, Cu^I atom, four PF_6^- anions, two MeCN and two $CHCl_3$ molecules (Figure A4a). The tetrahedral metal node is bonded to one MeCN molecule and three ligands in such a way that each ligand is bonded via different bpy arm (N2, N4 or N6). This essentially creates two alternating loops between two ligands and two metal nodes that in turn creates the one-dimensional framework (Figure A4b). The ethyl-groups of the ligand are in all-*trans* -conformation and the bowl is occupied by PF_6^- anion located 4.791(3) Å from centroid of the benzene core to phosphorus atom in PF_6^-. Another PF_6^- anion is located near Cu^I node, while the remaining two anions are located around the +1-valent nitrogen atoms of bpy arms. The bend angle of bpy arms is between 114.06–116.15° and the distance between zero-valent nitrogen atoms is 11.820(9) Å for d(N2–N4), 12.194(9) Å for d(N4–N6) and 15.840(8) Å for d(N2–N6), respectively.

In the crystal lattice, methylene-bridge (C24) of one of the bpy arm comes near to another ethyl-group in different ligand, opposite to C24, with distance from methylene-bridge to end of ethyl-group being 4.874(7) Å ($d_{C24–C8}$). The MeCN bonded to metal node is pointing roughly towards its symmetry equivalent on another framework with distance from methyl end to Cu^I atom being 6.929(10) Å and the angle of ∡(Cu–CH_3–Cu') being 145.1(2)°. The packing of M1 in crystal lattice is shown in Figure A5 and crystallographic data is presented in Table A2.

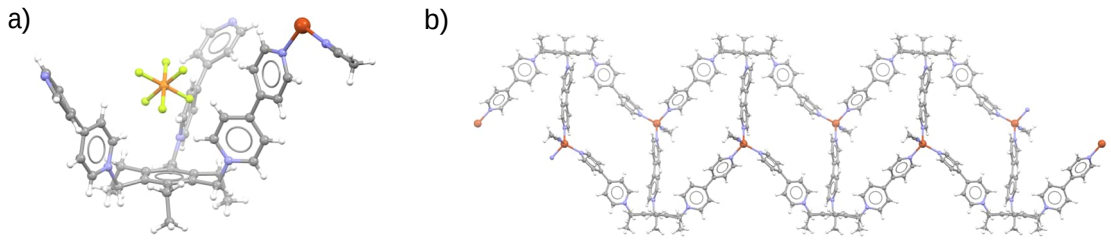

FIGURE A4 a) Monomer of M1 with encapsulated PF_6^- anion and b) 1D framework of M1. Free solvents and anions omitted for clarity.

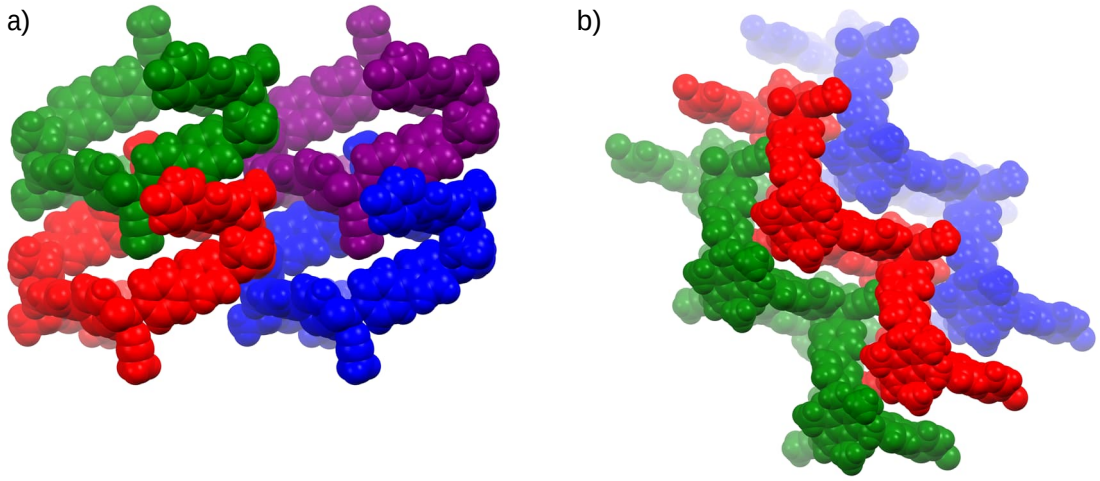

FIGURE A5 Packing of M1 viewed along the crystallographic a) *b*-axis and b) (-101) lattice plane. Free solvents and anions omitted for clarity.

Table A2. Crystallographic data for $[Cu(L2)(MeCN)](PF_6)_4$ (M1)

Compound	$[Cu(L2)(MeCN)](PF_6)_4$ (M1)
Empirical formula	$C_{51}H_{53}Cl_6CuF_{24}N_8P_4$
Formula weight	1634.13
Temperature / K	120.01(10)
Crystal system	triclinic
Space group	*P*-1
a / Å	11.0322(5)
b / Å	18.9657(11)
c / Å	19.3071(9)
α / °	92.132(4)
β / °	91.364(4)
γ / °	93.169(4)
Volume / Å^3	4029.4(4)
Z	2
ρ_{calc} g / cm^3	1.347
μ / mm^{-1}	3.791
F(000)	1644.0
Crystal size / mm^3	0.244 × 0.113 × 0.043
2Θ range for data collection / °	4.67 to 155.076
Reflections collected	33897
Independent reflections	16562 [R_{int} = 0.0743, R_{sigma} = 0.0927]
Data / restraints / parameters	16562 / 54 / 924
GOF on F^2	1.093
Final *R* indexes [$I \geq 2\sigma(I)$]	R_1 = 0.1074, wR_2 = 0.2982
Final *R* indexes [all data]	R_1 = 0.1431, wR_2 = 0.3457
Largest diff peak / hole / e Å^{-3}	1.78 / -1.34

Appendix 4. $[Ni_6(L2)_8Cl_{11}(NCS)_8(PF_6)](PF_6)_{15}Cl$ (C10)

Mixing MeCN / MeOH solution containing C4 cage unit and methanol solution of NH_4NCS in 1:12 ratio followed by slow vapor diffusion of $CHCl_3$ yielded blueish crystals and X-ray diffraction analysis of said crystals revealed a $[Ni_6(L2)_8Cl_{11}(NCS)_8(PF_6)](PF_6)_{15}Cl$ (C10) cube-like structure (Figure A6a) crystallizing in triclinic space group $P\bar{1}$ (a = 27.9733(5) Å, b = 28.1904(6) Å, c = 28.2330(5) Å, α = 79.961(2)°, β = 70.193(2)°, γ = 77.463(2)°, V = 20 323.9(7) Å^3, Z = 1). Asymmetric unit contains one half of the C10 cage unit with three crystallographically distinct Ni^{II} ions (Ni1, Ni2 and Ni3) each of which exhibit an octahedral coordination geometry where the four equatorial sites are occupied by ligands bpy arms and the two axial sites are occupied by 8 thiocyanate anions and 4 chloride anions all sharing the same 12 axial sites (Figure A6b-d). The bond lengths varied between 1.977–2.063 Å for d(Ni–NCS) and 2.194–2.373 Å for d(Ni–Cl). The distances between diagonal Ni^{II} ions are 21.105(3) Å for d_d(Ni1–Ni1'), 20.651(3) Å for d_d(Ni2–Ni2'), and 20.482(3) Å for d_d(Ni3–Ni3') respectively, while the distance between nearest Ni^{II} nodes are between 14.257–14.993 Å. The bridging angles between coordinated ligands are 179.0(3)° / 177.3(3)° for ∡(L–Ni1–L), 179.1(3)° / 178.0(3)° for ∡(L–Ni2–L) and 177.7(3)° / 178.8(3)° for ∡(L–Ni3–L), presented as $(L_a–M–L_c) / (L_b–M–L_d)$.

All expect one of the ligands possess all-*trans*-conformation regarding the ethyl-groups, with the bent angles of bpy arms being between of 111.5–115.5°. Two of 'bowls' are occupied by overlapping chlorides and PF_6^- anions with approximate occupancies of 0.75:0.25 (Cl^-:PF_6^-), while the rest encapsulate only chlorides. Encapsulated chlorides lie between 3.994–4.996 Å from benzyl ring centroid to, whereas PF_6 anions are located between 5.126–5.151 Å from benzyl ring centroid to phosphorus of the anion. No considerable disorder was observed in the M_6L_8 skeleton itself, but thiocyanate anions coordinated to the metal nodes are disordered over two or three orientations similarly thiocyanate disorder which was observed with C6 cage unit (see section 6.2.7). No free exo- or endohedral thiocyanate anions were observed, and all of the expected 36 anions (8x NCS^-, 16x PF_6^- and 12x Cl^-) could be assigned. Several solvent molecules are disordered among themselves with varying degree of disorder with $CHCl_3$ being most prominent. Overall, 16.1 % of unit cell volume remains unassigned according to solvent accessible surface calculated in Mercury as shown in Figure A6e.

In crystal lattice, the individual C10 cage units are packed similar to simple cubic packing model of regular spheres (Figure A6f-g) and each of the metal nodes from different C10 cage units come near to each other, with a distances of 8.853(3) Å, 10.480(3) Å and 8.691(2) Å between Ni1, Ni2 and Ni3 nodes respectively (Figure A6h-i). Crystallographic data for single crystal X-ray measurement of C10 is presented in Table A3.

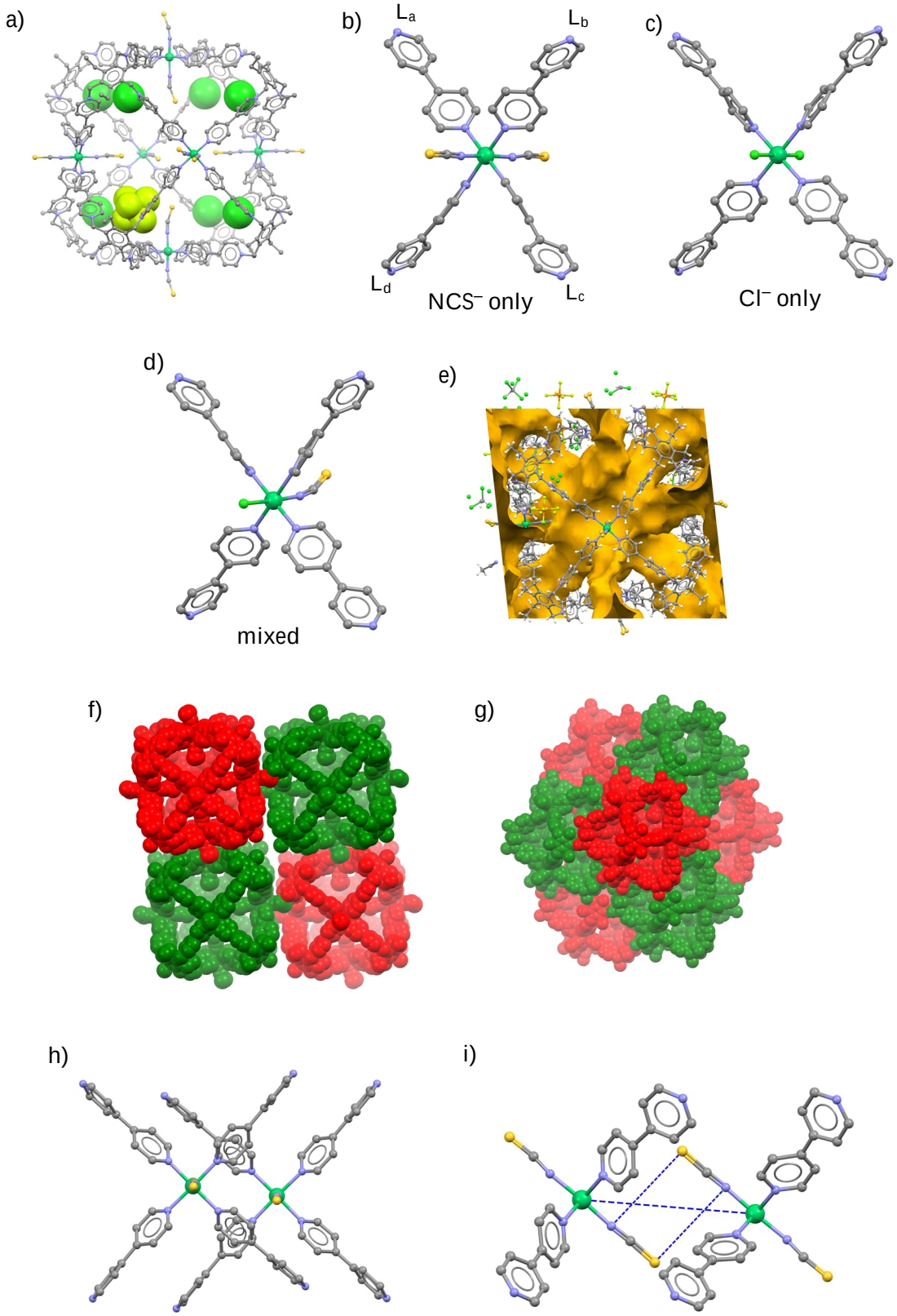

FIGURE A6 a) Structure of C10 cage unit with encapsulated anions, b-d) different metal node variations, e) solvent accessible surface area within the unit cell of C10, unit cell packing viewed along the crystallographic f) *a*-axis, g) along (111) lattice plane and h-i) proximity of metal nodes. Only relevant atoms are shown.

Table A3. Crystallographic data for C10.

Compound	C10
Empirical formula	$C_{386.5}H_{382}Cl_{37.5}F_{93.75}N_{60.5}Ni_6P_{16}S_8$
Formula weight	10089.39
Temperature / K	123.15
Crystal system	triclinic
Space group	*P*-1
a / Å	27.9733(5)
b / Å	28.1904(6)
c / Å	28.2330(5)
α / °	79.961(2)
β / °	70.193(2)
γ / °	77.463(2)
Volume / Å^3	20323.9(7)
Z	1
ρ_{calc} g / cm^3	0.824
μ / mm^{-1}	2.246
F(000)	5142.0
Crystal size / mm^3	0.573 × 0.417 × 0.281
2Θ range for data collection / °	3.408 to 143.996
Reflections collected	128813
Independent reflections	77513 [R_{int} = 0.0537, R_{sigma} = 0.0750]
Data / restraints / parameters	77513 / 3158 / 3662
GooF on F^2	1.456
Final *R* indexes [$I \geq 2\sigma(I)$]	R_1 = 0.1805, wR_2 = 0.4484
Final *R* indexes [all data]	R_1 = 0.2317, wR_2 = 0.4896
Largest diff peak / hole / e Å^{-3}	1.88 / -0.65

Appendix 5. $[Ni_6(L2)_8I_{3.5}(MeCN)_{10.5}(PF_6)_6](PF_6)_{24.7-n}I_{1.8+n}$ (C11)

Mixing acetonitrile solution containing C3* cage unit and methanol solution of NH_4I in 1:8 ratio followed by slow vapor diffusion of EtOAc yielded yellow crystals (Figure A7a) and X-ray diffraction analysis of said crystals revealed a $[Ni_6(L2)_8I_{3.5}(MeCN)_{10.5}(PF_6)_6](PF_6)_{24.7-n}I_{1.8+n}$ (C11) cube-like structure (Figure A7b) crystallizing in tetragonal space group *I4/m* ($a = b = 29.1921(6)$ Å, $c = 45.7041(12)$ Å, $\alpha = \beta = \gamma = 90°$, $V = 38\ 948.1(5)$ Å^3, $Z = 2$). Asymmetric unit consists of one eight of the cage unit of C11 and contains two crystallographically distinct Ni^{II} ions (Ni1 and Ni2) with Ni2 being disordered over two positions with approximate occupancies of 0.85 and 0.15 respectively and the two positions are separated by a distance of 0.50(5) Å. Each metal node exhibits an octahedral coordination geometry where the four equatorial sites are occupied by bpy arms of the ligands and the two axial sites are occupied by endohedral iodide anion or MeCN molecule (0.25:0.75) and single exohedral MeCN molecule (Figure A7c). The distances between diagonal NiI^{II} nodes are 24.401(2) Å for d_d(Ni1–Ni1'), 20.722(11) Å for d_d(Ni2A–Ni2'), and 21.72(16) Å for d_d(Ni2B–Ni2B') while the distance between nearest Ni^{II} nodes was 14.322(3) Å for d(Ni1–Ni1'), 14.488(3) Å for d(Ni1–Ni2A), and 14.85(4) Å for d(Ni1–Ni2B) with bridging angles between ligands being 177.4(3)° for ∡(L–Ni1–L), 172.3(9)° for ∡(L–Ni2A–L), and 161(3)° for ∡(L–Ni2B–L) with no difference between bridging angles of (L_a–M–L_c) and (L_b–M–L_d). Two of the ligands zero-valent pyridine rings are disordered over two orientations with approximate occupancies of 0.50 each and torsion angles of 77.6(5)° and 83.2(6)° between the two orientations.

All ligands of the cage unit are in *syn*-conformation where the bent angles of bpy arms are between of 112.7–117.2° and each bowl encapsulates one PF_6^- and I^- anion with approximate occupancies of 0.75 and 0.25 respectively (Figure A7d). Encapsulated anions are located 4.906(3) Å from benzyl ring centroid to iodide or phosphorus atom of the PF_6^- anion. The remaining charge of the cationic cage is balanced out *via* exohedral anions (21x PF_6^- and 1.8x I^-), meaning that total of 26.3 out of 36 anions could be positioned. The missing anions are most likely disordered among the large volume of highly disordered solvent molecules, with overall 23.3 % of unit cell volume remaining unassigned, based on voids calculated in Mercury (Figure A7e).

In the crystal lattice, the packing of individual C11 cage units follows the body-centered cubic (BCC) packing model, similarly to assemblies C1 and C9, with of the C11 cage units being orientated in the same direction with Ni2 nodes laying parallel with the crystallographic *c*-axis and Ni1 nodes laying parallel with *ab*-plane (Figure A7f-g). Furthermore, the Ni1 nodes of different C11 cage-units come near to each other, with 12.217(4) Å between Ni1 atoms, and MeCN molecules bonded to said Ni1 nodes come to a distance of 9.93(2) Å measured from carbon in CH_3 to nitrogen atom of the other MeCN molecule. This leaves enough room for one disordered PF_6^- anion to be located between two C11 cage units along the Ni1 plane as shown in Figure A7h-i. Crystallographic data for single crystal X-ray measurement of C11 is presented in Table A4.

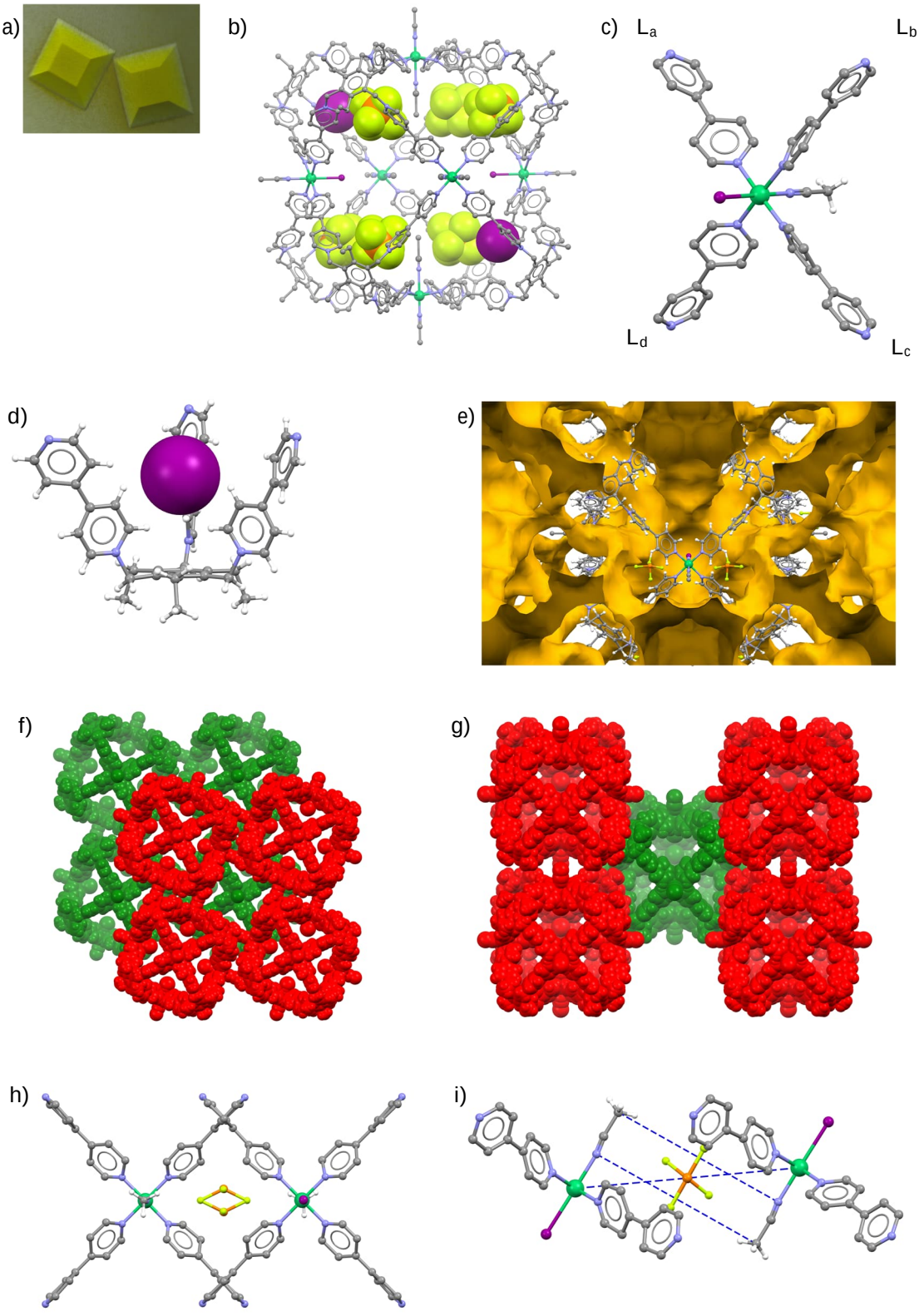

FIGURE A7 a) Crystals of C11, b) structure of C11 cage unit with encapsulated anions, c) metal node, d) encapsulated iodide anion, e) solvent accessible surface area within the unit cell of C11, packing of C11 cage units viewed along the crystallographic f) *c*-axis, g) *b*-axis, and h-i) PF_6^- anions between C11 cage units. Only relevant atoms are shown.

Table A4. Crystallographic data for C11.

Compound	C11
Empirical formula	$C_{332.5}H_{346}F_{110.5}I_{5.3}N_{50.5}Ni_6P_{21}$
Formula weight	8824.28
Temperature / K	120.15
Crystal system	tetragonal
Space group	*I*4/*m*
a / Å	29.1921(6)
b / Å	29.1921(6)
c / Å	45.7041(12)
α / °	90
β / °	90
γ / °	90
Volume / Å^3	38948.1(19)
Z	2
ρ_{calc} g / cm^3	0.752
μ / mm^{-1}	2.699
F(000)	8906.0
Crystal size / mm^3	0.25 × 0.21 × 0.17
2Θ range for data collection / °	3.592 to 140.32
Reflections collected	34212
Independent reflections	34212
Data / restraints / parameters	18108 [R_{int} = 0.0205, R_{sigma} = 0.0324]
GooF on F^2	18108 / 667 / 899
Final *R* indexes [$I \geq 2\sigma(I)$]	1.617
Final *R* indexes [all data]	R_1 = 0.2069, wR_2 = 0.4911
Largest diff peak / hole / e Å^{-3}	R_1 = 0.2570, wR_2 = 0.5371

Appendix 6. $[Ni_6(L2)_8I_8(MeCN)_{8.25}(PF_6)_{3.75}]I_{22-n}(PF_6)_{2.25+n}$ (C12)

Mixing acetonitrile solution containing C3* cage unit and methanol solution of NH_4I in 1:20 ratio followed by slow vapour diffusion of EtOAc yielded yellow crystals (Figure A8a) and the X-ray diffraction analysis of crystals revealed a $[Ni_6(L2)_8I_8(MeCN)_{8.25}(PF_6)_{3.75}]I_{22-n}(PF_6)_{2.25+n}$ (C12) cube-like structure (Figure A8b) crystallizing in trigonal space group $R\overline{3}$ ($a = b = 58.7031(15)$ Å, $c = 75.1394(14)$ Å, $\alpha = \beta = 90°$, $\gamma = 120°$, $V = 224\,244(9)$ Å^3, $Z = 12$). The asymmetric unit contains four crystallographically distinct Ni^{II} ions (Ni1–Ni4) each of which exhibit an octahedral coordination geometry where the four equatorial sites are occupied by ligands bpy arms and the two axial sites are endohedral iodide anion or MeCN molecule (0.67:0.33 or 0.50:0.50) and single exohedral MeCN molecule (Figure A8c). The asymmetric unit of assembly C12 consists of one half and one sixth of two individual $[Ni_6(L2)_8]^{36+}$ cationic cages with slightly different composition of encapsulated and coordinated anions. C12–I (Ni1–Ni3) encapsulates 4 iodide and 3.33 PF_6 anions, and coordinates 4 iodide anions in metal nodes, while C12–II (Ni4) encapsulates 5 iodide and 3 PF_6^- anions, and coordinates 3 iodide anions in the metal nodes. Beyond that only major difference is that the cationic skeleton of C12–II is less disordered than the one in C12–I. In C12–I one ligand is missing one of the methyl ends of an ethyl group, while another is missing two methyl ends and two of the +1-valent pyridine rings including the methylene bridges are disordered over two positions with a separation of 0.866 Å and 1.352 Å between centroids of the pyridine rings (Figure A8d)

In C12–I, one out of four bowls encapsulate a single iodide anion with approximate occupancy of 0.66 while being disordered over two positions (occup. 0.33 each), while the remaining bowls encapsulate both PF_6^- and iodide anions with approximate occupancies of either 0.50:0.50 (2x) or 0.66:0.33 (1x) in PF_6^-:I^- (Figure A8e). Additionally, each iodide anion coordinated to metal node has an approximate occupancy of 0.66 and is most likely disordered with MeCN molecules even though it was not possible to position all of the atoms in MeCN molecule. In C12–II, two of the bowls encapsulates a single iodide anion, while the remaining six bowls encapsulate both PF_6^- and iodide anions with approximate occupancies of either 0.50:0.50 in PF_6^-:I^-. Additionally the iodide anion coordinated to metal node has an approximate occupancy of 0.50 and is most likely disordered with MeCN molecules even though it was not possible to position the atoms of MeCN molecule. The remaining charge is balanced out by exohedral anions, of which 13.33 iodide and 2.25 could be positioned, while the remaining negarive charge (8.67) is most likely a mixture of PF_6^- and iodide anions being disordered among large volume of disordered free solvents, with overall 28.1 % of unit cell volume consisting of disordered molecules, based on voids calculated in Mercury (Figure A8f).

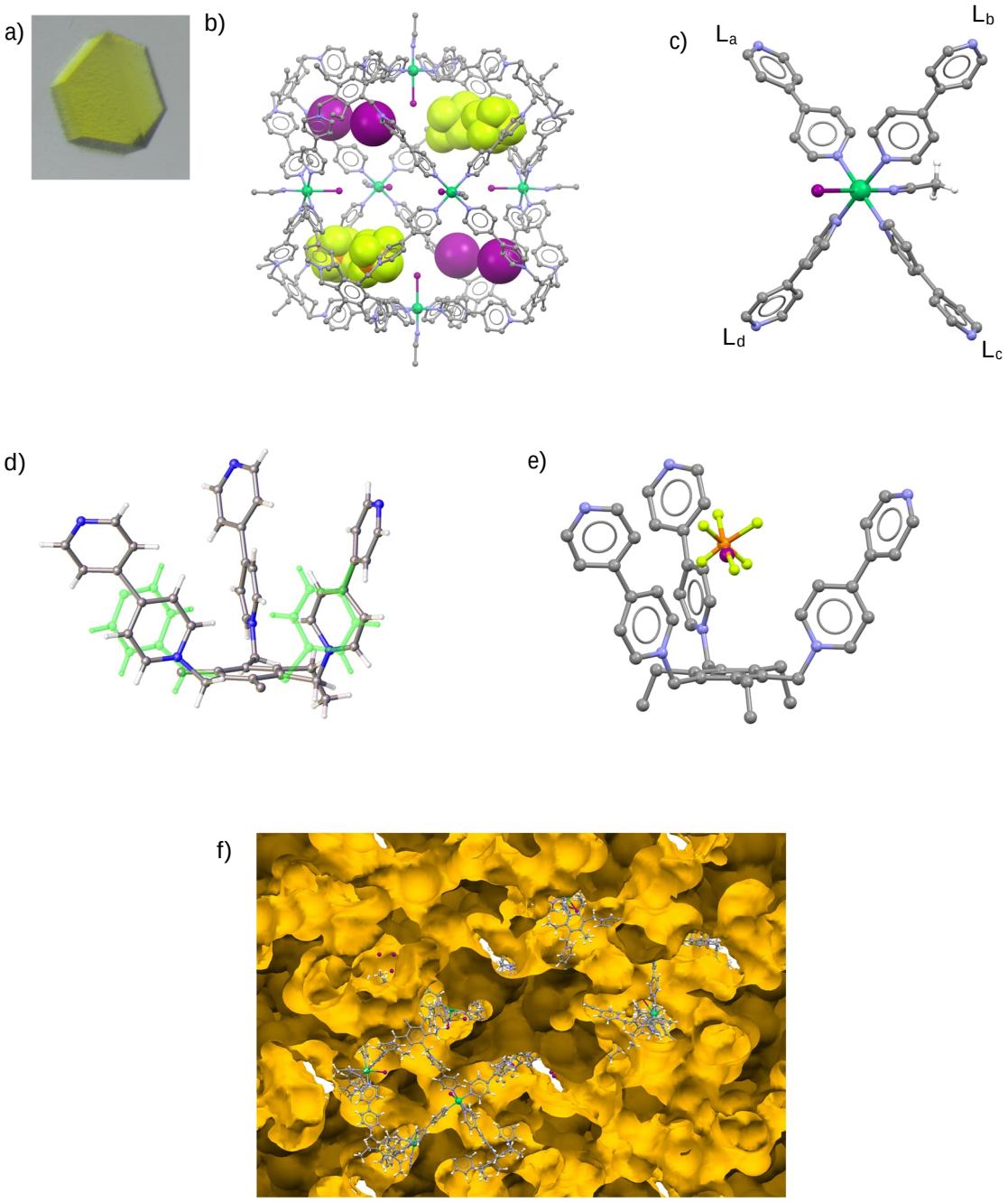

FIGURE A8 a) Crystals of C12, b) structure of C12 cage unit with encapsulated anions, c) metal node, d) disordered ligand in C12–I, e) disordered I^-/PF_6^- anions within the bowl, and f) solvent accessible surface area within the unit cell of C12. Only relevant atoms are shown.

The distances between diagonal Ni^{II} ions in C12–I are 19.411(2) Å for d_d(Ni1–Ni1'), 20.761(7) Å for d_d(Ni2–Ni2'), and 19.712(3) Å for d_d(Ni3–Ni3') while in C12–II the diagonal distances are 21.373(6) Å for d_d(Ni4–Ni4') respectively. The distance between nearest Ni^{II} nodes is between 13.649–15.479 Å in C12–I and between 15.03–15.508 Å in C12–II, while he bridging angles of bonded ligands in metal nodes were 177.3(3)° / 177.8(2)° for ∡(L–Ni1–L), 175.2(4)° / 177.3(4)° for ∡(L–Ni2–L), 177.8(2)° / 179.0(3)° for ∡(L–Ni3–L), and 162.8(12)° / 170.1(18)° for ∡(L–Ni4–L), presented as (L_a–M–L_c) / (L_b–M–L_d). The bend angles of bpy arms are between 109.6–115.8° in C12–I and between 113.2–117.0° in C12–II, with encapsulated PF_6^- anions laying 4.849–5.198 Å from benzene ring centroid to phosphorus atom and iodide were located 4.849–5.198 Å from benzene ring centroid. In C11–I, it was only possible to assign the some of the N-atoms of the endohedrally coordinated MeCN molecules, whereas in case of C12–II it was not possible to assign the endohedrally coordinated MeCN molecules.

The unit cell contains 12 C12 cage-units, out of which 9 are C12–I cage units and 3 are C12–II cage units. The C12–II cage units are located in the corners of the unit cell and along ($\bar{1}11$) lattice plane, while C12–I cage units are filling the rest of the unit cell (Figure A9a-d) reminiscent of assembly C3 (see p. 93). Crystallographic data for single crystal X-ray measurement of C12 is presented in Table A5.

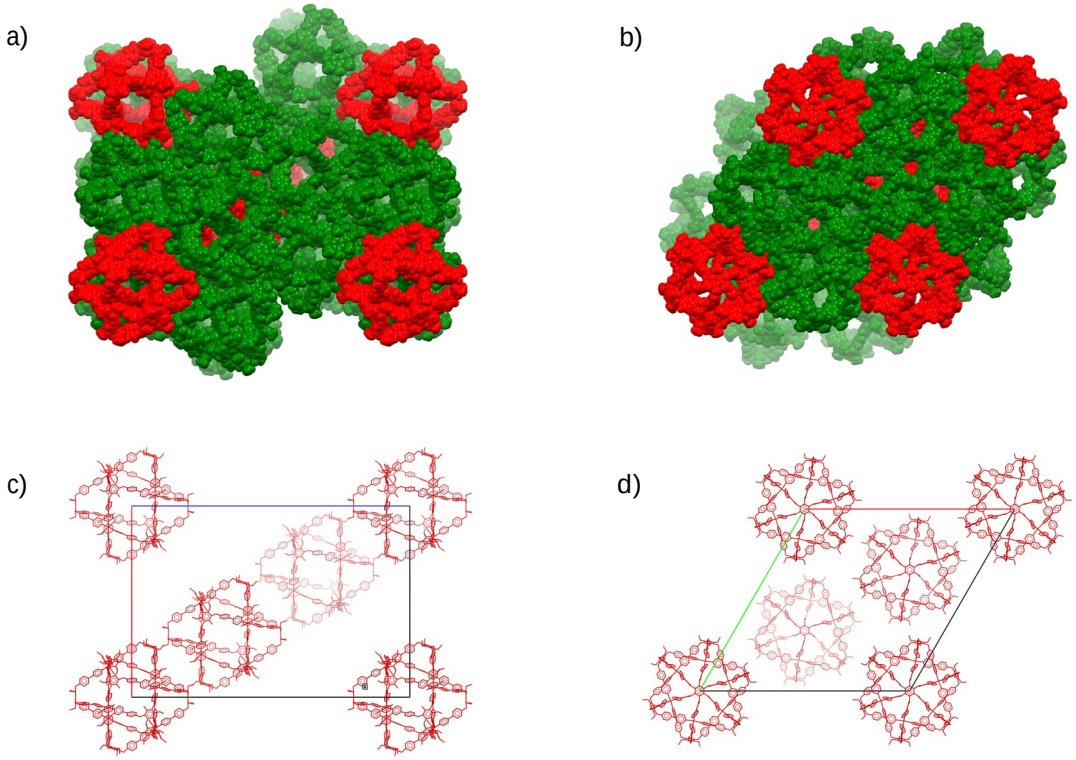

FIGURE A9 Unit cell packing viewed along the crystallographic a) *b*-axis and b) *c*-axis. Locations of C12–II cage units in the unit cell viewed along c) *b*-axis and *c*-axis. Green represents cage unit C12–I and red represents cage unit C12–II. Only relevant atoms are shown.

Table A5. Crystallographic data for C12.

Compound	C12
Empirical formula	$C_{354}H_{336}F_{28}I_{21.33}N_{53.75}Ni_6P_{5.5}$
Formula weight	9105.04
Temperature / K	120.15
Crystal system	trigonal
Space group	*R*-3
a / Å	59.2507(14)
b / Å	59.2507(14)
c / Å	74.7834(19)
α / °	90
β / °	90
γ / °	120
Volume / Å^3	227364(12)
Z	12
ρ_{calc} g / cm^3	0.798
μ / mm^{-1}	7.390
F(000)	53633.0
Crystal size / mm^3	0.41 × 0.26 × 0.08
2Θ range for data collection / °	3.544 to 133.986
Reflections collected	144939
Independent reflections	89314 [R_{int} = 0.0455, R_{sigma} = 0.0809]
Data / restraints / parameters	89314 / 542 / 2932
GooF on F^2	1.237
Final *R* indexes [$I \geq 2\sigma(I)$]	R_1 = 0.1933, wR_2 = 0.4663
Final *R* indexes [all data]	R_1 = 0.2615, wR_2 = 0.5420
Largest diff peak / hole / e Å^{-3}	2.10 / -0.85

Appendix 7. $[Pd_6(L2)_8(BF_4)_4(PF_6)_4](PF_6)_{23-n}(BF_4)_{5+n}$ (C13)

Mixing acetonitrile solutions of $(L2)\cdot(PF_6)_3$ and $[Pd(MeCN)_4](BF_4)_2$ in 4:3 ratio, followed by slow vapor diffusion of Et_2O yields colorless crystals and X-ray diffraction analysis of crystals revealed a $[Pd_6(L2)_8(BF_4)_4(PF_6)_4](PF_6)_{23-n}(BF_4)_{5+n}$ (C12) cube-like structure (Figure A10a) crystallizing in trigonal space group $R\bar{3}$ ($a = b = 42.1007(10)$ Å, $c = 37.9733(15)$ Å, $\alpha = \beta = 90°$, $\gamma = 120°$, $V = 58\ 289(3)$ Å^3, $Z = 2$). Due to high level of disorder it was not possible to determinate the structure to a satisfactory level, and therefore the assembly was instead determined in a triclinic space group $P\bar{1}$ ($a = 27.3683(11)$ Å, $b = 27.3977(9)$ Å, $c = 27.3946(9)$ Å, $\alpha = 100.385(3)°$, $\beta = 100.314(3)°$, $\gamma = 100.481(3)°$, $V = 19\ 385.3(13)$ Å^3, $Z = 1$). The asymmetric unit consists of one half of a C13 cage unit and contains three crystallographically distinct Pd^{II} ions (Pd1, Pd2 and Pd3) each of which exhibits a square-planar coordination geometry where the four coordination sites are occupied by ligands bpy arms (Figure A10b). The distances between diagonal Pd^{II} nodes are 20.5229(17) Å for d_d(Pd1–Pd1'), 20.5075(18) Å for d_d(Pd2–Pd2'), and 20.5210(17) Å for d_d(Pd3–Pd3'), while the distance between nearest Pd^{II} nodes was between 14.471–14.6541 Å. The bridging angles of bonded ligands in metal nodes were 177.0(3)° / 177.4(3)° for ∡(L–Pd1–L), 177.7(3)° / 179.4(5)° for ∡(L–Pd2–L) and 177.7(4)° / 178.0(3)° for ∡(L–Pd3–L), presented as $(L_a–M–L_c) / (L_b–M–L_d)$.

All ligands of the cationic cage unit are in *syn*-conformation where the bent angles of bpy arms are between of 110.5–116.2° and four of the ligands encapsulate one BF_4^- anions each and the remaining four ligands encapsulate four PF_6^- anions, and one encapsulated PF_6^- anion was disordered over two position with approximate occupancies of 0.50 each (Figure A10c). Encapsulated BF_4^- anions lie between 5.11–5.14 Å from benzyl ring centroid to boron of the anion, whereas encapsulated PF_6^- anions are located between 5.039–5.134 Å from benzyl ring centroid to phosphorus of the anion. Exohedral anions are a mixture of BF_4^- and PF_6^- anions and based on assigned anions and elemental analysis within Olex^2, the ratio of exohedral BF_4^-:PF_6^- is 5:13, which suggest that PF_6^- is preferred over BF_4^- but it is noteworthy that both anions are disordered among themselves. Out of expected 36 anions, 25.5 could be positioned (9x BF_4^- and 16.5x PF_6^-) with the remaining 10.5 anions most likely being disordered among the large volume of disordered free solvents as no free solvent molecules could be assigned. Overall, 28.4 % of unit cell volume consist of disordered molecules, based on solvent accessible voids calculated in Mercury (Figure A10d).

In crystal lattice, the individual C13 cage units are packed similar to simple cubic packing model of regular spheres (Figure A10e-f) and each of the metal nodes from different C13 cage units come near to each other, with the distances of 8.1340(14) Å, 8.1265(14) Å and 8,1337(14) Å between Pd1, Pd2 and Pd3 nodes respectively (Figure A10g-h). Crystallographic data for single crystal X-ray measurement of C13 is presented in Table A6.

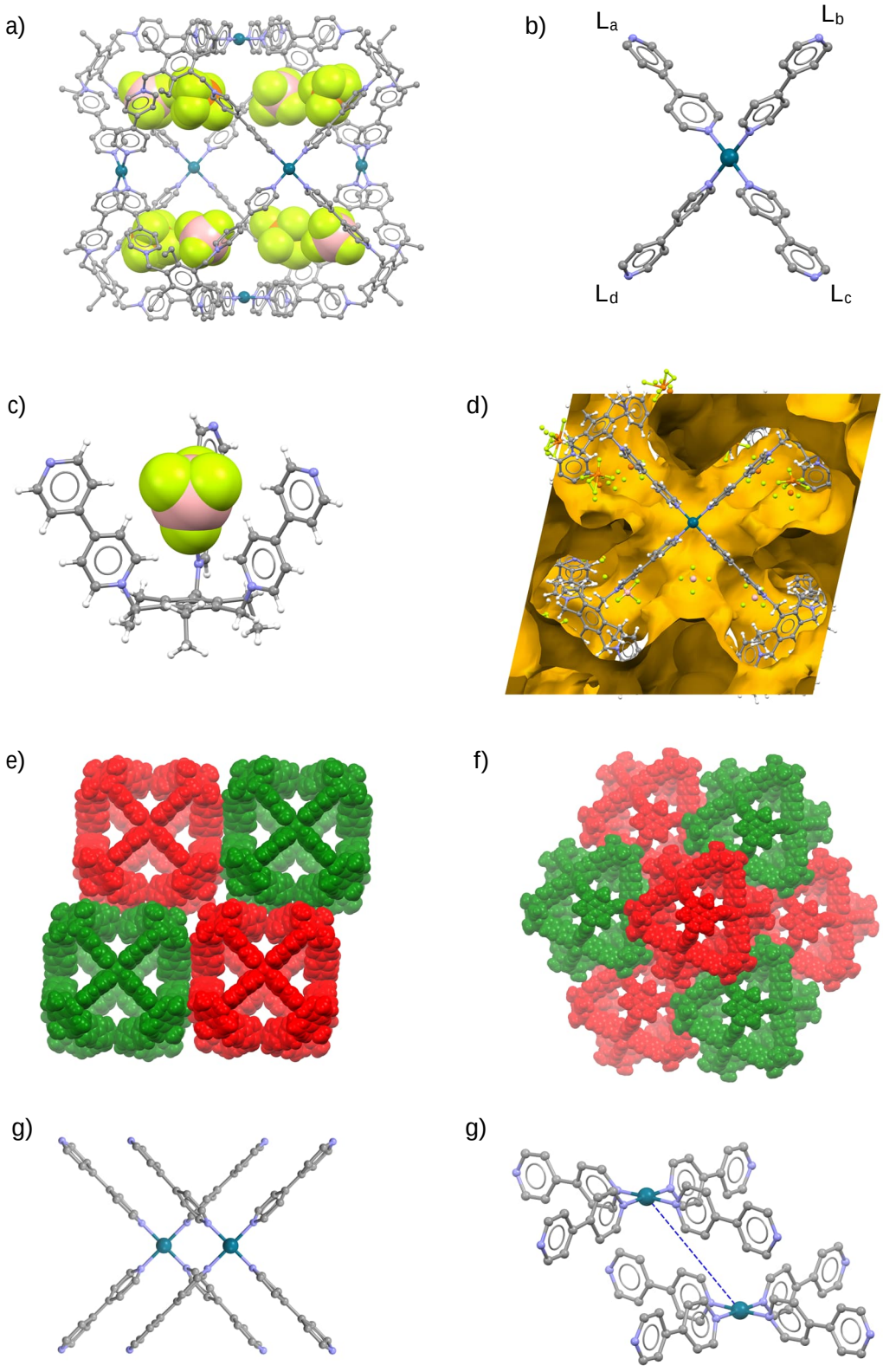

FIGURE A10 a) Structure of C13 cage unit with encapsulated anions, b) metal node, c) encapsulated BF_4^- anion, d) solvent accessible surface area within the unit cell of C13, unit cell packing viewed along the crystallographic e) *a*-axis, f) along (111) lattice plane and g-h) proximity of metal nodes. Only relevant atoms are shown.

Table A6. Crystallographic data for C13.

Compound	C13
Empirical formula	$C_{360}H_{360}B_9F_{120.5}N_{48}P_{16.5}Pd_6$
Formula weight	8895.13
Temperature / K	120.15
Crystal system	triclinic
Space group	*P*-1
a / Å	27.3683(11)
b / Å	27.3977(9)
c / Å	27.3946(9)
α / °	100.385(3)
β / °	100.314(3)
γ / °	100.481(3)
Volume / Å^3	19385.3(12)
Z	1
ρ_{calc} g / cm^3	0.762
μ / mm^{-1}	1.942
F(000)	4509.0
Crystal size / mm^3	0.57 × 0.44 × 0.33
2Θ range for data collection / °	3.36 to 137.998
Reflections collected	122149
Independent reflections	71370 [R_{int} = 0.0410, R_{sigma} = 0.0546]
Data / restraints / parameters	71370 / 2208 / 2813
GooF on F^2	1.338
Final *R* indexes [$I \geq 2\sigma(I)$]	R_1 = 0.1779, wR_2 = 0.4402
Final *R* indexes [all data]	R_1 = 0.2332, wR_2 = 0.5151
Largest diff peak / hole / e Å^{-3}	2.96 / -0.67

Table A7. Single crystal X-ray experimental details for ligands.

Identification code	(L1)·Br_3	(L1)·$(PF_6)_3$	(L2)·Br_3	(L2)·$(PF_6)_3$	(L2)·$(NTf_2)_3$
Empirical formula	$C_{43}H_{47}Br_3Cl_2N_6O_3$	$C_{85}H_{79.5}F_{36}N_{12.5}P_6$	$C_{50}H_{65}Br_3N_6O_5$	$C_{47}H_{48}F_{18}N_{6.34}P_3$	$C_{51}H_{47}F_{18}N_9O_{12.5}S_6$
Formula weight	1006.49	2145.93	1069.81	1136.51	1538.35
Temperature / K	120.00(10)	120.01(10)	120.01(10)	120.00(10)	120.00(10)
Crystal system	triclinic	orthorhombic	orthorhombic	hexagonal	monoclinic
Space group	*P*-1	$Pna2_1$	$Pna2_1$	$P6_3$	$P2_1/c$
a / Å	10.7684(10)	30.3451(6)	23.6932(3)	11.9234(3)	10.4945(7)
b / Å	11.6237(8)	11.1987(2)	11.1282(2)	11.9234(3)	27.068(2)
c / Å	18.1308(13)	27.2537(6)	19.2861(3)	19.9434(4)	22.880(3)
α / °	95.087(6)	90	90	90	90
β / °	103.175(7)	90	90	90	101.995(9)
γ / °	104.053(7)	90	90	120	90
Volume / Å^3	2118.5(3)	9261.5(3)	5085.03(14)	2455.44(13)	6357.7(11)
Z	2	4	4	2	4
ρ_{calc} g / cm^3	1.578	1.539	1.397	1.537	1.607
μ / mm^{-1}	5.072	2.205	3.343	2.114	3.087
F(000)	1020.0	4364.0	2208.0	1163.0	3136.0
Crystal size / mm^3	0.264 × 0.192 × 0.175	0.38 × 0.052 × 0.021	0.28 × 0.208 × 0.175	0.319 × 0.226 × 0.191	0.17 × 0.052 × 0.026
2Θ range for data collection / °	5.064 to 153.252	3.242 to 147.99	8.76 to 136	8.564 to 153.118	5.124 to 157.628
Reflections collected	13349	25606	11121	6639	22598
Independent reflections	8481 [R_{int} = 0.0292, R_{sigma} = 0.0357]	13215 [R_{int} = 0.0635, R_{sigma} = 0.0961]	6188 [R_{int} = 0.0219, R_{sigma} = 0.0280]	3018 [R_{int} = 0.0322, R_{sigma} = 0.0402]	12853 [R_{int} = 0.1449, R_{sigma} = 0.2176]
Data / restraints / parameters	8481 / 8 / 555	13215 / 91 / 1336	6188 / 2 / 638	3018 / 1 / 299	12853 / 0 / 919
GooF on F^2	1.038	1.067	1.054	1.075	0.963
Final *R* indexes [$I \geq 2\sigma(I)$]	R_1 = 0.0457, wR_2 = 0.1239	R_1 = 0.0754, wR_2 = 0.1599	R_1 = 0.0372, wR_2 = 0.1041	R_1 = 0.0437, wR_2 = 0.1194	R_1 = 0.1364, wR_2 = 0.3441
Final *R* indexes [all data]	R_1 = 0.0476, wR_2 = 0.1255	R_1 = 0.1097, wR_2 = 0.1796	R_1 = 0.0380, wR_2 = 0.1051	R_1 = 0.0452, wR_2 = 0.1215	R_1 = 0.3255, wR_2 = 0.4929
Largest diff peak / hole / e Å^{-3}	2.42 / -1.14	0.65 / -0.47	0.63 / -0.40	0.67 / -0.27	0.78 / -0.49
Flack parameter	-	0.03(5)	-0.032(11)	0.00(2)	-

Table A8. Single crystal X-ray experimental details for M_6L_8 assemblies.

Identification code	C1	C2	C3	C3*	C4
Empirical formula[a]	$C_{381.1}H_{368.1}Cl_{10.8}Cu_6F_{153.4}N_{78}P_{26.2}$	$C_{359}H_{351.5}Cl_{18.5}Cu_6F_{44.5}N_{57.5}O_{85}P_{7.5}$	$C_{368.75}H_{363.75}F_{133.88}N_{63.75}Ni_6O_{10.5}P_{22.5}$	$C_{382}H_{387}F_{191}N_{61}Ni_6P_{32}$	$C_{363.5}H_{362}Cl_{23}F_{85}N_{48.5}Ni_6OP_{14.5}$
Formula weight	10530.93	8946.30	9449.17	10804.80	8657.67
Temperature / K	100.15	120.15	123.15	123.15	120.15
Crystal system	tetragonal	monoclinic	trigonal	monoclinic	monoclinic
Space group	*I*4/*m*	*C*2/*c*	*R*-3	*C*2/*c*	*C*2/*c*
a / Å	27.5958(2)	49.8080(12)	58.7031(15)	40.9416(13)	40.1388(10)
b / Å	27.5958(2)	29.2146(6)	58.7031(15)	45.5508(13)	40.1148(9)
c / Å	48.8799(5)	55.7326(13)	75.1394(14)	41.8085(15)	46.1812(15)
α / °	90	90	90	90	90
β / °	90	113.168(3)	90	90.979(3)	103.279(3)
γ / °	90	90	120	90	90
Volume / Å^3	37223.4(7)	74557(3)	224244(12)	77958(4)	72371(3)
Z	2	4	12	4	4
ρ_{calc} g / cm^3	0.940	0.797	0.840	0.921	0.795
μ / mm^{-1}	1.753	1.437	1.232	1.503	1.726
F(000)	10664.0	18358.0	57802.0	21892.0	17728.0
Crystal size / mm^3	0.306 × 0.243 × 0.197	0.351 × 0.174 × 0.141	0.38 × 0.35 × 0.13	0.2 × 0.19 × 0.11	0.331 × 0.131 × 0.095
2Θ range for data collection / °	7.234 to 145.964	3.588 to 101.002	3.528 to 146.544	4.418 to 146.54	3.156 to 132.618
Reflections collected	35238	87024	145863	124040	110502
Independent reflections	18237 [R_{int} = 0.0216, R_{sigma} = 0.0300]	38774 [R_{int} = 0.0479, R_{sigma} = 0.0739]	95240 [R_{int} = 0.0296, R_{sigma} = 0.0570]	74523 [R_{int} = 0.0684, R_{sigma} = 0.1056]	61162 [R_{int} = 0.0485, R_{sigma} = 0.0646]
Data / restraints / parameters	18237 / 859 / 1148	38774 / 3046 / 4052	95240 / 2674 / 3887	74523 / 2150 / 3160	61162 / 2632 / 3154
GooF on F^2	1.499	1.289	1.342	1.131	1.317
Final *R* indexes [$I \geq 2\sigma(I)$]	R_1 = 0.1234, wR_2 = 0.3466	R_1 = 0.1227, wR_2 = 0.3222	R_1 = 0.1567, wR_2 = 0.4076	R_1 = 0.1587, wR_2 = 0.3993	R_1 = 0.1678, wR_2 = 0.4247
Final *R* indexes [all data]	R_1 = 0.1430, wR_2 = 0.3722	R_1 = 0.1481, wR_2 = 0.3517	R_1 = 0.2194, wR_2 = 0.4624	R_1 = 0.2231, wR_2 = 0.4549	R_1 = 0.2321, wR_2 = 0.4808
Largest diff peak / hole / e Å^{-3}	1.05 / -0.53	1.00 / -0.46	1.46 / -0.58	1.26 / -0.80	1.05 / -0.57

[a]Empirical formula does not include molecules excluded with solvent masking.

Table A9. Single crystal X-ray experimental details for M_6L_8 assemblies.

Identification code	C5	C6	C7	C8	C9
Empirical formula[a]	$C_{374.5}H_{381.75}Br_{13.1}F_{104.11}N_{55.25}Ni_6P_{18.15}$	$C_{432.6}H_{458.5}F_{143.6}N_{85.9}Ni_6O_{8.2}P_{24}S_{12}$	$C_{387}H_{363.5}Cl_{29.5}F_{72}N_{60.5}Ni_6O_{48}S_{24}$	$C_{382}H_{363.75}Br_{15}F_{48}N_{62.5}Ni_6O_{33.5}S_{18}$	$C_{380}H_{378.5}Cu_6F_{180}N_{60}P_{30}$
Formula weight	9595.86	11200.99	10165.34	9406.07	10516.25
Temperature / K	120.15	123.15	120.15	120.15	120.15
Crystal system	monoclinic	triclinic	trigonal	monoclinic	monoclinic
Space group	*P*2/*n*	*P*-1	*R*-3*c*	*C*2/*c*	*I*2/*m*
a / Å	41.5326(8)	27.8784(5)	33.1670(3)	41.0344(6)	29.6124(10)
b / Å	45.7321(7)	27.9602(8)	33.1670(3)	40.4562(9)	46.5621(13)
c / Å	41.5248(7)	29.0693(7)	124.0564(10)	49.2477(8)	29.6277(9)
α / °	90	62.560(3)	90	90	90
β / °	90.088(2)	70.3815(19)	90	100.310(2)	90.012(3)
γ / °	90	77.8548(19)	120	90	90
Volume / Å^3	78871(2)	18900.3(9)	118185(2)	80436(3)	40851(2)
Z	4	1	6	4	2
ρ_{calc} g / cm^3	0.808	0.984	0.857	0.777	0.855
μ / mm^{-1}	1.769	1.637	2.172	1.862	1.389
F(000)	19405.0	5733.0	31167.0	19097.0	10645.0
Crystal size / mm^3	0.55 × 0.48 × 0.37	0.661 × 0.565 × 0.403	0.354 × 0.248 × 0.192	0.56 × 0.48 × 0.4	0.24 × 0.22 × 0.18
2Θ range for data collection / °	3.574 to 146.498	3.562 to 148.13	4.192 to 147.962	6.852 to 148.576	3.534 to 132.988
Reflections collected	269551	114835	126969	137708	71420
Independent reflections	152677 [R_{int} = 0.0443, R_{sigma} = 0.0538]	72884 [R_{int} = 0.0363, R_{sigma} = 0.0560]	26323 [R_{int} = 0.0353, R_{sigma} = 0.0233]	78031 [R_{int} = 0.0259, R_{sigma} = 0.0361]	35438 [R_{int} = 0.0371, R_{sigma} = 0.0426]
Data / restraints / parameters	152677 / 4980 / 6094	72884 / 2905 / 4128	26323 / 882 / 1218	78031 / 476 / 3063	35438 / 2123 / 2059
GooF on F^2	1.603	1.224	1.680	1.449	1.520
Final *R* indexes [$I \geq 2\sigma(I)$]	R_1 = 0.1942, wR_2 = 0.4849	R_1 = 0.1048, wR_2 = 0.2939	R_1 = 0.1458, wR_2 = 0.4007	R_1 = 0.1347, wR_2 = 0.3754	R_1 = 0.1576, wR_2 = 0.4277
Final *R* indexes [all data]	R_1 = 0.2691, wR_2 = 0.5604	R_1 = 0.1290, wR_2 = 0.3268	R_1 = 0.1686, wR_2 = 0.4278	R_1 = 0.1566, wR_2 = 0.4029	R_1 = 0.1963, wR_2 = 0.4589
Largest diff peak / hole / e Å^{-3}	2.64 / -1.33	1.27 / -0.67	1.81 / -0.97	2.16 / -0.94	0.73 / -0.56

[a]Empirical formula does not include molecules excluded with solvent masking.

Table A10. Single crystal X-ray experimental details for dimeric capsules.

Identification code	D1	D2	D3	D4	D5
Empirical formula[a]	$C_{144}H_{149}Cl_7F_{60}N_{22}O_{0.5}P_{10}Zn_4$	$C_{149}H_{158}Br_7F_{60}N_{23}O_2P_{10}Zn_4$	$C_{153.5}H_{165.25}F_{57}I_7N_{24.75}O_{2.5}P_{9.5}Zn_4$	$C_{134}H_{130}F_{51}I_7N_{21}OP_{8.5}Zn_4$	$C_{193.75}H_{201.5}F_{35.2}I_{26.6}N_{31.5}OP_{7.8}Zn_5$
Formula weight	4155.17	4573.52	4923.84	4432.61	7600.11
Temperature / K	120.15	120.15	120.15	144(30)	120.15
Crystal system	triclinic	triclinic	monoclinic	triclinic	monoclinic
Space group	*P*-1	*P*-1	$P2_1/c$	*P*-1	*P2/n*
a / Å	22.1367(3)	22.4439(4)	22.6771(4)	22.7773(3)	27.4114(3)
b / Å	22.8679(3)	25.3852(5)	45.8546(8)	23.3081(4)	27.4257(3)
c / Å	25.2691(4)	26.1323(4)	25.7178(5)	24.5807(4)	44.0965(5)
α / °	112.6862(13)	61.3103(19)	90	102.8010(10)	90
β / °	101.4546(13)	72.1709(15)	100.7886(18)	109.0290(10)	90.0050(10)
γ / °	90.1222(12)	84.7924(16)	90	93.0280(10)	90
Volume / Å^3	11523.1(3)	12405.4(5)	26269.9(8)	11918.8(3)	33150.7(6)
Z	2	2	4	2	4
ρ_{calc} g / cm^3	1.198	1.224	1.245	1.235	1.523
μ / mm^{-1}	2.682	3.136	8.135	8.801	20.720
F(000)	4200.0	4568.0	9704.0	4333.0	14344.0
Crystal size / mm^3	0.296 × 0.229 × 0.127	0.49 × 0.199 × 0.107	0.248 × 0.204 × 0.114	0.416 × 0.109 × 0.061	0.2 × 0.193 × 0.166
2Θ range for data collection / °	6.756 to 145.992	3.976 to 145.992	3.966 to 148	3.924 to 147.998	3.794 to 135.996
Reflections collected	73242	81393	114597	93982	127217
Independent reflections	45186 [R_{int} = 0.0231, R_{sigma} = 0.0345]	48692 [R_{int} = 0.0254, R_{sigma} = 0.0400]	52886 [R_{int} = 0.0386, R_{sigma} = 0.0536]	47575 [R_{int} = 0.0621, R_{sigma} = 0.0773]	58766 [R_{int} = 0.0578, R_{sigma} = 0.0723]
Data / restraints / parameters	45186 / 1757 / 2412	48692 / 207 / 2498	52886 / 2455 / 2947	47575 / 204 / 2152	58766 / 2475 / 3495
GooF on F^2	1.061	1.036	1.035	1.035	1.053
Final *R* indexes [$I \geq 2\sigma(I)$]	R_1 = 0.0854, wR_2 = 0.2525	R_1 = 0.0731, wR_2 = 0.2223	R_1 = 0.0794, wR_2 = 0.2334	R_1 = 0.0881, wR_2 = 0.2470	R_1 = 0.0958, wR_2 = 0.2759
Final *R* indexes [all data]	R_1 = 0.0943, wR_2 = 0.2657	R_1 = 0.0834, wR_2 = 0.2405	R_1 = 0.0926, wR_2 = 0.2500	R_1 = 0.1429, wR_2 = 0.2911	R_1 = 0.1322, wR_2 = 0.3131
Largest diff peak / hole / e Å^{-3}	1.36 / -1.09	1.29 / -1.89	2.32 / -0.92	2.01 / -1.22	2.29 / -1.96

[a]Empirical formula does not include molecules excluded with solvent masking.

Appendix 11. ^{1}H NMR spectra of the ligands

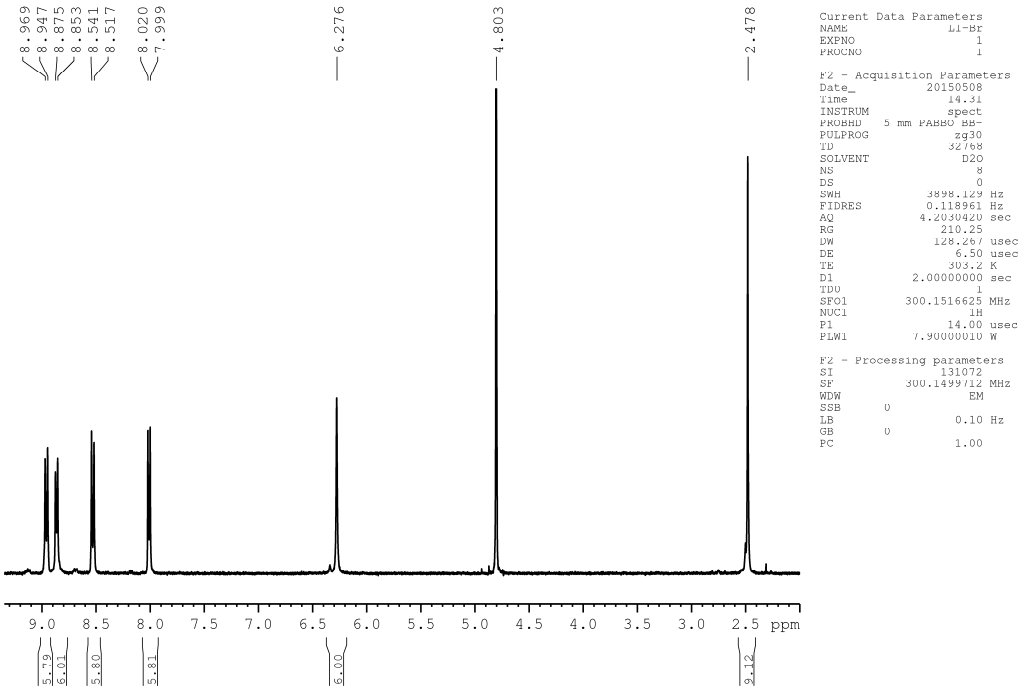

FIGURE A11 ^{1}H NMR spectrum (300 MHz, D_2O, room temperature) of (L1)·Br_3.

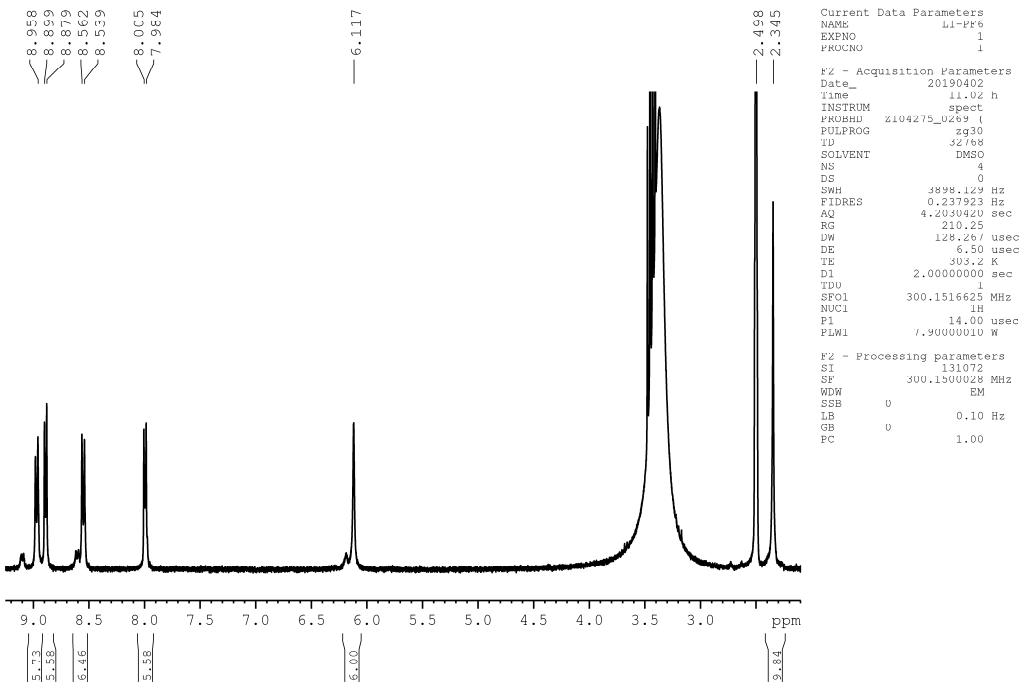

FIGURE A12 ^{1}H NMR spectrum (300 MHz, $(CD_3)_2SO$, room temperature) of (L1)·$(PF_6)_3$.

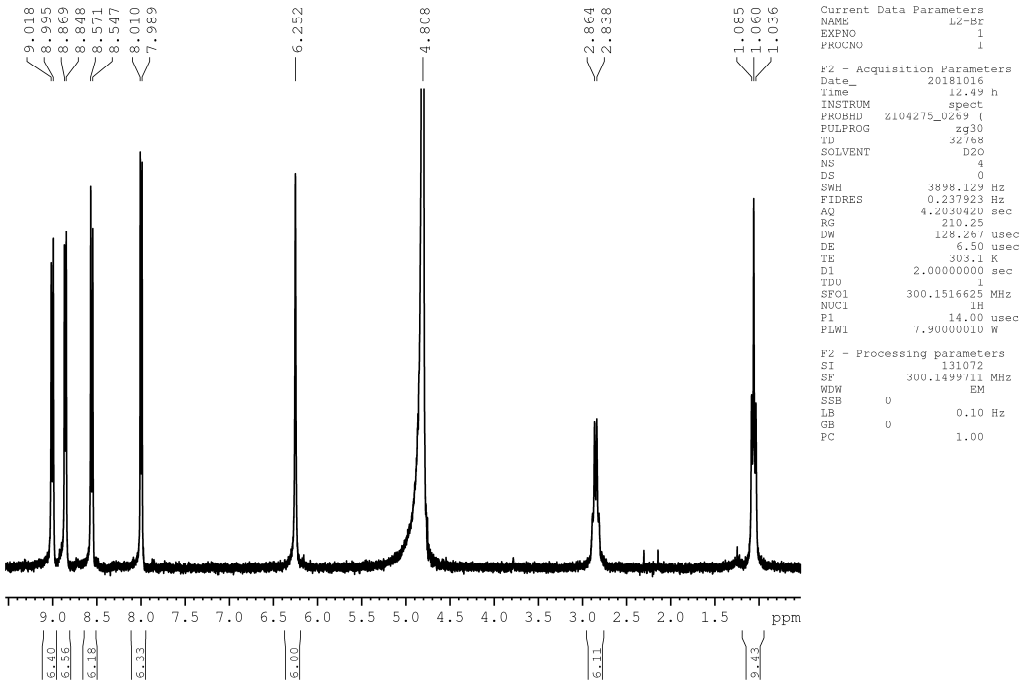

FIGURE A13 ^{1}H NMR spectrum (300 MHz, D_2O, room temperature) of (L2)·Br_3.

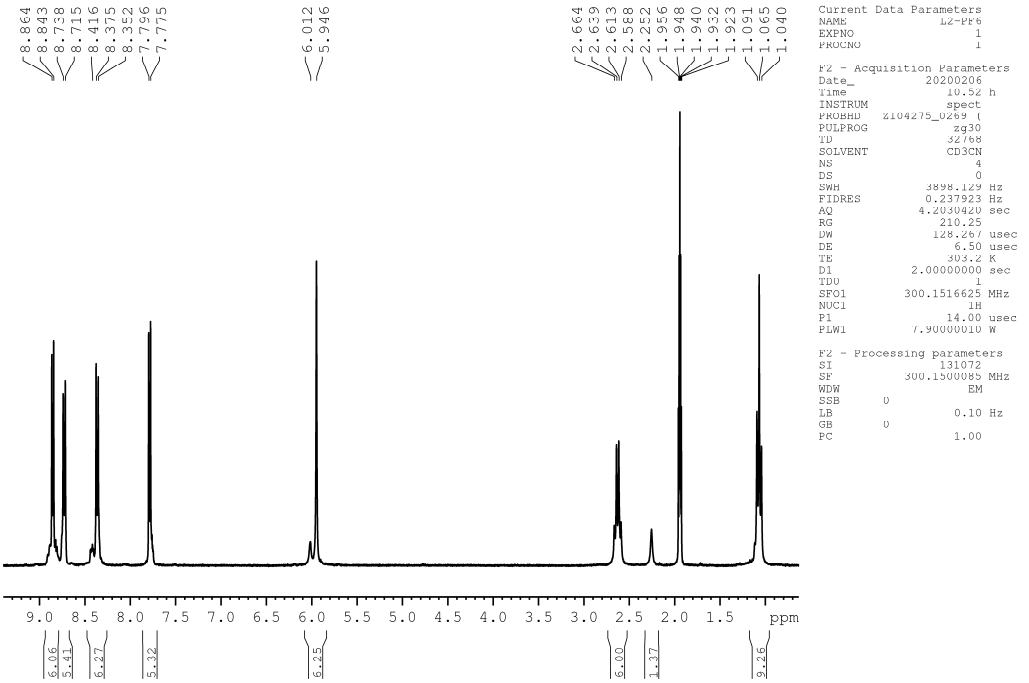

FIGURE A14 ^{1}H NMR spectrum (300 MHz, CD_3CN, room temperature) of (L2)·$(PF_6)_3$.

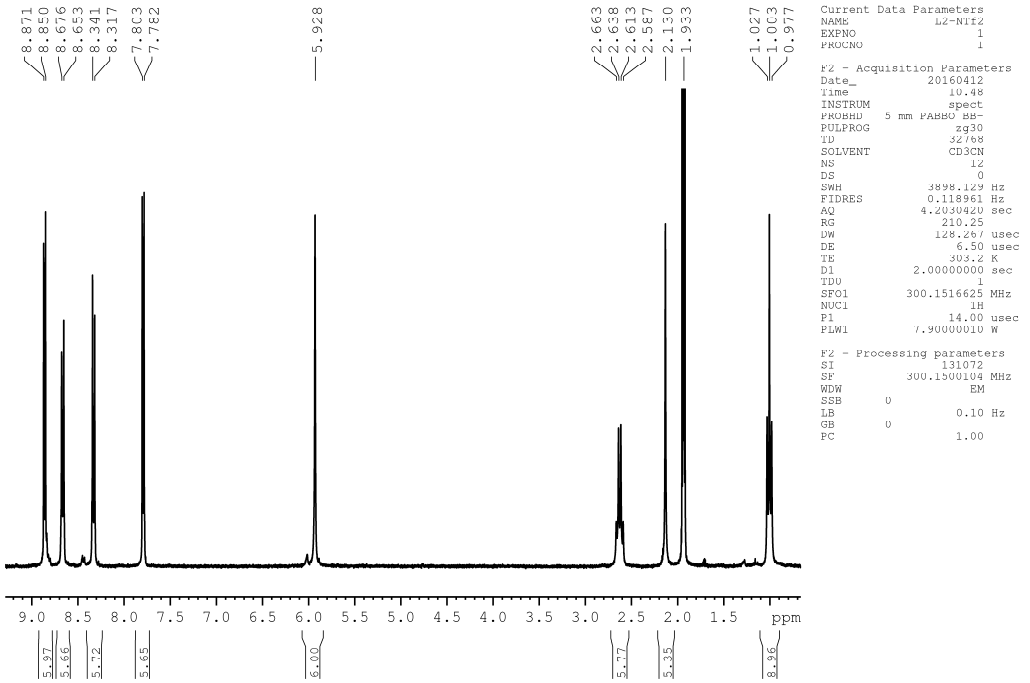

FIGURE A15 ^{1}H NMR spectrum (300 MHz, CD_3CN, room temperature) of $(L2)\cdot(NTf_2)_3$.

Appendix 12. ^{1}H NMR spectra of C3* assembly

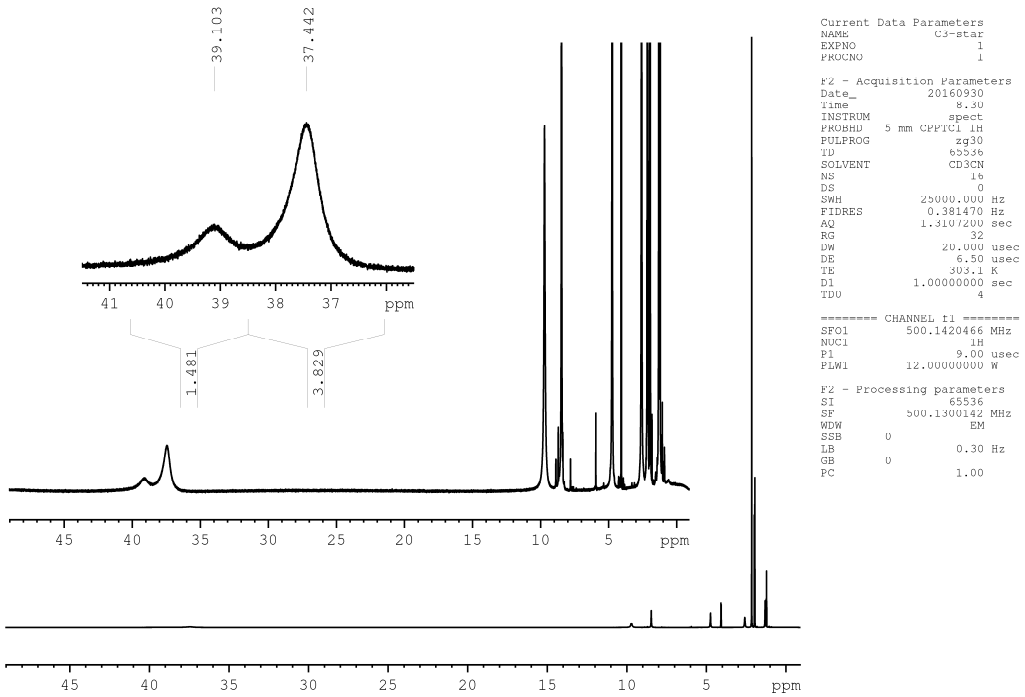

FIGURE A16 Full ^{1}H NMR spectrum (500 MHz, CD_3CN, room temperature) of crystallized C3* assembly, with detailed look at peaks around 37.4 ppm and 39.1 ppm.

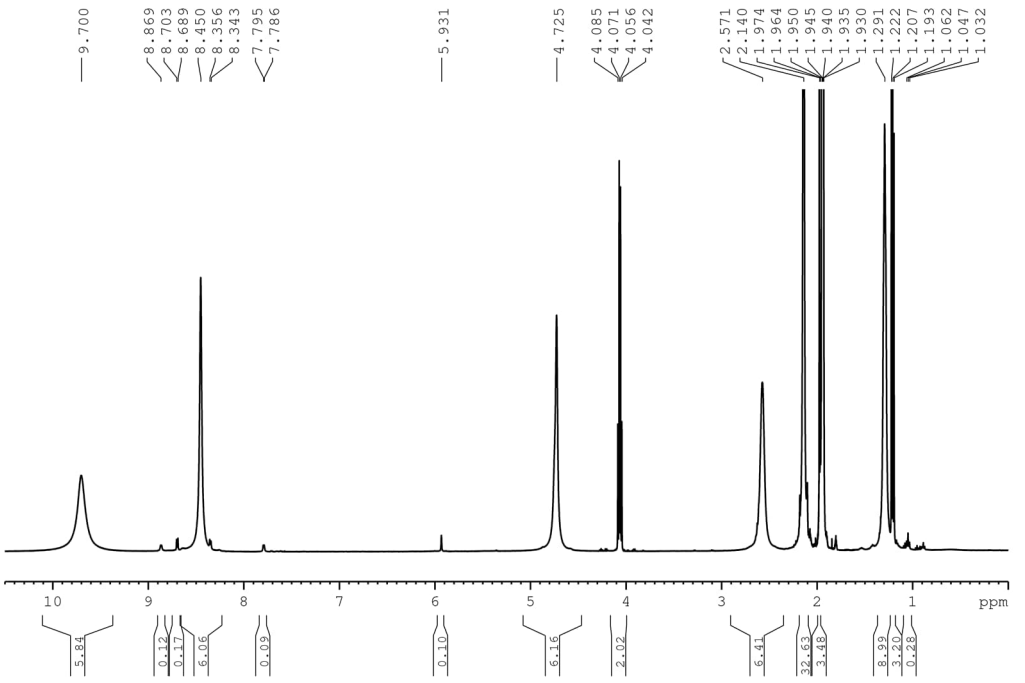

FIGURE A17 Detailed look at ^{1}H NMR spectrum of crystallized C3* assembly between 0-10 ppm.

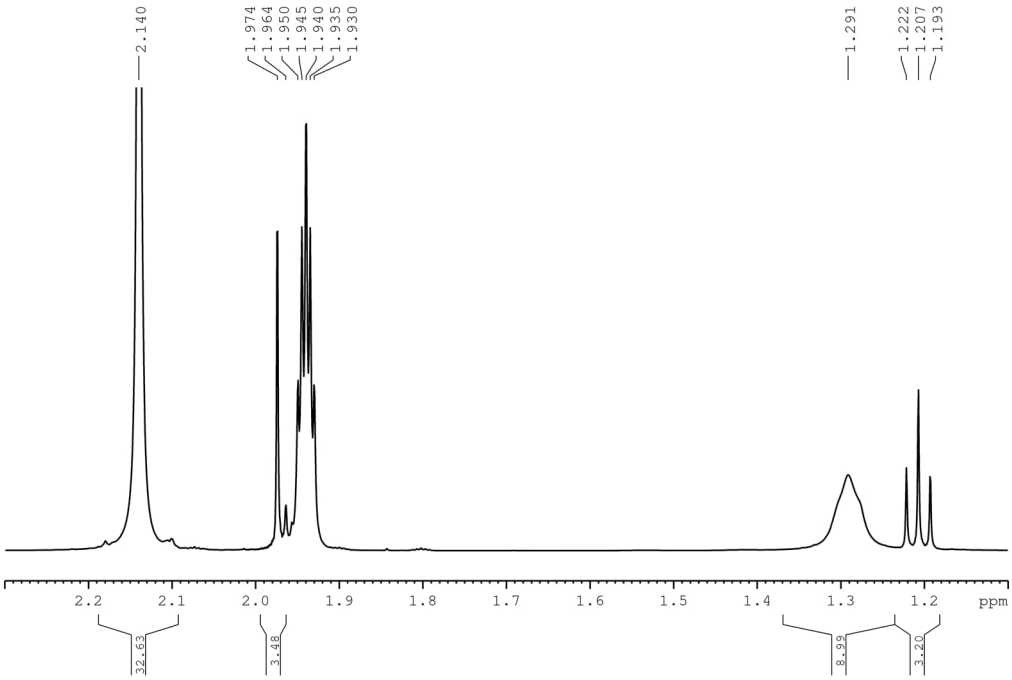

FIGURE A18 Detailed look at ^{1}H NMR spectrum of crystallized C3* assembly between 1.1–2.3 ppm.

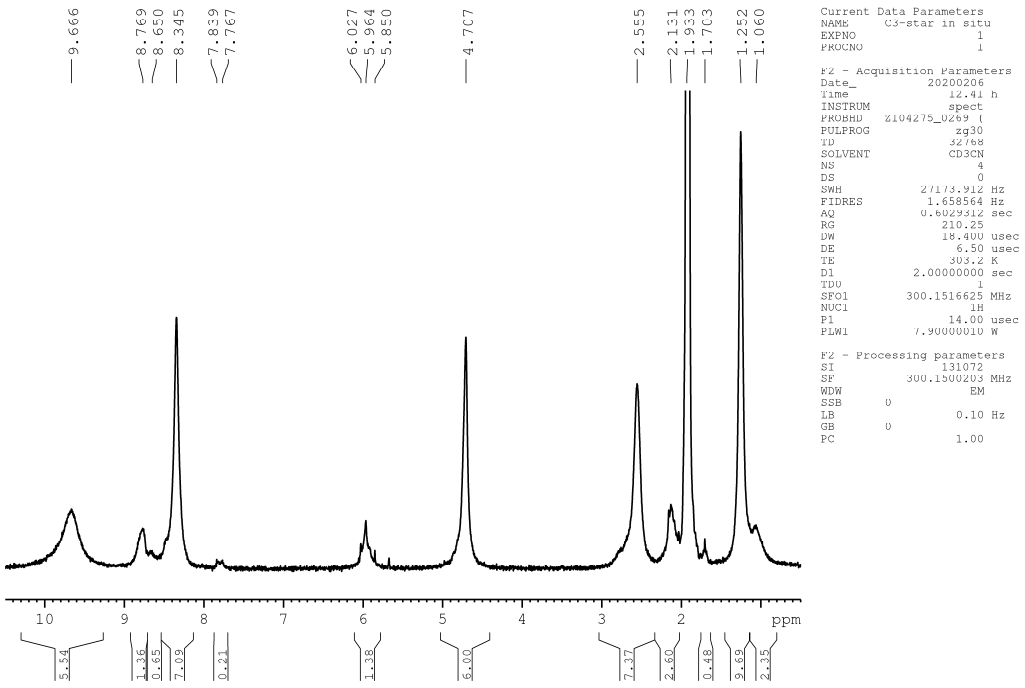

FIGURE A19 ^{1}H NMR spectrum (300 MHz, CD_3CN, room temperature) of *in situ* prepared C3* assembly.

Appendix 13. TG / DSC graphs of the ligands

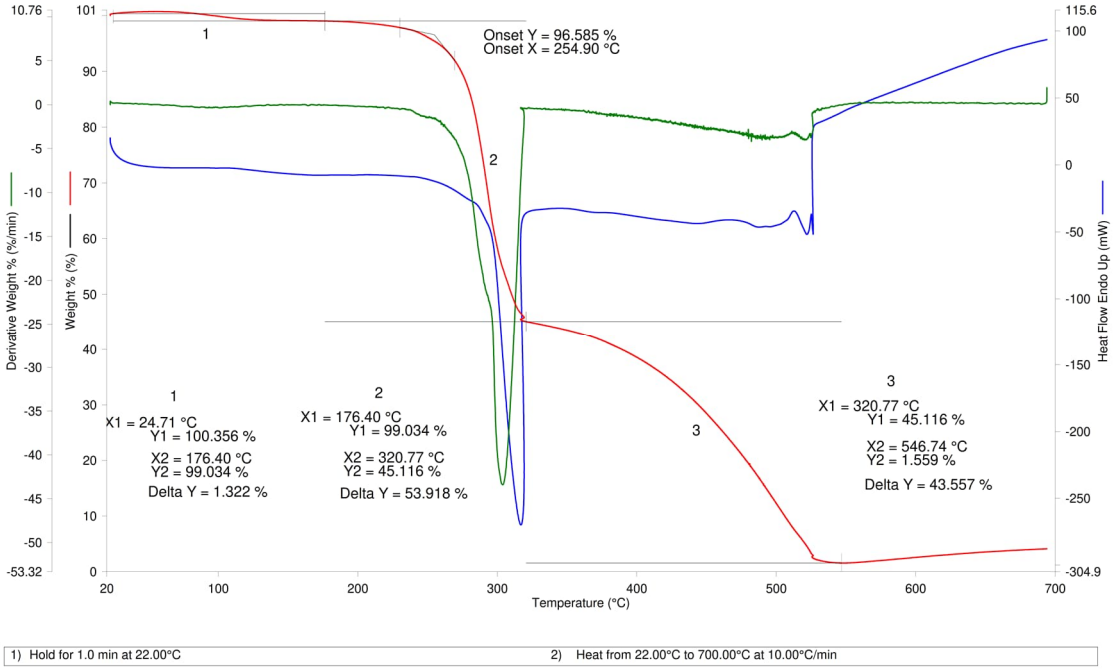

FIGURE A20 TG / DSC graph (Air, 40 ml min^{-1}) of ligand (L1)·Br_3.

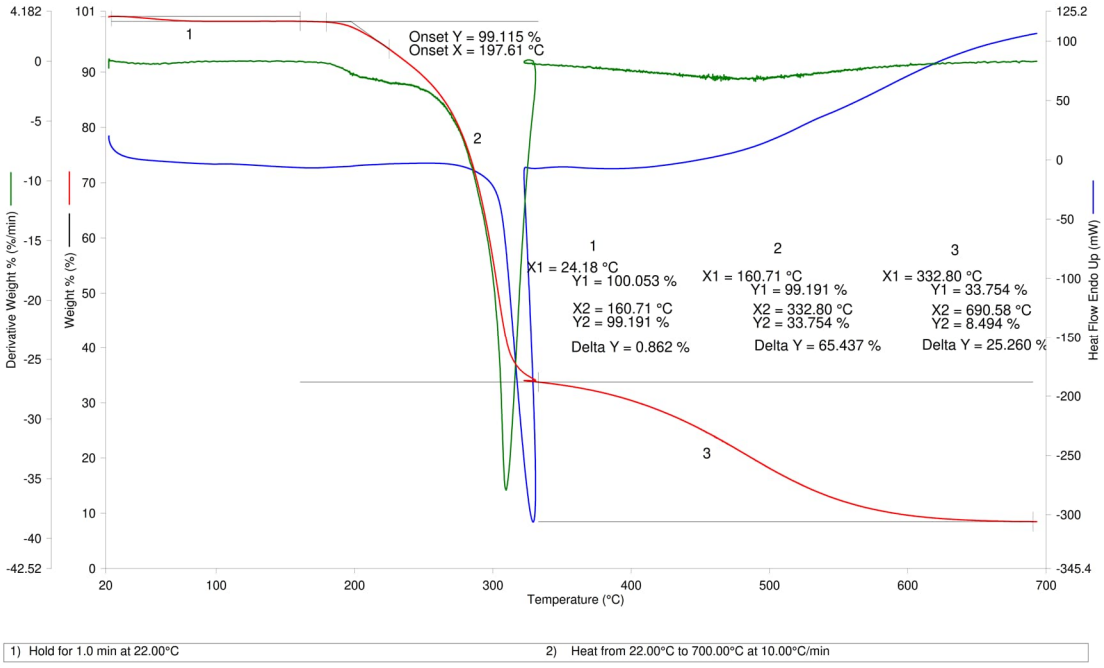

FIGURE A21 TG / DSC graph (Air, 40 ml min^{-1}) of ligand (L1)·$(PF_6)_3$.

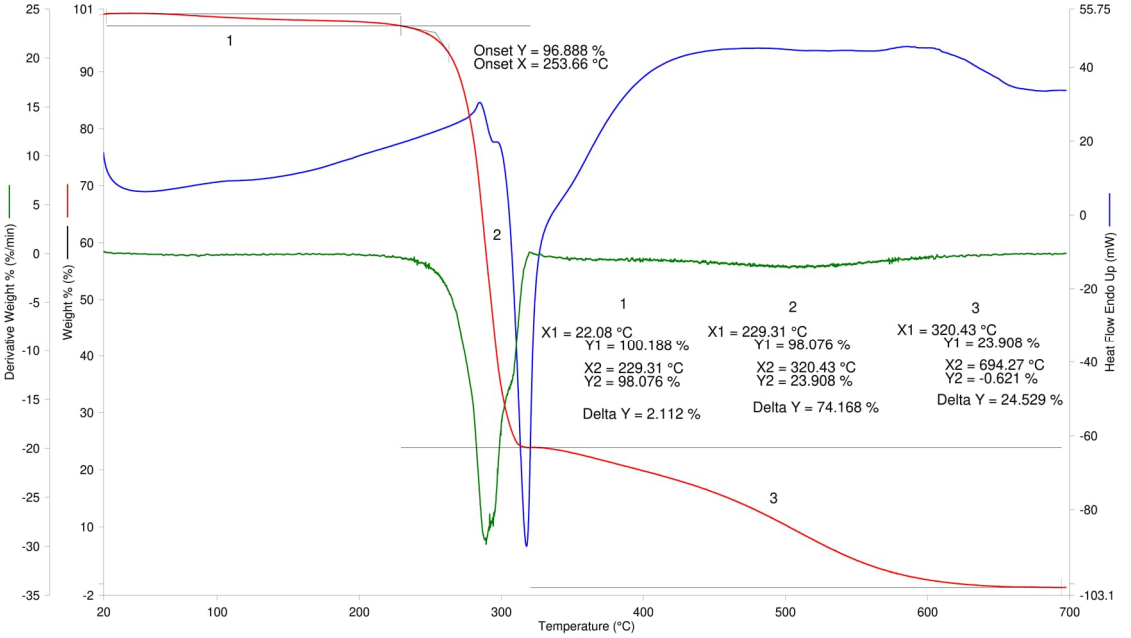

FIGURE A22 TG / DSC graph (Air, 40 ml min^{-1}) of ligand (L2)·Br_3.

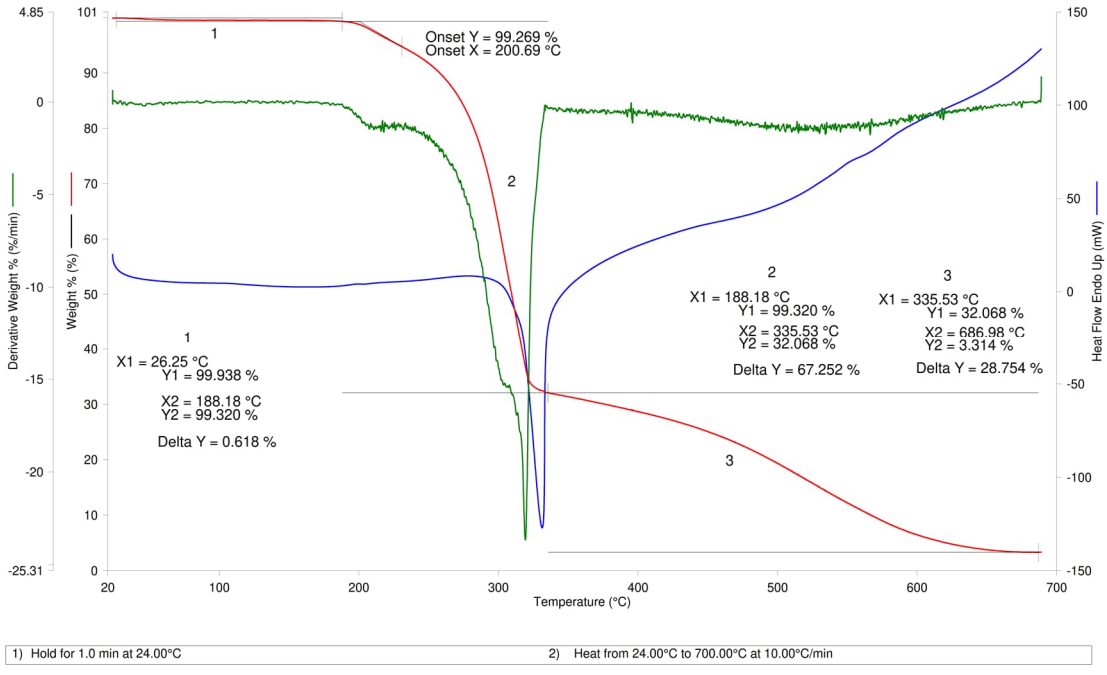

FIGURE A23 TG / DSC graph (Air, 40 ml min^{-1}) of ligand (L2)·$(PF_6)_3$.

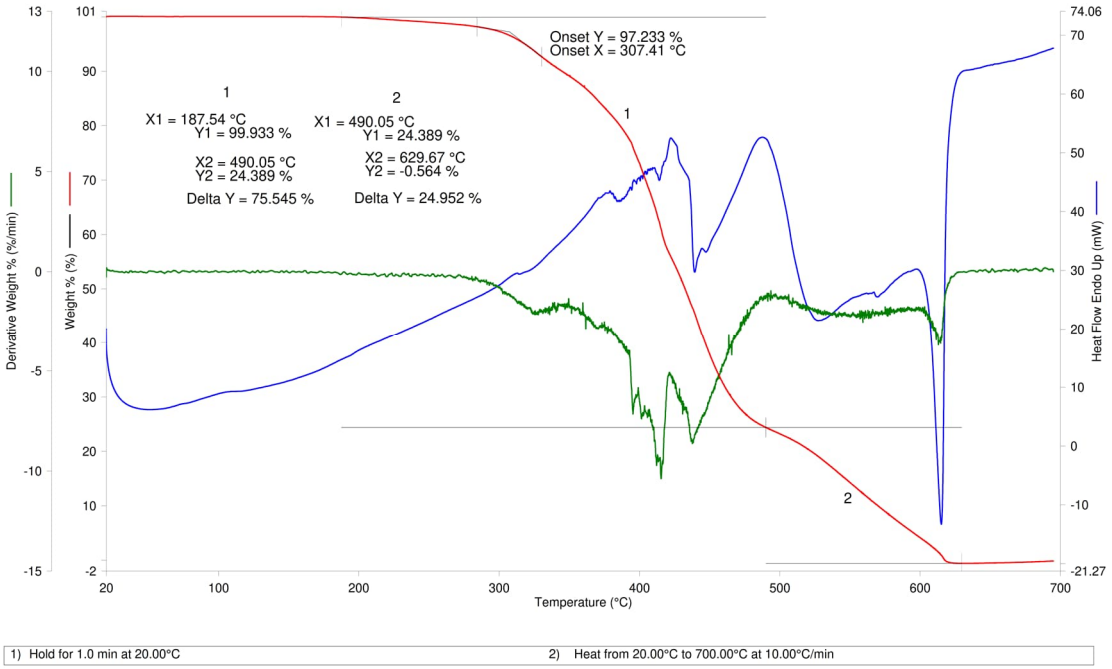

FIGURE A24 TG / DSC graph (Air, 40 ml min^{-1}) of ligand (L2)·$(NTf_2)_3$.

Appendix 14. TG / DSC graphs of selected M_6L_8 assemblies

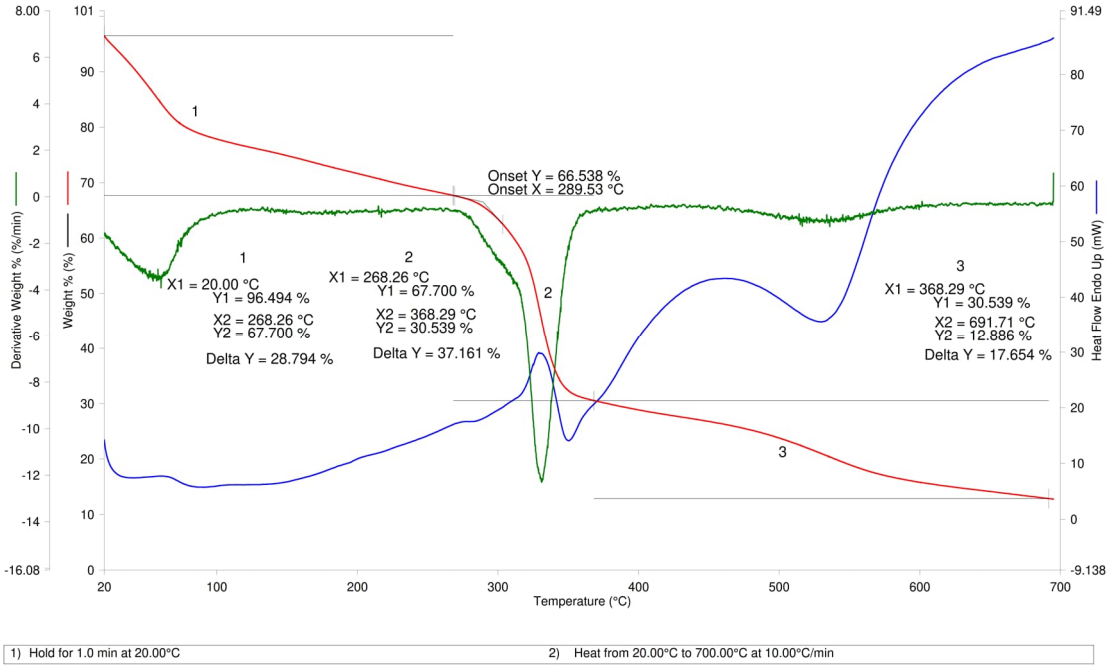

FIGURE A25 TG / DSC graph (Air, 40 ml min^{-1}) of fresh crystals of assembly C3*.

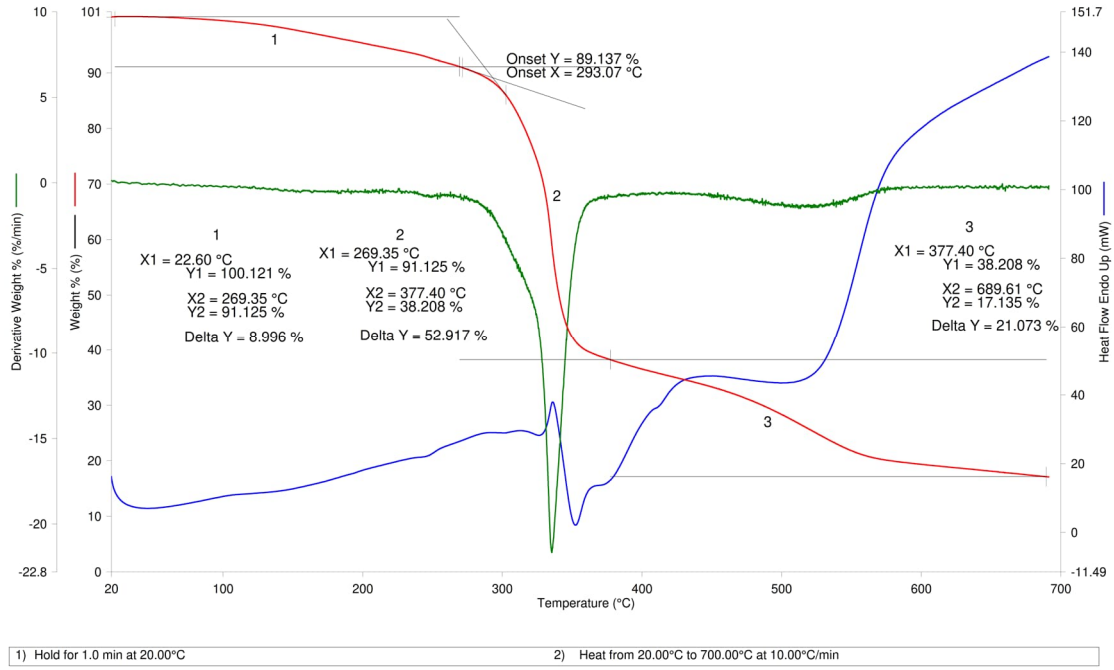

FIGURE A26 TG / DSC graph (Air, 40 ml min^{-1}) of N_2 dried crystals of assembly C3*.

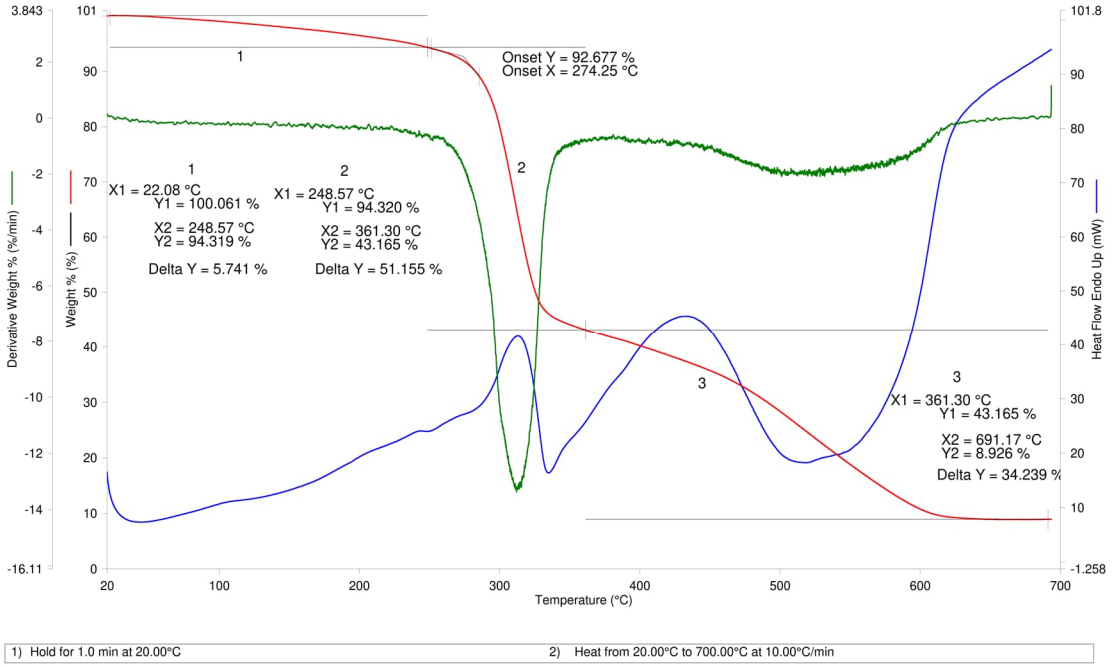

FIGURE A27 TG / DSC graph (Air, 40 ml min^{-1}) of assembly C4.

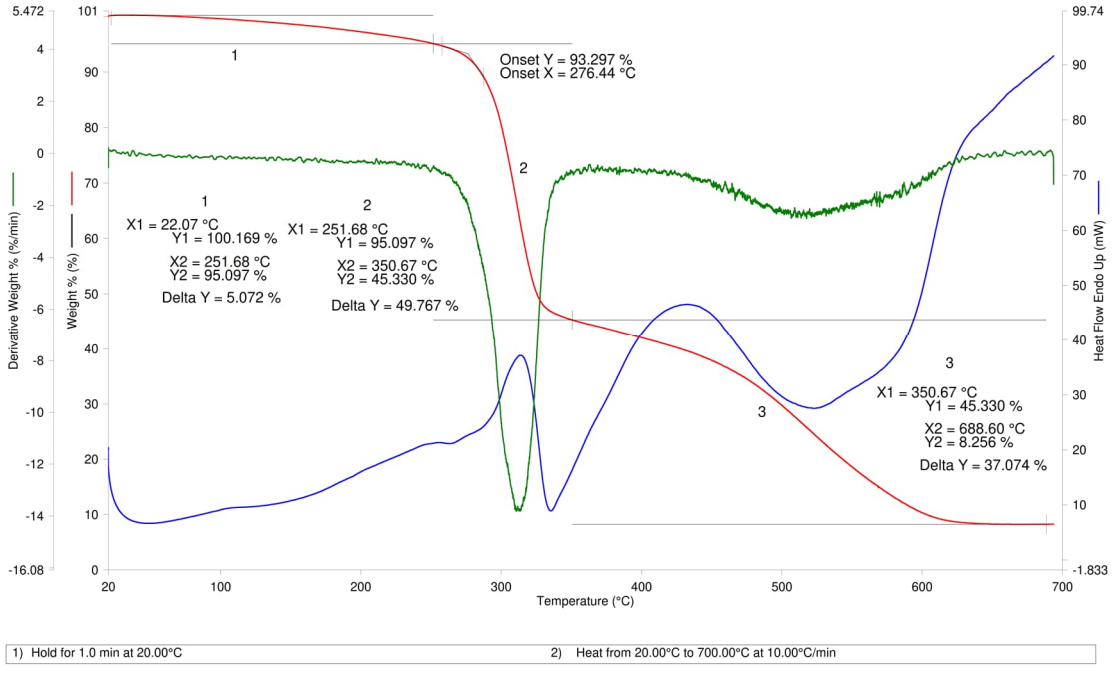

FIGURE A28 TG / DSC graph (Air, 40 ml min^{-1}) of assembly C5.

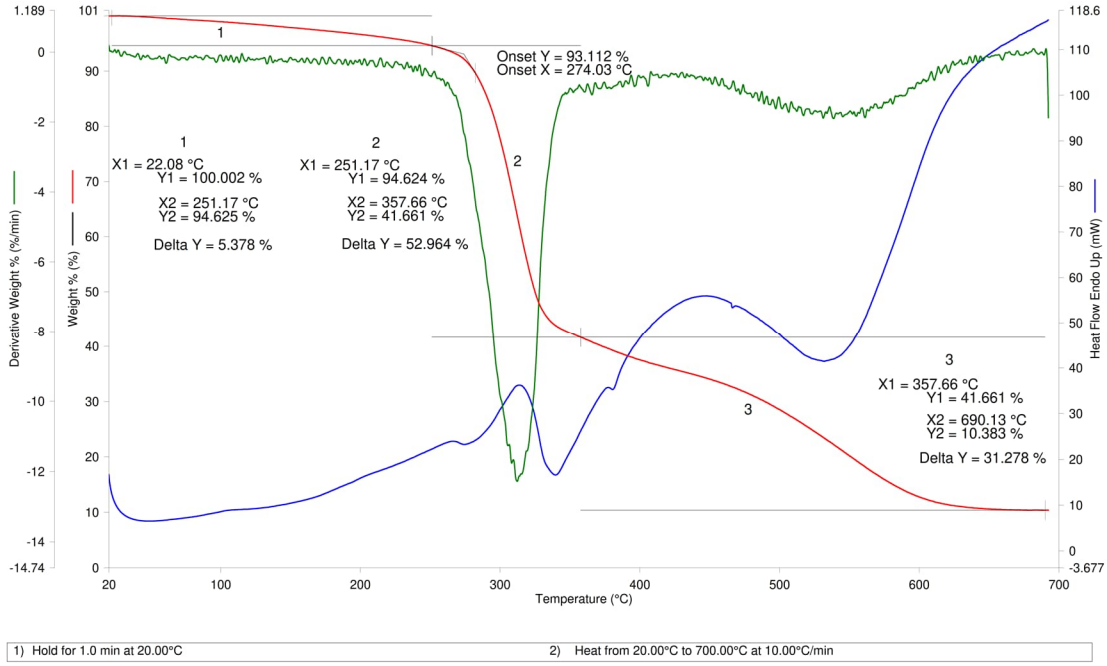

FIGURE A29 TG / DSC graph (Air, 40 ml min^{-1}) of assembly C6.

Appendix 15. TG / DSC graphs of selected dimeric capsules

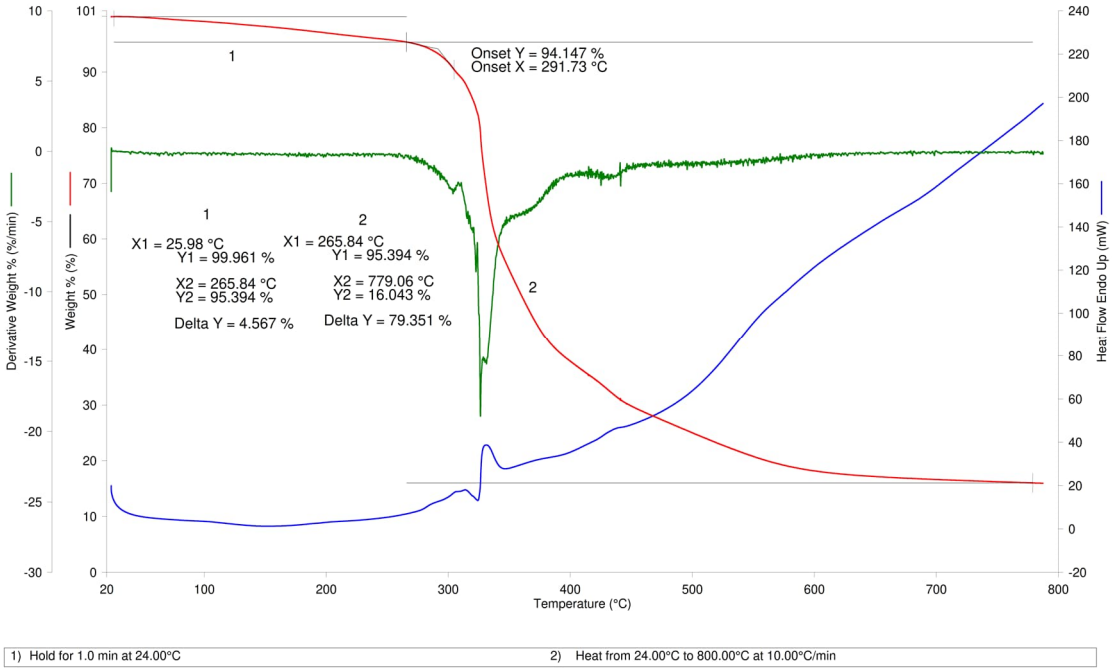

FIGURE A30 TG / DSC graph (N_2, 40 ml min^{-1}) of dimeric capsule D1.

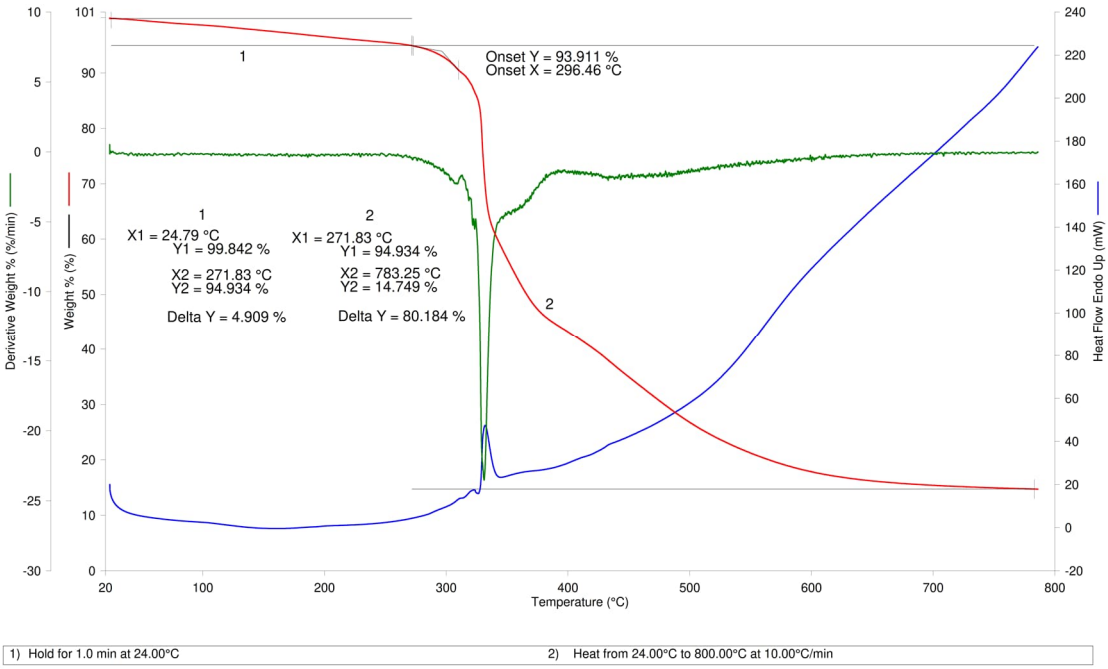

FIGURE A31 TG / DSC graph (N_2, 40 ml min^{-1}) of dimeric capsule D2.

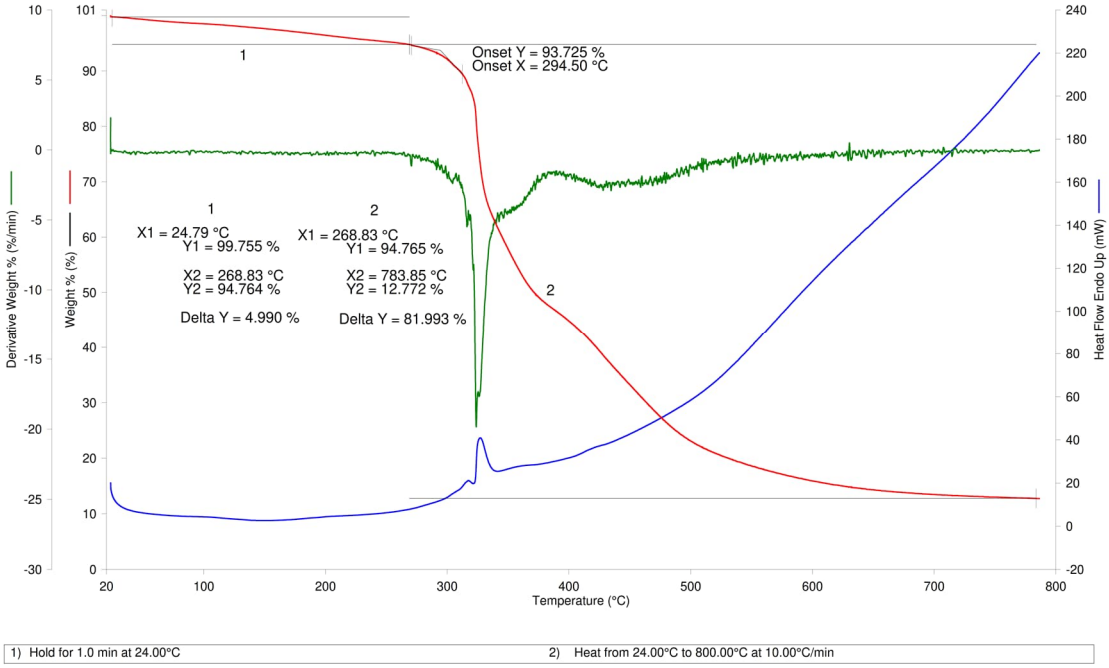

FIGURE A32 TG / DSC graph (N_2, 40 ml min^{-1}) of dimeric capsule D3.

DEPARTMENT OF CHEMISTRY, UNIVERSITY OF JYVÄSKYLÄ
RESEARCH REPORT SERIES

1. Vuolle, Mikko: Electron paramagnetic resonance and molecular orbital study of radical ions generated from (2.2)metacyclophane, pyrene and its hydrogenated compounds by alkali metal reduction and by thallium(III)trifluoroacetate oxidation. (99 pp.) 1976
2. Pasanen, Kaija: Electron paramagnetic resonance study of cation radical generated from various chlorinated biphenyls. (66 pp.) 1977
3. Carbon-13 Workshop, September 6-8, 1977. (91 pp.) 1977
4. Laihia, Katri: On the structure determination of norbornane polyols by NMR spectroscopy. (111 pp.) 1979
5. Nyrönen, Timo: On the EPR, ENDOR and visible absorption spectra of some nitrogen containing heterocyclic compounds in liquid ammonia. (76 pp.) 1978
6. Talvitie, Antti: Structure determination of some sesquiterpenoids by shift reagent NMR. (54 pp.) 1979
7. Häkli, Harri: Structure analysis and molecular dynamics of cyclic compounds by shift reagent NMR. (48 pp.) 1979
8. Pitkänen, Ilkka: Thermodynamics of complexation of 1,2,4-triazole with divalent manganese, cobalt, nickel, copper, zinc, cadmium and lead ions in aqueous sodium perchlorate solutions. (89 pp.) 1980
9. Asunta, Tuula: Preparation and characterization of new organometallic compounds synthesized by using metal vapours. (91 pp.) 1980
10. Sattar, Mohammad Abdus: Analyses of MCPA and its metabolites in soil. (57 pp.) 1980
11. Bibliography 1980. (31 pp.) 1981
12. Knuuttila, Pekka: X-Ray structural studies on some divalent 3d metal compounds of picolinic and isonicotinic acid N-oxides. (77 pp.) 1981
13. Bibliography 1981. (33 pp.) 1982
14. 6^{th} National NMR Symposium, September 9-10, 1982, Abstracts. (49 pp.) 1982
15. Bibliography 1982. (38 pp.) 1983
16. Knuuttila, Hilkka: X-Ray structural studies on some Cu(II), Co(II) and Ni(II) complexes with nicotinic and isonicotinic acid N-oxides. (54 pp.) 1983
17. Symposium on inorganic and analytical chemistry May 18, 1984, Program and Abstracts. (100 pp.) 1984
18. Knuutinen, Juha: On the synthesis, structure verification and gas chromatographic determination of chlorinated catechols and guaiacols occuring in spent bleach liquors of kraft pulp mill. (30 pp.) 1984
19. Bibliography 1983. (47 pp.) 1984
20. Pitkänen, Maija: Addition of BrCl, B_2 and Cl_2 to methyl esters of propenoic and 2-butenoic acid derivatives and ^{13}C NMR studies on methyl esters of saturated aliphatic mono- and dichlorocarboxylic acids. (56 pp.) 1985
21. Bibliography 1984. (39 pp.) 1985
22. Salo, Esa: EPR, ENDOR and TRIPLE spectroscopy of some nitrogen heteroaromatics in liquid ammonia. (111 pp.) 1985

23. Humppi, Tarmo: Synthesis, identification and analysis of dimeric impurities of chlorophenols. (39 pp.) 1985
24. Aho, Martti: The ion exchange and adsorption properties of sphagnum peat under acid conditions. (90 pp.) 1985
25. Bibliography 1985 (61 pp.) 1986
26. Bibliography 1986. (23 pp.) 1987
27. Bibliography 1987. (26 pp.) 1988
28. Paasivirta, Jaakko (Ed.): Structures of organic environmental chemicals. (67 pp.) 1988
29. Paasivirta, Jaakko (Ed.): Chemistry and ecology of organo-element compounds. (93 pp.) 1989
30. Sinkkonen, Seija: Determination of crude oil alkylated dibenzothiophenes in environment. (35 pp.) 1989
31. Kolehmainen, Erkki (Ed.): XII National NMR Symposium Program and Abstracts. (75 pp.) 1989
32. Kuokkanen, Tauno: Chlorocymenes and Chlorocymenenes: Persistent chlorocompounds in spent bleach liquors of kraft pulp mills. (40 pp.) 1989
33. Mäkelä, Reijo: ESR, ENDOR and TRIPLE resonance study on substituted 9,10-anthraquinone radicals in solution. (35 pp.) 1990
34. Veijanen, Anja: An integrated sensory and analytical method for identification of off-flavour compounds. (70 pp.) 1990
35. Kasa, Seppo: EPR, ENDOR and TRIPLE resonance and molecular orbital studies on a substitution reaction of anthracene induced by thallium(III) in two fluorinated carboxylic acids. (114 pp.) 1990
36. Herve, Sirpa: Mussel incubation method for monitoring organochlorine compounds in freshwater recipients of pulp and paper industry. (145 pp.) 1991
37. Pohjola, Pekka: The electron paramagnetic resonance method for characterization of Finnish peat types and iron (III) complexes in the process of peat decomposition. (77 pp.) 1991
38. Paasivirta, Jaakko (Ed.): Organochlorines from pulp mills and other sources. Research methodology studies 1988-91. (120 pp.) 1992
39. Veijanen, Anja (Ed.): VI National Symposium on Mass Spectrometry, May 13-15, 1992, Abstracts. (55 pp.) 1992
40. Rissanen, Kari (Ed.): The 7. National Symposium on Inorganic and Analytical Chemistry, May 22, 1992, Abstracts and Program. (153 pp.) 1992
41. Paasivirta, Jaakko (Ed.): CEOEC'92, Second Finnish-Russian Seminar: Chemistry and Ecology of Organo-Element Compounds. (93 pp.) 1992
42. Koistinen, Jaana: Persistent polychloroaromatic compounds in the environment: structure-specific analyses. (50 pp.) 1993
43. Virkki, Liisa: Structural characterization of chlorolignins by spectroscopic and liquid chromatographic methods and a comparison with humic substances. (62 pp.) 1993
44. Helenius, Vesa: Electronic and vibrational excitations in some

biologically relevant molecules. (30 pp.) 1993

45. Leppä-aho, Jaakko: Thermal behaviour, infrared spectra and x-ray structures of some new rare earth chromates(VI). (64 pp.) 1994
46. Kotila, Sirpa: Synthesis, structure and thermal behavior of solid copper(II) complexes of 2-amino-2- hydroxymethyl-1,3-propanediol. (111 pp.) 1994
47. Mikkonen, Anneli: Retention of molybdenum(VI), vanadium(V) and tungsten(VI) by kaolin and three Finnish mineral soils. (90 pp.) 1995
48. Suontamo, Reijo: Molecular orbital studies of small molecules containing sulfur and selenium. (42 pp.) 1995
49. Hämäläinen, Jouni: Effect of fuel composition on the conversion of fuel-N to nitrogen oxides in the combustion of small single particles. (50 pp.) 1995
50. Nevalainen, Tapio: Polychlorinated diphenyl ethers: synthesis, NMR spectroscopy, structural properties, and estimated toxicity. (76 pp.) 1995
51. Aittola, Jussi-Pekka: Organochloro compounds in the stack emission. (35 pp.) 1995
52. Harju, Timo: Ultrafast polar molecular photophysics of (dibenzylmethine)borondifluoride and 4-aminophthalimide in solution. (61 pp.) 1995
53. Maatela, Paula: Determination of organically bound chlorine in industrial and environmental samples. (83 pp.) 1995
54. Paasivirta, Jaakko (Ed.): CEOEC'95, Third Finnish-Russian Seminar: Chemistry and Ecology of Organo-Element Compounds. (109 pp.) 1995
55. Huuskonen, Juhani: Synthesis and structural studies of some supramolecular compounds. (54 pp.) 1995
56. Palm, Helena: Fate of chlorophenols and their derivatives in sawmill soil and pulp mill recipient environments. (52 pp.) 1995
57. Rantio, Tiina: Chlorohydrocarbons in pulp mill effluents and their fate in the environment. (89 pp.) 1997
58. Ratilainen, Jari: Covalent and non-covalent interactions in molecular recognition. (37 pp.) 1997
59. Kolehmainen, Erkki (Ed.): XIX National NMR Symposium, June 4-6, 1997, Abstracts. (89 pp.) 1997
60. Matilainen, Rose: Development of methods for fertilizer analysis by inductively coupled plasma atomic emission spectrometry. (41 pp.) 1997
61. Koistinen, Jari (Ed.): Spring Meeting on the Division of Synthetic Chemistry, May 15-16, 1997, Program and Abstracts. (36 pp.) 1997
62. Lappalainen, Kari: Monomeric and cyclic bile acid derivatives: syntheses, NMR spectroscopy and molecular recognition properties. (50 pp.) 1997
63. Laitinen, Eira: Molecular dynamics of cyanine dyes and phthalimides in solution: picosecond laser studies. (62 pp.) 1997
64. Eloranta, Jussi: Experimental and theoretical studies on some

quinone and quinol radicals. (40 pp.) 1997

65. Oksanen, Jari: Spectroscopic characterization of some monomeric and aggregated chlorophylls. (43 pp.) 1998
66. Häkkänen, Heikki: Development of a method based on laser-induced plasma spectrometry for rapid spatial analysis of material distributions in paper coatings. (60 pp.) 1998
67. Virtapohja, Janne: Fate of chelating agents used in the pulp and paper industries. (58 pp.) 1998
68. Airola, Karri: X-ray structural studies of supramolecular and organic compounds. (39 pp.) 1998
69. Hyötyläinen, Juha: Transport of lignin–type compounds in the receiving waters of pulp mills. (40 pp.) 1999
70. Ristolainen, Matti: Analysis of the organic material dissolved during totally chlorine-free bleaching. (40 pp.) 1999
71. Eklin, Tero: Development of analytical procedures with industrial samples for atomic emission and atomic absorption spectrometry. (43 pp.) 1999
72. Välisaari, Jouni: Hygiene properties of resol-type phenolic resin laminates. (129 pp.) 1999
73. Hu, Jiwei: Persistent polyhalogenated diphenyl ethers: model compounds syntheses, characterization and molecular orbital studies. (59 pp.) 1999
74. Malkavaara, Petteri: Chemometric adaptations in wood processing chemistry. (56 pp.) 2000
75. Kujala Elena, Laihia Katri, Nieminen Kari (Eds.): NBC 2000, Symposium on Nuclear, Biological and Chemical Threats in the 21st Century. (299 pp.) 2000
76. Rantalainen, Anna-Lea: Semipermeable membrane devices in monitoring persistent organic pollutants in the environment. (58 pp.) 2000
77. Lahtinen, Manu: *In situ* X-ray powder diffraction studies of Pt/C, CuCl/C and Cu_2O/C catalysts at elevated temperatures in various reaction conditions. (92 pp.) 2000
78. Tamminen, Jari: Syntheses, empirical and theoretical characterization, and metal cation complexation of bile acid-based monomers and open/closed dimers. (54 pp.) 2000
79. Vatanen, Virpi: Experimental studies by EPR and theoretical studies by DFT calculations of α-amino-9,10-anthraquinone radical anions and cations in solution. (37 pp.) 2000
80. Kotilainen, Risto: Chemical changes in wood during heating at 150-260 °C. (57 pp.) 2000
81. Nissinen, Maija: X-ray structural studies on weak, non-covalent interactions in supramolecular compounds. (69 pp.) 2001
82. Wegelius, Elina: X-ray structural studies on self-assembled hydrogen-bonded networks and metallosupramolecular complexes. (84 pp.) 2001
83. Paasivirta, Jaakko (Ed.): CEOEC'2001, Fifth Finnish-Russian Seminar: Chemistry and Ecology of Organo-Element Compounds. (163 pp.) 2001
84. Kiljunen, Toni: Theoretical studies on spectroscopy and

atomic dynamics in rare gas solids. (56 pp.) 2001

85. Du, Jin: Derivatives of dextran: synthesis and applications in oncology. (48 pp.) 2001
86. Koivisto, Jari: Structural analysis of selected polychlorinated persistent organic pollutants (POPs) and related compounds. (88 pp.) 2001
87. Feng, Zhinan: Alkaline pulping of non-wood feedstocks and characterization of black liquors. (54 pp.) 2001
88. Halonen, Markku: Lahon havupuun käyttö sulfaattiprosessin raaka-aineena sekä havupuun lahontorjunta. (90 pp.) 2002
89. Falábu, Dezsö: Synthesis, conformational analysis and complexation studies of resorcarene derivatives. (212 pp.) 2001
90. Lehtovuori, Pekka: EMR spectroscopic studies on radicals of ubiquinones Q-*n*, vitamin K_3 and vitamine E in liquid solution. (40 pp.) 2002
91. Perkkalainen, Paula: Polymorphism of sugar alcohols and effect of grinding on thermal behavior on binary sugar alcohol mixtures. (53 pp.) 2002
92. Ihalainen, Janne: Spectroscopic studies on light-harvesting complexes of green plants and purple bacteria. (42 pp.) 2002
93. Kunttu, Henrik, Kiljunen, Toni (Eds.): 4th International Conference on Low Temperature Chemistry. (159 pp.) 2002
94. Väisänen, Ari: Development of methods for toxic element analysis in samples with environmental concern by ICP-AES and ETAAS. (54 pp.) 2002
95. Luostarinen, Minna: Synthesis and characterisation of novel resorcarene derivatives. (200 pp.) 2002
96. Louhelainen, Jarmo: Changes in the chemical composition and physical properties of wood and nonwood black liquors during heating. (68 pp.) 2003
97. Lahtinen, Tanja: Concave hydrocarbon cyclophane π-prismands. (65 pp.) 2003
98. Laihia, Katri (Ed.): NBC 2003, Symposium on Nuclear, Biological and Chemical Threats – A Crisis Management Challenge. (245 pp.) 2003
99. Oasmaa, Anja: Fuel oil quality properties of wood-based pyrolysis liquids. (32 pp.) 2003
100. Virtanen, Elina: Syntheses, structural characterisation, and cation/anion recognition properties of nano-sized bile acid-based host molecules and their precursors. (123 pp.) 2003
101. Nättinen, Kalle: Synthesis and X-ray structural studies of organic and metallo-organic supramolecular systems. (79 pp.) 2003
102. Lampiselkä, Jarkko: Demonstraatio lukion kemian opetuksessa. (285 pp.) 2003
103. Kallioinen, Jani: Photoinduced dynamics of $Ru(dcbpy)_2(NCS)_2$ – in solution and on nanocrystalline titanium dioxide thin films. (47 pp.) 2004
104. Valkonen, Arto (Ed.): VII Synthetic Chemistry Meeting and XXVI Finnish NMR Symposium. (103 pp.) 2004

105. Vaskonen, Kari: Spectroscopic studies on atoms and small molecules isolated in low temperature rare gas matrices. (65 pp.) 2004
106. Lehtovuori, Viivi: Ultrafast light induced dissociation of $Ru(dcbpy)(CO)_2I_2$ in solution. (49 pp.) 2004
107. Saarenketo, Pauli: Structural studies of metal complexing Schiff bases, Schiff base derived *N*-glycosides and cyclophane π-prismands. (95 pp.) 2004
108. Paasivirta, Jaakko (Ed.): CEOEC'2004, Sixth Finnish-Russian Seminar: Chemistry and Ecology of Organo-Element Compounds. (147 pp.) 2004
109. Suontamo, Tuula: Development of a test method for evaluating the cleaning efficiency of hard-surface cleaning agents. (96 pp.) 2004
110. Güneş, Minna: Studies of thiocyanates of silver for nonlinear optics. (48 pp.) 2004
111. Ropponen, Jarmo: Aliphatic polyester dendrimers and dendrons. (81 pp.) 2004
112. Vu, Mân Thi Hong: Alkaline pulping and the subsequent elemental chlorine-free bleaching of bamboo (*Bambusa procera*). (69 pp.) 2004
113. Mansikkamäki, Heidi: Self-assembly of resorcinarenes. (77 pp.) 2006
114. Tuononen, Heikki M.: EPR spectroscopic and quantum chemical studies of some inorganic main group radicals. (79 pp.) 2005
115. Kaski, Saara: Development of methods and applications of laser-induced plasma spectroscopy in vacuum ultraviolet. (44 pp.) 2005
116. Mäkinen, Riika-Mari: Synthesis, crystal structure and thermal decomposition of certain metal thiocyanates and organic thiocyanates. (119 pp.) 2006
117. Ahokas, Jussi: Spectroscopic studies of atoms and small molecules isolated in rare gas solids: photodissociation and thermal reactions. (53 pp.) 2006
118. Busi, Sara: Synthesis, characterization and thermal properties of new quaternary ammonium compounds: new materials for electrolytes, ionic liquids and complexation studies. (102 pp.) 2006
119. Mäntykoski, Keijo: PCBs in processes, products and environment of paper mills using wastepaper as their raw material. (73 pp.) 2006
120. Laamanen, Pirkko-Leena: Simultaneous determination of industrially and environmentally relevant aminopolycarboxylic and hydroxycarboxylic acids by capillary zone electrophoresis. (54 pp.) 2007
121. Salmela, Maria: Description of oxygen-alkali delignification of kraft pulp using analysis of dissolved material. (71 pp.) 2007
122. Lehtovaara, Lauri: Theoretical studies of atomic scale impurities in superfluid ^{4}He. (87 pp.) 2007
123. Rautiainen, J. Mikko: Quantum chemical calculations of structures, bonding, and spectroscopic properties of some sulphur and selenium iodine cations. (71 pp.) 2007
124. Nummelin, Sami: Synthesis, characterization, structural and

retrostructural analysis of self-assembling pore forming dendrimers. (286 pp.) 2008

125. Sopo, Harri: Uranyl(VI) ion complexes of some organic aminobisphenolate ligands: syntheses, structures and extraction studies. (57 pp.) 2008
126. Valkonen, Arto: Structural characteristics and properties of substituted cholanoates and *N*-substituted cholanamides. (80 pp.) 2008
127. Lähde, Anna: Production and surface modification of pharmaceutical nano- and microparticles with the aerosol flow reactor. (43 pp.) 2008
128. Beyeh, Ngong Kodiah: Resorcinarenes and their derivatives: synthesis, characterization and complexation in gas phase and in solution. (75 pp.) 2008
129. Välisaari, Jouni, Lundell, Jan (Eds.): Kemian opetuksen päivät 2008: uusia oppimisympäristöjä ja ongelmalähtöistä opetusta. (118 pp.) 2008
130. Myllyperkiö, Pasi: Ultrafast electron transfer from potential organic and metal containing solar cell sensitizers. (69 pp.) 2009
131. Käkölä, Jaana: Fast chromatographic methods for determining aliphatic carboxylic acids in black liquors. (82 pp.) 2009
132. Koivukorpi, Juha: Bile acid-arene conjugates: from photoswitchability to cancer cell detection. (67 pp.) 2009
133. Tuuttila, Tero: Functional dendritic polyester compounds: synthesis and characterization of small bifunctional dendrimers and dyes. (74 pp.) 2009
134. Salorinne, Kirsi: Tetramethoxy resorcinarene based cation and anion receptors: synthesis, characterization and binding properties. (79 pp.) 2009
135. Rautiainen, Riikka: The use of first-thinning Scots pine (*Pinus sylvestris*) as fiber raw material for the kraft pulp and paper industry. (73 pp.) 2010
136. Ilander, Laura: Uranyl salophens: synthesis and use as ditopic receptors. (199 pp.) 2010
137. Kiviniemi, Tiina: Vibrational dynamics of iodine molecule and its complexes in solid krypton - Towards coherent control of bimolecular reactions? (73 pp.) 2010
138. Ikonen, Satu: Synthesis, characterization and structural properties of various covalent and non-covalent bile acid derivatives of N/O-heterocycles and their precursors. (105 pp.) 2010
139. Siitonen, Anni: Spectroscopic studies of semiconducting single-walled carbon nanotubes. (56 pp.) 2010
140. Raatikainen, Kari: Synthesis and structural studies of piperazine cyclophanes – Supramolecular systems through Halogen and Hydrogen bonding and metal ion coordination. (69 pp.) 2010
141. Leivo, Kimmo: Gelation and gel properties of two- and three-component Pyrene based low molecular weight organogelators. (116 pp.) 2011
142. Martiskainen, Jari: Electronic energy transfer in light-harvesting complexes isolated from *Spinacia oleracea* and from three

photosynthetic green bacteria *Chloroflexus aurantiacus*, *Chlorobium tepidum*, and *Prosthecochloris aestuarii*. (55 pp.) 2011

143. Wichmann, Oula: Syntheses, characterization and structural properties of [O,N,O,X´] aminobisphenolate metal complexes. (101 pp.) 2011
144. Ilander, Aki: Development of ultrasound-assisted digestion methods for the determination of toxic element concentrations in ash samples by ICP-OES. (58 pp.) 2011
145. The Combined XII Spring Meeting of the Division of Synthetic Chemistry and XXXIII Finnish NMR Symposium. Book of Abstracts. (90 pp.) 2011
146. Valto, Piia: Development of fast analysis methods for extractives in papermaking process waters. (73 pp.) 2011
147. Andersin, Jenni: Catalytic activity of palladium-based nanostructures in the conversion of simple olefinic hydro- and chlorohydrocarbons from first principles. (78 pp.) 2011
148. Aumanen, Jukka: Photophysical properties of dansylated poly(propylene amine) dendrimers. (55 pp.) 2011
149. Kärnä, Minna: Ether-functionalized quaternary ammonium ionic liquids – synthesis, characterization and physicochemical properties. (76 pp.) 2011
150. Jurček, Ondřej: Steroid conjugates for applications in pharmacology and biology. (57 pp.) 2011
151. Nauha, Elisa: Crystalline forms of selected Agrochemical actives: design and synthesis of cocrystals. (77 pp.) 2012
152. Ahkola, Heidi: Passive sampling in monitoring of nonylphenol ethoxylates and nonylphenol in aquatic environments. (92 pp.) 2012
153. Helttunen, Kaisa: Exploring the self-assembly of resorcinarenes: from molecular level interactions to mesoscopic structures. (78 pp.) 2012
154. Linnanto, Juha: Light excitation transfer in photosynthesis revealed by quantum chemical calculations and exiton theory. (179 pp.) 2012
155. Roiko-Jokela, Veikko: Digital imaging and infrared measurements of soil adhesion and cleanability of semihard and hard surfaces. (122 pp.) 2012
156. Noponen, Virpi: Amides of bile acids and biologically important small molecules: properties and applications. (85 pp.) 2012
157. Hulkko, Eero: Spectroscopic signatures as a probe of structure and dynamics in condensed-phase systems – studies of iodine and gold ranging from isolated molecules to nanoclusters. (69 pp.) 2012
158. Lappi, Hanna: Production of Hydrocarbon-rich biofuels from extractives-derived materials. (95 pp.) 2012
159. Nykänen, Lauri: Computational studies of Carbon chemistry on transition metal surfaces. (76 pp.) 2012
160. Ahonen, Kari: Solid state studies of pharmaceutically important molecules and their derivatives. (65 pp.) 2012

161. Pakkanen, Hannu: Characterization of organic material dissolved during alkaline pulping of wood and non-wood feedstocks. (76 pp.) 2012
162. Moilanen, Jani: Theoretical and experimental studies of some main group compounds: from closed shell interactions to singlet diradicals and stable radicals. (80 pp.) 2012
163. Himanen, Jatta: Stereoselective synthesis of Oligosaccharides by *De Novo* Saccharide welding. (133 pp.) 2012
164. Bunzen, Hana: Steroidal derivatives of nitrogen containing compounds as potential gelators. (76 pp.) 2013
165. Seppälä, Petri: Structural diversity of copper(II) amino alcohol complexes. Syntheses, structural and magnetic properties of bidentate amino alcohol copper(II) complexes. (67 pp.) 2013
166. Lindgren, Johan: Computational investigations on rotational and vibrational spectroscopies of some diatomics in solid environment. (77 pp.) 2013
167. Giri, Chandan: Sub-component self-assembly of linear and non-linear diamines and diacylhydrazines, formulpyridine and transition metal cations. (145 pp.) 2013
168. Riisiö, Antti: Synthesis, Characterization and Properties of Cu(II)-, Mo(VI)- and U(VI) Complexes With Diaminotetraphenolate Ligands. (51 pp.) 2013
169. Kiljunen, Toni (Ed.): Chemistry and Physics at Low Temperatures. Book of Abstracts. (103 pp.) 2013
170. Hänninen, Mikko: Experimental and Computational Studies of Transition Metal Complexes with Polydentate Amino- and Aminophenolate Ligands: Synthesis, Structure, Reactivity and Magnetic Properties. (66 pp.) 2013
171. Antila, Liisa: Spectroscopic studies of electron transfer reactions at the photoactive electrode of dye-sensitized solar cells. (53 pp.) 2013
172. Kemppainen, Eeva: Mukaiyama-Michael reactions with α-substituted acroleins – a useful tool for the synthesis of the pectenotoxins and other natural product targets. (190 pp.) 2013
173. Virtanen, Suvi: Structural Studies of Dielectric Polymer Nanocomposites. (49 pp.) 2013
174. Yliniemelä-Sipari, Sanna: Understanding The Structural Requirements for Optimal Hydrogen Bond Catalyzed Enolization – A Biomimetic Approach.(160 pp.) 2013
175. Leskinen, Mikko V: Remote β-functionalization of β'-keto esters. (105 pp.) 2014
176. 12th European Conference on Research in Chemistry Education (ECRICE2014). Book of Abstracts. (166 pp.) 2014
177. Peuronen, Anssi: N-Monoalkylated DABCO-Based N-Donors as Versatile Building Blocks in Crystal Engineering and Supramolecular Chemistry. (54 pp.) 2014
178. Perämäki, Siiri: Method development for determination and recovery of rare earth elements from industrial fly ash. (88 pp.) 2014

179. Chernyshev, Alexander, N.: Nitrogen-containing ligands and their platinum(IV) and gold(III) complexes: investigation and basicity and nucleophilicity, luminescence, and aurophilic interactions. (64 pp.) 2014
180. Lehto, Joni: Advanced Biorefinery Concepts Integrated to Chemical Pulping. (142 pp.) 2015
181. Tero, Tiia-Riikka: Tetramethoxy resorcinarenes as platforms for fluorescent and halogen bonding systems. (61 pp.) 2015
182. Löfman, Miika: Bile acid amides as components of microcrystalline organogels. (62 pp.) 2015
183. Selin, Jukka: Adsorption of softwood-derived organic material onto various fillers during papermaking. (169 pp.) 2015
184. Piisola, Antti: Challenges in the stereoselective synthesis of allylic alcohols. (210 pp.) 2015
185. Bonakdarzadeh, Pia: Supramolecular coordination polyhedra based on achiral and chiral pyridyl ligands: design, preparation, and characterization. (65 pp.) 2015
186. Vasko, Petra: Synthesis, characterization, and reactivity of heavier group 13 and 14 metallylenes and metalloid clusters: small molecule activation and more. (66 pp.) 2015
187. Topić, Filip: Structural Studies of Nano-sized Supramolecular Assemblies. (79 pp.) 2015
188. Mustalahti, Satu: Photodynamics Studies of Ligand-Protected Gold Nanoclusters by using Ultrafast Transient Infrared Spectroscopy. (58 pp.) 2015
189. Koivisto, Jaakko: Electronic and vibrational spectroscopic studies of gold-nanoclusters. (63 pp.) 2015
190. Suhonen, Aku: Solid state conformational behavior and interactions of series of aromatis oligoamide foldamers. (68 pp.) 2016
191. Soikkeli, Ville: Hydrometallurgical recovery and leaching studies for selected valuable metals from fly ash samples by ultrasound-assisted extraction followed by ICP-OES determination. (107 pp.) 2016
192. XXXVIII Finnish NMR Symposium. Book of Abstracts. (51 pp.) 2016
193. Mäkelä, Toni: Ion Pair Recognition by Ditopic Crown Ether Based bis-Urea and Uranyl Salophen Receptors. (75 pp.) 2016
194. Lindholm-Lehto, Petra: Occurrence of pharmaceuticals in municipal wastewater treatment plants and receiving surface waters in Central and Southern Finland. (98 pp.) 2016
195. Härkönen, Ville: Computational and Theoretical studies on Lattice Thermal conductivity and Thermal properties of Silicon Clathrates. (89 pp.) 2016
196. Tuokko, Sakari: Understanding selective reduction reactions with heterogeneous Pd and Pt: climbing out of the black box. (85 pp.) 2016
197. Nuora, Piia: Monitapaustutkimus LUMA-Toimintaan liittyvissä oppimisympäristöissä tapahtuvista kemian oppimiskokemuksista. (171 pp.) 2016

198. Kumar, Hemanathan: Novel Concepts on The Recovery of By-Products from Alkaline Pulping. (61 pp.) 2016
199. Arnedo-Sánchez, Leticia: Lanthanide and Transition Metal Complexes as Building Blocks for Supramolecular Functional Materials. (227 pp.) 2016
200. Gell, Lars: Theoretical Investigations of Ligand Protected Silver Nanoclusters. (134 pp.) 2016
201. Vaskuri, Juhani: Oppiennätyksistä opetussuunnitelman perusteisiin - lukion kemian kansallisen opetussuunnitelman kehittyminen Suomessa vuosina 1918-2016. (314 pp.) 2017
202. Lundell Jan, Kiljunen Toni (Eds.): 22nd Horizons in Hydrogen Bond Research. Book of Abstracts. 2017
203. Turunen, Lotta: Design and construction of halogen-bonded capsules and cages. (61 pp.) 2017
204. Hurmalainen, Juha: Experimental and computational studies of unconventional main group compounds: stable radicals and reactive intermediates. (88 pp.) 2017
205. Koivistoinen Juha: Non-linear interactions of femtosecond laser pulses with graphene: photo-oxidation, imaging and photodynamics. (68 pp.) 2017
206. Chen, Chengcong: Combustion behavior of black liquors: droplet swelling and influence of liquor composition. (39 pp.) 2017
207. Mansikkamäki, Akseli: Theoretical and Computational Studies of Magnetic Anisotropy and Exchange Coupling in Molecular Systems. (190 p. + included articles) 2018.
208. Tatikonda, Rajendhraprasad: Multivalent N-donor ligands for the construction of coordination polymers and coordination polymer gels. (62 pp.) 2018
209. Budhathoki, Roshan: Beneficiation, desilication and selective precipitation techniques for phosphorus refining from biomass derived fly ash. (64 pp.) 2018
210. Siitonen, Juha: Synthetic Studies on 1-azabicyclo[5.3.0]decane Alkaloids. (140 pp.) 2018
211. Ullah, Saleem: Advanced Biorefinery Concepts Related to Non-wood Feedstocks. (57 pp.) 2018
212. Ghalibaf, Maryam: Analytical Pyrolysis of Wood and Non-Wood Materials from Integrated Biorefinery Concepts. (106 pp.) 2018

DEPARTMENT OF CHEMISTRY, UNIVERSITY OF JYVÄSKYLÄ
DISSERTATIONS PUBLISHED IN THE JYU DISSERTATIONS RESEARCH SERIES

1. Bulatov, Evgeny: Synthetic and structural studies of covalent and non-covalent interactions of ligands and metal center in platinum(II) complexes containing 2,2′-dipyridylamine or oxime ligands. (58 pp.) 2019. JYU Dissertations 70.
2. Annala, Riia: Conformational Properties and Anion Complexes of Aromatic Oligoamide Foldamers. (80 pp.) 2019. JYU Dissertations 84.
3. Isoaho, Jukka Pekka: Dithionite Bleaching of Thermomechanical Pulp - Chemistry and Optimal Conditions. (73 pp.) 2019. JYU Dissertations 85.
4. Nygrén, Enni: Recovery of rubidium from power plant fly ash. (98 pp.) 2019. JYU Dissertations 136.
5. Kiesilä, Anniina: Supramolecular chemistry of anion-binding receptors based on concave macromolecules. (68 pp.) 2019. JYU Dissertations 137.
6. Sokolowska, Karolina: Study of water-soluble p-MBA-protected gold nanoclusters and their superstructures. (60 pp.) 2019. JYU Dissertations 167.
7. Lahtinen, Elmeri: Chemically Functional 3D Printing: Selective Laser Sintering of Customizable Metal Scavengers. (71 pp.) 2019. JYU Dissertations 175.
8. Larijani, Amir: Oxidative reactions of cellulose under alkaline conditions. (102 pp.) 2020. JYU Dissertations 217.
9. Kolari, Kalle: Metal-metal contacts in late transition metal polymers. (60 pp.) 2020. JYU Dissertations 220.
10. Kauppinen, Minttu: Multiscale computational investigation of catalytic properties of zirconia supported noble metals. (87 pp.) 2020. JYU Dissertations 231.
11. Ding, Xin: Halogen Bond in Crystal Engineering: Structural Studies on Crystals with Ruthenium Centered Complexes and 1-(4-Pyridyl)-4-thiopyridine Zwitterion as Halogen Bond Acceptors. (59 pp.) 2020. JYU Dissertations 323.
12. Neuvonen, Antti: Toward an Understanding of Hydrogen-Bonding Bifunctional Organocatalyst Conformations and Their Activity in Asymmetric Mannich Reactions. (77 pp.) 2020. JYU Dissertations 336.
13. Kortet, Sami: 2,5-Diarylpyrrolidines and Pyroglutamic-Acid-Derived 2-Diarylmethyl-5-Aryl-Pyrrolidines: Their Synthesis and Use in Asymmetric Synthesis. (221 pp.) 2020. JYU Dissertations 337.
14. Saarnio, Ville: Fluorescent probes, noble metal nanoparticles and their nanocomposites: detection of nucleic acids and other biological targets. (80 pp.) 2021. JYU Dissertations 361.
15. Chernysheva, Maria: σ-hole interactions: the effect of the donors and acceptors nature in selenoureas, thioureas, halogenated species, substituted benzenes, and their adducts. (72 pp.) 2021. JYU Dissertations 370.
16. Bulatova, Margarita: Noncovalent interactions as a tool for supramolecular self-assembly of metallopolymers. (62 pp.) 2021. JYU Dissertations 377.

17. Romppanen, Sari: Laser-spectroscopic studies of rare earth element- and lithium-bearing minerals and rocks. (66 pp.) 2021. JYU Dissertations 393.
18. Kukkonen, Esa: Nonlinear optical materials through weak interactions and their application in 3D printing. (58 pp.) 2021. JYU Dissertations 441.
19. Kuosmanen, Riikka: The Effect of Structure on the Gel Formation Ability and the Properties of Bile Acid Based Supramolecular Organogels. (68 pp.) 2021. JYU Dissertations 465.
20. Reuna, Sini: Development of a Method for Phosphorus Recovery from Wastewaters. (67 pp.) 2022. JYU Dissertations 486.
21. Taipale, Essi: Synthetic and Structural Studies on the Effect of Non-Covalent Interactions on N(*sp2*)-Heterocyclic Molecules. (67 pp.) 2022. JYU Dissertations 496.
22. Järvinen, Teemu: Molecular Dynamics View on Matrix Isolation. (143 pp.) 2022. JYU Dissertations 544.
23. Kumar, Parveen: Synthesis and Structural Studies on Halogen(I) Complexes. (160 pp.) 2022. JYU Dissertations 549.